

COMPTES RENDUS DE L'ACADÉMIE DES SCIENCES

1878-1543 (electronic)

Chimie



Volume 24, Special Issue S3, 2021

Special issue / Numéro thématique

MAPYRO: the French Fellowship of the Pyrrolic Macrocyclic Ring /
MAPYRO : la communauté française des macrocycles pyrroliques

Guest editors / Rédacteurs en chef invités

Bernard Boitrel, Jean Weiss

Académie des sciences — Paris



INSTITUT DE FRANCE
Académie des sciences



Comptes Rendus

Chimie

Objective of the journal

Comptes Rendus Chimie is a peer-reviewed electronic journal of international standing, covering all areas of the discipline. It publishes mainly thematic issues, but also original research articles, preliminary announcements, review articles, historical perspectives, pedagogical texts or conference proceedings, without length limit, in English or in French. Comptes Rendus Chimie is published according to a virtuous policy of diamond open access, free for authors (no publication fees) as well as for readers (immediate and permanent open access).

Editorial director: Pascale Cossart

Editors-in-Chief: Pierre Braunstein

Advisory Board: Rick D. Adams, Didier Astruc, Guy Bertrand, Azzedine Bousseksou, Bruno Chaudret, Avelino Corma, Janine Cossy, Patrick Couvreur, Stefanie Dehnen, Paul J. Dyson, Odile Eisenstein, Marc Fontecave, Pierre Grandclaoudon, Robert Guillaumont, Paul Knochel, Daniel Mansuy, Bernard Meunier, Armando J. L. Pombeiro, Michel Pouchard, Didier Roux, João Rocha, Clément Sanchez, Philippe Sautet, Jean-Pierre Sauvage Patrice Simon, Pierre Sinaÿ

Scientific secretary: Julien Desmarets

About the journal

All journal's information, including the text of published articles, which is fully open access, is available from the journal website at <https://comptes-rendus.academie-sciences.fr/chimie/>.

Author enquiries

For enquiries relating to the submission of articles, please visit this journal's homepage at <https://comptes-rendus.academie-sciences.fr/chimie/>.

Contact

Académie des sciences

23, quai de Conti, 75006 Paris, France

Tel: (+33) (0)1 44 41 43 72

CR-Chimie@academie-sciences.fr



The articles in this journal are published under the license
Creative Commons Attribution 4.0 International (CC-BY 4.0)
<https://creativecommons.org/licenses/by/4.0/deed.en>



Contents / Sommaire

Bernard Boitrel, Jean Weiss	
MAPYRO: the French Fellowship of the Pyrrolic Macrocyclic Ring	1-2
Guest editors	3-4
Manel Hanana, Christophe Kahlfuss, Jean Weiss, Renaud Cornut, Bruno Jusselme, Jennifer A. Wytko, Stéphane Campidelli	
ORR activity of metalated phenanthroline-strapped porphyrin adsorbed on carbon nanotubes	5-12
Wael Barakat, Ismail Hijazi, Thierry Roisnel, Vincent Dorcet, Stéphane Le Gac, Bernard Boitrel	
Stereoselective formation of bismuth complexes by transmetalation of lead with adaptable overhanging carboxylic acid 5,10-strapped porphyrins	13-26
Paul-Gabriel Julliard, Simon Pascal, Olivier Siri, Diego Cortés-Arriagada, Luis Sanhueza, Gabriel Canard	
Functionalized porphyrins from <i>meso</i> -poly-halogeno-alkyl-dipyrrromethanes: synthesis and characterization	27-45
Amy Edo-Osagie, Daniel Sánchez-Resca, Dylan Serillon, Elisa Bandini, Christophe Gourlaouen, Henri-Pierre Jacquot de Rouville, Barbara Ventura, Valérie Heitz	
Synthesis, electronic and photophysical properties of a bisacridinium-Zn(II) porphyrin conjugate	47-55
Dandan Yao, Limiao Shi, Zhipeng Sun, Mireille Blanchard-Desce, Olivier Mongin, Frédéric Paul, Christine O. Paul-Roth	
New fluorescent tetraphenylporphyrin-based dendrimers with alkene-linked fluorenyl antennae designed for oxygen sensitization	57-70
W. Ryan Osterloh, Yuanyuan Fang, Nicolas Desbois, Mario L. Naitana, Stéphane Brandès, Sandrine Pacquelet, Claude P. Gros, Karl M. Kadish	
Here's looking at the reduction of noninnocent copper corroles <i>via</i> anion induced electron transfer	71-82
Clémence Rose, Laure Lichon, Morgane Daurat, Sébastien Clément, Magali Gary-Bobo, Sébastien Richeter	
<i>In vitro</i> toxicity and photodynamic properties of porphyrinoids bearing imidazolium salts and N-heterocyclic carbene gold(I) complexes	83-99
Adelais Trapali, Philipp Gotico, Christian Herrero, Minh-Huong Ha-Thi, Thomas Pino, Winfried Leibl, Georgios Charalambidis, Athanassios Coutsolelos, Zakaria Halime, Ally Aukauloo	
Imbroglio at a photoredox-iron-porphyrin catalyst dyad for the photocatalytic CO ₂ reduction	101-114

Raphaël Lamare, Romain Ruppert, Mourad Elhabiri, Gilles Ulrich, Laurent Ruhlmann, Jean Weiss	
Design and synthesis of charged porphyrin dimers for polyoxometalate recognition .	115-126
Soukaina Bouramtane, Ludovic Bretin, Jérémy Godard, Aline Pinon, Yves Champavier, Yann Launay, David Léger, Bertrand Liagre, Vincent Sol, Vincent Chaleix, Frédérique Brégier	
Design and synthesis of triphenylphosphonium-porphyrin@xylylene nanoparticles for anticancer photodynamic therapy	127-140
Zhaohui Huo, Vasilica Badets, Antoine Bonnefont, Corinne Boudon, Laurent Ruhlmann	
Photocatalytic recovery of metals by Lindqvist-type polyoxometalate–porphyrin copolymer	141-155
Thibaut Baron, Ximena Zarate, Yoan Hidalgo-Rosa, Michael Zambrano-Angulo, Kevin Mall-Haidaraly, Ricardo Pino-Rios, Yann Pellegrin, Fabrice Odobel, Gloria Cárdenas-Jirón	
Zinc phthalocyanine absorbance in the near-infrared with application for transparent and colorless dye-sensitized solar cells	157-170



Foreword / *Avant-propos*

MAPYRO: the French Fellowship of the Pyrrolic Macrocyclic Ring

MAPYRO : la communauté française des macrocycles pyrroliques

Bernard Boitrel and Jean Weiss

For the last 50 years, pyrrolic macrocycles in general (porphyrins and their structural isomers, expanded or contracted porphyrins, phthalocyanines, ...) are the core of a very active research in France.

In the 70s, renowned French scientists promoted the chemistry of porphyrins in various scientific areas such as biomimetic chemistry, supramolecular chemistry, catalysis (i.e. oxidation) and material science. At the turn of the century, structural isomers and contracted or expanded isomers of porphyrins joined the family of pyrrolic macrocycles and corroles, with their robust structure, have proven their ability to stabilize high oxidation degree of transition metals. Over the past years, research involving pyrrolic macrocycles has evolved according to societal and industrial challenges and the fundamental progresses in the catalytic reduction of either oxygen or carbon dioxide are the best proof of it. However, although researchers endure growing pressure to develop applications, research involving pyrrolic macrocycles requires fundamental know-how combining synthesis, catalysis, analysis, electrochemistry, photochemistry and life science. To avoid a dispersion of knowledge and skills, the community of the macrocyclic polypyrroles needed to be organized in a Groupement De Recherche and the CNRS responded to this need in a favorable way, leading to the creation of the GDR MAPYRO two years ago (<https://mapyro.chimie.unistra.fr>).

So far, 23 research groups comprising 75 permanent staff are members of the GDR which comprises 3 main research topics:

- Biomimetic chemistry for the activation of small molecules,
- Supramolecular chemistry of porphyrinic assemblies,
- Pyrrolic macrocycles in therapeutic chemistry.

In these categories, this special issue gathers 12 remarkable contributions of which several are highlighting results from collaborative work that has developed over the years between GDR members.

The Comptes-Rendus Chimie being a diamond open access, thanks to the efforts of our colleagues who were convinced of the open science benefits, we would like to thank the Editor in Chief Pierre Braunstein for his enthusiasm when we discussed this special issue and Julien Desmarests for his help during the preparation of the following pages. We definitely hope that the readers will enjoy reading this issue as much as we enjoyed the making of it. We also hope that this issue will be a source of inspiration for anyone attracted by the colorful chemistry of macrocyclic polypyrroles.

Enjoy your reading,

Bernard Boitrel
France
bernard.boitrel@univ-rennes1.fr

Jean Weiss
France
jweiss@unistra.fr

Avant-propos

Les macrocycles pyrroliques au sens large du terme (porphyrines, isomères de porphyrines, porphyrines contractées, porphyrines étendues, phtalocyanines, ...) représentent depuis au moins un demi-siècle un domaine de recherche très actif en France.

Dans les années 70, des scientifiques français réputés ont développé la chimie des porphyrines dans des domaines aussi variés que la chimie biomimétique, la chimie supramoléculaire, la catalyse notamment d'oxydation, ou encore les matériaux. À la fin du siècle dernier, les isomères structuraux et analogues contractés et étendus des porphyrines se sont invités dans la famille des macrocycles pyrroliques et les corroles se sont établis comme des structures robustes essentielles pour stabiliser les hauts degrés d'oxydation de métaux de transition. Ces dernières années, les thématiques de recherche impliquant les macrocycles pyrroliques ont évolué en même temps que les préoccupations sociétales et industrielles et les avancées fondamentales dans la catalyse de la réduction de l'oxygène ou du dioxyde de carbone en sont de parfaites illustrations. Cependant, et même si la nécessité d'orienter nos recherches vers des domaines applicatifs est de plus en plus palpable, la recherche faisant appel aux macrocycles pyrroliques requiert un cœur de métier fondamental alliant synthèse, catalyse, analyse, électrochimie, photochimie et sciences du vivant. Pour que ces multiples facettes de la chimie des macrocycles pyrroliques n'aboutissent pas à une dispersion des savoirs et des savoir-faire, le besoin de structurer notre communauté a trouvé un écho favorable auprès du CNRS et le GDR « MAPYRO » a vu le jour il y a deux ans (<https://mapyro.chimie.unistra.fr>).

Actuellement, 23 équipes rassemblant 75 chercheurs permanents composent le GDR fédéré autour de trois thématiques principales :

- Catalyseurs biomimétiques et activation de petites molécules,
- Chimie supramoléculaire des assemblages porphyriniques,
- Macrocycles pyrroliques en chimie thérapeutique.

Dans ces trois domaines, ce numéro spécial dédié au GDR MAPYRO rassemble 12 contributions remarquables d'équipes du GDR dont un certain nombre fait apparaître le tissu de collaborations établies au fil des ans.

Les Compte-Rendus Chimie étant maintenant en accès libre « diamant » grâce aux efforts de collègues convaincus par les bienfaits de la science ouverte, nous tenons à remercier le Directeur de Publication Pierre Braunstein pour son enthousiasme lors de la discussion de ce numéro spécial et Julien Desmarests pour son assistance dans sa réalisation pratique. Nous espérons que nos lecteurs auront autant de plaisir à lire les pages qui suivent que nous en avons eu à leur faire voir le jour. Nous souhaitons également que ces pages soient source d'inspiration pour celles et ceux qui voudraient s'aventurer dans la chimie colorée des macrocycles polypyrrroliques.

Bonne lecture !

Bernard Boitrel
France
bernard.boitrel@univ-rennes1.fr

Jean Weiss
France
jweiss@unistra.fr



MAPYRO: the French Fellowship of the Pyrrolic Macrocyclic Ring / *MAPYRO: la communauté française des macrocycles pyrroliques*

Guest editors

Rédacteurs invités



Bernard Boitrel



Jean Weiss

Bernard Boitrel, Research Director for the CNRS at the Institute of Chemical Sciences in Rennes (Brittany), was born in Lille (France) but studied biochemistry and then chemistry in Paris at Université Pierre and Marie Curie where he obtained his PhD with Dr. Eric Rose in 1989. He was appointed CNRS researcher and moved to Dijon in 1992 (Burgundy) working with Professor Roger Guilard in the fields of both porphyrins and tetraazamacrocycles. In 1993, he was a postdoctoral fellow in Professor Jim Collman's group at Stanford University, working on the very first functional models of cytochrome c oxidase. His current research interests, since 2001 in Rennes where he was appointed CNRS Director of Research, include bioinspired dioxygen activation, the design and synthesis of new metal carriers for therapeutic applications and polypyrrolic macrocycles. He developed quite simple synthetic pathways leading to functionalized metalloporphyrins that found possible applications in the coordination of post-transition metals as well as the modulation of the binding of small gaseous molecules.

Bernard Boitrel, directeur de recherche au CNRS à l'Institut des Sciences Chimiques de Rennes (Bretagne), est né à Lille (France) mais a étudié la biochimie puis la chimie à Paris à l'Université Pierre et Marie Curie où il a obtenu son doctorat avec le Dr. Eric Rose en 1989. Il a été nommé chercheur au CNRS et s'est installé à Dijon en 1992 (Bourgogne), travaillant avec le professeur Roger Guilard dans les domaines des porphyrines

et des tétraazacycles. En 1993, il est devenu chercheur postdoctoral dans le groupe du Professeur Jim Collman à l'Université de Stanford, travaillant sur les tout premiers modèles fonctionnels de la cytochrome c oxydase. Ses recherches actuelles, depuis 2001 à Rennes où il a été nommé directeur de recherche CNRS, portent sur l'activation bioinspirée du dioxygène, la conception et la synthèse de nouveaux supports métalliques pour des applications thérapeutiques et les macrocycles polypyrrroliques. Il a notamment développé des voies de synthèse très simples conduisant à des métalloporphyrines fonctionnalisées qui ont trouvé des applications possibles dans la coordination de métaux post-transition ainsi que dans la modulation du transport de petites molécules gazeuses.

Jean WEISS is Research Director for the CNRS at the Institute of Chemistry in Strasbourg and head of this Institute since February 2013. After his PhD on catenanes under the supervision of Jean-Pierre Sauvage in 1986, he joined respectively Professor D. J. Cram at UCLA and Professor H. A. Staab at the Max Planck Institute of Heidelberg as post-doctoral fellow and Alexander von Humboldt fellow. He was appointed CNRS researcher in 1988 in the group of Professor Maurice Gross in Strasbourg and promoted Research Director in 1998. He occupied several positions in foreign institutions as NSF-CNRS fellow with Professor Andrew D. Hamilton in Pittsburgh and at the AIST in Tsukuba or as invited Professor at the Universities of Osaka and Hokkaido. Since 2004, he leads the CLAC team of the Institute of Chemistry in Strasbourg. His scientific interests range from bio-inspired chemical processes to self-organization on surfaces and the design and synthesis of photo- and electroactive molecular devices.

Jean WEISS est directeur de recherches au CNRS à l'Institut de Chimie de Strasbourg et directeur de l'UMR 7177 depuis février 2013. Après son doctorat sur les caténanes sous la direction du Dr. Jean-Pierre Sauvage en 1986 il a effectué deux stages post-doctoraux successifs à UCLA sous la direction du Professeur D. J. Cram puis au Max Planck Institut de Heidelberg en tant que boursier Alexander von Humboldt sous la direction du Professeur H. A. Staab. Recruté Chargé de Recherche au CNRS en 1988 chez le Professeur Maurice Gross à Strasbourg et promu DR en 1998, il a effectué plusieurs séjours à l'étranger en tant que chercheur NSF-CNRS chez le Professeur Andrew D. Hamilton à Pittsburgh ou en tant que chercheur invité à l'AIST de Tsukuba, à l'université d'Osaka et à l'université de Hokkaido. Depuis 2004, il dirige l'équipe CLAC à l'Institut de Chimie de Strasbourg. Ses centres d'intérêt vont de la modélisation de processus bio-inspirés à l'auto-organisation sur surface en passant par la conception et synthèse de composants moléculaires photo- ou électro-actifs.



MAPYRO: the French Fellowship of the Pyrrolic Macrocyclic Ring / *MAPYRO: la communauté française des macrocycles pyrroliques*

ORR activity of metalated phenanthroline-strapped porphyrin adsorbed on carbon nanotubes

Manel Hanana^a, Christophe Kahlfuss^b, Jean Weiss^b, Renaud Cornut^a,
Bruno Jusselme^a, Jennifer A. Wytko^{*,b} and Stéphane Campidelli^{*,a}

^a Université Paris-Saclay, CEA, CNRS, NIMBE, LICSEN, 91191, Gif-sur-Yvette, France

^b Institut de Chimie de Strasbourg, UMR 7177 CNRS-Université de Strasbourg, 4 rue Blaise Pascal, 67008 Strasbourg, France

E-mails: manelhanana@yahoo.fr (M. Hanana), christophe.kahlfuss@gmail.com (C. Kahlfuss), jweiss@unistra.fr (J. Weiss), renaud.cornut@cea.fr (R. Cornut), bruno.jusselme@cea.fr (B. Jusselme), jwytko@unistra.fr (J. A. Wytko), stephane.campidelli@cea.fr (S. Campidelli)

Abstract. Developing efficient noble metal-free systems for electrocatalysis and the reduction of oxygen (ORR) is crucial for hydrogen economy. Bioinspired hybrids combining iron or copper/iron porphyrins with multiwalled carbon nanotubes were tested for ORR using a rotating ring-disk electrode at pH 13 to 8. The porphyrin-nanotube hybrids exhibited better electrocatalytic properties than their constituents alone due to the electrical network formed by the nanotubes, and they reduced oxygen via a four-electron pathway to produce water. Whereas the presence of Cu was not mandatory to reduce oxygen, its presence improved ORR activity and decreased the overpotential compared to monometallic (iron porphyrin) hybrids.

Résumé. La conception de matériaux sans métaux nobles pour la réaction de réduction de l'oxygène (ORR) est cruciale pour le développement d'une économie basée sur l'hydrogène. Ici, des matériaux hybrides bioinspirés à base de porphyrines métallées et de nanotubes de carbone multi-parois ont été testés pour l'ORR avec un système d'électrode disque-anneau entre pH 8 et 13. Les matériaux hybrides présentent systématiquement de meilleures propriétés électrocatalytiques que celles de leurs constituants pris individuellement et permettent de réduire l'oxygène par un processus à quatre électrons. La présence du cuivre dans les hybrides n'est pas obligatoire mais elle améliore légèrement les propriétés électrocatalytiques.

Keywords. Porphyrin, Carbon nanotubes, Oxygen reduction, Electrocatalysis, Energy.

Mots-clés. Porphyrine, Nanotubes de carbone, Réduction de l'oxygène, Électrocatalyse, Énergie.

Available online 8th June 2021

* Corresponding authors.

1. Introduction

For the last decade, the development of non-noble metal or metal-free catalysts for energy sources has been a field of growing interest. The electrocatalytic reduction of oxygen (oxygen reduction reaction—ORR) is the key reaction for the efficiency of fuel cells. Its slow kinetics, multistep process and the competition between the two-electron and four-electron pathway make ORR the limiting reaction in fuel cells. Whereas the best catalysts for this electrocatalytic reaction remain platinum-based materials, in the last ten years, much effort has been devoted to the development of nonprecious metal or metal-free catalysts for ORR [1–15]. In addition, recently, the composition and the morphology of the Fe–N–C active sites in pyrolyzed catalyst materials have been investigated [16–20].

In Nature, the reduction of oxygen is performed by the active center composed of an iron porphyrin and copper-histidine complexes in cytochrome *c* oxidase (CcO). In 1964, Jasinski discovered that a relatively simple macrocycle like cobalt phthalocyanine was able to reduce oxygen [21]. In metalated phthalocyanines, the metal core is coordinated in a plane of four nitrogen atoms bearing a global -2 charge. Consequently, other tetrapyrrolic macrocycles, such as metalated porphyrins, phthalocyanines or corroles, have been extensively studied in the literature as mimics of cytochrome *c* oxidase and/or as catalysts for the reduction of oxygen to water in fuel cells [11–14,22–41]. In these systems, the macrocycle containing an inexpensive metal (mostly Fe or Co) constitutes the active part of the catalyst and the electrons and protons required for the reaction have to be properly delivered to ensure the efficiency of the reduction. However, the electrocatalytic properties of a material appear to be extremely dependent on its environment [37]. In this context, we have systematically investigated the properties of porphyrin and phthalocyanine complexes in the presence of carbon nanotubes as electron transporters and Nafion as proton source [33,34,40,41].

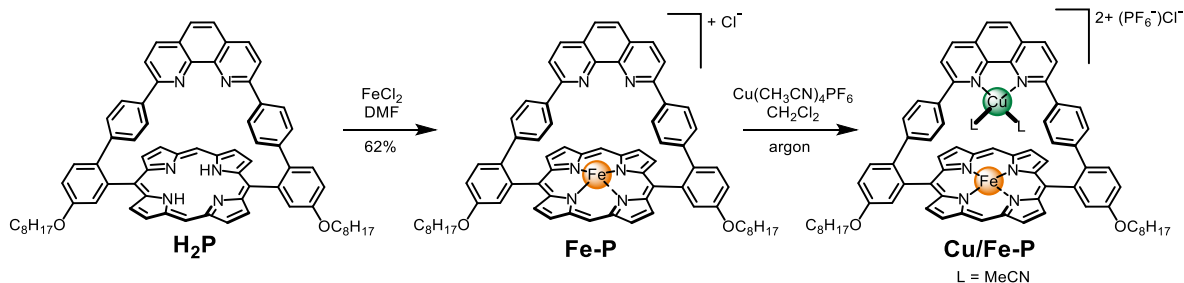
Inspired by Nature, early, elaborate, covalent models of CcO reported by Collman [22,23] and Boitrel [24] are considered as milestones in the design of artificial hemoproteins. These models employed caps and straps that served to differentiate both faces of tetra-aryl-porphyrin derivatives and

to create steric hindrance that mimicked the distal site of the hemoprotein. Over the past years, the properties of a phenanthroline-strapped porphyrin have been exploited in several domains such as the specific recognition of imidazole or the formation of hetero-bimetallic structures containing Fe and Cu for the electrocatalytic reduction of oxygen [42]. In these ditopic ligands, the phenanthroline binds and stabilizes a copper(I) ion at a distance of approximately 4.7 Å from an iron porphyrin, mimicking a heme. In previous studies, these structures, decorated with pendant pyridine or imidazole ligands were evaluated as models of cytochrome *c* oxidase in physiological media [43] (phosphate buffer) but were never studied under the working conditions of a proton exchange membrane fuel-cell (PEMFC). The absorption of phenanthroline-strapped iron (Fe-P) and iron(III)/copper(I) porphyrins (Cu/Fe-P) on multiwalled carbon nanotubes (MWNTs) and their electrocatalytic properties are reported hereafter. These studies demonstrate that the MWNT-Fe-P and Cu/Fe-P hybrids efficiently reduce oxygen *via* a four-electron pathway to yield water. In contrast to our previous work in which a multilayer of porphyrins decorated the nanotube surface [34], here, the presence of the rigid phenanthroline strap on the porphyrin prevents the formation of a multilayer on the MWNTs and the porphyrins likely interact with the nanotubes by π -stacking and C–H– π interactions.

2. Results and discussion

The porphyrin complexes Fe-P and Cu/Fe-P were prepared from the phenanthroline-strapped porphyrin (H₂P) [44] as shown in Scheme 1. Metalation of the porphyrin with FeCl₂ in refluxing DMF afforded Fe-P in 62% yield. The insertion of iron(III) and the presence of an axial chloride on the iron center were confirmed by mass spectrometry. The bimetallic Cu/Fe-P complex was prepared quantitatively by subsequent reaction of Fe-P with [Cu(CH₃CN)₄]PF₆ under inert atmosphere.

The nanotube-porphyrin hybrids were prepared by mixing MWNT with porphyrins Fe-P or Cu/Fe-P (in a 3:1 ratio by weight) in tetrahydrofuran (THF) in an ultrasound bath. It was assumed that the presence of the phenanthroline strap would eliminate stacking and subsequent formation of multilayers on the side-walls of the nanotube. The 3:1 ratio was chosen by



Scheme 1. Synthesis of the porphyrin metal complexes.

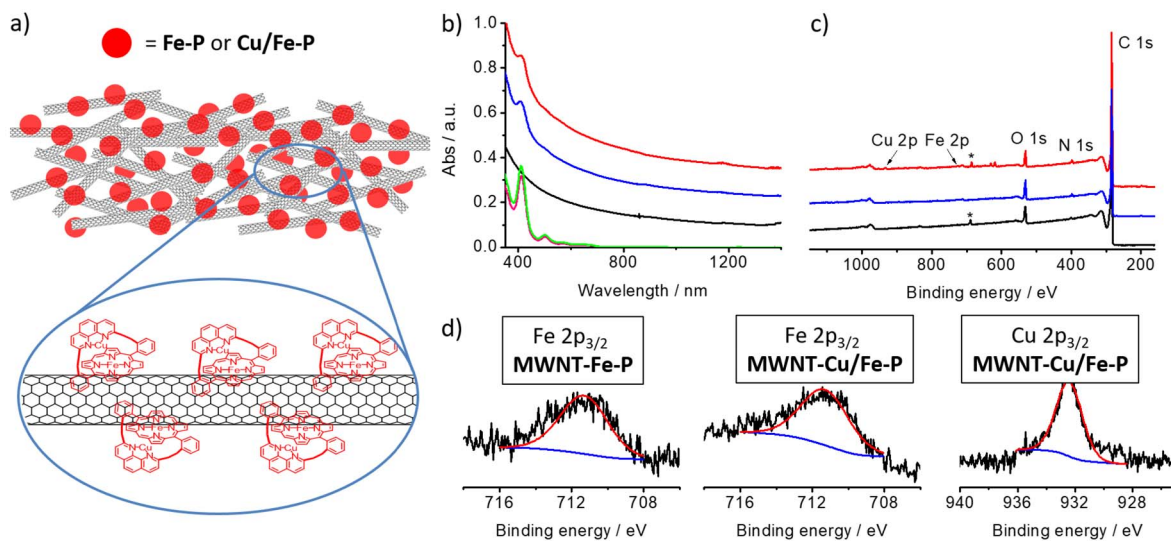


Figure 1. (a) Representation of MWNT-Fe-P and MWNT-Cu/Fe-P hybrids; (b) absorption spectra of Fe-P (pink) and Cu/Fe-P (green) and of MWNT (black), MWNT-Fe-P (blue) and MWNT-Cu/Fe-P (red) recorded in *N*-methylpyrrolidone; (c) XPS Spectra of MWNT (black), MWNT-Fe-P (blue) and MWNT-Cu/Fe-P (red). The signals labeled (*) are due to fluorine from the PTFE membrane. (d) High resolution XPS spectra of Fe $2p_{3/2}$ of MWNT-Fe-P and MWNT-Cu/Fe-P and Cu $2p_{3/2}$ of MWNT-Cu/Fe-P.

assuming that the specific surface area of the MWNTs was *ca.* 320 m²/g [45] and that a porphyrin (without alkyl chains) could be represented by a rectangle of $1.7 \times 0.9 \approx 1.5$ nm². The available surface of 3 mg of nanotubes is estimated to be 1 m² that roughly corresponds to the surface occupied by 1 mg of porphyrin: $m_{\text{porph}}/M_{\text{porph}} \times N_A \times A_{\text{porph}} \cong 0.8$ m².

After mixing, THF was evaporated with a N₂ flow and the catalytic inks were prepared by dispersing by ultrasound sonication the MWNT/porphyrin hybrids (3 mg) of interest in 750 mL of ethanol and 75 mL of Nafion solution (5% in alcohol). Similarly, the inks of the reference compounds MWNT, Fe-P and Cu/Fe-P

were prepared by mixing the nanotubes or the porphyrins in 750 mL of ethanol and 75 mL of Nafion solution (5% in alcohol). The different catalysts and reference materials were drop-casted on a glassy carbon disk and tested in a series of rotating ring-disk electrode (RRDE) experiments at pH 13 (0.1 M NaOH), 10 and 8 (phosphate buffer).

A representation of the nanotube-porphyrin hybrids is shown in Figure 1a and their absorption spectra are given in Figure 1b. The spectra of MWNT-Fe-P and MWNT-Cu/Fe-P are the sum of the absorption of the two counterparts (nanotubes and porphyrins), thus confirming the presence of the porphyrins. The

Table 1. Atomic composition of the MWNT-Fe-P and MWNT-Cu/Fe-P hybrids

	%C	%N	%O	%Fe	%Cu
MWNT-Fe-P	92.22	1.20	6.50	0.09	—
MWNT-Cu/Fe-P	94.09	1.30	4.39	0.11	0.11

hybrids were characterized by absorption and X-ray photoelectron spectroscopies (XPS). The XPS spectra of MWNT, MWNT-Fe-P and MWNT-Cu/Fe-P are shown in Figure 1c. The spectrum of MWNT shows an intense peak of carbon, the presence of oxygen and a small peak at *ca.* 690 eV coming from the PTFE membrane that supports the nanotubes for the analysis. This peak is also observed in the spectrum of MWNT-Cu/Fe-P. The spectra of MWNT-Fe-P and MWNT-Cu/Fe-P show additional peaks attributed to the presence of nitrogen, iron and copper (for MWNT-Cu/Fe-P) (Figure 1d). The extremely weak peaks of iron and copper reflect the low amount of porphyrins absorbed on the nanotubes. The weak signals of the Soret band in the UV-Vis-NIR spectra of MWNT-Fe-P and MWNT-Cu/Fe-P (Figure 1b) also support this observation. The composition of the MWNT-Fe-P and MWNT-Cu/Fe-P determined by XPS is summarized in Table 1. *Note that the percentage of iron and copper must be considered with caution because of the uncertainty of the XPS measurements.*

The redox potentials of the metals in the porphyrins and in the phenanthroline strap were determined by cyclic voltammetry with 1 mM solutions of Fe-P or Cu/Fe-P porphyrin in a 0.1 M tetrabutylammonium hexafluorophosphate (NBu₄PF₆) THF solution. The electrochemical cell was equipped with a glassy carbon working electrode, a platinum counter electrode and an Ag/AgNO₃ (10 mM) reference electrode. The potentials are reported *vs* ferrocene used as internal reference. The solutions were degassed by bubbling argon and the cyclic voltammetry was performed at a scan rate of 20 mV/s. The voltammograms of Fe-P and Cu/Fe-P (Figure S1) show a reversible reduction peak (I) attributed to the first reduction of the porphyrin macrocycles at -1.57 and -1.60 V, respectively. A second more complex signal (II), observed between -0.50 and -0.90 V, is attributed to the reduction of Fe(III)/Fe(II) in the porphyrins. The complex shape of this redox couple associated with this process is attributable to the

presence and exchange of an axial ligand (residual H₂O, a solvent molecule, Cl⁻ or no ligand) on the iron(III) center. As previously observed, when copper is present in the phenanthroline strap (Cu/Fe-P), the apical ligand exchange is slow or hindered and can result in an irreversible reduction wave [43,46]. Finally, in the Cu/Fe-P derivative, an additional reversible signal (III) is observed at 0.09 V and corresponds to the oxidation of Cu(I) to Cu(II).

The ORR electrocatalytic properties of two hybrids (MWNT-Fe-P and MWNT-Cu/Fe-P) and of MWNT, Fe-P and Cu/Fe-P used as references, were investigated by rotating ring-disk electrode (RRDE) measurements. Figure 2 presents the ORR activity at different pHs of the catalyst inks deposited on the glassy carbon (GC) electrode (0.196 cm²). The rotating ring electrode (RDE) curves are the average currents calculated from the forward (reduction) and backward (re-oxidation) scans. Figures 2a and b show the polarization curves at 0, 400, 800, 1200, 1600 and 2000 rpm at pH 10 of the MWNT-Fe-P and MWNT-Cu/Fe-P series, respectively. First, the catalyst inks made by mixing the nanotubes with the porphyrins (MWNT-Fe-P and MWNT-Cu/Fe-P) exhibit higher current density and lower overpotential (by about 0.2 V) than Fe-P and Cu/Fe-P alone and also higher current density than bare MWNT. These differences can be explained by the difficulty for electrons to reach the porphyrins embedded in Nafion and by the [2 + 2] electron pathway of the ORR for pure carbon materials [47], respectively. Figures 2c-h show the polarization curves recorded at 800 rpm at different pH, from pH 13 to 8. In all cases, the nanotube/porphyrin hybrids exhibit better ORR properties than the materials (MWNT and Fe-P or Cu/Fe-P) taken separately. The polarization curves of MWNT, Fe-P, Cu/Fe-P, MWNT-Fe-P and MWNT-Cu/Fe-P between 0 and 2000 rpm at pH 13 and 8 are summarized in Figure S2. For all pH considered, Fe-P and Cu/Fe-P alone exhibit an overpotential between 130 to 240 mV (determined for current density at the disk of -0.1 mA·cm⁻²) compared to the nanotubes hybrids (MWNT-Fe-P and MWNT-Cu/Fe-P). Moreover, on the RDE curves, it is interesting to note that, for the hybrid catalysts, the disk currents reach a plateau, indicating that the reduction of oxygen is limited by diffusion (by the supply of oxygen) and not by the catalyst itself. Finally, comparison of the properties of the monometallic and bimetallic hybrid

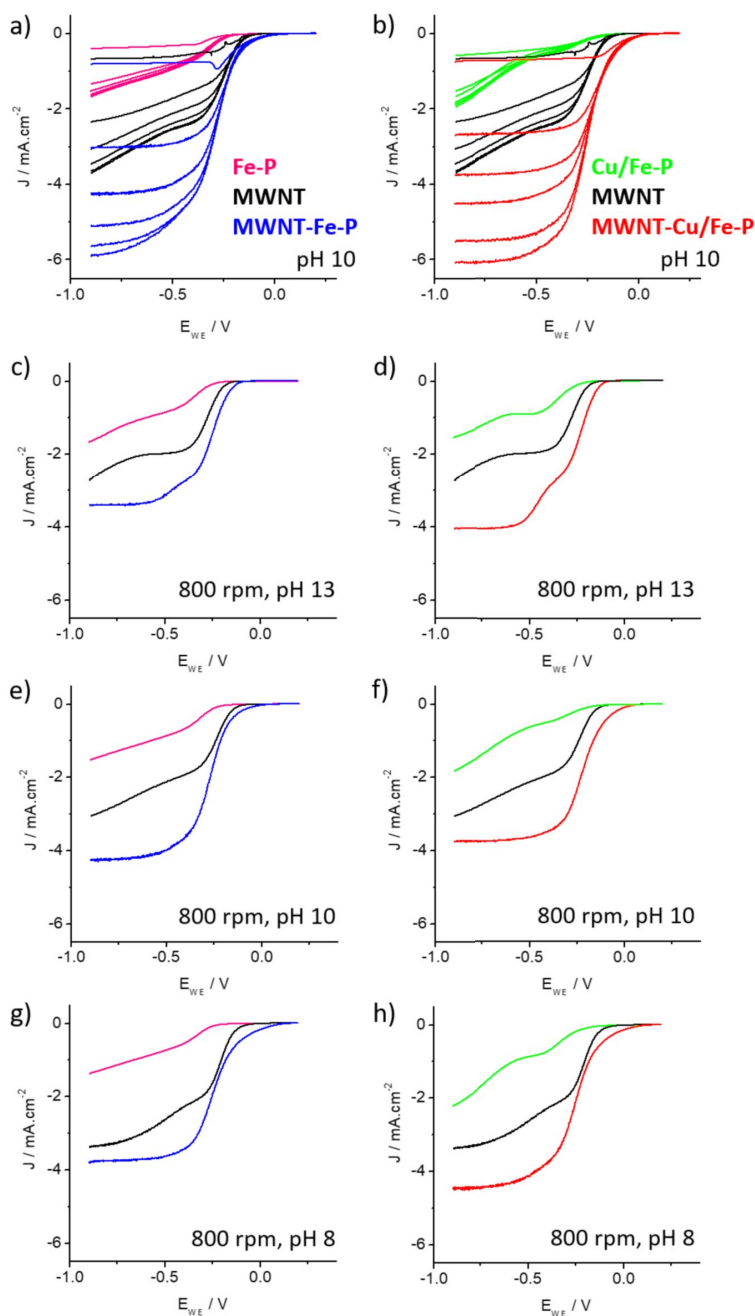


Figure 2. (a, b) Polarization curves at different rotation rates (0, 400, 800, 1200, 1600 and 2000 rpm) for (a) Fe-P (pink curves), MWNT (black curves) and MWNT-Fe-P (blue curves) and for (b) Cu/Fe-P (green curves), MWNT (black curves) and MWNT-Cu/Fe-P (red curves) recorded for ORR in O_2 -saturated phosphate buffer solutions at pH 10 (scan rate = 5 mV/s, room temperature). (c, e, g) Polarization curves recorded at different pH at a rotation rate of 800 rpm for Fe-P (pink curves), MWNT (black curves) and MWNT-Fe-P (blue curves). (d, f, h) Polarization curves recorded at different pH at a rotation rate of 800 rpm for Cu/Fe-P (green curves), MWNT (black curves) and MWNT-Cu/Fe-P (red curves).

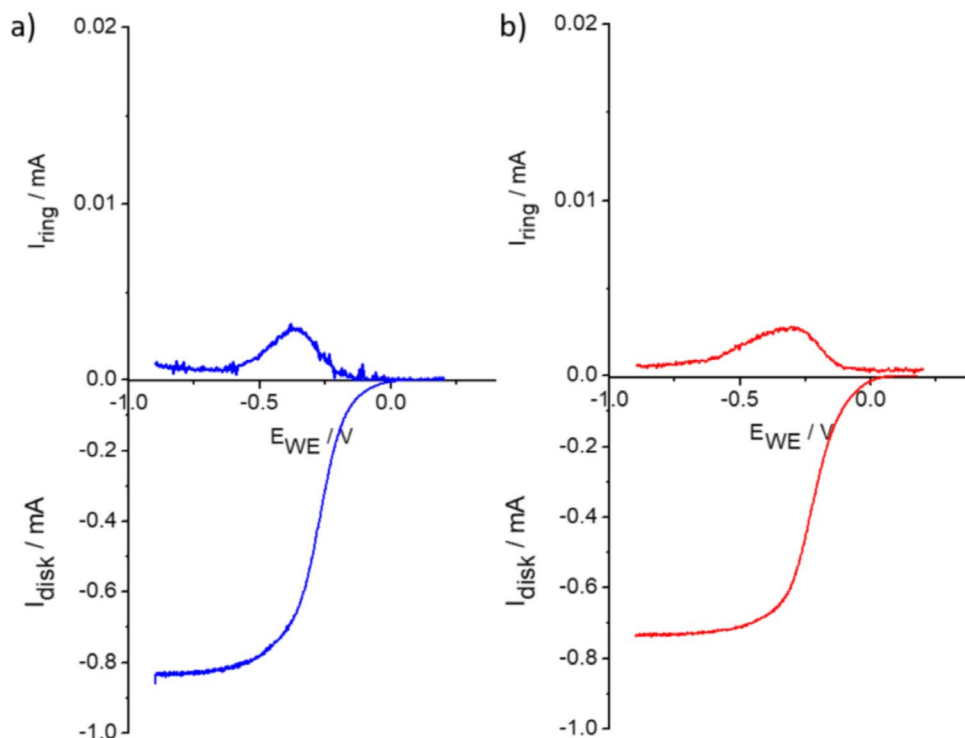


Figure 3. Example RRDE curves with disk and ring currents for (a) MWNT-Fe-P (blue) and (b) MWNT-Cu/Fe-P (red) at pH 10 with a rotation rate of 800 rpm.

catalysts demonstrates that the presence of copper slightly improves the reduction potential and the current density (see Figures 2a, b and S2).

The electrocatalytic properties of Fe-P and Cu/Fe-P and of their nanotube hybrids (MWNT-Fe-P and MWNT-Cu/Fe-P) degrade rapidly in acidic conditions (pH 6 and below—result not shown), thus requiring the deposition of a new catalyst ink for each rotation cycle. This observation is in agreement with our previous report [41] and could be due to demetallation and/or degradation of the porphyrin [48–50]. Therefore, the catalytic properties of these materials in acidic media were not investigated in detail.

The number of electrons involved in the reduction of oxygen was determined from the disk and ring currents at -0.75 V according to the equation: $n = 4I_D / (I_D + I_R / N_c)$ with a collection coefficient $N_c = 0.2$ determined using the one-electron $[\text{Fe}(\text{CN})_6]^{3-} / [\text{Fe}(\text{CN})_6]^{4-}$ redox couple. Figure 3 shows the ring and disk current for MWNT-Fe-P and MWNT-Cu/Fe-P at pH 10 for a rotation rate of 800 rpm; the RRDE curves of the reference materials

MWNT, Fe-P and Cu/Fe-P and those of MWNT-Fe-P and MWNT-Cu/Fe-P at pH 13, 10 and 8 are given in Figure S3. The number of electrons for the reduction of oxygen is reported in Table 2. The RRDE curves (Figures 3 and S3) show that the reduction of O_2 is accompanied by the production of hydrogen peroxide for MWNT, Fe-P and Cu/Fe-P. Conversely, for MWNT-Fe-P and MWNT-Cu/Fe-P, almost no production of H_2O_2 is detected at the plateau and the reduction proceeds *via* a four-electron pathway. As seen in Table 2, in the absence of nanotubes, Cu/Fe-P seems more active in ORR than the copper-free porphyrin Fe-P. In the absence of nanotubes, the limited conductivity of electrons may affect the performance of the monometallic porphyrin. This assumption is supported by a report of Collman [23], which suggests that under limited electron flux, copper and phenol are required to enhance the selective reduction of oxygen to water. In the presence of the nanotubes, the two porphyrins behave similarly and no noticeable differences are observed between MWNT-Fe-P and MWNT-Cu/Fe-P in terms of reduction of

Table 2. Summary of the number of electrons involved in the reduction of oxygen for MWNT, Fe-P, Cu/Fe-P, MWNT-Fe-P and MWNT-Cu/Fe-P

	MWNT	Fe-P	Cu/Fe-P	MWNT-Fe-P	MWNT-Cu/Fe-P
pH 13	3.62	3.08	3.61	3.99	3.98
pH 10	3.86	3.34	3.72	3.98	3.98
pH 8	3.91	3.73	3.95	3.99	3.98

oxygen because MWNTs ensure a sufficient flux of electrons to the iron porphyrin reactive sites for the reduction.

The data in Table 2 are also consistent with previous studies of Fe-P and Cu/Fe-P adsorbed on edge-oriented pyrolytic graphite (EOPG) electrodes [51] and reports by Boitrel and coworkers [24] showing that Fe-porphyrins alone can perform four-electron reduction of oxygen to some extent, possibly due to the presence of face-to-face oriented species.

Beyond their academic interest for the reduction of oxygen, it is clear that carbon nanotube/porphyrin hybrids cannot compete with the performance of platinum-based materials or platinum alloys for PEMFC. However, the recent development of noble metal-free pyrolyzed materials for fuel cells sheds light on the need for comprehensive studies to understand the structures of the ORR active sites. Iron porphyrins combined with nanotubes can play a role in this understanding. Moreover, the combination of the electronic properties of the nanotubes with the catalytic properties of iron or other metalated porphyrins may be of interest for CO₂ reduction [52,53] and small molecule activation [54,55].

3. Conclusion

Iron and copper/iron strapped porphyrins were combined with multiwalled carbon nanotubes and the electrocatalytic properties of the hybrids were investigated for the oxygen reduction reaction in alkaline media. The combination of nanotubes with the iron or copper/iron porphyrins systematically gave better catalytic ORR properties in terms of overpotential and current density than for the components taken separately. In particular, when the porphyrin inks were directly deposited on the glassy carbon electrode, a low efficiency was observed. This behavior is due to the lack of electrons available for the reduction of oxygen. In the catalyst ink, the porphyrins

are embedded in Nafion and only the molecules directly in contact with the glassy carbon disk can benefit from efficient electron transfers from the electrodes. The bimetallic porphyrin (Cu/Fe-P) exhibited slightly better ORR properties than the monometallic Fe-P. When carbon nanotubes were added, both the MWNT-Fe-P and MWNT-Cu/Fe-P hybrids were able to reduce oxygen *via* a four-electron pathway.

Acknowledgments

This work was supported by the JST-ANR grant ANR-14-JTIC-0002-01 (MECANO), the ANR grant ANR-16-CE29-0027-01 (MAGMA), a public grant overseen by the French National Research Agency as part of the “Investissements d’Avenir” program (Labex NanoSaclay, reference: ANR-10-LABX-0035), the CNRS, the Université de Strasbourg.

Supplementary data

Supporting information for this article is available on the journal’s website under <https://doi.org/10.5802/crchim.86> or from the author.

References

- [1] F. Jaouen, E. Proietti, M. Lefèvre, R. Chenitz, J.-P. Dodelet, G. Wu, H. T. Chung, C. M. Johnston, P. Zelenay, *Energy Environ. Sci.*, 2011, **4**, 114.
- [2] A. Morozan, B. Jousselme, S. Palacin, *Energy Environ. Sci.*, 2011, **4**, 1238.
- [3] M. Shao, Q. Chang, J.-P. Dodelet, R. Chenitz, *Chem. Rev.*, 2016, **116**, 594.
- [4] Z. Chen, D. Higgins, A. Yu, L. Zhang, J. Zhang, *Energy Environ. Sci.*, 2011, **4**, 3167.
- [5] D.-W. Wang, D. Su, *Energy Environ. Sci.*, 2014, **7**, 576.
- [6] H. Wang, T. Maiyalagan, X. Wang, *ACS Catal.*, 2012, **2**, 781.
- [7] Q. Wei, X. Tong, G. Zhang, J. Qiao, Q. Gong, S. Sun, *Catalysts*, 2015, **5**, 1574.
- [8] J. H. Zagal, S. Griveau, J. F. Silva, T. Nyokong, F. Bedioui, *Coord. Chem. Rev.*, 2010, **254**, 2755.

- [9] M. A. Thorseth, C. E. Tornow, E. C. M. Tse, A. A. Gewirth, *Coord. Chem. Rev.*, 2013, **257**, 130.
- [10] W. He, Y. Wang, C. Jiang, L. Lu, *Chem. Soc. Rev.*, 2016, **45**, 2396.
- [11] A. Mahammed, Z. Gross, *Isr. J. Chem.*, 2016, **56**, 756.
- [12] W. Zhang, W. Lai, R. Cao, *Chem. Rev.*, 2017, **117**, 3717.
- [13] M. L. Pegis, C. F. Wise, D. J. Martin, J. M. Mayer, *Chem. Rev.*, 2018, **118**, 2340.
- [14] Y.-M. Zhao, G.-Q. Yu, F.-F. Wang, P.-J. Wei, J.-G. Liu, *Chem. Eur. J.*, 2019, **25**, 3726.
- [15] C. Zhang, W. Zhang, W. Zheng, *ChemElectroChem*, 2019, **11**, 655.
- [16] M. Liu, L. Wang, K. Zhao, S. Shi, Q. Shao, L. Zhang, X. Sun, Y. Zhao, J. Zhang, *Energy Environ. Sci.*, 2019, **12**, 2890.
- [17] U. I. Koslowski, I. Abs-Wurmbach, S. Fiechter, P. Bogdanoff, *J. Phys. Chem. C*, 2008, **112**, 15356.
- [18] U. I. Kramm, J. Herranz, N. Larouche, T. M. Arruda, M. L. Lefèvre, F. Jaouen, P. Bogdanoff, S. Fiechter *et al.*, *Phys. Chem. Chem. Phys.*, 2012, **14**, 11673.
- [19] A. Zitolo, V. Goelner, V. Armel, M.-T. Sougrati, T. Mineva, L. Stievano, E. Fonda, F. Jaouen, *Nat. Mater.*, 2015, **14**, 937.
- [20] T. Mineva, I. Matanovic, P. Atanassov, M.-T. Sougrati, L. Stievano, M. Clémancey, A. Kochem, J.-M. Latour, F. Jaouen, *ACS Catal.*, 2019, **9**, 9359.
- [21] R. Jasinski, *Nature*, 1964, **201**, 1212.
- [22] J. P. Collman, L. Fu, P. C. Herrmann, X. Zhang, *Science*, 1997, **275**, 949.
- [23] J. P. Collman, N. K. Devaraj, R. A. Decréau, Y. Yang, Y.-L. Yan, W. Ebina, T. A. Eberspacher, C. E. D. Chidsey, *Science*, 2007, **315**, 1565.
- [24] D. Ricard, B. Andrioletti, M. L'Her, B. Boitrel, *Chem. Commun.*, 1999, 1523.
- [25] F. Melin, A. Trivella, M. Lo, C. Ruzié, I. Hijazi, N. Oueslati, J. A. Wytko *et al.*, *J. Inorg. Biochem.*, 2012, **108**, 196.
- [26] J. P. Collman, S. Ghosh, *Inorg. Chem.*, 2010, **49**, 5798.
- [27] D. Ricard, A. Didier, M. L'Her, B. Boitrel, *Chem. Bio. Chem.*, 2001, **2**, 144.
- [28] D. Ricard, M. L'Her, P. Richard, B. Boitrel, *Chem. Eur. J.*, 2001, **7**, 3291.
- [29] D. K. Dogutan, S. A. Stoian, R. McGuire Jr., M. Schwalbe, T. S. Teets, D. G. Nocera, *J. Am. Chem. Soc.*, 2011, **133**, 131.
- [30] J. Rosenthal, D. G. Nocera, *Acc. Chem. Res.*, 2007, **40**, 543.
- [31] R. McGuire, D. K. Dogutan, T. S. Teets, J. Suntivich, Y. Shao-Horn, D. G. Nocera, *Chem. Sci.*, 2010, **1**, 411.
- [32] C. J. Chang, Z.-H. Loh, C. Shi, F. C. Anson, D. G. Nocera, *J. Am. Chem. Soc.*, 2004, **126**, 10013.
- [33] A. Morozan, S. Campidelli, A. Filoramo, B. Jusselme, S. Palacin, *Carbon*, 2011, **49**, 4839.
- [34] I. Hijazi, T. Bourgeteau, R. Cornut, A. Morozan, A. Filoramo, J. Leroy, V. Derycke, B. Jusselme, S. Campidelli, *J. Am. Chem. Soc.*, 2014, **136**, 6348.
- [35] N. Levy, A. Mahammed, M. Kosa, D. T. Major, Z. Gross, L. Elbaz, *Angew. Chem. Int. Ed.*, 2015, **54**, 14080.
- [36] A. Friedman, L. Landau, S. Gonen, Z. Gross, L. Elbaz, *ACS Catal.*, 2018, **8**, 5024.
- [37] M. L. Rigsby, D. J. Wasylenko, M. L. Pegis, J. M. Mayer, *J. Am. Chem. Soc.*, 2015, **137**, 4296.
- [38] X. Wang, B. Wang, J. Zhong, F. Zhao, N. Han, W. Huang, M. Zeng, J. Fan, Y. Li, *Nano Res.*, 2016, **9**, 1497.
- [39] H. Jia, Z. Sun, D. Jiang, S. Yang, P. Du, *Inorg. Chem. Front.*, 2016, **3**, 821.
- [40] M. Hanana, H. Arcostanzo, P. K. Das, M. Bouget, S. Le Gac, H. Okuno, R. Cornut *et al.*, *New J. Chem.*, 2018, **42**, 19749.
- [41] B. Boitrel, M. Bouget, P. K. Das, S. Le Gac, T. Roisnel, M. Hanana, H. Arcostanzo, R. Cornut *et al.*, *J. Porphyr. Phthalocyanines*, 2020, **24**, 675.
- [42] C. Kahlfuss, J. A. Wytko, J. Weiss, *ChemPlusChem*, 2017, **82**, 584.
- [43] P. Vorburger, M. Lo, S. Choua, M. Bernard, F. Melin, N. Oueslati, C. Boudon *et al.*, *Inorg. Chim. Acta*, 2017, **468**, 232.
- [44] M. Koepf, F. Melin, J. Jaillard, J. Weiss, *Tetrahedron Lett.*, 2005, **46**, 139.
- [45] J.-P. Tessonier, D. Rosenthal, T. W. Hansen, C. Hess, M. E. Schuster, R. Blume *et al.*, *Carbon*, 2009, **47**, 1779.
- [46] M. Lo, D. Mahajan, J. A. Wytko, C. Boudon, J. Weiss, *Org. Lett.*, 2009, **11**, 2487.
- [47] X. Lu, L. Dai, *Nat. Rev. Mater.*, 2016, **1**, article no. 16064.
- [48] J. H. Espenson, R. J. Christensen, *Inorg. Chem.*, 1977, **16**, 2561.
- [49] J. A. R. van Veen, H. A. Colijn, *Ber. Bunsenges. Phys. Chem.*, 1981, **85**, 700.
- [50] D. Banham, S. Ye, K. Pei, J.-I. Ozaki, T. Kishimoto, Y. Imashiro, *J. Power Sources*, 2015, **285**, 334.
- [51] F. Melin, C. Boudon, M. Lo, K. J. Schenk, M. Bonin, P. Ochsenbein, M. Gross, J. Weiss, *J. Porphyr. Phthalocyanines*, 2007, **11**, 212.
- [52] C. Costentin, S. Drouet, M. Robert, J.-M. Savéant, *Science*, 2012, **338**, 90.
- [53] C. Costentin, J.-M. Savéant, *Nat. Rev. Chem.*, 2017, **1**, article no. 0087.
- [54] E. Anxolabéhère-Mallart, J. Bonin, C. Fave, M. Robert, *Dalton Trans.*, 2019, **48**, 5869.
- [55] S. J. Thompson, M. R. Brennan, S. Y. Lee, G. Dong, *Chem. Soc. Rev.*, 2018, **47**, 929.



MAPYRO: the French Fellowship of the Pyrrolic Macrocyclic Ring / *MAPYRO: la communauté française des macrocycles pyrroliques*

Stereoselective formation of bismuth complexes by transmetalation of lead with adaptable overhanging carboxylic acid 5,10-strapped porphyrins

Wael Barakat^a, Ismail Hijazi^{b, c}, Thierry Roisnel^{✉ a}, Vincent Dorcet^{✉ a}, Stéphane Le Gac^{✉ *, a} and Bernard Boitrel^{✉ *, a}

^a Univ Rennes, CNRS, ISCR (Institut des Sciences Chimiques de Rennes), UMR 6226, Rennes F-35000, France

^b Faculty of Arts and Sciences, Lebanese International University LIU/BIU, PO Box 146404 Beirut, Lebanon

^c Faculty of Sciences, Lebanese University, Beirut, Lebanon

E-mails: wael-barakat1@hotmail.com (W. Barakat), i.hijazi@outlook.com (I. Hijazi), thierry.roisnel@univ-rennes1.fr (T. Roisnel), vincent.dorcet@univ-rennes1.fr (V. Dorcet), stephane.legac@univ-rennes1.fr (S. Le Gac), bernard.boitrel@univ-rennes1.fr (B. Boitrel)

Abstract. Out-of-plane deformations of metalloporphyrin skeletons have been well documented as playing important roles in relevant biological processes. In contrast, out-of-plane binding to the N-core of large metal cations as period 6 post-transition elements has remained poorly investigated. We describe herein monometallic complexes of Pb(II) and Bi(III) with 5,10 single strapped porphyrin ligands bearing a carboxylic acid group with two possible “in/out” orientations, in which the metal ions are bound to the N-core of the macrocycle either from the strap side or from the naked side. In the case of Pb(II), both the kinetics of insertion and resulting OOP stereoselectivity are influenced by the “in/out” stereoisomerism of the overhanging COOH. Remarkably, Bi(III) insertion proceeded quasi-instantaneously at RT owing to the transmetalation of its Pb(II) counterpart. The addition of a cyano group in α position of the carboxylic acid group generates a ligand exhibiting an increased stereoselectivity in the metalation processes with Pb(II) and Bi(III): these cations are coordinated exclusively from the naked and strap side of the macrocycle, respectively. This difference in behavior is likely explained by steric hindrance for the divalent cation, which is counterbalanced by the establishment of the second sphere of coordination with the strap for the trivalent cation. Such a behavior is thought of interest for the further design of adaptable supramolecular coordination assemblies.

Keywords. Coordination, Transmetalation, Bismuth, Lead, Porphyrins.

Available online 30th July 2021

* Corresponding authors.

1. Introduction

Lead(II) and bismuth(III) porphyrin complexes are known to form generally under harsh conditions [1–3] and to be mononuclear, that is one metal cation for one porphyrin unit although dimeric structures have also been reported [4,5]. However, these observations are valid for unfunctionalized macrocycles and the behavior of the porphyrin can be changed if not domesticated by additional functional groups around its binding site. With this target in mind, coordination of either lead(II) or bismuth(III) cations [6, 7] have been significantly investigated in decorated porphyrin ligands, particularly those bearing one or two straps in diametrically opposed meso positions [8–10]. The formation of such a structure is due to the grafting of the strap(s) on the 5,15 or 10,20 meso positions of the macrocycle. Our group has previously studied the influence of different types of functionalities such as the overhanging carboxylic acid porphyrins that open the way to a new supramolecular coordination chemistry. These ligands exhibit a carboxylic acid group in the apical position above the N-core binding site. As a result, different coordination modes of lead(II) complex have been observed as either coordinated to the N-core, or bound at the level of the strap stabilized by an exogenous acetate group [9], further leading to unusual pentanuclear supramolecular assemblies (Scheme 1, top) [11].

These types of complexes are of importance in supramolecular chemistry of porphyrins which usually rely on the coordination/decoordination of ligand(s) on the N₄-bound metal [12]. Indeed, with such dynamic bimetallic complexes, compartmentalized and non-compartmentalized translocations were observed and opened the way to photoredox processes [13–15] dynamic constitutional evolution [16] or stereoselective metalations [17] for instance. However, as suspected with bis-strapped “pearl oysterlike” porphyrins [18], the very same strap connected in adjacent meso positions (5,10 and/or 15,20) can also deliver an overhanging carboxylic acid but with an increased flexibility of the strap [19]. Indeed, comparison of “5,10-strapped” Zn(II) and Bi(III) complexes evidenced conformational adaptation of the strap leading to different orientations of the overhanging carboxylic acid (towards/outwards the N-core, Scheme 1, bottom).

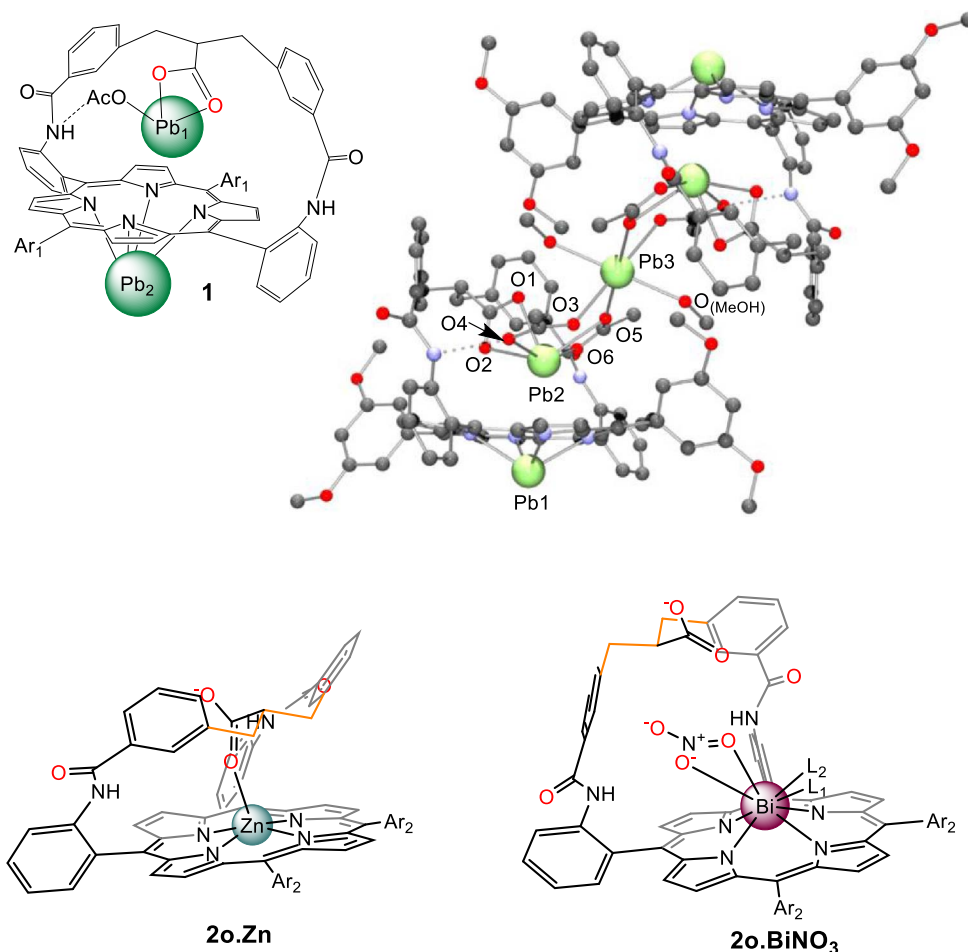
This is the reason why we decided to investigate the coordination properties of single strapped porphyrins **2** and **3** (Schemes 1 and 2) for which two stereoisomers are present depending on the position of the carboxylic acid group relative to the N-core. The coordination chemistry of overhanging carboxylic acid porphyrin **3** bearing an additional coordinating function (cyano) above the center of the macrocycle may be of interest to form adaptable supramolecular coordination assemblies [12,20,21].

2. Results and discussion

As described earlier for porphyrins **2** [19] the preparation of porphyrin **3** (Scheme 2) was performed via the same procedure by condensation of ethyl-2-cyanoacetate in basic medium on porphyrin **5** which led to the formation of porphyrin **4** as two different isomers (**4o** and **4i**) separated by flash chromatography on silica gel column, and obtained with a yield of 10% and 75%, respectively. Porphyrins **4o** and **4i** were then saponified by treatment with KOH in ethanol for 2 h, to give porphyrins **3o** and **3i** in quantitative yields. The corresponding conformation of these isomers was determined at the stage of ester compounds, where the ethoxy carbonyl group is located in different positions (“in” or “out”).¹ The formation of the two isomers in different yields (**4o**: 10% yield and **4i**: 75% yield) can be explained by the steric hindrance generated by the cyano group, smaller than that of the carbethoxy group in the W-shaped conformation as reported for previous cyano compounds [22].

Conventionally, the overhanging ester group (i) (position “in”) represents the location of the group with respect to the macrocycle, which is closer to the macrocycle than ester (o) (position “out”) when the strap adopts a broken-shape conformation (footnote 1) [23,24]. ¹H NMR shows that the ethoxy carbonyl group resonates at 2.97 ppm and 0.11 ppm in **4i** but at 1.64 ppm and 0.5 ppm in **4o**. This indicates that the “out” position is actually closer to the porphyrin plane than the “in” position. Moreover, proton Ha resonates at 3.50 ppm and 3.29 ppm for

¹Note that the “in” and “out” labeling was initially chosen with the strap in a broken-shape conformation before we realized that most of these ligands adopt a W-shape conformation; see Ref. [18].



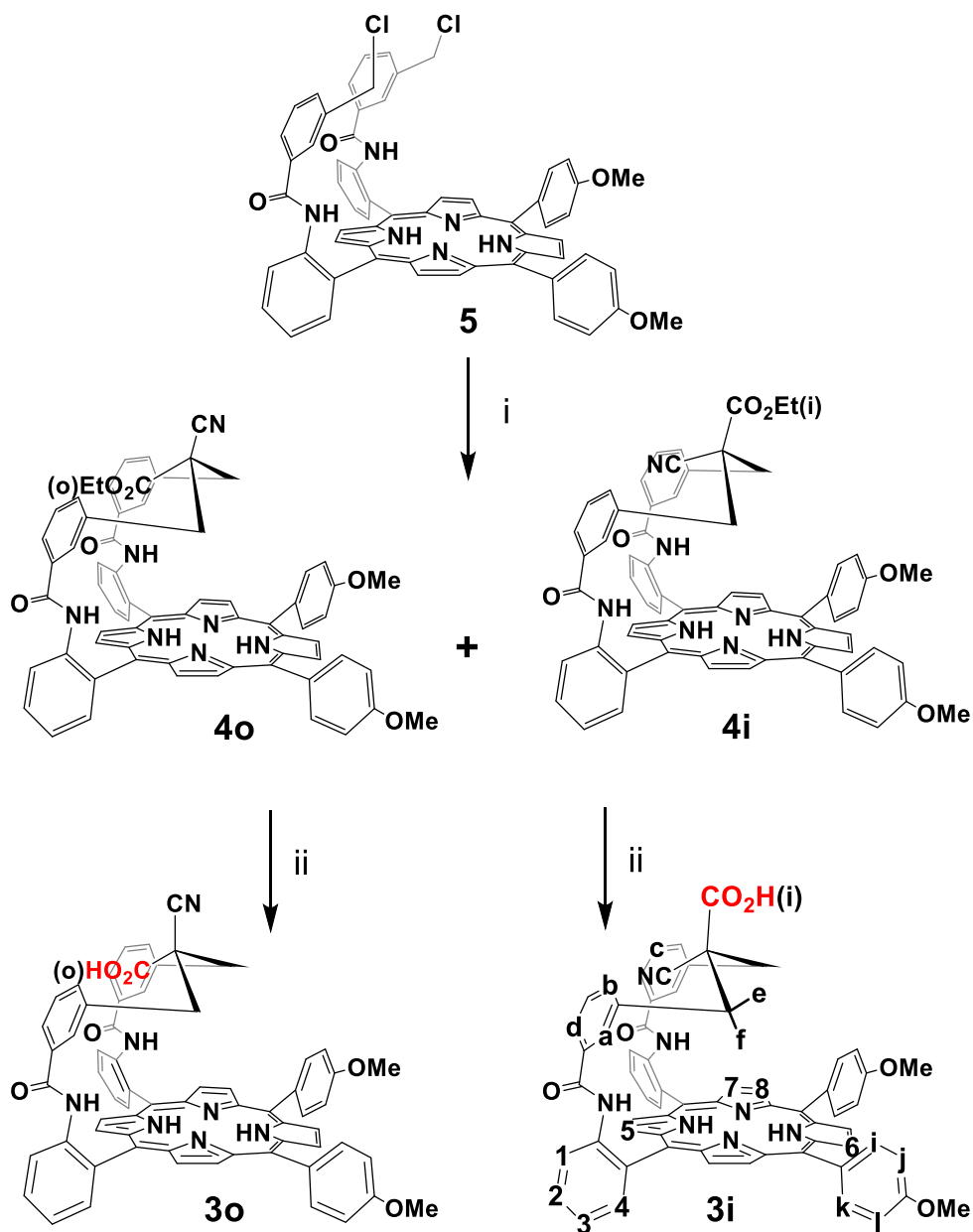
Scheme 1. Top: dinuclear lead complex of **1** (left, Ar₁ = 3,5-dimethoxyphenyl) which assembles as a pentanuclear complex in the solid state (ball and stick view, X-ray structure, right). Bottom: zinc and bismuth complexes of porphyrin **2o** (Ar₂ = 4-methoxyphenyl) exhibiting two different conformations of the strap, either bent-over or straight-up, respectively.

4i and **4o** respectively. This conformational analysis deduced from proton NMR spectroscopy is consistent with a bent conformation of the strap exhibiting a W-shaped structure as depicted in Scheme 2. Later on, this conformation was confirmed at the stage of the acid with compound **3i**. Indeed, an X-ray single-crystal analysis was performed and confirmed a W-shaped structure of the CH₂ benzylic carbon atoms C1 and C3 (Figure 1).

The X-ray structure of **3i** also indicates that the porphyrin is saddle-shaped with an average displacement of four diametrically opposed β-pyrrolic carbon atoms above the 24-atom mean macrocyclic

plane (24MP) (0.369 Å) while the four other ones are displaced of −0.368 Å below the 24MP of the porphyrin. This distortion is observed together with only a light ruffling (4°) [25]. The W-shaped strap is bent over the macrocycle with a mean angle of 40° relative to the 24MP. In this conformation of the free-base ligand, the carboxylic group is rejected away from the coordination site.

In order to compare the two series of ligands, with and without a cyano group, we first investigated the coordination of **2o** and **2i** toward Pb(II) (Scheme 3). Complexation properties of porphyrins **2o** and **2i** towards Pb(II) were studied at 298 K by ¹H NMR



Scheme 2. Synthesis of single strapped ligands (labeling detailed for **3i**). (i) ethyl-2-cyanoacetate (50 eq), THF, EtONa, RT, 2 h (**4o**: 10% yield and **4i**: 75% yield). (ii) EtOH, KOH (30 eq), THF, 2 h, RT, quantitative yields.

titration experiments in DMSO- d_6 with an excess of diisopropylethylamine (DIPEA). In contrast to harsh conditions usually required for non-functionalized porphyrins, the insertion of Pb(II) was instantaneous with **2o** whereas it took 4 h with **2i** (Scheme 3a, b).

The addition of 1.5 equiv of $\text{Pb}(\text{NO}_3)_2$ to **2o** in the NMR tube led to the observation of a broad ^1H NMR spectrum (Figure 2b). No significant change in the spectrum was observed with an excess of this salt (3.5 eq) (Figure 2c), indicating the formation of a

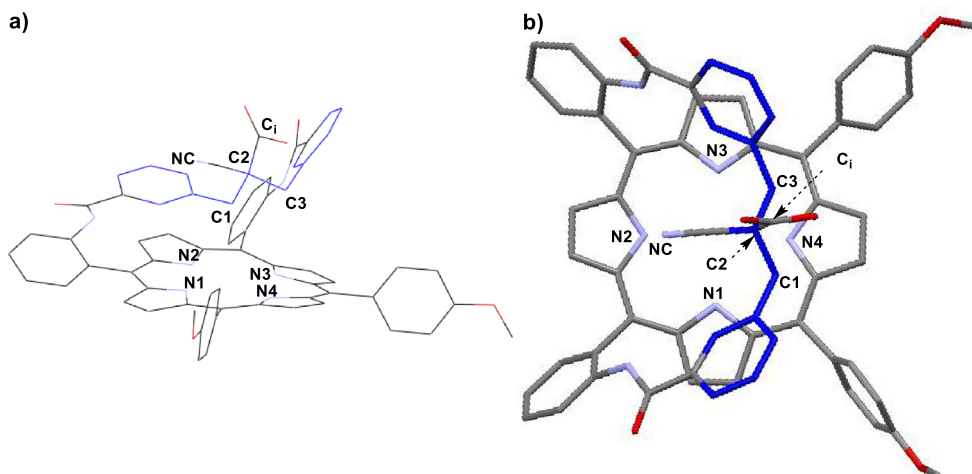


Figure 1. X-ray structure of **3i** (CCDC 1971401): (a) side view and (b) apical view. Note: solvents of crystallization and hydrogen atoms were omitted for clarity.

mononuclear species. A well-resolved spectrum was obtained by recording the NMR tube at 333 K (Figure 2d), and indicated the formation of two compounds in a 9:1 ratio. Two different conformations of the strap were observed based on the chemical shift changes of protons Ha, He and Hf. For instance, Ha which resonates at 4.42 ppm in **2o** is split into two protons upon coordination, as Ha' deshielded at 5.59 ppm (major, $\Delta\delta\text{Ha}' = 1.17$ ppm) and Ha shielded at 4.37 ppm (minor, $\Delta\delta\text{Ha} = -0.05$ ppm) (Figure 2d). Similarly, He resonating at 1.07 ppm in **2o**, is split at 1.45 ppm (major, $\Delta\delta\text{He}' = 0.38$ ppm) and 0.14 ppm (minor, $\Delta\delta\text{He} = -0.93$ ppm). Finally, Hf resonating at -0.61 ppm in **2o**, becomes downfield shifted to 1.32 ppm (major, $\Delta\delta\text{Hf}' = 0.71$ ppm) and -0.24 ppm (minor, $\Delta\delta\text{Hf} = 0.37$ ppm) during the metal insertion. These observations are consistent with the presence of two major and minor compounds (**2o.Pb_{os}** and **2o.Pb_{ss}**). On the one hand, **2o.Pb_{ss}** incorporates Pb(II) on the same side of the strap, promoting a conformational change of the strap from a shielded “bent-over” position to a deshielded “straight-up” one. On the other hand, **2o.Pb_{os}** has Pb(II) attached to the N-core of the macrocycle on the opposite side of the strap (Scheme 3a).² It should be noted that the coordination of Pb(II) from the naked side of the

macrocyclic allows the strap to stay bent over the porphyrin plane.

The complexation of Pb(II) with **2i** is quite similar to **2o**, where two compounds (**2i.Pb_{ss}** and **2i.Pb_{os}**) were observed but in equal proportions (Scheme 3b). One complex (**2i.Pb_{ss}**) has Pb(II) coordinated from the same side of the strap, while the second (**2i.Pb_{os}**) has Pb(II) coordinated from naked side of the macrocycle. Although there is no evidence for a coordination bond between the overhanging carboxylic group and the lead cation, an assistance mechanism in the insertion of lead cation by the carboxylic acid group can easily explain the 9:1 ratio in the case of **2o** in which the overhanging group could perform a deconvolution [26,27] of the metal salt with lead cation bound at the level of the strap before coordinating the N-core.

Having understood the coordination behaviors of the two isomers of **2** with lead, the coordination of Pb(NO₃)₂ was investigated with compound **3i** bearing an additional cyano group as the more abundant isomer of porphyrins **3**. Similarly to the case of **2i**, titration with up to 3 equiv of Pb(NO₃)₂ showed the formation of a broad ¹H NMR spectrum at 298 K after 5 h. No evolution occurred in the spectrum even after 24 h at room temperature. The coordination of Pb(II) occurred from the opposite side of the strap (Scheme 3c) as deduced from the shielding of Ha, He and Hf during coordination. For instance, Ha shifted from 3.35 to 2.66 ppm ($\Delta\delta\text{Ha} =$

²**ss**: metal coordinates from the same side of the strap. **os**: metal coordinates from the opposite side of the strap.

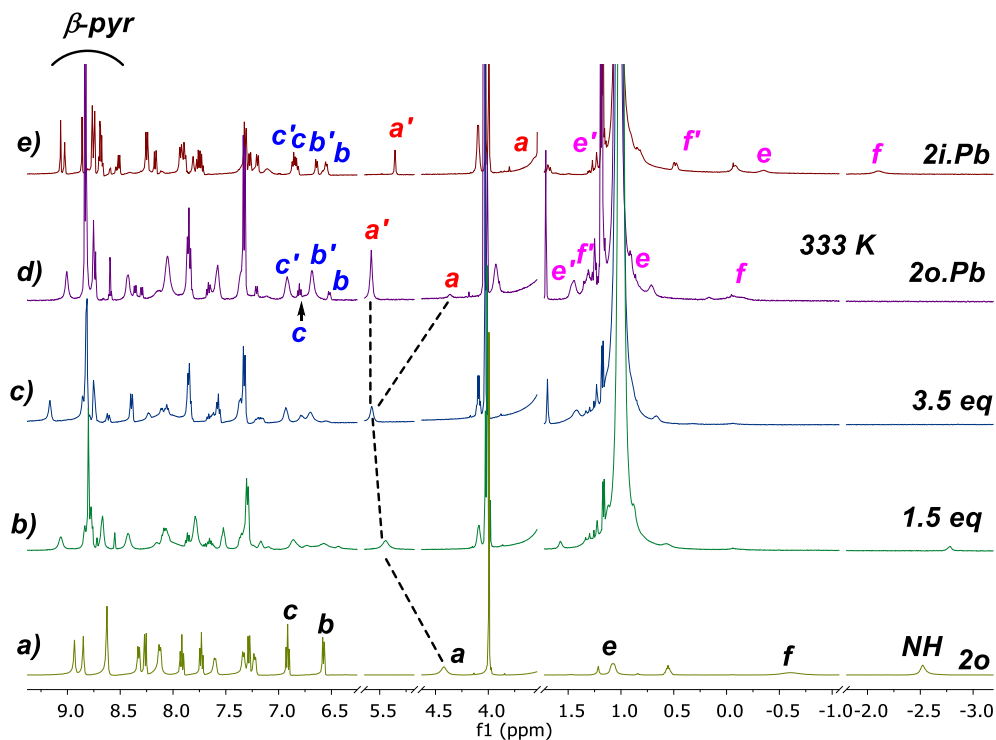


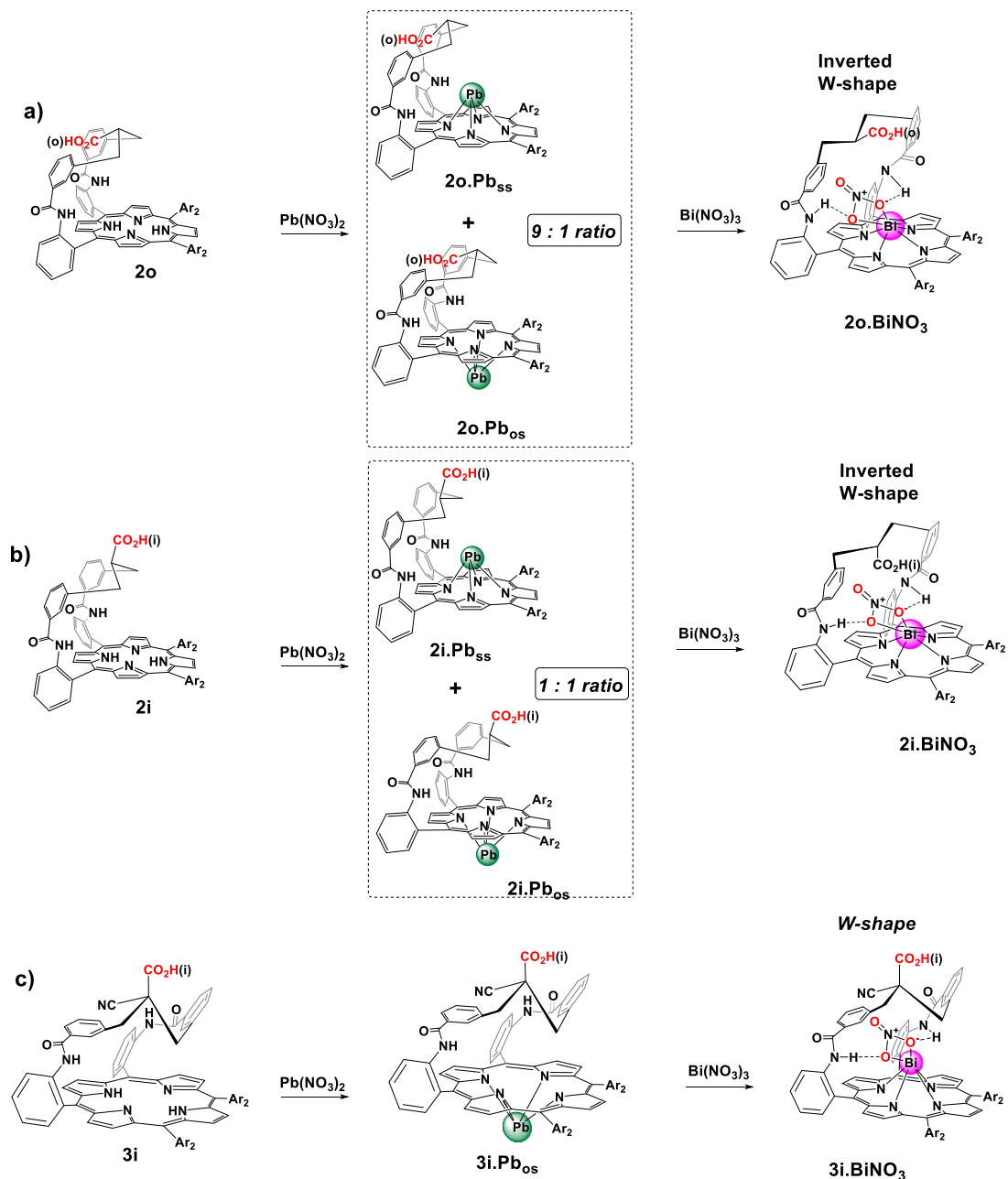
Figure 2. ^1H NMR spectra (selected regions) in $\text{DMSO-}d_6$ at 298 K of: (a) **2o**, (b) **2o** with 1.5 eq $\text{Pb}(\text{NO}_3)_2$, (c) **2o** with 3.5 eq $\text{Pb}(\text{NO}_3)_2$, (d) **2o.Pb** at 333 K, (e) **2i.Pb**.

–0.69 ppm), He shifted from 1.05 ppm to 0.59 ppm ($\Delta\delta_{\text{He}} = -0.46$ ppm) and Hf from –2.47 ppm to –3.30 ppm ($\Delta\delta_{\text{Hf}} = -0.83$ ppm).

An X-ray structure was obtained and established the coordination of Pb(II) from the opposite side of the strap (Figure 3). The coordination sphere of lead in **3i.Pb_{os}** contains only the four nitrogen atoms of the macrocycle with an average bond length N–Pb of 2.382 Å with the metal cation standing 1.333 Å away from the 24MP. The strap exhibits a W-shaped structure and is bent over the coordination site with a mean angle of 40° relative to the 24MP, as in the free-base. It should be noted that the cyano group is located between two aromatic groups of the strap with its nitrogen atom at 3.354 Å from the 24MP whereas the carboxy residue is oriented outside of the cavity with its carbon atom 5.544 Å away from the 24MP. Therefore, the coordination of Pb(II) in the presence of an additional cyano group in α position of the carboxylic acid group (**3i.Pb_{os}**) leads to the exclusive formation of a complex in which the metal coordinates from the opposite side of the strap. This can

be explained by the steric hindrance created by the cyano group which forces the metal to approach the N-core of the macrocycle from the naked side.

It was also interesting to investigate bismuth(III) insertion in these new ligands. The formation of a bismuth complex with a single strapped porphyrin (**2o** and **2i**) requires a long time of reaction (4–16 h at 85 °C) in the case of bismuth nitrate [19]. To increase the kinetics of Bi(III) insertion, a transmetalation of Pb(II) by Bi(III) was envisaged as it was found efficient with related porphyrins [28,29]. The transmetalation process was achieved by the addition of bismuth nitrate on the two lead complexes, **2i.Pb** and **2o.Pb**. In both cases, the formation of the bismuth complex was observed quasi instantaneously as attested by the ^1H NMR spectra (Figure 4a, d). As an example, in the case of **2i**, the addition of $\text{Bi}(\text{NO}_3)_3$ bismuth salt to the mixture of Pb(II) complexes **2i.Pb_{ss}** and **2i.Pb_{os}** led to the formation of a single bismuth complex, in which the metal coordinates from the side of the strap (Scheme 3b and Figure 4a). Likely, in this complex, the bismuth



Scheme 3. Coordination of **2o** (a), **2i** (b), and **3i** (c) with $\text{Pb}(\text{NO}_3)_2$ (3.5 eq) in $\text{DMSO}-d_6$ at 298 K, followed by instantaneous formation of bismuth complex by transmetalation of $\text{Pb}(\text{II})$ by $\text{Bi}(\text{III})$ (3 eq of $\text{Bi}(\text{NO}_3)_3$ added). Note: **ss** = $\text{Pb}(\text{II})$ coordinates from the same side of the strap. **os** = $\text{Pb}(\text{II})$ coordinates from opposite side of the strap. Ar_2 = 4-methoxyphenyl.

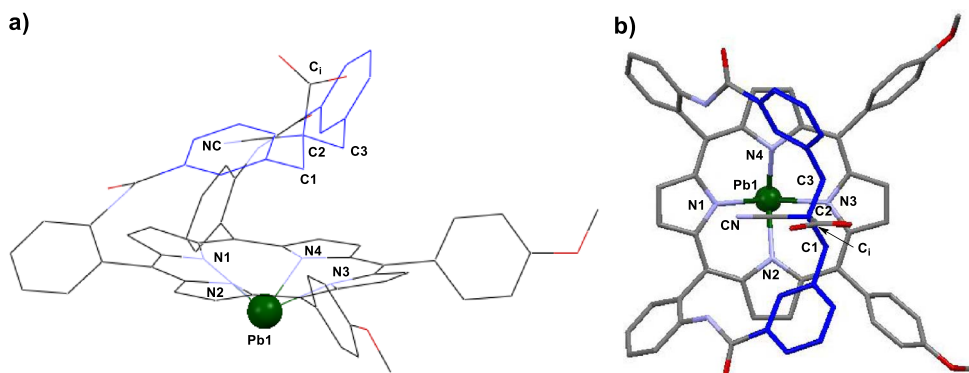


Figure 3. X-ray structure of **3i.Pb_{Os}** (CCDC 1971367): (a) side view and (b) apical view. Note: solvents of crystallization and hydrogen atoms were omitted for clarity. Selected distances: N1–Pb 2.387 Å, N2–Pb 2.387 Å, N3–Pb 2.392 Å, N4–Pb 2.365 Å, Pb–24MP 1.333 Å.

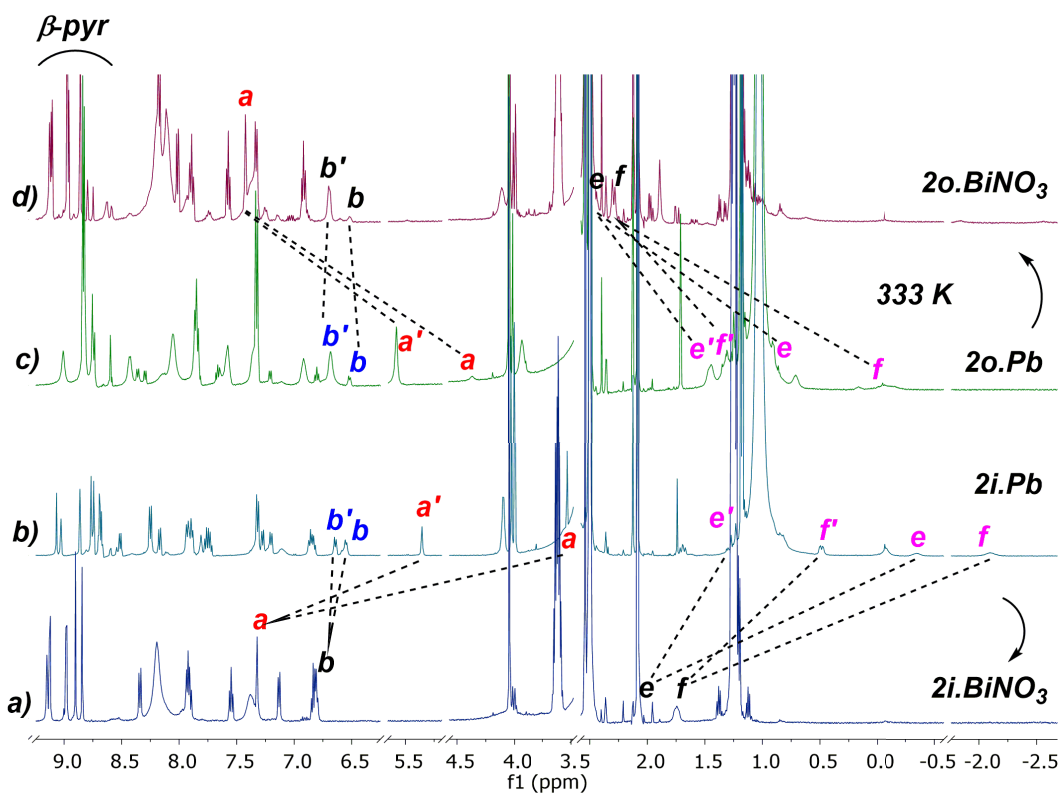


Figure 4. ^1H NMR (selected regions) in $\text{DMSO-}d_6$ at 298 K of (a) **2i.BiNO₃**, (b) **2i.Pb** (1:1 mixture), (c) **2o.Pb** at 333 K (9:1 mixture), (d) **2o.BiNO₃**.

nitrate counter-ion is stabilized by two hydrogen bonds with the amide functions of the strap, which stands in a straight-up position to accommodate the “BiNO₃” moiety in the cavity, in an inverted W-shape

conformation. This was deduced by analogy with the previously reported X-ray structure of the **2o.BiNO₃** bismuth complex obtained directly from the free-base (Scheme 1, bottom) [19]. Therefore, owing to

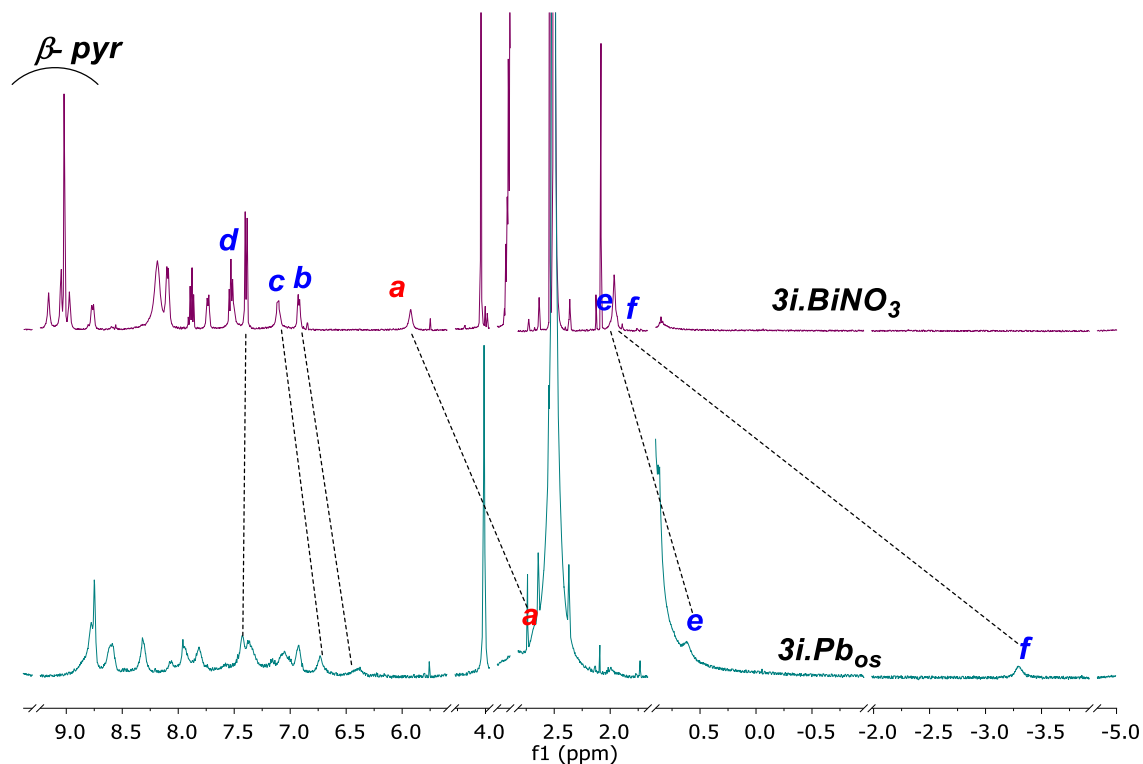


Figure 5. ^1H NMR spectra (selected regions) of **3i.Pb_{os}** treated with 3 eq $\text{Bi}(\text{NO}_3)_3$ in $\text{DMSO-}d_6$ at 298 K, leading to the formation of **3i.BiNO₃**.

the specific arrangement of this strap, it becomes possible to form instantaneously a bismuth complex at room temperature by transmetalation instead of heating 4–16 h at 85 °C.

We applied with success this strategy to the coordination of Bi(III) with **3i**, difficult to achieve at room temperature as no coordination was observed after the addition of 3 eq of $\text{Bi}(\text{NO}_3)_3$ to the free base. Furthermore, heating the NMR tube up to 353 K to insert Bi(III) into the N-core led to decarboxylation. Thus, the bismuth complex was formed instantaneously through transmetalation of lead complex **3i.Pb_{os}** with 3 eq of bismuth salt (Scheme 3c). The ^1H NMR spectrum recorded at 298 K evidenced the coordination of Bi(III) with changes in the conformation of the strap from bent-over to straight-up (Figure 5) as revealed by the variation of the chemical shifts of Ha, He and Hf. For instance, Ha which initially resonated at 2.66 ppm was shifted to 5.93 ppm during the transmetalation process ($\delta\Delta\text{Ha} = 3.27$ ppm). In the same line, He and Hf shifted from 0.59 ppm and

–3.30 ppm in **3i.Pb_{os}** to 1.96 ppm and 1.93 ppm, respectively after Bi(III) insertion. Therefore, bismuth likely coordinates from the strap side and could be stabilized by an exogenous nitrate molecule, likely linked to the strap by two hydrogen bonds as in the case of **2i.BiNO₃**. With this type of complex, the strap is likely arranged in an inverted W-shape straight-up conformation with the Ha protons lightly oriented outward the center of the macrocycle. This conformation remains consistent with its chemical shift at 5.93 ppm (instead of Ha = 7.32 ppm in case of **2i.BiNO₃**). However, only the resolution of the X-ray structure of this bismuth complex would allow a definite structural validation of its conformation.

3. Conclusions

We have designed new strapped porphyrins bearing a cyano group in α position of the overhanging carboxylic acid group. Coordination studies of Pb(II) and Bi(III) cations with/without cyano group

beside the carboxylic acid have shown different conformational behaviors of the strap leading to unexpected metal complexes. The coordination of Pb(II) with compound **2** lacking the cyano group led to the formation of two metal complexes in which Pb(II) coordinates either from the side of the strap or from the naked side of the macrocycle with different stereoselectivity depending on the considered stereoisomer **2i** or **2o**. For the former, no stereoselectivity was observed as both complexes (**2i.Pb_{ss}** and **2i.Pb_{os}**) were formed. In contrast, for the latter, a significant stereoselectivity was achieved as **2o.Pb_{ss}** was formed with a 9:1 ratio. Conversely, the steric hindrance generated by the presence of the cyano group in compound **3i** resulted in the stereoselective formation of a single metal complex with Pb(II) coordinated on the naked side. Moreover, transmetalation of Pb(II) by Bi(III) was shown to be an efficient method for the instantaneous and stereoselective formation of the bismuth complex, which forms exclusively from the side of the strap with **3i**. Coordination of these isomers at the level of the strap with different metals, targeting supramolecular coordination assemblies, is currently being under investigation by our group.

4. Experimental section

4.1. General

¹H and ¹³C NMR spectra were recorded at respectively 500 MHz and 125 MHz and referenced to the residual protonated solvents. THF was distilled over Na/benzophenone according to a standard procedure. Other chemicals were used as received without any further purification. All reactions were performed under argon and monitored by TLC (silica, CH₂Cl₂/CH₃OH). Column flash chromatography was performed on silica gel (Merck TLC-Kieselgel 60 H, 15 μm).

Typical procedure for the porphyrin synthesis here detailed in case of 3i: sodium (50 eq) in EtOH was stirred at room temperature for 30 min in a two-neck round bottom flask and ethyl-2-cyanoacetate (50 eq) was added. After 1 h, the resulting mixture was added to a solution of porphyrin **5** (1 eq) in CH₂Cl₂. The reaction mixture was stirred for 2 h at RT, then water was added. The organic layer was separated from water and evaporated under vacuum. Finally, the two isomers **4o** and **4i** were separated on a

silica gel chromatography column eluted with 0.1% MeOH/CH₂Cl₂ with a yield of 10% and 75%, respectively. In the next step, a 100 ml two-neck round bottom flask equipped with stir bar was charged with KOH (30 eq) in distilled ethanol. After 30 min, porphyrin **4i** (38 μmol, 40 mg, 1 eq) was dissolved in 80 mL THF and slowly added to the reaction mixture, which was stirred for 2 h at room temperature. The reaction was quenched by adding distilled water, neutralized by 1 M HCl, and filtrated. The resulted product was recovered by MeOH/CH₂Cl₂. The solvent was removed under vacuum. The product was obtained in quantitative yield.

α-5,10-bis{2,2'-[3,3'-(2-(cyano)-2-(ethoxycarbonyl)propane-1,3-diyl)benzoylamino]phenyl}-15,20-bis(4-methoxyphenyl)porphyrin: 4o. ¹H NMR (CDCl₃, 298 K, 500 MHz): δ_H, ppm 8.96 (2H, s, H₅), 8.93 (2H, s, H₆), 8.67 (2H, d, *J* = 4.2 Hz, H₇), 8.65 (2H, d, *J* = 8.3 Hz, H₁), 8.61 (2H, d, *J* = 4.2 Hz, H₈), 8.52 (2H, d, *J* = 7.5 Hz, H₄), 8.21 (2H, d, *J* = 8.3 Hz, H₁), 7.95 (2H, t, *J* = 7.7 Hz, H₂), 7.75 (2H, t, *J* = 8 Hz, H₃), 7.72 (2H, d, *J* = 8 Hz, H_d), 7.30 (2H, d, *J* = 7.5 Hz, H₁), 7.27 (2H, d, *J* = 8.2 Hz, H_k), 7.09 (2H, t, *J* = 7.6 Hz, H_c), 7.07 (2H, m, H_j), 7.06 (2H, s, NHCO), 6.74 (2H, d, *J* = 6.8 Hz, H_b), 4.07 (6H, s, O-CH₃), 3.29 (2H, s, H_a), 1.64 (2H, q, *J* = 7 Hz, CH₂ester), 0.89 (2H, d, *J* = 12.4 Hz, H_e), -0.5 (3H, t, *J* = 7 Hz, CH₃ester), -1.97 (2H, d, *J* = 12.6 Hz, H_f), -2.06 (2H, s, NH pyr).HSQC (CDCl₃, 298 K, 500 MHz): δ_C, ppm, 135.82 (C_k), 135.64 (C_i), 135.22 (C_g), 134.18 (C₄), 132.54 (C₇), 131.95 (C_b), 129.99 (C₂), 129.15 (C_c), 129.11 (C₅), 128.98 (C₆), 127.90 (C_d), 124.42 (C_a), 123.67 (C₃), 121.85 (C₁), 112.33 (C_j), 112.57 (C_l), 59.77 (C_{ester}), 56.11 (C_{OMe}), 39.98 (C_e), 39.98 (C_f), 12.33 (C_{ester}). UV-vis (CHCl₃): λ/nm (ε, dm³·mol⁻¹·cm⁻¹): 426 (272120), 520 (26710), 556 (14080), 595 (5000), 652 (6800). ESI-HRMS: *m/z* calcd. 1050.39734 [M + H]⁺ for C₆₇H₅₂N₇O₆, found 1050.3968 (0 ppm).

α-5,10-bis{2,2'-[3,3'-(2-(cyano)-2-(ethoxycarbonyl)propane-1,3-diyl)benzoylamino]phenyl}-15,20-bis(4-methoxyphenyl)porphyrin: 4i. ¹H NMR (CDCl₃, 298 K, 500 MHz): δ_H, ppm 8.98 (2H, s, H₅), 8.97 (2H, s, H₆), 8.71 (2H, d, *J* = 4.3 Hz, H₇), 8.61 (2H, d, *J* = 4.3 Hz, H₈), 8.56 (2H, d, *J* = 7.5 Hz, H₁), 8.54 (2H, d, *J* = 8.7 Hz, H₄), 8.22 (2H, d, *J* = 7.9 Hz, H₁), 7.95 (2H, t, *J* = 8 Hz, H₂), 7.78 (2H, t, *J* = 7.4 Hz, H₃), 7.67 (2H, d, *J* = 7.7 Hz, H_d), 7.31 (2H, d, *J* = 7.9 Hz, H₁), 7.24 (2H, d, *J* = 8.2 Hz, H_k), 7.05 (2H, d, *J* = 7.6 Hz,

H_j), 6.94 (2H, s, NHCO), 6.92 (2H, t, $J = 7.8$ Hz, H_c), 6.27 (2H, d, $J = 7.5$ Hz, H_b), 4.06 (6H, s, O-CH₃), 3.50 (2H, s, H_a), 2.97 (2H, q, $J = 7$ Hz, CH₂ester), 1.06 (2H, d, $J = 12.5$ Hz, H_e), 0.11 (3H, t, $J = 7$ Hz, CH₃ester), -2.15 (2H, s, NH pyr), -2.44 (2H, d, $J = 13.2$ Hz, H_f). HSQC (CDCl₃, 298 K, 500 MHz): δ_c , ppm, 136.12 (C_k), 135.53 (C_i), 135.28 (C₈), 133.44 (C₁), 132.72 (C₇), 130.95 (C_b), 129.83 (C₂), 128.51 (C_c), 128.35 (C₆), 127.94 (C₅), 127.71 (C_d), 125.54 (C_a), 123.98 (C₃), 123.43 (C₄), 112.80 (C_l), 112.21 (C_j), 61.32 (C_{ester}), 56.06 (C_{OMe}), 39.44 (C_e), 39.44 (C_f), 12.77 (C_{ester}). UV-vis (CHCl₃): λ /nm (ϵ , dm³·mol⁻¹·cm⁻¹): 426 (264950), 520 (41900), 557 (20200), 593 (8400), 650 (3800). ESI-HRMS: m/z calcd. 1050.39736 [M + H]⁺ for C₆₇H₅₂N₇O₆, found 1050.3970 (0 ppm).

α -5,10-bis{2,2'-[3,3'-(2-(cyano)-2-(carboxyl)prop-ane-1,3-diyl)benzoylamino]phenyl}-15,20-bis-(4-methoxyphenyl)porphyrin: 3o. ¹H NMR (DMSO, 298 K, 500 MHz): δ_H , ppm 8.92 (2H, s, H₅), 8.81 (2H, s, H₆), 8.55 (2H, broad, H₇), 8.52 (2H, d, $J = 4.3$ Hz, H₈), 8.35 (2H, d, $J = 7.7$ Hz, H₁), 8.27 (2H, d, $J = 8.1$ Hz, H₄), 8.19 (2H, s, NHCO), 8.11 (2H, d, $J = 8.1$ Hz, H_i), 7.91 (2H, t, $J = 8$ Hz, H₃), 7.73 (2H, d, $J = 7.9$ Hz, H₂), 7.51 (2H, t, $J = 8.2$ Hz, H_k), 7.33 (2H, broad, H_d), 7.32 (2H, broad, H_l), 7.17 (2H, d, $J = 7.8$ Hz, H_j), 6.94 (2H, t, $J = 7.6$ Hz, H_c), 6.69 (2H, d, $J = 7.6$ Hz, H_b), 4.31 (2H, s, H_a), 3.99 (6H, s, O-CH₃), 0.72 (2H, d, $J = 12.8$ Hz, H_e), -0.63 (2H, broad, H_f), -2.48 (2H, s, NH pyr), 1H of carboxylic acid was not observed. HSQC (CDCl₃, 298 K, 500 MHz): δ_c , ppm, 135.73 (C_k), 135.48 (C_i), 134.80 (C₁), 132.59 (C₆), 132.11 (C_b), 129.81 (C₃), 128.02 (C_c), 127.77 (C_a), 126.10 (C_d), 124.95 (C₂), 123.36 (C₄), 112.74 (C_j), 112.98 (C_l), 40.45 (C_e), 40.45 (C_f). UV-vis (DMSO): λ /nm (ϵ , dm³·mol⁻¹·cm⁻¹): 426 (218250), 520 (24600), 560 (15440), 592 (10080), 649 (7810). ESI-HRMS: m/z calcd. 1022.36606 [M + H]⁺ for C₆₅H₄₈N₇O₆, found 1022.36660 (0 ppm).

α -5,10-bis{2,2'-[3,3'-(2-(cyano)-2-(carboxyl)prop-ane-1,3-diyl)benzoylamino]phenyl}-15,20-bis-(4-methoxyphenyl)porphyrin: 3i. ¹H NMR (DMSO, 298 K, 500 MHz): δ_H , ppm 9 (2H, s, H₅), 8.97 (2H, s, H₆), 8.55 (2H, broad, H₇), 8.6 (2H, d, $J = 7.6$ Hz, H₁), 8.55 (2H, broad, H₈), 8.40 (2H, d, $J = 8$ Hz, H₄), 8.23 (2H, d, $J = 7.9$ Hz, H_i), 7.98 (2H, t, $J = 8.5$ Hz, H₃), 7.9 (2H, d, $J = 7.1$ Hz, H_j), 7.84 (2H, t, $J = 7.2$ Hz, H₂), 7.50 (2H, d, $J = 8.8$ Hz, H_d), 7.37 (2H, d, $J = 8.8$ Hz, H_l), 7.21 (2H, d, $J = 7.4$ Hz,

H_k), 6.92 (2H, s, NHCO), 7.05 (2H, t, $J = 7.6$ Hz, H_c), 6.43 (2H, d, $J = 7.7$ Hz, H_b), 3.98 (6H, s, O-CH₃), 3.35 (2H, s, H_a), 1.05 (2H, d, $J = 12.5$ Hz, H_e), -2.32 (2H, s, NH pyr), -2.47 (2H, d, $J = 13.2$ Hz, H_f), 1H of carboxylic acid was not observed. HSQC (CDCl₃, 298 K, 500 MHz): δ_c , ppm, 135.70 (C_k), 135.49 (C₈), 135.37 (C_i), 133.60 (C₁), 132.40 (C₇), 131.88 (C_b), 130.25 (C₃), 129.51 (C₅), 129.34 (C_c), 128.35 (C₆), 127.33 (C_d), 124.93 (C₂), 124.56 (C_a), 123.36 (C₄), 113.10 (C_j), 113.03 (C_l), 55.61 (C_{OMe}), 37.70 (C_e), 37.70 (C_f). UV-vis (DMSO): λ /nm (ϵ , dm³·mol⁻¹·cm⁻¹): 427 (167810), 519 (22270), 556 (9050), 592 (5640), 650 (3760). ESI-HRMS: m/z calcd. 1022.36606 [M + H]⁺ for C₆₅H₄₈N₇O₆, found 1022.36662 (0 ppm).

4.2. Typical procedure for metal insertion

A solution (S₁) of Pb(NO₃)₂ (37.6 μ mol, 12.4 mg, 12.5 eq) in DMSO-*d*₆ (500 μ L) was prepared. Pb(II) insertion was performed in an NMR tube by mixing either **2o** or **2i** (3.012 μ mol, 3 mg, 1 eq), DMSO-*d*₆ (500 μ L), DIPEA (17.2 μ mol, 3 μ L, 5.7 eq), and S₁ (200 μ L, 3 eq). Leaving the NMR tube at room temperature for respectively a few minutes and 4 hours led quantitatively to **2o.Pb** and **2i.Pb**, as attested by ¹H NMR spectra recorded at 333 K and 298 K, respectively.

A solution (S₂) of Bi(NO₃)₃ (37.6 μ mol, 18.2 mg, 12.5 eq) in DMSO-*d*₆ (500 μ L) was prepared. The complexes **2o.BiNO₃** and **2i.BiNO₃** were formed instantaneously by adding 3 eq from S₂ (200 μ L) to each NMR tube (**2o.Pb** and **2i.Pb**). The proton NMR spectrum was recorded at 298 K.

A solution (S₃) of PbNO₃ (36.6 μ mol, 11.9 mg, 12.5 eq) in DMSO-*d*₆ (500 μ L) was prepared. The complex **3i.Pb_{oss}** was formed by mixing **3i** (2.93 μ mol, 3 mg, 1 eq), DMSO-*d*₆ (500 μ L), DIPEA (16.7 μ mol, 2.9 μ L, 5.7 eq), and S₃ (120 μ L, 3 eq) for 5 h at room temperature. The proton NMR spectrum was recorded at 353 K.

A solution (S₄) of Bi(NO₃)₃ (36.6 μ mol, 17.8 mg, 12.5 eq) in DMSO-*d*₆ (500 μ L) was prepared. The complex **3i.BiNO₃** was formed instantaneously by transmetalation through mixing **3i.Pb_{oss}** and S₄ (120 μ L, 3 eq). The proton NMR spectrum was recorded at 298 K.

2o.Pb_{ss}: ¹H NMR (DMSO-*d*₆, 333 K, 500 MHz): δ_H , ppm 8.84 (2H, s, H₅), 8.82 (2H, s, H₆), 8.75 (2H, broad, H₇), 8.73 (2H, broad, H₈), 8.43 (2H, broad, H₁), 8.05

(2H, broad, H_k), 8.05 (2H, broad, H_i), 7.87 (2H, broad, H₄), 7.85 (2H, t, $J = 7.7$ Hz, H₂), 7.58 (2H, broad, H₃), 7.36 (2H, broad, H_d), 7.33 (2H, d, $J = 8.5$ Hz, H_j), 7.33 (2H, d, $J = 8.5$ Hz, H_i), 6.92 (2H, broad, H_c), 6.69 (2H, broad, H_b), 5.59 (2H, s, H_a), 4.04 (6H, s, O-CH₃), 1.45 (2H, broad, H_e), 1.32 (2H, broad, H_f), 0.72 (1H, s, H_α), 2H of NHCO and 1H of carboxylic acid were not observed. HSQC (DMSO-*d*₆, 333 K, 500 MHz): δ_c, ppm 135.97 (C_k), 135.97 (C_i), 134.95 (C₄), 132.67 (C₆), 132.39 (C₅), 132.52 (C_b), 132.30 (C₈), 131.82 (C₇), 129.30 (C₂), 128.04 (C_c), 126.40 (C_a), 126.19 (C_d), 124.23 (C₁), 123.67 (C₃), 112.38 (C_j), 112.38 (C_i), 56.13 (C_{OMe}), 50.87 (C_α), 36.16 (C_e), 35.97 (C_f).

2o.Pb_{os}: ¹H NMR (DMSO-*d*₆, 333 K, 500 MHz): δ_H, ppm 8.37 (2H, d, $J = 8.1$ Hz, H₁), 8.31 (2H, d, $J = 7$ Hz, H₄), 7.85 (2H, broad, H₂), 7.67 (2H, d, $J = 7.9$ Hz, H₃), 7.21 (2H, d, $J = 7.9$ Hz, H_d), 6.81 (2H, d, $J = 8.2$ Hz, H_c), 6.52 (2H, d, $J = 7.1$ Hz, H_b), 4.37 (2H, s, H_a), 4.01 (6H, s, O-CH₃), 0.92 (1H, s, H_α), 0.14 (2H, broad, H_e), -0.24 (2H, broad, H_f), 2H of H₅, 2H of H₆, 2H of H₇, 2H of H₈, 2H of H_i, 2H of H_j, 2H of H_k, 2H of H_l, 2H of NHCO and 1H of carboxylic acid were not observed. UV-vis (DMSO): λ_{max}, nm (rel. abs). 439 (0.38), 471 (1), 661 (0.02).

2i.Pb_{ss}: ¹H NMR (DMSO-*d*₆, 298 K, 500 MHz): δ_H, ppm 9.08 (2H, s, H_{5'}), 9.08 (2H, s, H_{6'}), 9.06 (2H, s, NH'CO), 8.69 (2H, d, $J = 4.3$ Hz, H_{7'}), 8.67 (2H, d, $J = 4.7$ Hz, H_{8'}), 8.51 (2H, d, $J = 7$ Hz, H_{1'}), 8.27 (2H, d, $J = 7.7$ Hz, H_{4'}), 7.93 (2H, m, H_{3'}), 7.76 (2H, m, H_{2'}), 7.28 (2H, d, $J = 7.6$ Hz, H_{d'}), 6.86 (2H, d, $J = 7.5$ Hz, H_{c'}), 6.64 (2H, d, $J = 7.1$ Hz, H_{b'}), 5.37 (2H, s, H_{a'}), 4.55 (6H, s, O-CH_{3'}), 1.7 (2H, broad, H_{e'}), 1.25 (1H, s, H_{α'}), 0.5 (2H, broad, H_{f'}), 2H of H_i, 2H of H_j, 2H of H_k, 2H of H_l, and 1H of carboxylic acid were not observed.

2i.Pb_{os}: ¹H NMR (DMSO-*d*₆, 298 K, 500 MHz): δ_H, ppm 8.87 (2H, s, H₅), 8.87 (2H, s, H₆), 8.77 (2H, d, $J = 3.2$ Hz, H₇), 8.75 (2H, d, $J = 3.8$ Hz, H₈), 8.22 (2H, d, $J = 7.7$ Hz, H₁), 8.16 (2H, d, $J = 7.7$ Hz, H₄), 8.05 (2H, broad, H_k), 8.05 (2H, broad, H_i), 7.93 (2H, broad, H₃), 7.82 (2H, s, NHCO), 7.75 (2H, m, H₂), 7.33 (2H, d, $J = 8.5$ Hz, H_j), 7.33 (2H, d, $J = 8.5$ Hz, H_i), 7.18 (2H, d, $J = 8$ Hz, H_d), 6.85 (2H, d, $J = 6.9$ Hz, H_c), 6.5 (2H, d, $J = 6.6$ Hz, H_b), 4.03 (6H, s, O-CH₃), 3.65 (2H, s, H_a), 0.85 (1H, s, H_α), -0.32 (2H, broad, H_e), -2.06 (2H, broad, H_f), 1H of carboxylic acid was not observed. UV-vis (DMSO): λ/nm: 438 (0.41), 472 (1), 664 (0.02).

3i.Pb_{os}: ¹H NMR (DMSO-*d*₆, 353 K, 500 MHz): δ_H, ppm 8.80 (2H, s, H₅), 8.75 (2H, s, H₆), 8.75 (2H, broad, H₇), 8.75 (2H, broad, H₈), 8.66 (2H, broad, H₁), 8.41 (2H, broad, H₄), 7.9 (2H, t, $J = 7.9$ Hz, H₂), 7.72 (2H, broad, H₃), 7.45 (2H, d, $J = 7.7$ Hz, H_d), 7.25 (2H, broad, H₁), 7.25 (2H, broad, H_j), 6.95 (2H, t, $J = 7.7$ Hz, H_c), 6.56 (2H, broad, H_b), 4.02 (6H, s, O-CH₃), 2.68 (2H, s, H_a), 0.88 (2H, broad, H_e), -3.31 (2H, broad, H_f), 2H of H_k, 2H of H_l, 2H of NHCO, 1H of carboxylic acid was not observed. HSQC (DMSO-*d*₆, 353 K, 500 MHz): δ_c, ppm 132.20 (C₅), 132.20 (C_b), 131.75 (C₆), 131.75 (C₇), 131.75 (C₈), 131.25 (C₁), 129.34 (C₂), 128.74 (C_c), 126.75 (C_d), 124.24 (C₃), 123.41 (C₄), 112.82 (C_j), 112.82 (C_i), 55.93 (C_{OMe}). UV-vis (DMSO): λ_{max}, nm (rel. abs). 472 (1), 615 (0.02), 666 (0.05).

3i.BiNO₃: ¹H NMR (DMSO-*d*₆, 298 K, 500 MHz): δ_H, ppm 9.16 (2H, s, H₅), 9.05 (2H, d, $J = 4.6$ Hz, H₇), 9.02 (2H, s, NHCO), 9.01 (2H, d, $J = 4.5$ Hz, H₈), 8.97 (2H, s, H₆), 8.77 (2H, d, $J = 8.4$ Hz, H₁), 8.10 (2H, d, $J = 7.6$ Hz, H_k), 8.10 (2H, d, $J = 7.6$ Hz, H_i), 7.88 (2H, t, $J = 8.2$ Hz, H₂), 7.73 (2H, $J = 7.7$ Hz, H₄), 7.53 (2H, m, H₃), 7.53 (2H, m, H_d), 7.39 (2H, d, $J = 8.6$ Hz, H₁), 7.39 (2H, d, $J = 8.6$ Hz, H_j), 7.10 (2H, broad, H_c), 6.92 (2H, d, $J = 7$ Hz, H_b), 5.93 (2H, s, H_a), 4.04 (6H, s, O-CH₃), 1.96 (2H, broad, H_e), 1.93 (2H, broad, H_f), 1H of carboxylic acid was not observed. HSQC (DMSO-*d*₆, 298 K, 500 MHz): δ_c, ppm 136.28 (C_k), 136.28 (C_i), 135.68 (C₄), 134.72 (C₇), 134.61 (C_b), 133.30 (C₆), 133.12 (C₅), 132.72 (C₈), 130.24 (C₂), 128.81 (C_c), 127.62 (C_a), 127.26 (C_d), 123.75 (C₃), 123.21 (C₁), 113 (C_j), 113 (C_i), 55.98 (C_{OMe}), 40.45 (C_e), 40.45 (C_f). UV-vis (DMSO): λ_{max}, nm (rel. abs). 354 (0.26), 476 (1), 606 (0.045), 649 (0.05).

4.3. X-ray crystallographic studies

Data were collected with a D8 VENTURE Bruker AXS diffractometer (founded by FEDER) equipped with a (CMOS) PHOTON 100 detector, Mo-K α radiation ($\lambda = 0.71073$ Å, multilayer monochromator), $T = 150$ K. The structure was resolved by dual-space algorithm using the *SHELXT* program [30], and then refined with full-matrix least-squares methods based on F^2 (*SHELXL*) [31]. The contribution of the disordered solvents to the calculated structure factors was estimated following the *BYPASS* algorithm [32] implemented as the *SQUEEZE* option in *PLATON* [33]. A new data set, free of solvent contribution, was

then used in the final refinement. All non-hydrogen atoms were refined with anisotropic atomic displacement parameters. Except nitrogen-linked hydrogen atoms that were introduced in the structural model through Fourier difference maps analysis, H atoms were finally included in their calculated positions and treated as riding on their parent atom with constrained thermal parameters. The crystals of both complexes were crystallized by the same method. Typically, the samples were dissolved in the mixture of two (chloroform, methanol) or three solvents (dimethyl sulfoxide, methanol, chloroform) in a vial fitted with a needle to allow very slow evaporation. 5–6 drops of water were gently added to the mixture before closing the vial. The vials were stored in the dark at room temperature for approximately one month, until single crystals were obtained.

3i: CCDC 1971401, crystals grown from chloroform, methanol, and water, (C₆₅H₄₇N₇O₆, CHCl₃, CH₄O); monoclinic $P 2_1/n$ (I.T.#14), $a = 14.1676(17)$, $b = 16.033(2)$, $c = 24.954(4)$ Å, $\beta = 93.491(5)^\circ$, $V = 5657.9(14)$ Å³, $Z = 4$, $d = 1.378$ g·cm⁻³, $\mu = 0.226$ mm⁻¹. Except nitrogen and oxygen linked hydrogen atoms that were introduced in the structural model through Fourier difference maps analysis, H atoms were finally included in their calculated positions and treated as riding on their parent atom with constrained thermal parameters. A final refinement on F^2 with 12658 unique intensities and 789 parameters converged at $\omega R(F^2) = 0.2357$ ($R(F) = 0.1006$) for 6618 observed reflections with $I > 2\sigma(I)$.

3i.Pb₀₈: CCDC 1971367, single crystals grown from dimethyl sulfoxide, methanol, chloroform and water (C₆₅H₄₄N₇O₆Pb); triclinic $P -1$ (I.T.#2), $a = 13.462(2)$, $b = 14.764(2)$, $c = 21.115(3)$ Å, $\alpha = 93.891(6)$, $\beta = 99.656(5)$, $\gamma = 94.702(6)^\circ$, $V = 4108.9(10)$ Å³, $Z = 2$, $d = 0.991$ g·cm⁻³, $\mu = 2.093$ mm⁻¹. The contribution of the disordered solvents to the calculated structure factors was estimated following the *BYPASS* algorithm, implemented as the *SQUEEZE* option in *PLATON*. A final refinement on F^2 with 18330 unique intensities and 516 parameters converged at $\omega R_F^2 = 0.0870$ ($R_F = 0.0383$) for 16483 observed reflections with $I > 2\sigma(I)$.

Acknowledgment

Région Bretagne is acknowledged for financial support to WB.

Supplementary data

Supporting information for this article is available on the journal's website under <https://doi.org/10.5802/crchim.94> or from the author.

References

- [1] A. Treibs, *Justus Liebigs Ann. Chem.*, 1969, **728**, 115-148.
- [2] K. M. Barkigia, J. Fajer, A. Adler, G. J. B. Williams, *Inorg. Chem.*, 1980, **19**, 2057-2061.
- [3] J. W. Buchler, K. L. Lay, *Inorg. Nucl. Chem. Lett.*, 1974, **10**, 297-300.
- [4] J. Barbour, W. J. Belcher, P. J. Brothers, C. E. F. Rickard, D. C. Ware, *Inorg. Chem.*, 1992, **31**, 746-754.
- [5] L. Michaudet, D. Fasseur, R. Guillard, Z. Ou, K. M. Kadish, S. Dahoui, C. Lecomte, *J. Porphyr. Phthalocyanines*, 2000, **4**, 261-270.
- [6] C. M. Lemon, P. J. Brothers, B. Boitrel, *Dalton Trans.*, 2011, **40**, 6591-6609.
- [7] S. Le Gac, B. Boitrel, *New J. Chem.*, 2016, **40**, 5650-5655.
- [8] Z. Halime, M. Lachkar, T. Roisnel, E. Furet, J.-F. Halet, B. Boitrel, *Angew. Chem. Int. Ed.*, 2007, **46**, 5120-5124.
- [9] S. Le Gac, B. Najjari, L. Fusaro, T. Roisnel, V. Dorcet, M. Luhmer, E. Furet, J.-F. Halet, B. Boitrel, *Chem. Commun.*, 2012, **48**, 3724-3726.
- [10] B. Najjari, S. Le Gac, T. Roisnel, V. Dorcet, B. Boitrel, *J. Am. Chem. Soc.*, 2012, **134**, 16017-16032.
- [11] S. Le Gac, E. Furet, T. Roisnel, I. Hijazi, J.-F. Halet, B. Boitrel, *Inorg. Chem.*, 2014, **53**, 10660-10666.
- [12] I. Beletskaya, V. S. Tyurin, A. Y. Tsivadze, R. Guillard, C. Stern, *Chem. Rev.*, 2009, **109**, 1659-1713.
- [13] V. Ndoiyom, L. Fusaro, V. Dorcet, B. Boitrel, S. Le Gac, *Angew. Chem. Int. Ed.*, 2015, **54**, 3806-3811.
- [14] V. Ndoiyom, L. Fusaro, T. Roisnel, S. Le Gac, B. Boitrel, *Chem. Commun.*, 2016, **52**, 517-520.
- [15] S. Le Gac, V. Ndoiyom, L. Fusaro, V. Dorcet, B. Boitrel, *Chem. Eur. J.*, 2019, **25**, 845-853.
- [16] S. Le Gac, L. Fusaro, T. Roisnel, B. Boitrel, *J. Am. Chem. Soc.*, 2014, **136**, 6698-6715.
- [17] N. Motreff, S. Le Gac, M. Luhmer, E. Furet, J.-F. Halet, T. Roisnel, B. Boitrel, *Angew. Chem. Int. Ed.*, 2011, **50**, 1560-1564.
- [18] Z. Halime, M. Lachkar, T. Roisnel, P. Richard, B. Boitrel, *Inorg. Chem.*, 2007, **46**, 6338-6346.
- [19] W. Barakat, I. Hijazi, T. Roisnel, V. Dorcet, B. Boitrel, S. Le Gac, *Eur. J. Inorg. Chem.*, 2019, 3005-3014.
- [20] R. Chakrabarty, P. S. Mukherjee, P. J. Stang, *Chem. Rev.*, 2011, **111**, 6810-6918.
- [21] T. R. Cook, Y.-R. Zheng, P. J. Stang, *Chem. Rev.*, 2013, **113**, 724-777.
- [22] Z. Halime, S. Balieu, B. Najjari, M. Lachkar, T. Roisnel, B. Boitrel, *J. Porphyr. Phthalocyanines*, 2010, **14**, 412-420.

- [23] S. Le Gac, B. Najjari, V. Dorcet, T. Roisnel, L. Fusaro, M. Lohmer, E. Furet, J.-F. Halet, B. Boitrel, *Chem. Eur. J.*, 2013, **19**, 11021-11038.
- [24] I. Hijazi, T. Roisnel, P. Even-Hernandez, E. Furet, J.-F. Halet, O. Cador, B. Boitrel, *J. Am. Chem. Soc.*, 2010, **132**, 10652-10653.
- [25] W. Jentzen, X.-Z. Song, J. A. Shelnutt, *J. Phys. Chem. B*, 1997, **101**, 1684-1699.
- [26] J. W. Buchler, "Stairic coordination chemistry of metalloporphyrins", in *Porphyrins Metalloporphyrins* (K. M. Smith, ed.), Elsevier, Amsterdam, 1975, 157-231.
- [27] S. Le Gac, B. Boitrel, "Dynamics Relying on Porphyrin Metal Exchange through Unusual Coordination Modes", in *Handbook of Porphyrin Science* (K. M. Kadish, K. M. Smith, R. Guilard, eds.), vol. 37, World Scientific, Singapore, 2016, Ch. 184, 1-73.
- [28] S. Le Gac, B. Najjari, N. Motreff, P. Remaud-Le Saec, A. Faivre-Chauvet, M.-T. Dimanche-Boitrel *et al.*, *Chem. Commun.*, 2011, **47**, 8554-8556.
- [29] P. Hambright, "Chemistry of Water Soluble Porphyrins", in *The Porphyrin Handbook. Inorganic, Organometallic and Coordination Chemistry* (K. M. Kadish, K. M. Smith, R. Guilard, eds.), vol. 3, Academic Press, Boston, 2003, 129-210.
- [30] G. M. Sheldrick, *Acta Cryst.*, 2015, **A71**, 3-8.
- [31] G. M. Sheldrick, *Acta Cryst.*, 2015, **C71**, 3-8.
- [32] P. van der Sluis, A. L. Spek, *Acta Cryst.*, 1990, **A46**, 194-201.
- [33] A. L. Spek, *J. Appl. Cryst.*, 2003, **36**, 7-13.



MAPYRO: the French Fellowship of the Pyrrolic Macrocyclic Ring / *MAPYRO: la communauté française des macrocycles pyrroliques*

Functionalized porphyrins from *meso*-poly-halogeno-alkyl-dipyrromethanes: synthesis and characterization

*Porphyrines fonctionnalisées au départ de
meso-poly-halogéno-alkyle-dipyrrométhanes. Synthèse et
caractérisation*

Paul-Gabriel Julliard^{® a}, Simon Pascal^{® a}, Olivier Siri^{® a}, Diego Cortés-Arriagada^{® b},
Luis Sanhueza^{® *, c, d} and Gabriel Canard^{® *, a}

^a Aix Marseille Univ, CNRS, CINaM, UMR 7325, Campus de Luminy, 13288 Marseille Cedex 09, France

^b Programa Institucional de Fomento a la Investigación, Desarrollo e Innovación, Universidad Tecnológica Metropolitana, Ignacio Valdivieso 2409, San Joaquín, Santiago, Chile

^c Departamento de Ciencias Biológicas y Químicas, Facultad de Recursos Naturales, Universidad Católica de Temuco, Temuco, Chile

^d Núcleo de Investigación en Bioproductos y Materiales Avanzados (BioMA), Universidad Católica de Temuco, Av. Rudecindo Ortega 02950, Temuco, Chile

E-mails: paul-gabriel.julliard@etu.univ-amu.fr (P.-G. Julliard),
pascal@cinam.univ-mrs.fr (S. Pascal), olivier.siri@univ-amu.fr (O. Siri),
dcortes@utem.cl (D. Cortés-Arriagada), luis.sanhueza@uct.cl (L. Sanhueza),
gabriel.canard@univ-amu.fr (G. Canard)

Abstract. Starting from pyrrole-carbinol derivatives, a set of three optimized experimental conditions was used to prepare six dipyrromethanes (DPM) bearing *meso*-poly-halogeno-alkyl chains. On the one hand, the condensation of *p*-anisaldehyde and the DPMs bearing a perfluoroalkyl chain (CF₃, C₃F₇ or C₇F₁₅) produced, after oxidation, the expected *trans*-A₂B₂-porphyrins in reasonable yields. On the other hand, 5,15-diformyl-10,20-diarylporphyrin was directly obtained starting from the *meso*-(dichloromethyl)dipyrromethane, while traces of an unprecedented porphyrin bearing two *meso*-acyl fluoride groups were isolated from the use of the *meso*-(chlorodifluoromethyl)dipyrromethane. The straightforward formation of *bis*-formyl porphyrins is competitive compared to previously reported methods and has been extended to other benzaldehydes. The electron-withdrawing character of the

* Corresponding authors.

different substituents appended to porphyrins is enlightened through a combination of photophysical, electrochemical, structural and theoretical studies.

Résumé. En utilisant et en optimisant trois types de conditions expérimentales, six dipyrrométhanés (DPM) substitués en *meso* par des chaînes poly-halogénoalkyles ont été préparés. La condensation du *p*-anisaldéhyde sur les DPMS comportant des chaînes perfluoroalkyles (CF₃, C₃F₇ ou C₇F₁₅) produit, après oxydation, les porphyrines trans-A₂B₂ attendues avec des rendements corrects. En revanche, cette condensation conduit directement à des 5,15-diformyl-10,20-diaryl porphyrines au départ du *meso*-(dichlorométhyl)dipyrrométhane tandis que des traces d'une porphyrine originale comportant deux groupes fluorure d'acyle ont été isolées lorsque le *meso*-(difluoro-chlorométhyl)dipyrrométhane a été utilisé. La formation directe de *bis*-formyl porphyrines est compétitive et a été étendue à d'autres benzaldéhydes. Le caractère électro-attracteur des différents substituants introduits sur les porphyrines est mis en évidence par une combinaison d'études photophysiques, électrochimiques, structurales et théoriques.

Keywords. Dipyrromethanes, Porphyrins, Formylation, Acyl fluoride, Photophysics.

Mots-clés. Dipyrrométhanés, Porphyrines, Formylation, Fluorure d'acyle, Photophysique.

Available online 30th July 2021

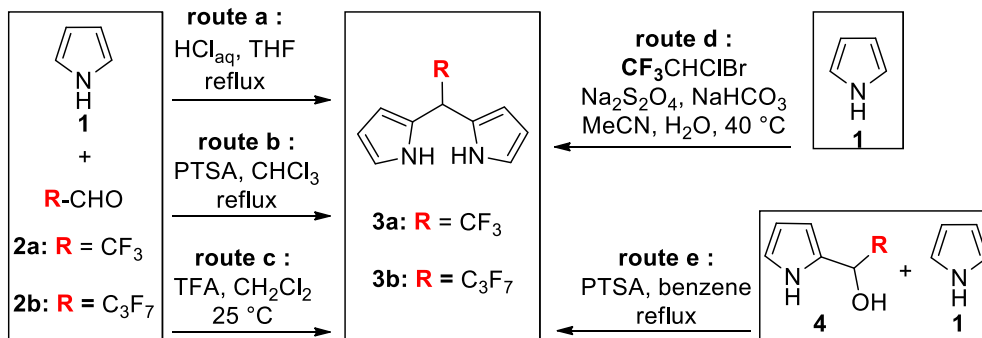
1. Introduction

The synthesis and functionalization of porphyrinoid macrocycles are still the ongoing subjects of intense research activities because these exciting compounds are applied in numerous areas such as catalysis, biology or materials science [1–5]. One of the reasons for this major interest lies in the easy preparation of *meso*-substituted derivatives from the simple condensation of pyrrole and aldehydes which can produce, after oxidation and depending on the experimental conditions, a huge number of polypyrrolic and aromatic macrocycles such as porphyrins, corroles, contracted and expanded porphyrins [1–8]. The physico-chemical properties of these macrocycles can be tuned by the introduction of different *meso*-substituents that often require the prior synthesis of oligopyrrole precursors such as the widely used *meso*-substituted dipyrromethanes (DPMs). Though various synthetic procedures of *meso*-substituted-DPMs are described [9–12], very few are devoted to or can be applied to the preparation of derivatives bearing a *meso*-poly-halogenoalkyl group or a *meso*-perfluoroalkyl chain [13–23]. These specific substituents are however of major interest because, beyond their high electron-withdrawing character, they can confer to molecules a certain lipophilicity and/or an increased metabolic stability [24,25]. Moreover *meso*-perfluoroalkyl chains were shown to induce an important non-planar distortion [26–29] and a high photo-stability [30] when they occupy the *meso*-positions of porphyrins.

To the best of our knowledge, the DPMs **3a** and **3b** bearing respectively a *meso*-CF₃ group or a *meso*-C₃F₇ group are the only DPMs substituted by a *meso*-perfluoroalkyl chain for which synthetic procedures are described (Scheme 1). The common preparation of *meso*-substituted DPMs relies on the acid-catalyzed condensation of an aldehyde and pyrrole [9–12]. In boiling tetrahydrofuran (THF) and concentrated aqueous HCl (Scheme 1, route a), the condensation of stoichiometric amounts of pyrrole **1** and aldehydes **2a** or **2b** (as hemiacetal or as hydrate) gave for the first time the *meso*-perfluoroalkyl DPMs **3a** and **3b** with high yields (50–70% for **3a** and 35–50% for **3b**) [13]. Similar yields of **3b** were obtained by repeating this procedure [14–17] or by replacing the acid and the refluxing solvent by *p*-toluene sulfonic acid (PTSA) and CHCl₃, respectively (Scheme 1, route b) [18]. It was later shown that milder experimental conditions (Scheme 1, route c) also give high yields of **3a** (20–40%) and **3b** (35%) [19,20]. An original preparation of **3a** was reported by Dmowski *et al.* who used the sodium dithionite coupling of 1-bromo-1-chloro-2,2,2-trifluoroethane with **1** (Scheme 1, route d) [21,22].

If this simple and inexpensive procedure gives high yields of **3a** (49–58%), it can only be applied to incorporate this specific *meso*-substituent.

A key intermediate during the aldehyde-pyrrole condensation is the pyrrole-carbinol derivative **4** (Scheme 1). Such an intermediate bearing a heptafluoropropyl chain was prepared and dissolved with an excess of pyrrole in refluxing benzene containing PTSA (Scheme 1, route e) [23]. This stepwise strategy



Scheme 1. Previous preparations of *meso*-perfluoroalkyl DPMs **3a** and **3b** (PTSA: *p*-toluene sulfonic acid).

produced **3b** with a high yield (77%). Having in mind that several 2-(polyhalogeno)acyl-pyrroles are easily prepared (or commercially available) and knowing that they are quantitatively reduced into the corresponding pyrrole-carbinol derivatives, we report herein how this latter strategy can be adapted, leading to a variety of *meso*-polyhalogenoalkyl DPMs. For this purpose, a set of three experimental conditions was selected and/or optimized to prepare the known **3a** and **3b** but also the unprecedented DPMs **3c–f** bearing on the *meso* position a perfluoroheptyl (**3c**), a chlorodifluoromethyl (**3d**), a dichloromethyl (**3e**) or a trichloromethyl group (**3f**).

These DPMs were involved in the synthesis of *trans*- A_2B_2 -*meso*-substituted porphyrins through their acid-catalyzed condensation with *p*-anisaldehyde. The DPMs **3a–c** gave the expected porphyrins **6a–c** whereas the condensation of DPMs **3d** and **3e** led surprisingly to porphyrins bearing two *meso*-fluoroacyl groups (**6d**) and two *meso*-formyl groups (**6e**), respectively (Table 2). Other benzaldehydes were used to illustrate the straightforward access to 5,10-*bis*-(formyl)-15,20-diarylporphyrin because it is really competitive compared to previously described ones that were based on multistep elegant strategies such as: (a) the Vilsmeier formylation of copper porphyrins and their subsequent demetallations [31]; (b) the palladium catalyzed formation of *meso-bis*-(trimethyl)silylmethylporphyrins followed by their oxidation [32]; (c) the preparations and/or derivations of protected formyl groups (dithiane or acetal moieties) before the DPM-aldehyde condensation and their deprotections after the porphyrin ring formation [33,34].

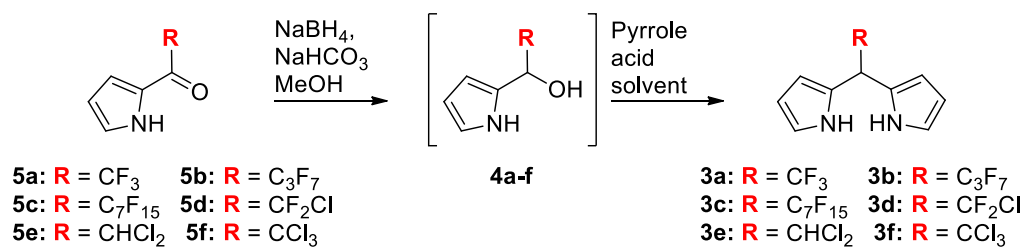
Because the physico-chemical properties of *meso*-perfluoro alkyl and *meso*-formyl porphyrins have been rarely described, those of the eight new free base porphyrins **6a–e**, **7**, **8** and **9** will be investigated in this contribution by a combination of photophysical, electrochemical and theoretical studies.

2. Results and discussion

2.1. Synthesis

The reaction of a slight excess of acyl-chloride or acid anhydride and pyrrole gave the 2-acyl pyrroles **5a–f** according to previously reported procedures (Table 1) [27,31]. These compounds were at first reduced to the corresponding carbinol derivatives **4a–f** using a slight excess of NaBH_4 (2 equiv.) in MeOH containing 2 equivalents of NaHCO_3 [35]. Because TLC analyses showed a complete conversion of the acylpyrroles **5a–f** and the formation of the alcohols **4a–f** with no observable side products, the pyrrole-carbinols **4a–f** were not isolated (nor characterized) but were always freshly prepared and used directly in the next condensation step (Table 1).

In 2011, a pyrrole-carbinol derivative analogous to **4a** but bearing an aryl group on the second α -position was condensed with pyrrole (2 equiv.) in dichloromethane (DCM) during 16 h at room temperature and using P_2O_5 (1 equiv.) as the activating agent [35]. These conditions gave very high yields of an asymmetrical *meso*- CF_3 DPM. Consequently, they were applied, in the present study, at the millimolar scale (condensation at 0.07 M in DCM) and using pyrrole **5a** to give **3a** with a yield of 60% (Table 1, entry 1).

Table 1. Optimization of the synthesis of DPMs **3a–f**

Entry	Procedure	Reactant	R	[4a–f] (M)	Solvent ^a	Acid	Pyrrole/ 4a–f /acid	<i>t</i> (h)	Product	Yield (%)
1	A	4a	CF₃	0.07	DCM	P₂O₅	2:1:2	16	3a	60
2		4a	CF ₃	0.23	DCM	P ₂ O ₅	2:1:2	16	3a	39
3		4a	CF ₃	7.28	—	P ₂ O ₅	2:1:2	16	3a	44
4		4a	CF ₃	0.58	Pyrrole	P ₂ O ₅	25:1:2	16	3a	0
5		4a	CF ₃	3.64	Pyrrole	Eaton's reagent ^f	4:1:1	1	3a	0 ^b
6		4a	CF ₃	0.2	THF ^c	HCl _{aq}	2:1:1.5	2	3a	26
7		4a	CF ₃	0.15 ^d	H ₂ O	HCl _{aq}	2:1:1.2	4	3a	22
8	B	4a	CF₃	0.15^d	H₂O	HCl_{aq}	2:1:1.2	16	3a	24 (28)^e
9		4a	CF ₃	0.15 ^d	H ₂ O	HCl _{aq}	2:1:1.2	40	3a	35
10		4a	CF ₃	0.15 ^d	H ₂ O	HCl _{aq}	4:1:1.2	16	3a	20
11	A	4b	C₃F₇	0.07	DCM	P₂O₅	2:1:2	16	3b	52 (41)^e
12	B	4b	C ₃ F ₇	0.15 ^d	H ₂ O	HCl _{aq}	2:1:1.2	16	3b	0
13	A	4c	C₇F₁₅	0.07	DCM	P₂O₅	2:1:2	16	3c	65 (87)^e
14	B	4c	C ₇ F ₁₅	0.15 ^d	H ₂ O	HCl _{aq}	2:1:1.2	16	3c	0
15	A	4d	CF ₂ Cl	0.07	DCM	P ₂ O ₅	2:1:2	16	3d	0–2
16	B	4d	CF₂Cl	0.15^d	H₂O	HCl_{aq}	2:1:1.2	16	3d	18 (18)^e
17	B	4e	CHCl₂	0.15^d	H₂O	HCl_{aq}	2:1:1.2	16	3e	60 (67)^e
18	A	4f	CCl ₃	0.07	DCM	P ₂ O ₅	2:1:2	16	3f	0
19	B	4f	CCl ₃	0.15 ^d	H ₂ O	HCl _{aq}	2:1:1.2	16	3f	0
20		4f	CCl ₃	0.2	DCM	TFA	1:1:1.2	16	3f	0
21		4f	CCl ₃	0.2	THF ^c	HCl _{aq}	1:1:1.2	2	3f	3
22	C	4f	CCl₃	0.2	THF^c	HCl^g	11:1:0.9	2	3f	9

^aAll reactions were performed at room temperature unless otherwise noted. ^bPyrrole polymerization occurs.

^cReactions at reflux. ^dResulting concentrations if pyrrole carbinol **4** was soluble in water. ^eGram-scale yields are noted in brackets. ^fEaton's reagent: P₂O₅ (7.7 wt%) in CF₃SO₃H. ^gHCl in Et₂O (1 M).

Higher concentrations or using pyrrole as the solvent did not improve the reaction yield (Table 1, entries 2–5). This procedure (Table 1, procedure A) was extended to pyrroles **5b,c** and afforded high amounts of **3b** (52%) and **3c** (65%) but only traces of **3d** (0–2%) and no **3f** (Table 1, entries 11, 13, 15 and 18). The preparation of **3b** and **3c** were repeated on a gram scale and gave DPMs with high yields.

To ensure better yields of **3d**, new experimental conditions were applied in the preparation of **3a**

from **4a** (used as a model compound). The utilization of refluxing THF and concentrated aqueous HCl was moderately efficient (Table 1, entry 6) but proved that the presence of water in the solvent was not detrimental to get *meso*-polyhalogeno alkyl DPMs. Several works have shown that *meso*-aryl-oligopyrrole syntheses can be performed in water and using concentrated aqueous HCl as catalyst [36–38]. The application of the conditions of Dehaen *et al.* [39] ([HCl] = 0.18 M, [**4a**] = 0.15 M, 2

equiv. of pyrrole, room temperature, 4 h) afforded **3a** with a yield of 22% that increases with the reaction time whereas higher amounts of pyrrole do not have any beneficial effect (Table 1, entries 7–10). We selected a reaction time of around one night (16 h) and applied these conditions (procedure B) to get DPMs **3b–f** (Table 1, entries 12, 14, 16 and 19). This procedure failed to give DPMs **3b,c** and **3f**, but produced **3d** and **3e** with up-scalable yields of 18% and 66% respectively.

Since mild conditions did not afford the DPM **3f**, and because the only example of a β -substituted DPM bearing a *meso*-CCl₃ group was obtained through harsh conditions (TFA as solvent, 40 °C) [40], we used again refluxing THF and HCl_(aq) during the condensation step (Table 1, entry 21). A low yield of **3f** was obtained (3%) but reached 9% when using the experimental conditions described to synthesize a *meso*-CF₃ tripyrromethane from a DPM-mono-carbinol (Table 1, entry 22) [41]. Because no porphyrin could be, up to now, obtained from this particular DPM (*vide infra*), we have not pursued this optimization.

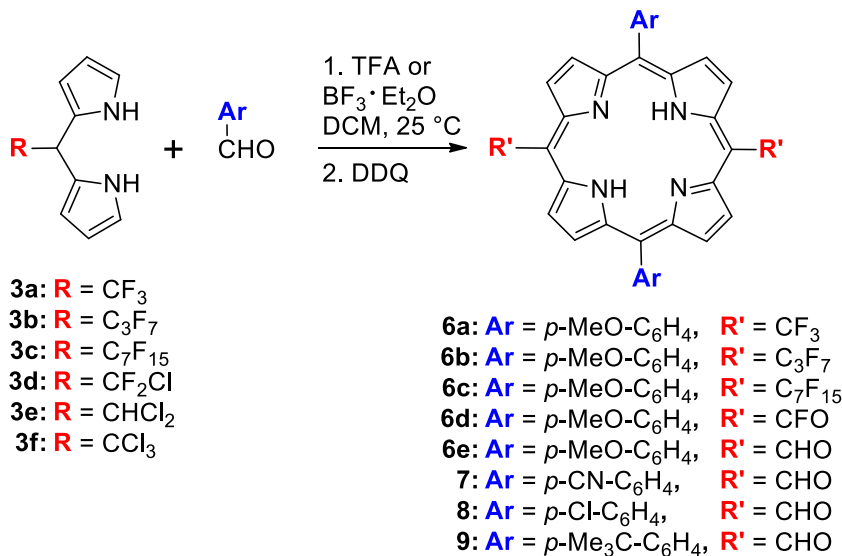
The DPMs **3a–f** were used as building blocks in the synthesis of porphyrins (Table 2). For this purpose, we chose to apply the conditions of the acid-catalyzed condensation of the DPMs **3a,b** with various aromatic aldehydes that were shown to be effective in the preparation of *trans*-A₂B₂ porphyrins bearing two *meso*-perfluoroalkyl groups (Table 2) [19]. The reaction of *p*-anisaldehyde (0.01 M) with DPMs **3a–f** catalyzed by TFA (10 equiv.) or by BF₃·OEt₂ (0.33 equiv.) in DCM was stopped after the complete disappearance of the DPMs (TLC analysis). The two catalysts have been tested and this contribution reports only the conditions giving the highest yields.

After oxidation by DDQ (1.5 equiv.) and purification by chromatography, modest yields (4–9%) of the *trans*-A₂B₂ porphyrins **6a–c** were obtained from the DPMs **3a–c** although, as previously described, no scrambling occurred during the condensation step [19].¹ It has to be noted that, in addition to the expected porphyrin, each experiment led to the formation of several other colored chromophores but

in too low yields to ensure their characterization. On the one hand, no porphyrin was detected from the reactions involving the DPM **3f** bearing a sterically hindered trichloromethyl group, while on the other hand, the less chlorinated DPMs **3d** and **3e** gave quite unexpected results (Table 2).

Unlike the common purple spots on TLC and purple solutions observed during the purification of porphyrin **3a–c**, green colored TLC spots and solutions were obtained while running the chromatography on the crude mixture from **3e**. The red-shifted UV–visible absorption of the isolated compound combined with its ¹H NMR spectrum featuring a downfield singlet located at 12.54 ppm were the first evidence of the exclusive formation of the *bis*-formyl porphyrin **6e** which was further confirmed by its HRMS analysis and its IR spectrum displaying an intense carbonyl stretching band at 1672 cm⁻¹ (see the Supporting Information). The hydrolysis of the two CHCl₂ groups remains unexplained because it was neither observed during the preparation of DPM **3e** though being performed in acidic water, nor during its purification, which was also performed on silica gel. Suspecting that this hydrolysis would not have been quantitative, we performed another synthesis of **6e** and washed the reaction mixture with water after the oxidation step. This supplementary treatment led to an identical yield of **6e**. The CHCl₂ groups of the intermediate porphyrinogen have probably stability close to the CHCl₂ group of DPM **3e**. Their hydrolysis could occur during the oxidation step as it was previously observed after the condensation of a *meso*-nitromethyl DPM with an aromatic aldehyde leading to *meso*-formyl porphyrins [42]. Such hydrolysis was also observed during the metal-assisted cyclization of a *meso*-CHCl₂- β -substituted-*a,c*-biladiene into *meso*-formyl metalloporphyrins [43]. Because the simple use of DPM **3e** gives straightforward access to *trans-meso*-bis(formyl) porphyrin, it was extended to *p*-cyano-, *p*-chloro and *p*-*tert*-butyl-benzaldehydes and led in the same way to porphyrins **7**, **8** and **9** with respective yields of 9%, 2% and 12% (Table 2). The low isolated yield of **8** comes partly from its delicate purification due to its very low solubility in common organic solvents. In the same way, pure and solid **7** has only a slightly higher solubility. Consequently, a protonation–deprotonation sequence was used to ensure the complete dissolution of **7**, **8** and **9** when

¹No other porphyrin was detected by TLC or during the chromatographic purification.

Table 2. Syntheses of porphyrins **6a–e**, **7**, **8** and **9**

DPM	R	Acid	Porphyrin	Ar	R'	Yield (%)
3a	CF ₃	BF ₃	6a	<i>p</i> -MeO-C ₆ H ₄ -	CF ₃	9
3b	C ₃ F ₇	TFA	6b	<i>p</i> -MeO-C ₆ H ₄ -	C ₃ F ₇	4
3c	C ₇ F ₁₅	TFA	6c	<i>p</i> -MeO-C ₆ H ₄ -	C ₇ F ₁₅	4
3d	CFCl ₂	BF ₃	6d	<i>p</i> -MeO-C ₆ H ₄ -	CFO	2
3e	CHCl ₂	TFA	6e	<i>p</i> -MeO-C ₆ H ₄ -	CHO	11
3e	CHCl ₂	TFA	7	<i>p</i> -CN-C ₆ H ₄ -	CHO	9
3e	CHCl ₂	TFA	8	<i>p</i> -Cl-C ₆ H ₄ -	CHO	2
3e	CHCl ₂	TFA	9	<i>p</i> -Me ₃ C-C ₆ H ₄ -	CHO	12

R' groups are at the 5,15 positions, **Ar** are at the 10,20 positions.

recording their physico-chemical properties (see the experimental part).

As observed during the porphyrin synthesis starting from DPM **3e**, the acid-catalyzed condensation of DPM **3d** with *p*-anisaldehyde gave, after oxidation, a green spot on TLC and a green solution during the purification on silica. After purification, the red-shifted UV-visible spectrum of the isolated porphyrin **6d** together with the presence of a single signal at -62.63 ppm in its ¹⁹F NMR spectrum indicated that the former CF₂Cl group borne by DPM **3d** had probably disappeared in **6d**. The unexpected structure of the *bis*-fluoro-acyl derivative **6d** was elucidated thanks to its HRMS analysis and its IR spectrum featuring a carbonyl stretching band at 1796 cm⁻¹ (see the Supporting Information). Although the yield of this transformation is low (≤2%), it gave repeatedly

the first example of a porphyrin-bearing *meso*-fluoro acyl groups. As for **6e**, we are not able yet to give the causes and/or the mechanism of the peculiar hydrolysis that has been rarely observed [44] although it has been reported that C-X bonds of *meso*-perfluoroalkyl groups borne by DPMs or porphyrins are prone to be involved in eliminations, intramolecular cyclization or solvolysis processes [45–50].

2.2. Electrochemical analysis of porphyrins **6a–e** and **9**

The cyclic voltammograms (CVs) of **6a–e** and **9** were recorded in DCM containing 0.1 M of [(*n*Bu₄N)PF₆] (Figure 1 and Figure S1 in the Supporting Information). The corresponding oxidation and reduction half-wave and peak potential values are listed

Table 3. Half-wave and peak potentials (V versus SCE) of porphyrins **6a–e**, **9**, $(\text{CF}_3)_4\text{PH}_2$ and $(\text{C}_3\text{F}_7)_4\text{PH}_2$ measured in CH_2Cl_2 containing 0.1 M of $[(n\text{Bu}_4\text{N})\text{PF}_6]$ (scan rate of 100 mV/s)

	R10,20	R5,R15	Reduction		Oxidation		ΔE (V) ^a
			Second	First	First	Second	
6a	4-OCH ₃ -C ₆ H ₄	CF ₃	-1.33 ^b	-0.81 (100) ^c	1.32 ^b	1.79 ^b	2.11
6b	4-OCH ₃ -C ₆ H ₄	C ₃ F ₇	-1.34 ^{b,d}	-0.80 (80) ^c	1.31 ^b	1.75 ^b	2.09
6c	4-OCH ₃ -C ₆ H ₄	C ₇ F ₁₅		-0.81 (100) ^c	1.29 ^b	1.78 ^b	2.08
6d	4-OCH ₃ -C ₆ H ₄	CFO	-0.79 (107) ^c	-0.54 (72) ^c	1.39 ^b		1.93
6e	4-OCH ₃ -C ₆ H ₄	CHO	-0.89 (74) ^c	-0.57 (64) ^c	1.33 ^b	1.81 ^b	1.90
9	4-Me ₃ C-C ₆ H ₄	CHO	-0.90 (73) ^c	-0.58 (69) ^c	1.40 ^b	—	1.98
10 ^d	4-PO ₃ Et ₂ -C ₆ H ₄ ^d	C ₃ F ₇		-0.81	1.43		2.24
$(\text{CF}_3)_4\text{PH}_2$ ^e	CF ₃	CF ₃		-0.48 ^f (160) ^c			
$(\text{C}_3\text{F}_7)_4\text{PH}_2$ ^e	C ₃ F ₇	C ₃ F ₇		-0.44 ^f (158) ^c			

^aHOMO–LUMO electrochemical gap calculated by $\Delta E = E_{1/2}(\text{ox}_1) - E_{1/2}(\text{red}_1)$ or by $\Delta E = E_{\text{pa}}(\text{ox}_1) - E_{1/2}(\text{red}_1)$. ^bIrreversible peak potential at a scan rate of 100 mV/s. ^c $\Delta E_{\text{p}} = E_{\text{pa}} - E_{\text{pc}}$ in mV. ^dA third irreversible reduction peak is placed at $E_{\text{pc}} = -1.56$ V versus SCE. ^eFrom Ref. [17]. ^fFrom Ref. [51]. ^fMeasured in benzonitrile.

in Table 3 together with those of the *tetra-meso*-CF₃ porphyrin $(\text{CF}_3)_4\text{PH}_2$ [51], the *tetra-meso*-C₃F₇ porphyrin $(\text{C}_3\text{F}_7)_4\text{PH}_2$ [51], and of the porphyrin **10** analogous to **6b** but where the *p*-anisyl groups are replaced by *p*-diethylphosphonate-phenyl substituents [17]. Each CV features a first reversible reduction and a first irreversible oxidation centered on the porphyrin ring. For the perfluoro derivatives **6a–c**, this oxidation seemed to be reversible at a scan rate of 100 mV/s but proved to be irreversible when increasing the scan rate up to 800 mV/s. Depending on the substituents, a second oxidation and/or a second reduction were also enlightened by the CVs of **6a–e**.

No oxidation could be observed previously when recording the CVs of $(\text{CF}_3)_4\text{PH}_2$ and $(\text{C}_3\text{F}_7)_4\text{PH}_2$ (Table 3) [51]. The replacement of two of these chains by *p*-anisyl groups in **6a** and **6b** leads to a significant negative shift of the first reduction potential (~300 mV) and allows access to the data corresponding to the macrocycle oxidation ($E_{1/2} \sim 1.3$ V versus SCE).

Whereas the electrochemical properties of porphyrins are substantially varying with the number of *meso*-perfluoroalkyl chain, they are not notably tuned by the length of these lipophilic chains because the first oxidation/reduction potential values of **6a**, **6b** and **6c** are nearly the same (Table 3). Interestingly, the comparison between **6b** and **10**

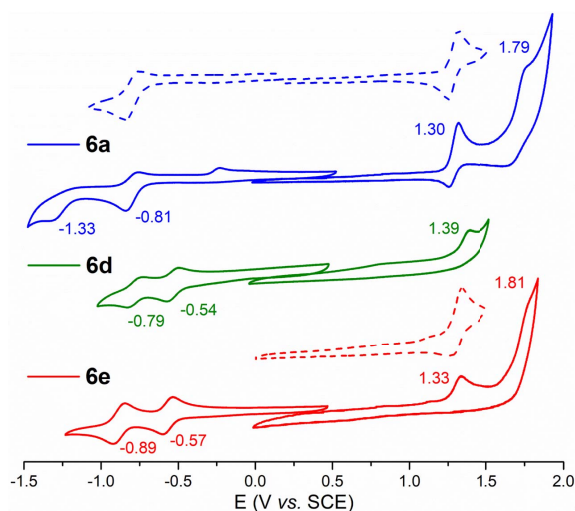


Figure 1. CVs of porphyrins **6a** (—), **6d** (—) and **6e** (—) in DCM containing 0.1 M of $[(n\text{Bu}_4\text{N})\text{PF}_6]$ (scan rate of 100 mV·s⁻¹). The dotted traces emphasize the reversibility of selected redox processes.

shows that decreasing the electron richness of the 10,20-aryl groups shifts, as expected, the first oxidation process to higher potential values but leaves unchanged the energy of the first reduction. Therefore, varying the nature of 10,20-aryl groups has probably little influence on the energy of the LUMO of such

trans-A₂B₂ porphyrins which is controlled by the *meso*-perfluoroalkyl chains.

The important anodic shift (+240 mV) affecting the first reduction process when replacing CF₃ moieties in **6a** by formyl groups in **6e** cannot be explained by a field/inductive effect because the latter is stronger for CF₃ than for CHO (Hammett parameters: σ_p (CF₃) = +0.54, σ_p (CHO) = +0.42) [52]. A positive shift is also observed between the two corresponding macrocycle-centered oxidations but has a little amplitude (~30 mV) (Table 3). As for the CF₃ porphyrins **6b** and **10**, modifying the aryl groups in the formyl-substituted macrocycles **6e** and **9** produces only a slight modification of the first oxidation potential whereas the reduction potentials remain unchanged. It has to be noted that the solubility of **7** and **8** was too low in DCM to record accurate electrochemical data.

Supplementary anodic shifts are affecting the first reduction and potential processes when two CFO groups are appended by the porphyrin ring in **6d**. Therefore, the remarkable reduced HOMO–LUMO electrochemical gaps of **6d** and **6e** compared to those of derivatives **6a–c** result from a π -conjugation between the carbonyl groups and the aromatic porphyrin ring that are put into evidence by theoretical calculations.

2.3. Spectral properties of the porphyrins

The absorption and corrected emission spectra of porphyrins **6a–e**, **7**, **8** and **9** were recorded in DCM at room temperature and are shown in Figure 2 and Figure S2 in the Supporting Information. The molar absorption coefficients and absorption maxima of these seven novel compounds are gathered in Table 4 with their emission maxima (excitation at λ = 590 nm) and fluorescence quantum yields. In order to give structure–properties relationships, selected photophysical data of **10** [17], (CF₃)₄PH₂ [53] and of (C₃F₇)₄PH₂ [53] are also given in Table 4 together with those of the porphyrins **11** [19] and **12** [32] analogous to **6a** and **6e** but where the *p*-anisyl groups are replaced by simple phenyl substituents.

As reported for the *meso*-bis-CF₃ porphyrin **11** [19], porphyrins **6a–c** exhibit absorption spectra that are distinct from that of the well known *tetra*-phenylporphyrin (TPP). Compared to TPP, their Soret bands are blue-shifted and broadened

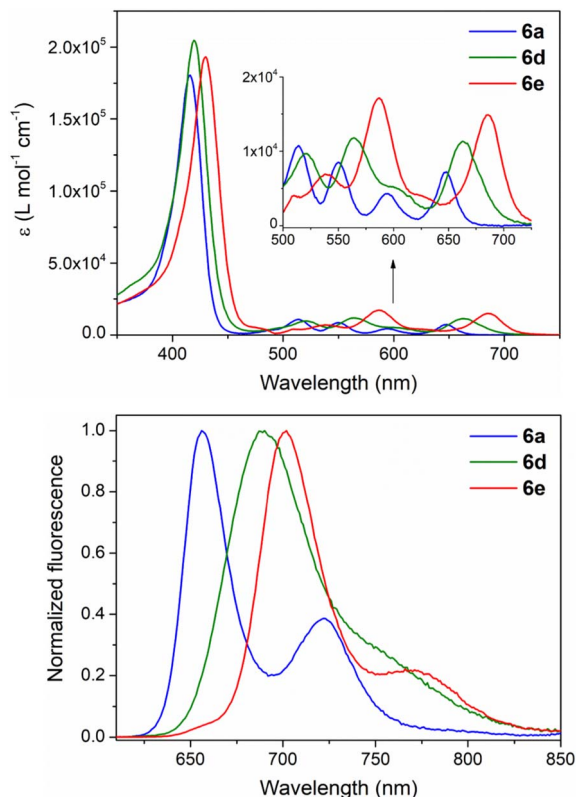


Figure 2. Electronic absorption spectra and normalized corrected emission spectra of porphyrins **6a** (—), **6d** (—) and **6e** (—) in aerated dichloromethane at room temperature.

(fwhm 27–28 nm) but significantly red-shifted compared to those of the *tetra*-perfluoroalkyl derivatives (CF₃)₄PH₂ and (C₃F₇)₄PH₂.

In the same way, as shown for **11**, the Q bands of **6a–c** have absorption maxima close to those of TPP but with a different pattern. For example, the UV–visible spectra of the *trans*-A₂B₂ **6a–c** feature, as **10** and **11**, a noticeable increased intensity for the 0–0 component corresponding to a band at ca. 646 nm (Table 4). The length of the perfluoroalkyl chain has only a minor impact on the light-absorption and light-emission properties of **6a–c** that give similar fluorescence spectra and fluorescence quantum yields of ca. 7–9%. When comparing on the one hand the analogous **6a** and **11**, and on the other hand the analogous dyes **6b** and **10**, it can be noted that enhancing the electron richness of the aromatic

Table 4. UV-Vis and fluorescence data of porphyrins **6a–e**, **7**, **8**, **9–12**, $(\text{CF}_3)_4\text{PH}_2$ and $(\text{C}_3\text{F}_7)_4\text{PH}_2$ recorded in aerated dichloromethane at 298 K

	Absorption				Fluorescence	
	R10,20	R5,15	Soret band	Q bands	$\lambda_{\text{max}}^{\text{a}}$ (nm)	$\Phi_{\text{fl}}^{\text{b}}$
			λ_{max} (nm) (ϵ ($10^4 \text{ M}^{-1} \cdot \text{cm}^{-1}$))	λ_{max} (nm) (ϵ ($10^4 \text{ M}^{-1} \cdot \text{cm}^{-1}$))		
6a	4-OCH ₃ -C ₆ H ₄	CF ₃	416 (18.05) fwhm (28) ^c	514 (1.07), 550 (0.85), 595 (0.43), 648 (0.72)	658, 722	0.063
6b	4-OCH ₃ -C ₆ H ₄	C ₃ F ₇	414 (18.90) fwhm (28) ^c	514 (0.99), 551 (1.14), 595 (0.46), 646 (1.07)	656, 719	0.086
6c	4-OCH ₃ -C ₆ H ₄	C ₇ F ₁₅	415 (19.81) fwhm (27) ^c	514 (1.04), 552 (1.27), 596 (0.51), 647 (1.06)	655, 720	0.089
6d	4-OCH ₃ -C ₆ H ₄	CFO	419 (20.46) fwhm (31) ^c	521 (0.97), 564 (1.18), 663 (1.13)	690	0.100
6e	4-OCH ₃ -C ₆ H ₄	CHO	430 (19.32) fwhm (31) ^c	510 (0.40), 538 (0.69), 587 (1.71), 686 (1.49)	707, 771	0.079
7^d	4-CN-C ₆ H ₄	CHO	427 (10.30) fwhm (28) ^c	508 (0.23), 535 (0.38), 579 (0.85), 680 (0.75)	688, 757	0.057
8^d	4-Cl-C ₆ H ₄	CHO	427 (11.69) fwhm (30) ^c	535 (0.36), 583 (1.03), 682 (0.91)	692, 763	0.077
9^d	4-Me ₃ C-C ₆ H ₄	CHO	427 (20.64) fwhm (30) ^c	539 (0.62), 585 (1.75), 684 (1.54)	696, 767	0.081
10^e	4-PO ₃ Et ₂ -C ₆ H ₄	C ₃ F ₇	410 (19.1)	510 (1.1), 546 (1.2), 590 (0.5), 643 (1.1)	647, 715	
11^f	C ₆ H ₅	CF ₃	414 (16.50) fwhm (27) ^c	511 (1.01), 546 (1.01), 592 (0.53), 647 (0.77)	650, 720 ^f	0.044
12^g	C ₆ H ₅	CHO	426 (15.85)	535 (0.50), 586 (1.26), 685 (1.00)		
$(\text{CF}_3)_4\text{PH}_2^{\text{h}}$	CF ₃	CF ₃	408 (9.55)	512 (0.87), 546 (0.88), 596 (0.43), 651 (0.96)	654, 721	0.016
$(\text{C}_3\text{F}_7)_4\text{PH}_2^{\text{h}}$	C ₃ F ₇	C ₃ F ₇	409 (9.23)	513 (0.92), 547 (0.75), 596 (0.43), 649 (0.97)	651, 718	0.021
TPPⁱ	C ₆ H ₅	C ₆ H ₅	419 (47.00)	514 (1.87), 549 (0.77), 591 (0.54), 647 (0.34)	650, 715 ^j	0.15 ^j

^a λ_{max} for the bands derived from corrected emission spectra. ^bLuminescence quantum yields in air-equilibrated dichloromethane by comparing corrected emission spectra and using tetraphenylporphyrin (TPP) in aerated acetonitrile as a standard ($\Phi_{\text{fl}} = 0.15$ [54]). Excitation at $\lambda = 590$ nm. ^cFull width of half maximum in nm. ^dA protonation-deprotonation sequence was used to ensure a complete dissolution. ^eFrom Ref. [17], measured in $\text{CHCl}_3/\text{MeOH}$. ^fFrom Ref. [19], λ_{abs} and Φ_{fl} measured in toluene, λ_{em} measured in $\text{CH}_2\text{Cl}_2/\text{EtOH}$ (3:1). ^gFrom Ref. [32], measured in CHCl_3 . ^hFrom Ref. [53], measured in benzene. ⁱFrom Ref. [19], measured in benzene. ^jRecorded in acetonitrile.

substituents induces a little red shift of the absorption and fluorescence maxima.

As observed when recording the electrochemical data, introducing *meso*-formyl groups produces a noticeable lower HOMO–LUMO optical gap. The UV-visible absorption and fluorescence bands of **6e** are importantly red-shifted. For example, the Soret band maximum of **6e** is at 430 nm and the 0–0 component of its Q bands can be found at 686 nm. Its quantum yield is as for **6a–c** of ca. 8%. Replacing electron-withdrawing aryl groups in **7** and **8** by electron-donating ones in **9** and **6e** produces a supplementary red shift of the absorption and emission bands.

For the unique **6d**-bearing *meso*-fluoro acyl moieties, it can be noted that its light-absorption and

emission bands are also red-shifted compared to those of **6a–c** and of TPP but with a lower amplitude. Its fluorescence spectrum has also a unique pattern with a single and broadened band at 690 nm corresponding to a quantum yield of 10%.

2.4. Theoretical and structural studies of selected porphyrins

DFT and Time-dependent DFT (TD-DFT) calculations were performed to analyze the effects of the *meso*-substituents CF₃, C₃F₇, C₇F₁₅, CFO and CHO on the structural, electronic and optical properties of porphyrins **6a–e**. The structures of **6a–e** were fully optimized and gave values of geometrical parameters

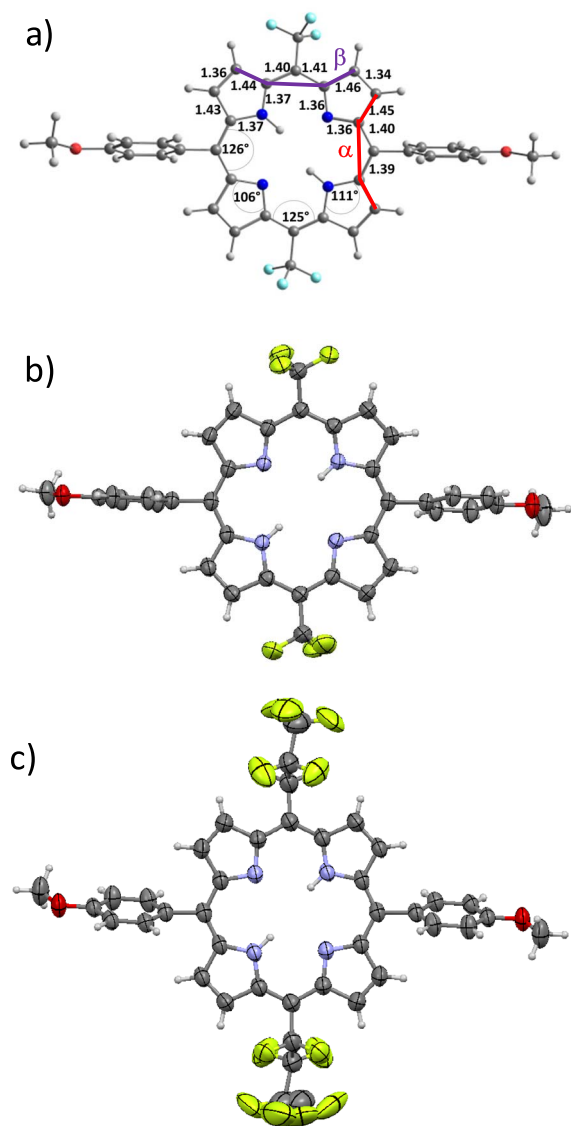


Figure 3. (a) Bond distances (Å), angle values (°) and external dihedral angles α and β of the optimized structure of **6a**; views of the single X-ray structures of (b) **6a** and (c) **6b** (solvent molecules are omitted for the sake of clarity).

such as bond distances, angles and dihedral angles that are illustrative of the effect of the *meso* substitutions on their core structures (Figure 3 and Figure S3 in the Supporting Information). Although there were no symmetry constraints in the calculation procedures, results did provide symmetric structures. Therefore, only parameters corresponding to

one-half of the porphyrin macrocycles are detailed in Figures 3 and S3. Very slight differences are observed between the bond distances and angle values of **6a–e** despite the variation of the nature of 5,15 *meso*-substituents (Figures 3 and S3). In fact, most relevant differences in the geometrical parameters are related to the values of the calculated external dihedral angles α and β which are listed in Table 5 and represented in Figure 3. These dihedral angles stand for the plane torsion regarding two adjacent pyrrole units of the porphyrin core center. As observed in Table 5, the α values are about 5.0° for **6a**-bearing CF₃ moieties and increase up to 10.6° for **6b** and **6c** substituted respectively by the more bulky C₃F₇ and C₇F₁₅ substituents. The β values are quite low with values in the range of ~0.7°. On the other hand, the presence of CFO and CHO as highly acceptor moieties in **6d** and **6e** induces decreased α values of 7.8° and 7.2°, respectively, while significantly increased β values of 12.4° (**6d**) and 8.5° (**6e**) are observed for these systems. These results indicate that the introduction of CHO or CFO groups on the *meso*-positions produce a noticeable supplementary out-of-plane distortion of the macrocycles in **6d** and **6e** compared to those of the alkyl appended porphyrins **6a–c**.

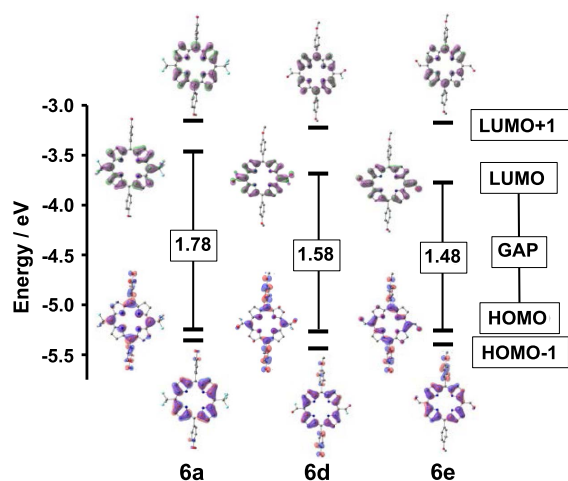
During the final editing stages of this contribution, we were glad to get diffracting single crystals of porphyrins **6a** and **6b** (Figures 3(b) and (c)). As for the calculated geometries, the corresponding experimental structures feature a small out-of-plane distortion of the porphyrin **6a** and **6b** which is higher for **6b** and correspond to a slight ruffling of the macrocycles.

The frontier molecular orbitals (FMOs) of **6a–e** were also studied by DFT calculations. The energies of the two HOMOs and of the two LUMOs are listed in Table 5 and their plots are displayed in Figure 4 and Figure S4 in the Supporting Information. The calculated HOMO–LUMO gaps are in accordance with the experimental data and decrease in importance when fluoro acyl or formyl groups are borne by the 5 and 15 *meso*-positions. As observed during the UV–Vis absorption and electrochemical experiments, the lowest HOMO–LUMO gap is obtained for the bis-formyl derivative **6e**. For **6a–e**, the HOMO appears mainly to be located at the *p*-anisyl substituents, the core-*N* atoms and the *meso*-bridging carbon atoms at the 5,15 positions. Therefore, the lack of any apparent

Table 5. Calculated dihedral angles ($^{\circ}$), experimental dihedral angles ($^{\circ}$) and orbital energies (eV) of porphyrins **6a–e**

	R5,15	α ($^{\circ}$)	β ($^{\circ}$)	HOMO–1 (eV)	HOMO (eV)	LUMO (eV)	LUMO+1 (eV)
6a	CF ₃	4.3 3.3 ^a	0.7 6.4 ^a	–5.36	–5.25	–3.47	–3.16
6b	C ₃ F ₇	10.6 13.4 ^a	0.7 6.5 ^a	–5.37	–5.23	–3.49	–3.16
6c	C ₇ F ₁₅	10.6	0.6	–5.38	–5.24	–3.50	–3.16
6d	CFO	7.8	12.4	–5.44	–5.27	–3.69	–3.23
6e	CHO	7.2	8.5	–5.40	–5.26	–3.78	–3.18

^aExperimental dihedral angle values from the single crystal X-ray diffraction structures of **6a** and **6b**.

**Figure 4.** Plots of the calculated frontier orbitals and values of the HOMO–LUMO gaps (in eV) of **6a**, **6d** and **6e**.

contribution from the 5,15 substituents results in similar HOMO energy values differing by less than 1% for the **6a–e** series. Similarly, the five HOMO–1 and the five LUMO+1 of **6a–e** have energy values and electron density distributions that are only slightly varying with the nature of the 5,15 *meso*-substituents.

On the contrary, substantial differences appear when comparing the energies of the LUMOs. Those of **6a–c** have electron density distributions barely affected by the length of their perfluoroalkyl chains. Consequently, **6a**, **6b** and **6c** have quite identical FMOs energies and HOMO–LUMO gap values in accordance with the corresponding photophysical and electrochemical data. The LUMO iso-surfaces of **6d** and **6e** feature a remarkable participation of the π -conjugated *meso*-electron-withdrawing groups CFO

and CHO that are responsible for the concomitant lower LUMO energies and lower HOMO–LUMO gaps. The simulation of the UV–visible spectra of **6a–e** was obtained from further TD-DFT calculations and is detailed in the Supporting Information together with the corresponding compositions, vertical excitation energies, oscillator strengths and hole–electron excited states' surface distributions. For **6a–e**, theory gives Soret bands between 380 and 450 nm and these are red-shifted for **6d** and **6e** as observed experimentally. On the contrary, few differences are obtained when comparing the locations and intensities of the calculated Q bands of **6a–e**, because the different 5,15 *meso* substituents have only a slight impact on the corresponding electronic transitions.

3. Conclusions

Meso-polyhalogeno alkyl dipyrromethanes were prepared by the reduction of 2-acyl pyrroles and their subsequent acid-catalyzed reaction with pyrrole. Three sets of experimental conditions were optimized depending on the starting compound. This procedure lead firstly to the known DPMs **3a** and **3b** substituted by a trifluoromethyl group and a heptafluoropropyl chain, respectively. New derivatives were also obtained, bearing on the *meso*-position a perfluoroheptyl (**3c**), a chlorodifluoromethyl (**3d**), a dichloromethyl (**3e**) or a trichloromethyl group (**3f**). Dipyrromethanes are useful compounds in the synthesis of various chromophores including BODIPYs, corroles or expanded porphyrins. Herein, they were used to build trans-A₂B₂ *meso*-substituted porphyrins through their condensation with aromatic aldehydes. The perfluoro DPMs produce the expected bis-alkylporphyrins while exciting *meso*-functionalized analogs were obtained from DPMs

3d and **3e**-bearing chlorine atoms. Indeed, several bis-formyl porphyrins were prepared directly from **3e** and illustrate an original and straightforward strategy to get such derivatives. Similarly, the use of **3d** leads to **6d** as a unique example of a porphyrin-bearing *meso*-fluoro acyl moieties. The electron-withdrawing character of the perfluoroalkyl chains and of the π -conjugated formyl and fluoro acyl groups were investigated and enlightened thanks to photophysical and electrochemical analyses supported by theoretical calculations. These studies revealed, for example, that when appended by porphyrins, formyl and fluoro acyl functional groups give to the macrocycles reduced HOMO–LUMO electrochemical gaps and red-shifted absorption and emission properties.

4. Experimental section

4.1. Materials

All reagents were used as received. Pyrrole was distilled before use. The distillation of THF was performed on sodium/benzophenone. Flash column chromatography was performed on silica gel 60 (230–400 mesh). Visualization of DPM **3a–f** TLC spots was achieved by staining the TLC plates with a solution of phosphomolybdic acid (2.5 g) in ethanol and by subsequent heating.

4.2. Physical measurements

^1H , ^{13}C and ^{19}F nuclear magnetic resonance (NMR) spectra were recorded on a JEOL ECS400 NMR spectrometer at room temperature. NMR chemical shifts are given in ppm (δ) relative to Me_4Si using solvent residual peaks as internal standards (CDCl_3 : $\delta = 7.26$ ppm for ^1H and 77.2 for ^{13}C ; Acetone- d_6 : $\delta = 2.05$ ppm for ^1H and 29.8 for ^{13}C ; DMSO- d_6 : $\delta = 2.50$ ppm for ^1H and 39.5 for ^{13}C). IR spectra were recorded on an Agilent Cary 630 FTIR equipped with an attenuated total reflectance (ATR) sampling. Melting points (M.P) were measured in open capillary tubes with a STUART SMP30 melting points apparatus and are uncorrected. High resolution mass spectrometry (HRMS-ESI) analyses were performed on a QStar Elite (Applied Biosystems SCIEX) spectrometer or on a SYNAPT G2 HDMS (Waters) spectrometer by the “Spectropole” of Aix-Marseille University.

These two instruments are equipped with an electrospray ionization (ESI) or a MALDI source and a TOF analyser.

4.3. Electronic absorption and fluorescence

UV–Vis absorption spectra were recorded in spectrophotometric grade solvents (ca. 10^{-6} M) on a Varian Cary 50 SCAN spectrophotometer. Ten equivalents of TFA were added to the suspension of the porphyrins **7**, **8** and **9** in order to ensure their complete dissolution as protonated and non-aggregated dyes. A subsequent addition of twelve equivalents of $^i\text{Pr}_2\text{NEt}$ afforded back the non-protonated free bases soluble in solution. Emission spectra were obtained using a Horiba-Jobin Yvon Fluorolog-3 spectrofluorimeter equipped with a three-slit double-grating excitation and a spectrograph emission monochromator with dispersions of $2.1 \text{ nm}\cdot\text{mm}^{-1}$ (1200 grooves per mm). A 450 W xenon continuous wave lamp provided excitation. Fluorescence of diluted solutions was detected at right angle using 10 mm quartz cuvettes. Fluorescence quantum yields Φ were measured in diluted dichloromethane solutions with an optical density lower than 0.1 using the following equation:

$$\frac{\Phi_x}{\Phi_r} = \left(\frac{A_r(\lambda)}{A_x(\lambda)} \right) \left(\frac{n_x^2}{n_r^2} \right) \left(\frac{D_x}{D_r} \right)$$

where A is the absorbance at the excitation wavelength (λ), n the refractive index and D the integrated intensity. “ r ” and “ x ” stand for reference and sample. The fluorescence quantum yields were measured relative to tetraphenylporphyrin (TPP) in acetonitrile ($\Phi = 0.15$) [54]. Excitation of reference and sample compounds was performed at the same wavelength (590 nm).

4.4. Electrochemistry

Cyclic voltammetric (CV) data were acquired using a BAS 100 Potentiostat (Bioanalytical Systems) and a PC computer containing BAS100W software (v2.3). A three-electrode system with a Pt working electrode (diameter 1.6 mm), a Pt counter electrode and a leak-free Ag/AgCl reference electrode (diameter 5 mm) was used. $[\text{Bu}_4\text{N}]\text{PF}_6$ (0.1 M in CH_2Cl_2) served as an inert electrolyte while the concentration of the electro-active compound is of ca. 5×10^{-4} M.

Cyclic voltammograms were recorded at a scan rate of 100 mV·s⁻¹. Ferrocene (0.46 V/SCE) was used as internal standard [55]. Solutions were degassed using argon and the working electrode surface (Pt) was polished before each scan recording. The solubility of porphyrins **7** and **8** in the solvent is too low to get accurate electrochemical values.

4.5. Computational details

All (TD-)DFT calculations have been performed using the Gaussian 16 program [56]. The geometry optimizations were carried out without symmetry constraints to ensure the minima energy. Calculations were performed using the CAM-B3LYP exchange functional (since this level of theory have been widely used in this type of compounds and also because this functional reproduces correctly the corresponding geometrical parameters) and the 6-311+G(d,p) basis set for all atoms [57,58]. Frequency calculations were also included to corroborate the optimized structures, showing only positive values in all vibrational modes. TD-DFT calculations were performed for the first 80 vertical excitations, in vacuum and in dichloromethane (DCM) as solvent, using the conductor-like polarizable continuum model (CPCM) [59]. Here, the BLYP functional was implemented in conjunction with the 6-311+G(d,p) basis set for all atoms. The BLYP functional was chosen because this level of theory accurately reproduces the experimental UV-Vis results [60].

4.6. Single crystal X-ray diffraction

Suitable diffracting single crystals of **6a** and **6b** were obtained by slow diffusion of *n*-pentane into concentrated solutions of the porphyrins in dichloromethane. The intensity data for compound **11a** were collected on a Rigaku Oxford Diffraction SuperNova diffractometer using CuK α radiation ($\lambda = 1.54184 \text{ \AA}$) at 293 K. Data collection, cell refinement and data reduction were performed with CrysAlisPro (Rigaku Oxford diffraction). Using Olex2 [61], the structures were solved with shelXT [62] and shelXL [62] was used for full matrix least squares refinement. CCDC-2074306 (**6a**) and CCDC-2074307 (**6b**) contain the supplementary crystallographic data. These data can be obtained free of charge from The Cambridge Crystallographic Data Centre via www.ccdc.cam.ac.uk/data_request:cif.

4.7. Synthetic methods

The 2-acylpyrroles **5a** (R = CF₃) [63], **5b** (R = C₃F₇) [26], **5c** (R = C₇F₁₅) [64], **5f** (R = CCl₃) [65] and **5e** (R = CHCl₂) [66] were prepared as previously reported.

4.7.1. 2-(Chlorodifluoroacetyl)pyrrole (**5d**)

This compound was prepared following a protocol adapted from the synthesis of 2-(trifluoroacetyl)pyrrole **5a** [63]. A solution of chlorodifluoroacetic anhydride (4.15 mL, 23 mmol, 1.1 equiv.) in anhydrous CH₂Cl₂ (15 mL) was cooled to -15 °C under an argon atmosphere. A solution of pyrrole (1.44 mL, 20.9 mmol, 1 equiv.) in anhydrous CH₂Cl₂ (15 mL) was then added dropwise under firm stirring. The mixture was stirred at -15 °C for 1.5 h, then at room temperature during an additional hour. The organic phase was washed with water, dried over Na₂SO₄, and the solvent removed by evaporation. The resulting residue was purified by flash chromatography (CH₂Cl₂/petroleum ether 1:1) to afford **5d** as a white solid (4.01 g, 22 mmol, 99%).

$R_F = 0.45$ (silica, CH₂Cl₂/petroleum ether 1:1). **Mp**: 41.9 °C; ¹H NMR (CDCl₃) $\delta = 10.27$ (br s, 1H, NH), 7.28 (m, 1H, α -H), 7.25 (m, 1H, β -H), 6.41 (m, 1H, β -H) ppm; ¹⁹F NMR (CDCl₃) $\delta = -61.5$ ppm; ¹³C {¹H} NMR (CDCl₃) $\delta = 172.2$ (t, ²J_{C,F} = 30.5, C), 129.6 (CH), 124.7 (C), 122.1 (t, ⁴J_{C-F} = 4.7, CH), 120.5 (t, ¹J_{C,F} = 302.5, C), 112.7 (CH) ppm; **IR**: $\tilde{\nu} = 3329$ (vs, N-H), 1638 (vs, C=O) cm⁻¹; **HMRS-ESI**: calcd. for C₆H₃NOF₂Cl [M-H]⁻ 177.9877. Found: 177.9877.

4.7.2. 5-(Trifluoromethyl)dipyrromethane (**3a**)

Procedure A: to a solution of 2-(trifluoroacetyl)pyrrole **5a** (500 mg, 3.07 mmol, 1 equiv.) and NaHCO₃ (514 mg, 6.13 mmol, 2 equiv.) suspended in methanol (46 mL) under firm stirring was added NaBH₄ (232 mg, 6.12 mmol, 2 equiv.) by portions. The mixture was stirred at room temperature for 30 min before removal of the solvent by evaporation. The crude product was dissolved in Et₂O. This organic phase was washed with water, dried over Na₂SO₄ and evaporated at 30 °C. The resulting residue and pyrrole (0.42 mL, 6.12 mmol, 2 equiv.) were dissolved in CH₂Cl₂ (40 mL) and under argon atmosphere. P₂O₅ (87 mg, 6.13 mmol, 2 equiv.) was then added and the mixture was stirred at room temperature for 16 h. A saturated aqueous NaHCO₃ solution (10 mL) was added, and the stirring maintained for 1 h. The

crude product was filtered and washed with DCM on a Büchner funnel equipped with sintered glass. The filtrate was dried on Na₂SO₄. The subsequent flash chromatography (CH₂Cl₂/petroleum ether 1:1, then 2:1) afforded **3a** as a white solid (395 mg, 1.8 mmol, 60%).

Procedure B: to a solution of 2-(trifluoroacetyl)pyrrole **5a** (250 mg, 1.53 mmol, 1 equiv.) and NaHCO₃ (257 mg, 3.06 mmol, 2 equiv.) suspended in methanol (4.6 mL) under firm stirring was added NaBH₄ (116 mg, 3.06 mmol, 2 equiv.) by portions. The mixture was stirred at room temperature for 30 min before removal of the solvent by evaporation. The crude product was extracted with Et₂O, then washed with water and dried over Na₂SO₄. The organic phase was evaporated at 30 °C then dissolved with pyrrole (0.21 mL, 3.06 mmol, 2 equiv.), in an aqueous HCl solution (0.18 M, 5 mL). The mixture was stirred at room temperature for 16 h. The mixture was then extracted with CH₂Cl₂. This organic phase was washed with water, dried on Na₂SO₄ before removal of the solvent by evaporation. The residue was finally purified by flash chromatography (CH₂Cl₂/petroleum ether 2:1) to afford **3a** as a gray solid (79 mg, 0.37 mmol, 24%). **Scale up:** starting from 2-(trifluoroacetyl)pyrrole **5a** (2.5 g, 15.3 mmol, 1 equiv.), **3a** was obtained as a gray solid (938 mg, 4.4 mmol, 28%).

R_F = 0.5 (CH₂Cl₂/petroleum ether 2:1). ¹H NMR (CDCl₃) δ = 8.10 (br s, 2H, NH), 6.77 (m, 2H, α-H), 6.25 (m, 2H, β-H), 6.22 (m, 2H, β-H), 4.85 (q, ³J_{H,F} = 9.0, 1H, *meso*-H) ppm; IR: ν̃ = 3366, 3346 (vs, N-H), 1242, 1161, 1119, 1092, 1043 (s, C-F) cm⁻¹. Other analytical data are consistent with literature values [13].

4.7.3. 5-(Perfluoropropyl)dipyrromethane (**3b**)

Procedure A: scale up: to a solution of 2-(perfluorobutyl)pyrrole **5b** (4.18 g, 15.9 mmol, 1 equiv.) and NaHCO₃ (2.67 g, 31.8 mmol, 2 equiv.) suspended in methanol (50 mL) under firm stirring was added NaBH₄ (1.20 g, 31.8 mmol, 2 equiv.) by portions. The mixture was stirred at room temperature for 30 min before removal of the solvent by evaporation. The crude product was dissolved in Et₂O. The organic phase was washed with water, dried over Na₂SO₄ and was evaporated at 30 °C. The resulting residue and pyrrole (2.21 mL, 31.8 mmol, 2 equiv.) were dissolved in CH₂Cl₂ (200 mL) under argon. P₂O₅ (4.51 g, 31.8 mmol, 1 equiv.) was then added

and the mixture was stirred at room temperature for 16 h. NaHCO₃ (3.47 g, 41.3 mmol, 2.6 equiv.) was added and the stirring maintained for 1 h. The mixture was filtrated and washed with DCM on a Büchner funnel equipped with sintered glass. The filtrate was dried on Na₂SO₄ before removal of the solvent by evaporation. The residue was finally purified by flash chromatography (CH₂Cl₂/petroleum ether 2:1) to afford **3b** as a white solid (2.05 g, 6.5 mmol, 41%).

R_F = 0.65 (silica, CH₂Cl₂/petroleum ether 2:1). ¹H NMR (CDCl₃) δ = 8.15 (br s, 2H, NH), 6.78 (m, 2H, α-H), 6.25 (m, 2H, β-H), 6.20 (m, 2H, β-H), 4.94 (t, ³J_{H,F} = 16.6, 1H, *meso*-H) ppm; IR: ν̃ = 3368 (s, N-H), 1233, 1207, 1175, 1113, 1093 (s, C-F) cm⁻¹. Other analytical data are consistent with literature values [13].

4.7.4. 5-(Perfluoroheptyl)dipyrromethane (**3c**)

Procedure A: scale up: to a solution of 2-(perfluoro-octanoyl)pyrrole **5c** (2.01 g, 4.31 mmol, 1 equiv.) and NaHCO₃ (722 mg, 8.60 mmol, 2 equiv.) suspended in methanol (16 mL) under firm stirring was added NaBH₄ (325 mg, 8.59 mmol, 2 equiv.) by portions. The mixture was stirred at room temperature for 30 min before removal of the solvent by evaporation. The crude product was dissolved in Et₂O. The organic phase was washed with water, dried over Na₂SO₄ and was evaporated at 30 °C. The resulting residue and pyrrole (0.6 mL, 8.62 mmol, 2 equiv.) were dissolved in CH₂Cl₂ (65 mL) under argon. P₂O₅ (1.22 g, 8.65 mmol, 2 equiv.) was then added and the mixture was stirred at room temperature for 16 h. NaHCO₃ (940 mg, 11.2 mmol, 2.6 equiv.) was added and the stirring maintained for 1 h. The crude product was filtrated and washed by DCM on a Büchner funnel equipped with sintered glass. The filtrate was dried on Na₂SO₄ before removal of the solvent by evaporation. The residue was finally purified by flash chromatography (CH₂Cl₂/petroleum ether) to afford **3c** as a light purple solid (1.92 g, 3.73 mmol, 87%).

R_F = 0.60 (silica, CH₂Cl₂/petroleum ether). ¹H NMR (CDCl₃) δ = 8.15 (br s, 2H, NH), 6.78 (m, 2H, α-H), 6.25 (m, H, β-H), 6.20 (m, 2H, β-H), 4.96 (t, ³J_{H,F} = 16.8, 2H, *meso*-H) ppm; ¹⁹F NMR (CDCl₃) δ = -80.7 (CF₃), -112.2, -120.5, -121.5, -121.9, -122.6, -126.0 ppm; ¹³C {¹H} NMR (CDCl₃) δ = 122.3 (C), 119.0 (CH), 109.7 (CH), 109.1 (CH), 108.3 (C), 41.2 (t, ²J_{C-F} = 23.0, C) ppm, other carbon atoms could not be assigned due the low intensity of the

perfluorinated chain peaks [67] and because of the rapid degradation of the compound in solution; **IR**: $\tilde{\nu} = 3405$ (br, N-H), 1235, 1198, 1143, 1095 (vs, C-F) cm^{-1} ; **HRMS-ESI**: calcd for $\text{C}_{16}\text{H}_8\text{F}_{15}\text{N}_2$ [M-H] $^-$: 513.0453. Found: 513.0461.

4.7.5. 5-(Chlorodifluoromethyl)dipyrromethane (**3d**)

Procedure B: to a solution of 2-(chlorodifluoroacetyl)pyrrole **5d** (100 mg, 0.56 mmol, 1 equiv.) and NaHCO_3 (94 mg, 1.12 mmol, 2 equiv.) suspended in methanol (1.7 mL) under firm stirring was added NaBH_4 (42 mg, 1.1 mmol, 2 equiv.) by portions. The mixture was stirred at room temperature for 30 min before removal of the solvent by evaporation. The crude product was dissolved with Et_2O . This organic phase was washed with water, dried over Na_2SO_4 and evaporated at 30 °C. The resulting residue was then dissolved in pyrrole (0.78 mL, 1.1 mmol, 2 equiv.) before the addition of an aqueous HCl solution (0.18 M, 2 mL). The mixture was stirred at room temperature for 16 h. The mixture was then extracted with CH_2Cl_2 , washed with water, and dried on Na_2SO_4 before removal of the solvent by evaporation. The subsequent flash chromatography (CH_2Cl_2 /petroleum ether 2:1) afforded **3d** as a white solid (23 mg, 0.1 mmol, 18%). **Scale up**: The same procedure at a larger scale and starting from **5d** (2.74 g, 15.3 mmol) afforded **3d** as a white solid (589 mg, 2.55 mmol, 18%).

$R_F = 0.65$ (silica, CH_2Cl_2 /petroleum ether 2:1). **Mp**: 75–80 °C; **$^1\text{H NMR}$** (CDCl_3) $\delta = 8.19$ (br s, 2H, NH), 6.79 (m, 2H, α -H), 6.27 (m, 2H, β -H), 6.22 (m, 2H, β -H), 4.96 (t, $^3J_{\text{H,F}} = 11.1$, 1H, *meso*-H) ppm; **$^{19}\text{F NMR}$** (CDCl_3) $\delta = -53.3$ (d, $^3J_{\text{F,H}} = 11.1$) ppm; **^{13}C { ^1H } NMR** (CDCl_3) $\delta = 118.7$ (CH), 117.8 (C), 109.6 (t, $^2J_{\text{C,F}} = 1.4$, CH), 109.1 (CH), 108.3 (CH), 49.8 (t, $^1J_{\text{C,F}} = 26.0$, C) ppm; **IR**: $\tilde{\nu} = 3351$ (vs, N-H) cm^{-1} ; **HRMS-ESI**: calcd. for $\text{C}_{10}\text{H}_8\text{ClF}_2\text{N}_2$ [M-H] $^-$: 229.0350. Found: 229.0351.

4.7.6. 5-(Dichloromethyl)dipyrromethane (**3e**)

Procedure B: to a solution of 2-(dichloroacetyl)pyrrole **5e** (272 mg, 1.53 mmol, 1 equiv.) and NaHCO_3 (257 mg, 3.06 mmol, 2 equiv.) suspended in methanol (4.6 mL) under firm stirring was added NaBH_4 (116 mg, 3.06 mmol, 2 equiv.) by portions. The mixture was stirred at room temperature for 30 min before removal of the solvent by evaporation. The crude product was dissolved in Et_2O . This organic phase

was washed with water, dried over Na_2SO_4 and evaporated at 30 °C. The resulting solid was then dissolved in pyrrole (0.21 mL, 3.06 mmol, 2 equiv.) before the addition of an aqueous HCl solution (0.18 M, 5 mL). The mixture was stirred at room temperature for 16 h. The mixture was then extracted with CH_2Cl_2 . The organic phase was washed with water, dried on Na_2SO_4 and evaporated to dryness. The final purification by flash chromatography (CH_2Cl_2 /petroleum ether 2:1) afforded **3e** as a gray solid (212 mg, 0.9 mmol, 60%). **Scale up**: the same procedure at a ten-fold larger scale starting from **5e** (2.72 g, 15.3 mmol) afforded **3e** as a white solid (2.37 g, 10.3 mmol, 67%).

$R_F = 0.4$ (silica, CH_2Cl_2 /petroleum ether 2:1). **Mp**: > 60 °C (degradation) **$^1\text{H NMR}$** (CDCl_3) $\delta = 8.26$ (br s, 2H, NH), 6.75 (m, 2H, α -H), 6.25 (m, 2H, β -H), 6.21 (m, 3H, β -H and CHCl_2), 4.83 (d, $^3J_{\text{H,H}} = 3.5$, 1H, *meso*-H) ppm; **^{13}C { ^1H } NMR** (CDCl_3) $\delta = 126.8$ (C), 118.3 (CH), 108.8 (CH), 108.7 (CH), 74.9 (CH), 49.0 (CH) ppm; **IR**: $\tilde{\nu} = 3344$ (vs, N-H), 742 (vs, C-Cl) cm^{-1} ; **HRMS-ESI**: calcd. for $\text{C}_{10}\text{H}_8\text{Cl}_2\text{N}_4$ [M-H] $^-$: 227.0148. Found: 227.0151.

4.7.7. 5-(Trichloromethyl)dipyrromethane (**3f**)

Procedure C: to a solution of 2-(trichloroacetyl)pyrrole **5f** (1.63 g, 7.7 mmol, 1 equiv.) and NaHCO_3 (1.28 g, 15.3 mmol, 2 equiv.) suspended in methanol (23 mL) under firm stirring was added NaBH_4 (581 mg, 15.3 mmol, 2 equiv.) by portions. The mixture was stirred at room temperature for 30 min before removal of the solvent by evaporation. The crude product was dissolved in Et_2O . This organic phase was washed with water, dried over Na_2SO_4 and evaporated at 30 °C. The resulting solid and pyrrole (6.0 mL, 86 mmol, 11 equiv.) were dissolved in distilled THF (40 mL) under argon atmosphere before the addition of a solution of HCl in Et_2O (1 M, 6.9 mL, 6.9 mmol, 0.9 equiv.). The mixture was stirred at 85 °C for 2 h, quenched with a saturated aqueous NaHCO_3 solution. The mixture was extracted by diethyl ether. The organic phase was washed with water, dried over Na_2SO_4 and evaporated to dryness. The final purification by flash chromatography (CH_2Cl_2 /petroleum ether 2:1) afforded **3f** as a white solid (181 mg, 0.68 mmol, 9%).

$R_F = 0.45$ (silica, CH_2Cl_2 /petroleum ether 2:1). **Mp**: > 70 °C (decomposition); **$^1\text{H NMR}$** (CDCl_3) $\delta = 8.38$ (br s, 2H, NH), 6.78 (s, 2H, α -H), 6.41 (s, 2H, β -H), 6.23 (s, 2H, β -H), 5.16 (s, 1H, *meso*-H) ppm; **^{13}C**

$\{^1\text{H}\}$ NMR (CDCl_3) δ = 126.3 (C), 118.3 (CH), 110.2 (CH), 108.8 (CH), 59.2 (CH), 31.0 (C) ppm; **IR**: $\tilde{\nu}$ = 3340 (s, N–H), 741 (vs, C–Cl) cm^{-1} ; **HMRS-ESI**: calcd. for $\text{C}_{10}\text{H}_{10}\text{Cl}_3\text{N}_2$ $[\text{M}+\text{H}]^+$: 262.9904. Found: 262.9899.

4.7.8. 5,15-Bis(trifluoromethyl)-10,20-bis-(4-methoxyphenyl)porphyrin (**6a**)

Under argon, to a solution of 5-(trifluoromethyl)dipyrrromethane **3a** (643 mg, 3 mmol, 1 equiv.) and 4-methoxybenzaldehyde (0.36 mL, 3 mmol, 1 equiv.) in CH_2Cl_2 (300 mL) was added $\text{BF}_3\cdot\text{OEt}_2$ (2.5 M, 0.4 mL, 1 mmol, 0.33 equiv.). The mixture was stirred at room temperature for 4 h before DDQ (1.01 g, 4.5 mmol, 1.5 equiv.) was added and the stirring maintained for 10 min. The mixture was passed over a short silica gel plug (CH_2Cl_2 /petroleum ether 1:2). The following purification by flash chromatography (CH_2Cl_2 /petroleum ether 1:4) afforded **6a** as a dark purple solid (88 mg, 0.13 mmol, 9%).

R_F = 0.15 (silica, CH_2Cl_2 /petroleum ether 1:4); ^1H NMR (CDCl_3) δ = 9.59 (m, 4H, β -H), 8.93 (d, $^3J_{\text{H,H}}$ = 5.0, 4H, β -H), 8.06 (d, $^3J_{\text{H,H}}$ = 8.4, 4H, Ar–H), 7.31 (d, $^3J_{\text{H,H}}$ = 8.4, 4H, Ar–H), 4.13 (s, 6H, CH_3), –2.64 (br s, 2H, NH) ppm; ^{19}F NMR (CDCl_3) δ = –37.0, –45.5 ppm; ^{13}C $\{^1\text{H}\}$ NMR (CDCl_3) δ = 160.0 (C), 135.6 (CH), 134.3 (C), 133.8 (CH), 130.0 (CH), 128.1 (d, $^1J_{\text{C,F}}$ = 275, C), 122.0 (C), 112.5 (CH), 105.5 (d, $^2J_{\text{C,F}}$ = 30.5, C), 55.8 (CH), 53.6 (CH), 29.9 (CH_3) ppm; **IR**: $\tilde{\nu}$ = 3299.2 (w, N–H), 2918.7, 2843.1 (m, C_β -H) cm^{-1} ; **UV-Vis** (CH_2Cl_2): λ_{max} (ϵ) = 416.0 (180 530), 514.1 (10 730), 550.0 (8 490), 594.9 (4 300), 648.0 nm ($7220 \text{ mol}^{-1}\cdot\text{L}\cdot\text{cm}^{-1}$); **Fluorescence** (CH_2Cl_2): λ_{ex} = 590 nm, λ_{em} = 656, 722 nm; **HRMS-ESI**: calcd. for $\text{C}_{36}\text{H}_{25}\text{F}_6\text{N}_4\text{O}_2$ $[\text{M}+\text{H}]^+$: 659.1876. Found: 659.1877.

4.7.9. 5,15-Bis(perfluoropropyl)-10,20-bis-(4-methoxyphenyl)porphyrin (**6b**)

A solution of 5-(perfluoropropyl)dipyrrromethane **3b** (471 mg, 1.5 mmol, 1 equiv.) and 4-methoxybenzaldehyde (0.18 mL, 1.5 mmol, 1 equiv.) in CH_2Cl_2 (300 mL) was stirred under argon before the addition of TFA (1.16 mL, 15.1 mmol, 10 equiv.). The mixture was stirred at room temperature for 4 h before DDQ (570 mg, 2.25 mmol, 1.5 equiv.) was added. The resulting mixture was stirred for 16 h before being passed over a short silica gel plug (CH_2Cl_2 /petroleum ether 1:2). The following purification by flash chromatography (CH_2Cl_2 /petroleum

ether 1:4) afforded **6b** as a dark purple solid (29 mg, 0.03 mmol, 4.5%).

R_F = 0.25 (silica, CH_2Cl_2 /petroleum ether 1:4); ^1H NMR (CDCl_3) δ = 9.45 (br s, 4H, β -H), 8.94 (d, $^3J_{\text{H,H}}$ = 5.1, 4H, β -H), 8.07 (d, $^3J_{\text{H,H}}$ = 7.1, 4H, Ar–H), 7.31 (d, $^3J_{\text{H,H}}$ = 8.6, 4H, Ar–H), 4.13 (s, 6H, CH_3), –2.53 (br s, 2H, NH) ppm; ^{19}F NMR (CDCl_3) δ = –76.1 (CF_3), –81.8, –119.9 ppm; ^{13}C $\{^1\text{H}\}$ NMR spectra could not be obtained due to the poor solubility in deuterated solvents; **IR**: $\tilde{\nu}$ = 3271.6 (w, N–H) cm^{-1} ; **UV-Vis** (CH_2Cl_2): λ_{max} (ϵ) = 414 (189,000), 514 (9910), 551 (11,430), 595 (4640), 646 nm ($10,655 \text{ mol}^{-1}\cdot\text{L}\cdot\text{cm}^{-1}$); **Fluorescence** (CH_2Cl_2): λ_{ex} = 590 nm, λ_{em} = 656, 719 nm; **HRMS-ESI**: calcd. for $\text{C}_{48}\text{H}_{23}\text{F}_{30}\text{N}_4\text{O}_2$ $[\text{M}-\text{H}]^-$: 857.1603. Found: 857.1602.

4.7.10. 5,15-Bis(perfluoroheptyl)-10,20-bis-(4-methoxyphenyl)porphyrin (**6c**)

A solution of 5-(perfluoroheptyl)dipyrrromethane **3c** (771 mg, 1.5 mmol, 1 equiv.) and 4-methoxybenzaldehyde (0.18 mL, 1.5 mmol, 1 equiv.) in CH_2Cl_2 (300 mL) was stirred under argon before the addition of TFA (1.16 mL, 15.1 mmol, 10 equiv.). The mixture was stirred at room temperature for 4 h before DDQ (570 mg, 2.25 mmol, 1.5 equiv.) was added and the stirring maintained for 16 h. The mixture was passed over a short silica gel plug (CH_2Cl_2 /petroleum ether 1:2). The following purification by flash chromatography (CH_2Cl_2 /petroleum ether 1:4) afforded **6c** as a dark purple solid (37 mg, 0.03 mmol, 4%).

R_F = 0.4 (silica, CH_2Cl_2 /petroleum ether 1:4); ^1H NMR (CDCl_3) δ = 9.45 (br s, 4H, β -H), 8.94 (d, $^3J_{\text{H,H}}$ = 5.1, 4H, β -H), 8.07 (br s, 4H, Ar–H), 7.31 (d, $^3J_{\text{H,H}}$ = 8.4, 4H, Ar–H), 4.13 (s, 6H, CH_3), –2.52 (br s, 2H, NH) ppm; ^{19}F NMR (CDCl_3) δ = –80.5 (CF_3), –81.1, –115.1, –120.7, –121.4, –122.3, –125.9 ppm; ^{13}C $\{^1\text{H}\}$ NMR spectra could not be obtained due to the poor solubility in deuterated solvents; **IR**: $\tilde{\nu}$ = 2958, 2922, 2854 (s, C_β -H) cm^{-1} ; **UV-Vis** (CH_2Cl_2): λ_{max} (ϵ) = 415 (198,140), 514 (10,420), 552 (12,680), 596 (5070), 647 nm ($10,610 \text{ mol}^{-1}\cdot\text{L}\cdot\text{cm}^{-1}$); **Fluorescence** (CH_2Cl_2): λ_{ex} = 590 nm, λ_{em} = 655, 720 nm; **HRMS-ESI**: calcd for $\text{C}_{40}\text{H}_{23}\text{F}_{14}\text{N}_4\text{O}_2$ $[\text{M}-\text{H}]^-$: 1257.1347. Found: 1257.1349.

4.7.11. 5,15-Bis(fluoroacetyl)-10,20-bis-(4-methoxyphenyl)porphyrin (**6d**)

A solution of 5-(chlorodifluoromethyl)dipyrromethane **3d** (345 mg, 1.5 mmol, 1 equiv.) and 4-methoxybenzaldehyde (0.18 mL, 1.5 mmol, 1 equiv.) in CH₂Cl₂ (150 mL) was stirred under argon before the addition of BF₃·O(Et)₂ (2.5 M, 0.2 mL, 0.5 mmol, 0.33 equiv.). The mixture was stirred at room temperature for 4 h before DDQ (510 mg, 4.5 mmol, 1.5 equiv.) was added and the stirring maintained for 10 min. The crude product was passed over a short silica gel plug (CH₂Cl₂). The following purification by flash chromatography (CH₂Cl₂/petroleum ether 1:1 then 2:1) afforded **6d** as a dark purple solid (7 mg, 15 μmol, < 2%).

R_F = 0.6 (silica, CH₂Cl₂/petroleum ether 2:1). ¹H NMR (CDCl₃) δ = 9.61 (m, 4H, β-H), 9.01 (d, ³J_{H,H} = 4.9, 4H, β-H), 8.09 (d, ³J_{H,H} = 8.5, 4H, Ar-H), 7.34 (d, ³J_{H,H} = 8.5, 4H, Ar-H), 4.13 (s, 6H, CH₃), -2.68 (br s, 2H, NH) ppm; ¹⁹F NMR (CDCl₃) δ = -67.62 ppm; ¹³C {¹H} NMR spectra could not be obtained due to little quantity; IR: ν̃ = 2921, 2853 (vs, C_β-H) cm⁻¹; UV-Vis (CH₂Cl₂): λ_{max} (ε) = 419 (204,600), 521 (9650), 564 (11,780), 663 nm (11,290 mol⁻¹·L·cm⁻¹); Fluorescence (CH₂Cl₂): λ_{ex} = 590 nm, λ_{em} = 690 nm; HRMS-ESI: calcd. for C₃₆H₂₅N₄O₄F₂ [M+H]⁺: 615.1838. Found: 615.1838.

4.7.12. 5,15-Bis(formyl)-10,20-bis-(4-methoxyphenyl)porphyrin (**6e**)

A solution of 5-(dichloromethyl)dipyrromethane **3e** (230 mg, 1 mmol, 1 equiv.) and 4-methoxybenzaldehyde (0.12 mL, 1 mmol, 1 equiv.) in CH₂Cl₂ (200 mL) was stirred under argon before the addition of TFA (0.77 mL, 10 mmol, 10 equiv.). The mixture was stirred at room temperature for 4 h before DDQ (340 mg, 1.5 mmol, 1.5 equiv.) was added and the stirring maintained for 16 h. The mixture was passed over a short silica gel plug (CH₂Cl₂/AcOEt 9:1). The following purification by flash chromatography (CH₂Cl₂, then CH₂Cl₂/AcOEt 2.5%) afforded **6e** as a dark purple solid (31 mg, 0.05 mmol, 11%).

R_F = 0.6 (silica, CH₂Cl₂/AcOEt 97.5:2.5). ¹H NMR (CDCl₃) δ = 12.53 (s, 2H, CHO), 10.01 (d, ³J_{H,H} = 4.8, 4H, β-H), 9.01 (d, ³J_{H,H} = 4.8, 4H, β-H), 8.08 (d, ³J_{H,H} = 8.5, 4H, Ar-H), 7.33 (d, ³J_{H,H} = 8.5, 4H, Ar-H), 4.13 (s, 6H, CH₃), -2.30 (br s, 2H, NH) ppm; ¹³C {¹H} NMR spectra could not be obtained due

to the poor solubility in deuterated solvents; IR: ν̃ = 3318 (w, N-H), 2957, 2921, 2852 (m, C_β-H), 1672 (vs, C=O) cm⁻¹; UV-Vis (CH₂Cl₂): λ_{max} (ε) = 430 (193,270), 510 (4040), 538 (6900), 587 (17,130), 686 nm (14,880 mol⁻¹·L·cm⁻¹); Fluorescence (CH₂Cl₂): λ_{ex} = 590 nm, λ_{em} = 707, 771 nm; HRMS-ESI: calcd. for C₃₆H₂₇N₄O₄ [M+H]⁺: 579.2027. Found: 579.2031.

4.7.13. 5,15-Bis(formyl)-10,20-bis-(4-cyanophenyl)porphyrin (**7**)

A solution of 5-(dichloromethyl)dipyrromethane **3e** (345 mg, 1.5 mmol, 1 equiv.) and 4-cyanobenzaldehyde (197 mg, 1.5 mmol, 1 equiv.) in CH₂Cl₂ (300 mL) was stirred under argon before the addition of TFA (1.15 mL, 15 mmol, 10 equiv.). The mixture was stirred at room temperature for 2 h before DDQ (570 mg, 2.25 mmol, 1.5 equiv.) was added and the stirring maintained for 10 min. The mixture was passed over a short silica gel plug (CH₂Cl₂/AcOEt 9:1). The following purification by flash chromatography (CH₂Cl₂, then CH₂Cl₂/AcOEt 2.5%) afforded **7** as a dark purple solid (39 mg, 0.07 mmol, 9%).

R_F = 0.5 (silica, CH₂Cl₂/AcOEt 97.5:2.5). ¹H NMR (DMSO-*d*₆, 85 °C) δ = 12.56 (s, 2H, CHO), 10.19 (d, ³J_{H,H} = 5.1, 4H, β-H), 8.95 (d, ³J_{H,H} = 5.1, 4H, β-H), 8.43 (d, ³J_{H,H} = 8.0, 4H, Ar-H), 8.31 (d, ³J_{H,H} = 8.0, 4H, Ar-H), -2.40 (br s, 2H, NH) ppm; ¹³C {¹H} NMR spectra could not be obtained due to the poor solubility in deuterated solvents; IR: ν̃ = 3316 (w, N-H), 1671 (vs, C=O) cm⁻¹; UV-Vis (CH₂Cl₂): λ_{max} (ε) = 427 (102,970), 508 (2250), 535 (3840), 579 (8460), 680 nm (7470 mol⁻¹·L·cm⁻¹); Fluorescence (CH₂Cl₂): λ_{ex} = 590 nm, λ_{em} = 688, 757 nm; HRMS-ESI: calcd. for C₃₆H₂₁N₆O₂ [M+H]⁺: 569.1721. Found: 569.1716.

4.7.14. 5,15-Bis(formyl)-10,20-bis-(4-chlorophenyl)porphyrin (**8**)

A solution of 5-(dichloromethyl)dipyrromethane **3e** (345 mg, 1.5 mmol, 1 equiv.) and 4-chlorobenzaldehyde (0.21 mL, 1.5 mmol, 1 equiv.) in CH₂Cl₂ (300 mL) was stirred under argon before the addition of TFA (1.15 mL, 15 mmol, 10 equiv.). The mixture was stirred at room temperature for 2 h before DDQ (570 mg, 2.25 mmol, 1.5 equiv.) was added and the stirring maintained for 10 min. The mixture was passed over a short silica gel plug (CH₂Cl₂/AcOEt 9:1). The following purification by

flash chromatography (CH₂Cl₂) afforded **8** as a dark purple solid (8 mg, 13 μmol, < 2%).

R_F = 0.7 (silica, CH₂Cl₂). ¹H NMR (CDCl₃) δ = 12.54 (s, 2H, CHO), 10.04 (4H, β-H), 8.97 (d, ³J_{H,H} = 4.9, 4H, β-H), 8.11 (d, ³J_{H,H} = 7.9, 4H, Ar-H), 7.79 (d, ³J_{H,H} = 7.9, 4H, Ar-H), -2.38 (br s, 2H, NH) ppm; ¹³C {¹H} NMR spectra could not be obtained due to the poor solubility in deuterated solvents; IR: ν̄ = 1671 (vs, C=O) cm⁻¹; UV-Vis (CH₂Cl₂): λ_{max} (ε) = 427 (116,900), 535 (3630), 583 (10,310), 682 nm (9140 mol⁻¹·L·cm⁻¹); Fluorescence (CH₂Cl₂): λ_{ex} = 590 nm, λ_{em} = 692, 763 nm; HRMS-ESI: calcd. for C₃₄H₂₁Cl₂N₄O₂ [M+H]⁺: 587.1036. Found: 587.1038.

4.7.15. 5,15-Bis(formyl)-10,20-bis-(4-tert-butylphenyl)porphyrin (**9**)

A solution of 5-(dichloromethyl)dipyrromethane **3e** (173 mg, 0.75 mmol, 1 equiv.) and 4-tert-butylbenzaldehyde (0.13 mL, 0.75 mmol, 1 equiv.) in CH₂Cl₂ (150 mL) was stirred under argon before the addition of TFA (0.58 mL, 7.5 mmol, 10 equiv.). The mixture was stirred at room temperature for 2 h before DDQ (285 mg, 1.13 mmol, 1.5 equiv.) was added and the stirring maintained for 10 min. The mixture was passed over a short silica gel plug (CH₂Cl₂/AcOEt 9:1). The following purification by flash chromatography (CH₂Cl₂, then CH₂Cl₂/AcOEt 2.5%) afforded **9** as a dark purple solid (29 mg, 0.045 mmol, 12%).

R_F = 0.8 (silica, CH₂Cl₂). ¹H NMR (CDCl₃) δ = 12.51 (s, 2H, CHO), 9.98 (d, ³J_{H,H} = 4.8, 4H, β-H), 9.00 (d, ³J_{H,H} = 4.8, 4H, β-H), 8.09 (d, ³J_{H,H} = 8.1, 4H, Ar-H), 7.81 (d, ³J_{H,H} = 8.1, 4H, Ar-H), 1.64 (s, 18H, tertbutyl-H), -2.37 (br s, 2H, NH) ppm; ¹³C {¹H} NMR spectra could not be obtained due to the poor solubility in deuterated solvents; IR: ν̄ = 3302 (vw, N-H), 2962 (w, C_β-H), 1671 (vs, C=O) cm⁻¹; UV-Vis (CH₂Cl₂): λ_{max} (ε) = 427 (206,460), 539 (6160), 585 (17,490), 684 nm (15,410 mol⁻¹·L·cm⁻¹); Fluorescence (CH₂Cl₂): λ_{ex} = 590 nm, λ_{em} = 696, 767 nm; HRMS-ESI: calcd. for C₄₂H₃₉N₄O₂ [M+H]⁺: 631.3068. Found: 631.3068.

Acknowledgments

This contribution comes within the framework of the ECOS Sud-Chile project no. C19E07 supported by the Chilean *Comisión Nacional de Investigación Científica y Tecnológica* (CONICYT), the French *Ministère de l'Enseignement Supérieur, de la Recherche*

et de l'Innovation (MESRI) and the French *Ministère de l'Europe et des Affaires Étrangères* (MEAE). This work was supported in France by the *Centre National de la Recherche Scientifique* (CNRS) and by the MESRI. P-GJ acknowledges the MESRI (PhD grant). Michel Giorgi is gratefully acknowledged for solving the single crystal X-ray diffraction structures. In Chile, LS is indebted to financial support from the Fondecyt-Iniciación (grant no. 11181187) through the project MARCO. LS and DC-A thank the computational resources through the CONICYT-FONDEQUIP-EQM180180.

Supplementary data

Supporting information for this article is available on the journal's website under <https://doi.org/10.5802/crchim.97> or from the author.

The document contains ¹H, ¹⁹F and ¹³C NMR spectra, additional cyclic voltammograms, absorption and emission spectra, additional theoretical details.

References

- [1] K. M. Kadish, K. M. Smith, R. Guilard (eds.), *The Porphyrin Handbook*, vol. 1–10, Academic Press, San Diego, 2000.
- [2] K. M. Kadish, K. M. Smith, R. Guilard (eds.), *The Porphyrin Handbook*, vol. 11–20, Academic Press, San Diego, 2003.
- [3] K. M. Kadish, K. M. Smith, R. Guilard (eds.), *Handbook of Porphyrin Science*, vol. 1–10, World Scientific Publishing, Singapore, 2010.
- [4] K. M. Kadish, K. M. Smith, R. Guilard (eds.), *Handbook of Porphyrin Science*, vol. 11–15, World Scientific Publishing, Singapore, 2011.
- [5] K. M. Kadish, K. M. Smith, R. Guilard (eds.), *Handbook of Porphyrin Science*, vol. 16–25, World Scientific Publishing, Singapore, 2012.
- [6] Y. Inokuma, A. Osuka, *Dalton Trans.*, 2008, 2517–2526.
- [7] T. Tanaka, A. Osuka, *Chem. Rev.*, 2017, **117**, 2584–2640.
- [8] R. Orłowski, D. Gryko, D. T. Gryko, *Chem. Rev.*, 2017, **117**, 3102–3137.
- [9] J. K. Laha, S. Dhanalekshmi, M. Taniguchi, A. Ambroise, J. S. Lindsey, *Org. Process Res. Dev.*, 2003, **7**, 799–812.
- [10] D. T. Gryko, D. Gryko, C.-H. Lee, *Chem. Soc. Rev.*, 2012, **41**, 3780–3789.
- [11] N. A. M. Pereira, T. M. V. D. Pinho e Melo, *Org. Prep. Proced. Int.*, 2014, **46**, 183–213.
- [12] B. F. O. Nascimento, S. M. M. Lopes, M. Pineiro, T. M. V. D. Pinho e Melo, *Molecules*, 2019, **24**, article no. 4348.
- [13] T. P. Wijesekera, *Can. J. Chem.*, 1996, **74**, 1868–1871.
- [14] S. L. Gould, G. Kodis, R. E. Palacios, L. de la Garza, A. Brune, D. Gust, T. A. Moore, A. L. Moore, *J. Phys. Chem. B*, 2004, **108**, 10566–10580.

- [15] L. Li, B. Nguyen, K. Burgess, *Bioorg. Med. Chem. Lett.*, 2008, **18**, 3112-3116.
- [16] A. Nayak, J. Park, K. De Mey, X. Hu, T. V. Duncan, D. N. Beratan, K. Clays, M. J. Therien, *ACS Cent. Sci.*, 2016, **2**, 954-966.
- [17] A. Nayak, S. Roy, B. D. Sherman, L. Alibabaei, A. M. Lapidés, M. K. Brennaman, K.-R. Wee, T. J. Meyer, *ACS Appl. Mater. Interfaces*, 2016, **8**, 3853-3860.
- [18] A. Osuka, G. Noya, S. Taniguchi, T. Okada, Y. Nishimura, I. Yamazaki, N. Mataga, *Chem. Eur. J.*, 2000, **6**, 33-46.
- [19] N. Nishino, R. W. Wagner, J. S. Lindsey, *J. Org. Chem.*, 1996, **61**, 7534-7544.
- [20] R. Goldschmidt, I. Goldberg, Y. Balazs, Z. Gross, *J. Porphyr. Phthalocyanines*, 2006, **10**, 76-86.
- [21] W. Dmowski, K. Piasecka-Maciejewska, Z. Urbanczyk-Lipkowska, *Synthesis*, 2003, 841-844.
- [22] W. Dmowski, K. Piasecka-Maciejewska, Z. Urbańczyk-Lipkowska, *Kem. Ind.*, 2004, **53**, 339-341.
- [23] A. K. Wertsching, A. S. Koch, S. G. DiMagno, *J. Am. Chem. Soc.*, 2001, **123**, 3932-3939.
- [24] B. E. Smart, *J. Fluor. Chem.*, 2001, **109**, 3-11.
- [25] A. Rivkin, K. Biswas, T.-C. Chou, S. J. Danishefsky, *Org. Lett.*, 2002, **4**, 4081-4084.
- [26] S. G. DiMagno, R. A. Williams, M. J. Therien, *J. Org. Chem.*, 1994, **59**, 6943-6948.
- [27] S. G. DiMagno, A. K. Wertsching, C. R. Ross, *J. Am. Chem. Soc.*, 1995, **117**, 8279-8280.
- [28] K. E. Thomas, J. Conradie, L. K. Hansen, A. Ghosh, *Inorg. Chem.*, 2011, **50**, 3247-3251.
- [29] K. T. Moore, J. T. Fletcher, M. J. Therien, *J. Am. Chem. Soc.*, 1999, **121**, 5196-5209.
- [30] S. G. DiMagno, P. H. Dussault, J. A. Schultz, *J. Am. Chem. Soc.*, 1996, **118**, 5312-5313.
- [31] T. S. Balaban, A. D. Bhise, M. Fischer, M. Linke-Schaetzle, C. Roussel, N. Vanthuyne, *Angew. Chem. Int. Ed.*, 2003, **42**, 2140-2144.
- [32] N. Sugita, S. Hayashi, F. Hino, T. Takamami, *J. Org. Chem.*, 2012, **77**, 10488-10497.
- [33] M. O. Senge, S. S. Hatscher, A. Wiehe, K. Dahms, A. Kelling, *J. Am. Chem. Soc.*, 2004, **126**, 13634-13635.
- [34] A. Balakumar, K. Muthukumar, J. S. Lindsey, *J. Org. Chem.*, 2004, **69**, 5112-5115.
- [35] L. N. Sobenina, A. M. Vasil'tsov, O. V. Petrova, K. B. Petrusenko, I. A. Ushakov, G. Clavier, R. Meallet-Renault, A. I. Mikhaleva, B. A. Trofimov, *Org. Lett.*, 2011, **13**, 2524-2527.
- [36] V. Král, P. Vašek, B. Dolenský, *Collect. Czech. Chem. Commun.*, 2004, **69**, 1126-1136.
- [37] A. J. F. N. Sobral, N. G. C. L. Rebanda, M. da Silva, S. H. Lampreia, M. Ramos Silva, A. M. Beja, J. A. Paixão, A. M. d. A. Rocha Gonsalves, *Tetrahedron Lett.*, 2003, **44**, 3971-3973.
- [38] M. Bagherzadeh, M. A. Jonaghani, M. Amini, A. Mortazavi-Manesh, *J. Porphyr. Phthalocyanines*, 2019, **23**, 671-678.
- [39] T. Rohand, E. Dolusic, T. H. Ngo, W. Maes, W. Dehaen, *ARKIVOC*, 2007, 307-324.
- [40] H. Falk, H. Wöss, *Monatsh. Chem.*, 1988, **119**, 1031-1035.
- [41] S. Shimizu, N. Aratani, A. Osuka, *Chem. Eur. J.*, 2006, **12**, 4909-4918.
- [42] S.-J. Hong, M.-H. Lee, C.-H. Lee, *Bull. Korean Chem. Soc.*, 2004, **25**, 1545-1550.
- [43] R. Paolesse, L. Jaquinod, M. O. Senge, K. M. Smith, *J. Org. Chem.*, 1997, **62**, 6193-6198.
- [44] W. Schwertfeger, G. Siegemund, *J. Fluor. Chem.*, 1987, **36**, 237-246.
- [45] A. Wickramasinghe, L. Jaquinod, D. J. Nurco, K. M. Smith, *Tetrahedron*, 2001, **57**, 4261-4269.
- [46] M. Suzuki, S. Neya, Y. Nishigaichi, *Molecules*, 2016, **21**, article no. 252.
- [47] A. Nemes, E. Mérés, I. Jalsovszky, D. Szabó, Z. Böcskei, J. Rábai, *J. Fluor. Chem.*, 2017, **203**, 75-80.
- [48] L. Chen, L.-M. Jin, C.-C. Guo, Q.-Y. Chen, *Synlett*, 2005, 963-970.
- [49] Z. Zeng, C. Liu, L.-M. Jin, C.-C. Guo, Q.-Y. Chen, *Eur. J. Org. Chem.*, 2005, 306-316.
- [50] K. S. F. Lau, M. Sadilek, G. E. Khalil, M. Gouterman, C. Brückner, *J. Am. Soc. Mass. Spectrom.*, 2005, **16**, 1915-1920.
- [51] J. G. Goll, K. T. Moore, A. Ghosh, M. J. Therien, *J. Am. Chem. Soc.*, 1996, **118**, 8344-8354.
- [52] C. Hansch, A. Leo, R. W. Taft, *Chem. Rev.*, 1991, **91**, 165-195.
- [53] J. C. P. Grancho, M. M. Pereira, M. d. G. Miguel, A. M. R. Gonsalves, H. D. Burrows, *Photochem. Photobiol.*, 2002, **75**, 249-256.
- [54] A. M. Brouwer, *Pure Appl. Chem.*, 2011, **83**, 2213-2228.
- [55] N. G. Connelly, W. E. Geiger, *Chem. Rev.*, 1996, **96**, 877-910.
- [56] M. J. Frisch *et al.*, "GAUSSIAN 16 Revision C.01", 2016, Gaussian Inc. Wallingford CT.
- [57] D. Jacquemin, V. Wathelet, E. A. Perpète, C. Adamo, *J. Chem. Theory Comput.*, 2009, **5**, 2420-2435.
- [58] A. D. Laurent, D. Jacquemin, *Int. J. Quantum Chem.*, 2013, **113**, 2019-2039.
- [59] V. Barone, M. Cossi, *J. Phys. Chem. A*, 1998, **102**, 1995-2001.
- [60] B. Miehlich, A. Savin, H. Stoll, H. Preuss, *Chem. Phys. Lett.*, 1989, **157**, 200-206.
- [61] O. V. Dolomanov, L. J. Bourhis, R. J. Gildea, J. A. K. Howard, H. Puschmann, *J. Appl. Crystallogr.*, 2009, **42**, 339-341.
- [62] G. M. Sheldrick, *Acta Crystallogr.*, 2015, **C71**, 3-8.
- [63] W. J. Peláez, M. A. Burgos Paci, G. A. Argüello, *Tetrahedron Lett.*, 2009, **50**, 1934-1938.
- [64] J. Rábai, A. Nemes, I. Jalsovszky, D. Szabó, *Fluorine Notes*, 2016, **104**, 1-7.
- [65] Y. Çetinkaya, M. Balci, *Tetrahedron Lett.*, 2014, **55**, 6698-6702.
- [66] A. T. Dubis, M. Domagała, S. J. Grabowski, *New J. Chem.*, 2010, **34**, 556-566.
- [67] A. A. Ribeiro, *Magn. Reson. Chem.*, 1997, **35**, 215-221.



MAPYRO: the French Fellowship of the Pyrrolic Macrocyclic Ring / *MAPYRO: la communauté française des macrocycles pyrroliques*

Synthesis, electronic and photophysical properties of a bisacridinium-Zn(II) porphyrin conjugate

Amy Edo-Osagie^{® a}, Daniel Sánchez-Resa^{® b}, Dylan Serillon^{® a}, Elisa Bandini^{® b},
Christophe Gourlaouen^{® c}, Henri-Pierre Jacquot de Rouville^{® *, a}, Barbara Ventura^{® *, b}
and Valérie Heitz^{® *, a}

^a Laboratoire de Synthèse des Assemblages Moléculaires Multifonctionnels, Institut de chimie de Strasbourg, CNRS/UMR 7177, Université de Strasbourg, 4 rue Blaise Pascal, 67000 Strasbourg, France

^b Institute for Organic Synthesis and Photoreactivity (ISOF) – National Research Council (CNR), Via P. Gobetti 101, 40129 Bologna, Italy

^c Laboratoire de Chimie Quantique, Institut de Chimie de Strasbourg, CNRS/UMR 7177, 4 rue Blaise Pascal, 67000 Strasbourg, France

E-mails: edoosagie@unistra.fr (A. Edo-Osagie), daniel.resa@isof.cnr.it (D. Sánchez-Resa), dylan.serillon@etu.unistra.fr (D. Serillon), elisa.bandini@isof.cnr.it (E. Bandini), gourlaouen@unistra.fr (C. Gourlaouen), hpjacquot@unistra.fr (H.-P. Jacquot de Rouville), barbara.ventura@isof.cnr.it (B. Ventura), v.heitz@unistra.fr (V. Heitz)

Abstract. The synthesis of a novel bisacridinium-Zn(II) porphyrin is reported and its properties investigated via electrochemical, photophysical and computational studies. Cyclic voltammetry studies revealed a two-electron oxidation of the Zn(II) porphyrin and the simultaneous one electron reductions of the two acridiniums. Using absorption, emission and ultrafast transient absorption spectroscopies, the near total fluorescence quenching observed following excitation of either the acridinium or Zn(II) porphyrin units was assigned to ultrafast electron transfer (≤ 0.3 ps) leading to a reduced acridinium and an oxidized porphyrin unit in the bisacridinium-Zn(II) porphyrin conjugate. In addition, computational studies were found to complement experimental results, with calculations revealing two near degenerate HOMOs for the porphyrin.

Keywords. Acridinium, Porphyrin, Electron transfer, Electrochemistry, Transient absorption spectroscopy, Calculated spectra.

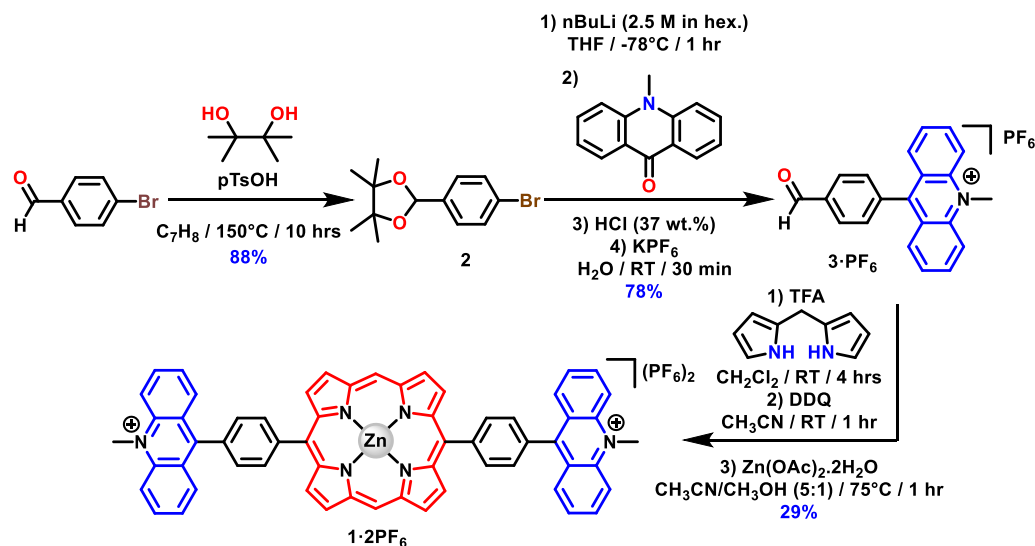
Available online 30th July 2021

1. Introduction

Porphyrins are versatile compounds that have found applications in various domains such as catalysis,

materials science and medicine [1–8]. Their properties which stand from their extended π -conjugated system and metal chelating capacity are easily tunable by functionalization of their *meso* or β -pyrrolic positions. Porphyrins associated to acridinium units have not received much attention yet despite the perspectives opened by such association. Indeed, N-

* Corresponding authors.



Scheme 1. Synthesis of the acridinium benzaldehyde **3·PF₆** and the bisacridinium–porphyrin conjugate **1·2PF₆**.

substituted acridiniums are multi-responsive units which modify their chemical and electronic features following chemical or redox stimuli [9]. N-substituted acridiniums and protonated acridines are also π -acceptors and as such, were incorporated in the host structure of various systems or used as a guest molecule for molecular recognition. As guest molecules, acridiniums were stabilized through charge transfer interactions in the cavities of bis-porphyrin systems based on clips or macrocyclic structures [10–12]. In some host–guest complexes, fast photoinduced electron transfer between the non-covalently linked porphyrin donor and acridinium acceptor units was demonstrated [13–15]. Regarding covalent porphyrin–acridinium associations, a free-base porphyrin connected to two acridiniums was reported as a fluorescent detector of superoxide anion. In this system, a fluorescence enhancement of the triad was detected following a two-electron reduction of the acridinium units by the superoxide anion [16].

Herein, the synthesis of a Zn(II) porphyrin *trans*-substituted with 9-phenyl-N-methyl-acridinium units is reported. The electrochemistry, absorption and emission properties of the conjugate are investigated as well as its photophysics, by means of ultrafast transient absorption spectroscopy. Computational studies have been performed to provide insights into the frontier molecular orbitals involved

in the electronic transitions of the conjugate.

2. Results and discussion

The synthesis of the bisacridinium-Zn(II) porphyrin **1·2PF₆** was inspired from Fukuzumi and coworkers [16]. It is based on a 2+2 condensation methodology developed by the Lindsey group to access *trans*-A2B2-type porphyrins [17]. It started from commercially available 4-bromobenzaldehyde and was performed in four synthetic steps (Scheme 1). The aldehyde functional group was first protected in the presence of pinacol (1.2 equiv.) in toluene [18]. The obtained 2-(4-bromophenyl)-4,4,5,5-tetramethyl-1,3-dioxolane (**2**) was reacted with nBuLi (0.8 equiv.) in THF at -78°C followed by addition of N-methylacridin-9(10H)-one (1 equiv.), obtained in one step from commercially available compounds [19]. After acidification of the reaction mixture using HCl (37 wt%), the freshly formed 9-(4-formylphenyl)-10-methylacridin-10-ium chloride (**3·Cl**) was converted to the corresponding hexafluorophosphate salt (**3·PF₆**) by anion metathesis and isolated in 78% yield. The key intermediate **3·PF₆** was then reacted under Lindsey conditions in the presence of di(1H-pyrrol-2-yl)methane (1 equiv.) [20], and trifluoroacetic acid (TFA, 0.6 equiv.) in CH_2Cl_2 . After aromatization of the porphyrinoid using DDQ

(3 equiv.), metalation of the free base porphyrin was undertaken using $\text{Zn}(\text{OAc})_2 \cdot 2\text{H}_2\text{O}$ (0.5 equiv.). After purification, the porphyrin–acridinium conjugate **1**· PF_6 was isolated in 29% yield.

3. Electrochemistry

Cyclic voltammograms (CV) were measured at 298 K under argon atmosphere, using tetrabutylammonium hexafluorophosphate (TBAPF₆) as the supporting electrolyte. It is worthwhile to note that due to the limited solubility of **1**· PF_6 in CH_3CN in the presence of supporting electrolyte, DMF was used to perform the experiments (Figure 1). In the cathodic regime, a reversible wave ($E_{\text{red}} = -0.475$ V versus SCE) corresponding to the reduction of the acridinium units followed by two reduction waves of half intensity ($E_{\text{red}} = -1.34$ V versus SCE and $E_{\text{red}} = -1.43$ V versus SCE) were recorded [21]. The observed ratio in intensity between the reduction processes suggests that the first reduction involves the reduction of both acridinium moieties at the same potential since no electronic coupling between these fragments is expected. The first reversible reduction process of the acridinium units allowed for the calculation of the half-wave reduction potential $E_{1/2} = -0.442$ V versus SCE. One of the two last reduction processes is related to the second electron injection to one of the acridinium fragments leading to a carbanionic species. Formation of this species is supported by the reduced intensity of the re-oxidation peak of the first reduction wave (-0.409 V versus SCE) leading to an EC mechanism (electron transfer–chemical). This carbanion is known to be highly reactive and capable of reacting with solvent molecules. The obtained CV in the anodic regime (Figure 1) consists of an irreversible anodic wave ($E_{\text{ox}} = +0.949$ V versus SCE) attributed to the oxidation of the porphyrin moiety. Interestingly, this wave has the same intensity ($I = 7.3 \mu\text{A}$) as the first cathodic process thus indicating that an equal number of electrons is exchanged in both processes. This surprising bi-electronic oxidation of the porphyrin core was further supported by rotating disk electrode (RDE) experiments recorded in benzonitrile (see ESI, Figure S23). These data allow the estimation of the HOMO–LUMO gap to be 1.4 eV.

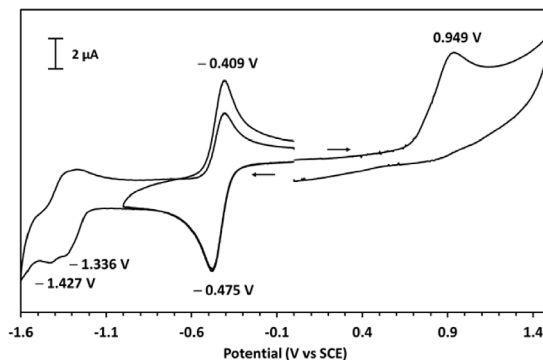


Figure 1. Cyclic voltammograms (DMF; WE: Pt, CE: Pt, RE: Hg/Hg₂Cl₂/KCl sat., 100 mV·s⁻¹) of a solution of **1**· PF_6 ($c = 1 \times 10^{-3}$ mol·L⁻¹) in the presence of TBAPF₆ as supporting electrolyte ($c = 0.1$ mol·L⁻¹).

4. Photophysical properties

The photophysical properties of the conjugate **1**· PF_6 were characterized in CH_3CN . Model compounds Zn-bisphenyl porphyrin (**Zn-bP**) and acridinium benzaldehyde (**3**· PF_6) (see ESI, Scheme S1) were also studied in the same solvent for comparison purposes.

The absorption spectrum of the conjugate is presented in Figure 2, compared with the spectra of its models **Zn-bP** and **3**· PF_6 and their weighted sum. It can be observed that the spectrum of **1**· PF_6 correlates reasonably well with the sum in the 280–400 nm region, while the Q-bands of the porphyrin (500–600 nm) are slightly red-shifted with respect to the model porphyrin, as well as the Soret band (400–450 nm) which also shows a decrease in intensity and a broadening. Theoretical analysis demonstrates that the latter absorption features are given by the contribution of three electronic π – π^* transitions either centered on the porphyrin or on the acridinium cores (see below).

Luminescence measurements were carried out both at room temperature and at 77 K in CH_3CN . At room temperature, model **3**· PF_6 shows a broad emission spectrum peaking at 515 nm, with a quantum yield of 0.045 and an excited state lifetime of 1.73 ns, while **Zn-bP** shows features typical of Zn-porphyrins, with maxima at 588 and 638 nm, $\phi_{\text{fl}} = 0.035$ and $\tau = 2.30$ ns (Figure S24 and Table 1).

Table 1. Emission data for models and conjugate in CH₃CN

		RT			77 K		E (eV) ^d
		λ_{\max} (nm) ^a	ϕ_{em} ^b	τ (ns) ^c	λ_{\max} (nm) ^a	τ (ns) ^c	
3·PF₆	3·PF ₆ ¹	515	0.045	1.73	471, 500	2.70 (20%); 16.6 (80%)	2.63
Zn-bP	Zn-bP ¹	588, 638	0.035	2.30	605, 648	2.31	2.05
	Zn-bP ³				794	—	1.56
1·2PF₆		590, 642 ^e	<1.0 × 10 ^{-4e}		—	—	—

^aEmission maxima from corrected spectra. ^bFluorescence quantum yields, measured with reference to TPP (*meso*-tetraphenylporphyrin) in aerated toluene as a standard for the porphyrin units and with reference to Coumarin 153 in ethanol for the acridinium units. ^cFluorescence lifetimes in the nanosecond range, excitation at 465 nm for **Zn-bP** and at 368 nm for **3·PF₆**. ^dEnergy of the excited state determined as the energy of the 0–0 emission band collected at 77 K. ^eUpon selective excitation of the Zn-porphyrin at 543 nm, the yield is below the minimum value measurable with steady-state experiments, i.e. 1.0 × 10⁻⁴.

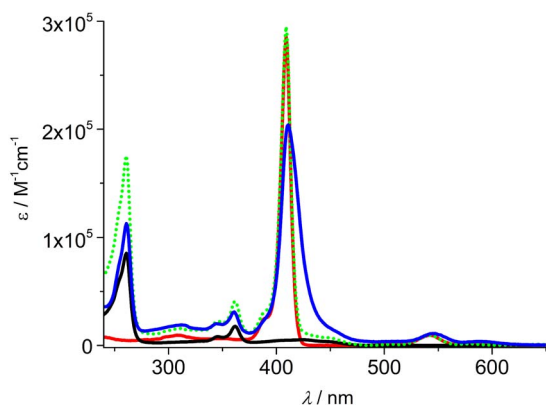


Figure 2. Absorption spectra of bisacridinium-porphyrin conjugate **1·2PF₆** (blue), model compounds **Zn-bP** (red) and **3·PF₆** (black) and the sum of the spectrum of **Zn-bP** with twice the spectrum of **3·PF₆** (green dotted) in CH₃CN.

Conversely, the conjugate **1·2PF₆** is weakly emissive, displaying a strong quenching of both the acridinium and the porphyrin units. Selective excitation of the porphyrin component in **1·2PF₆** at 543 nm, led to evaluate an emission quantum yield below 10⁻⁴, i.e. reduced to less than 0.3% the yield of model **Zn-bP** (Table 1). In order to estimate the quenching of the acridinium unit in **1·2PF₆**, excitation of isoabsorbing solutions of the conjugate, the porphyrin model and acridinium benzaldehyde model at 262 nm, wavelength at which prevalent excitation of the acridinium units (ca. 96%) is achieved, was car-

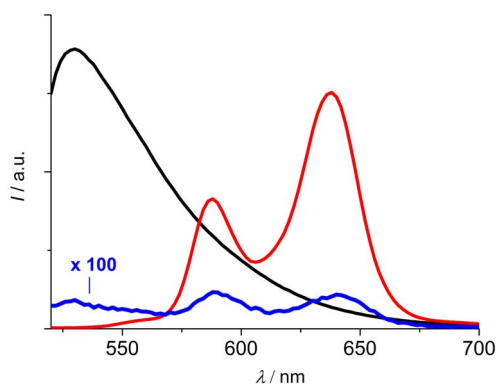
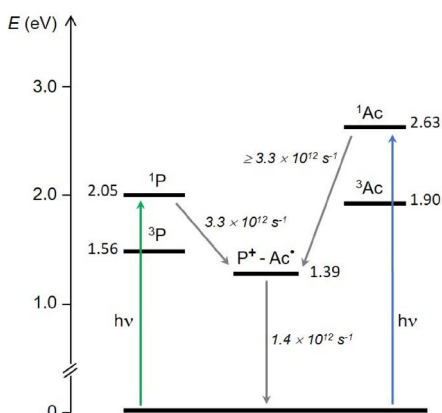


Figure 3. Uncorrected emission spectra of CH₃CN solutions of **1·2PF₆** (blue) and models **3·PF₆** (black) and **Zn-bP** (red), isoabsorbing at 262 nm ($A_{262} = 0.1$). $\lambda_{\text{exc}} = 262$ nm. The blue spectrum has been multiplied by a factor of 100.

ried out and the results are shown in Figure 3. The residual porphyrin fluorescence in **1·2PF₆** is far below the 4% of the model emission, percentage which would correspond to the direct excitation of the porphyrin unit in the array, confirming the quenching already observed. Moreover, the weak residual acridinium emission points to a quenching higher than 99% of these units in the array. The observed features indicate that a very fast and efficient photoinduced process depopulates the lowest singlet excited states of both components in the array, likely an electron transfer reaction. This hypothesis is confirmed



Scheme 2. Energy level diagram and kinetics of the photoinduced processes occurring in the conjugate **1·2PF₆** in CH₃CN. The singlet and triplet energy levels are taken from data of the present paper and from literature [22]. The energy of the charge separated state (1.39 eV) has been approximated as $E_{\text{ox}} - E_{\text{red}}$ (with E_{ox} and E_{red} as “redox energy”, expressed in eV), by considering the oxidation potential of the porphyrin unit ($E_{\text{ox}} = +0.949$ V versus SCE) and the reduction potential of the acridinium unit ($E_{1/2} = -0.442$ V versus SCE) measured in DMF, whose polarity is similar to that of CH₃CN.

by transient absorption analysis, as discussed in detail below.

The electron transfer reaction does not exclude a possible energy transfer from the acridinium to the porphyrin singlet excited states, a process thermodynamically allowed (Scheme 2) and supported by a non-zero overlap between the emission spectrum of the acridinium unit and the absorption spectrum of the porphyrin component (Figures 2 and S24). In order to investigate this event, the excitation spectrum of **1·2PF₆** was collected at 660 nm, wavelength at which only the emission of the porphyrin component is present and compared to the absorption spectrum (Figure S25). Even if noisy, due to the very weak emission, the excitation spectrum clearly contains the absorption bands of the porphyrin and lacks the characteristic absorption peaks of the acridinium unit at 262 and 362 nm. This outcome leads to conclude that an energy transfer process from the acridinium units to the central porphyrin is not occur-

ring in the conjugate, probably due to the competition with the ultrafast electron transfer process.

Emission measurements conducted at 77 K showed fluorescence spectra with higher vibrational resolution for the models **3·PF₆** and **Zn-bP** (Figure S26). In **Zn-bP**, moreover, phosphorescence emission at 794 nm is clearly observed. The conjugate **1·2PF₆** appears to be weakly emissive also at 77 K and its spectrum is hardly detectable due to scattering issues that affect these measurements. This outcome leads to deduce that the decrease in temperature is not affecting the efficiency of the quenching process occurring within the components of the array.

In order to get insights into the fast photoinduced processes occurring within the conjugate, pump-probe transient absorption measurements with femtosecond resolution were performed on **1·2PF₆** and its relevant models.

Two excitation wavelengths were chosen: 560 nm, where a selective population of the porphyrin singlet is achieved and 360 nm, where the acridinium units are prevalently excited (the peak at 262 nm of the acridinium is not experimentally accessible).

The time evolution of the transient spectrum of model **Zn-bP** upon excitation at 560 nm is reported in Figure 4(a). The initial spectrum with a positive band below 530 nm, ground state bleaching at 542 and 580 nm and stimulated emission at 640 nm evolves into a new spectrum with a positive maximum at 463 nm, with clear isosbestic points. The kinetics reflects the fluorescence lifetime of the molecule (the time profiles are reported in Figure S27), i.e. 2.3 ns; the final spectrum is thus attributed to the triplet state and the process is assigned to S1→T1 intersystem crossing.

The scenario is completely different for the conjugate **1·2PF₆** (Figure 4(b)). The end of pulse spectrum shows maxima at 480, 520, 620 and 662 nm, as well as bleaching bands at 545 and 586 nm. In the region 620–660 nm an ultrafast signal rise, of the order of the time resolution of the system, is observed. This spectrum quickly decays, with a lifetime of 0.65 ps (Figure S28a). The observed transient spectrum can be safely ascribed to the charge separated state P⁺–Ac[·] (P: porphyrin, Ac: acridinium), since the bands between 600 and 700 nm well resembles those reported for a Zn-porphyrin cation, [23] and bands at ca. 480 nm and 520 nm have been reported for the

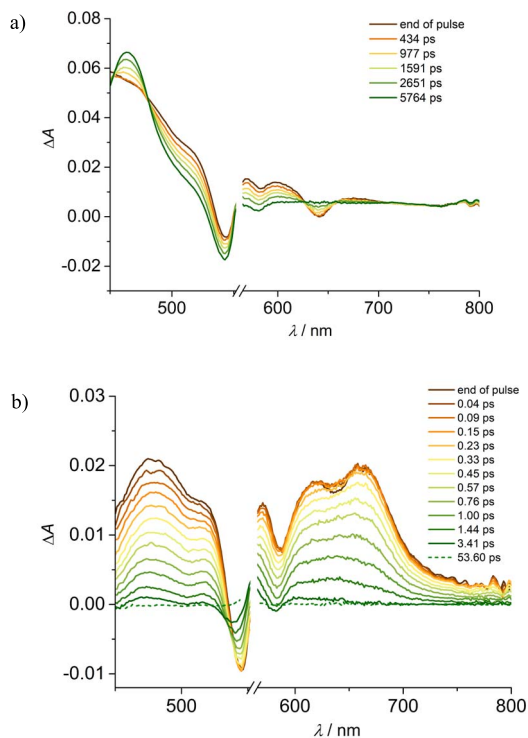


Figure 4. Transient absorbance of (a) **Zn-bP** and (b) **1·2PF₆** in CH₃CN at different delays. Excitation at 560 nm ($A_{560} = 0.1, 0.2$ cm optical path, 2 μ J/pulse).

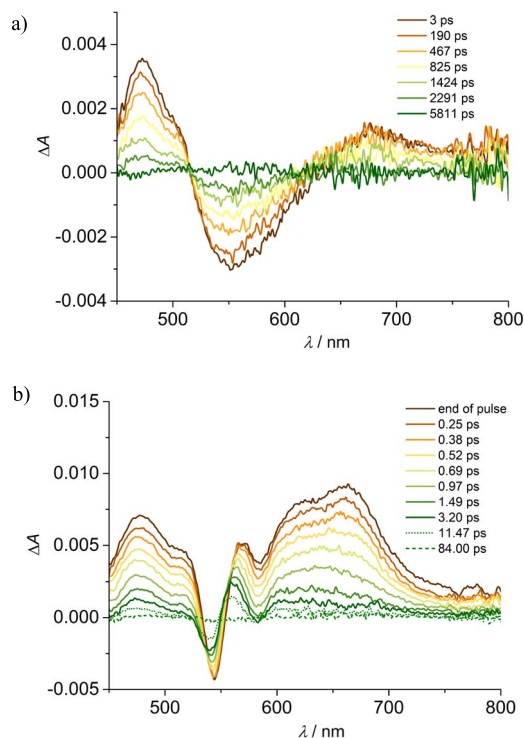


Figure 5. Transient absorbance of (a) **3·PF₆** and (b) **1·2PF₆** in CH₃CN at different delays. Excitation at 360 nm ($A_{360} = 0.2, 0.2$ cm optical path, 2 μ J/pulse).

reduced species of N-alkyl substituted acridinium compounds [14,15,24,25]. The singlet excited state of the porphyrin is thus depopulated in ca. 0.3 ps to yield the charge separated state, which in turn lives less than 1 ps. It can be noticed that the decay of the spectrum shows a second component, accounting for a very small fraction of the signal (ca. 2%), with a lifetime of ca. 32 ps (Figure S28b). This second component can be tentatively ascribed to a slower charge recombination occurring in a different conformation of the array, or deriving from another minimum of the first excited singlet potential energy surface. This is consistent with the molecular flexibility in the excited state highlighted by the theoretical results (see below).

Transient absorption analysis with excitation at 360 nm has been performed for **1·2PF₆** and models **3·PF₆** and **Zn-bP**. In model acridinium benzaldehyde, **3·PF₆**, the initial formation of a signal with a risetime of 1 ps, ascribable to vibrational relaxation,

is observed (Figure S29). The formed spectrum displays positive bands in the 450–510 nm and 630–800 nm regions, with maxima at 472 nm and 680 nm, and stimulated emission at 550 nm, red-shifted with respect to that detected from luminescence measurements due to the sum with the positive absorption bands. The signal decays with a lifetime of 1.6 ns, in good agreement with the fluorescence lifetime (Figures 5(a) and S30), and with defined isosbestic points, allowing to ascribe the process to S1→T1 intersystem crossing, even if the spectral features of the triplet are hardly detectable. **Zn-bP** shows a behaviour similar to that observed upon excitation at 560 nm, with intersystem crossing occurring in 2.3 ns, but preceded by an initial fast evolution of 1 ps, ascribable to internal conversion (Figures S31 and S32) [26].

The end of pulse spectrum of **1·2PF₆** does not present any of the spectral features of the singlet excited states absorption of the respective components,

but recall those observed upon excitation at 560 nm (Figure 5(b)) with clear features of the charge separated state. There is no evidence of signal formation, implying that the process, upon prevalent excitation of the acridinium component, occurs on an ultrafast scale (≤ 0.3 ps). The spectrum evolves quickly, almost disappearing with $\tau = 0.70$ ps. A minor component, accounting for ca. 5% of the decay and with a lifetime of 33 ps (Figures 5(b) and S33) is detected, in agreement with that observed upon excitation of the porphyrin unit.

The observed photoinduced electron transfer process is, indeed, thermodynamically allowed upon excitation of both the porphyrin ($\Delta G = -0.66$ eV) and the acridinium units ($\Delta G = -1.24$ eV), as indicated in Scheme 2 and, in the latter case, a higher energy gap accounts for the increased reaction rate, placing the reaction in normal Marcus region [27].

5. Computational studies

The structure of **1**·**2PF₆** was first optimized without any symmetry and revealed that the phenyl rings are orthogonal to the porphyrin rings (88°) and to the acridinium moieties (88°). Interestingly, the frontier orbitals are mainly composed of two sets of degenerated orbitals localized on the porphyrin fragment for the HOMOs and on the acridinium units for the LUMOs (Figure S34). This observation unambiguously confirms the interpretation of the electrochemical investigation for the anodic and cathodic process involving the oxidation of the porphyrin and the reduction of the acridinium moieties, respectively. It is worthwhile to note that no contribution from the phenyl rings linking the porphyrin and acridinium units was observed (see ESI). The theoretical absorption spectrum (Figure 6) is composed of two intense absorbing bands at 332 and 406 nm and two weak absorbing bands at 512 and 610 nm, matching the experimental optical transitions observed at 361, 411, 545 and 586 nm (Figure S17).

The nature of the electronic transitions of **1**·**2PF₆** is presented in Figure 7. The main band at 406 nm results from the contribution of three electronic transitions at 397, 406, and 408 nm corresponding to π - π^* excitations either centered on the porphyrin or on the acridinium cores (Figure S35). The band at 331 nm is attributed to two π - π^* transitions centered on the acridinium moieties exclusively. Finally, the

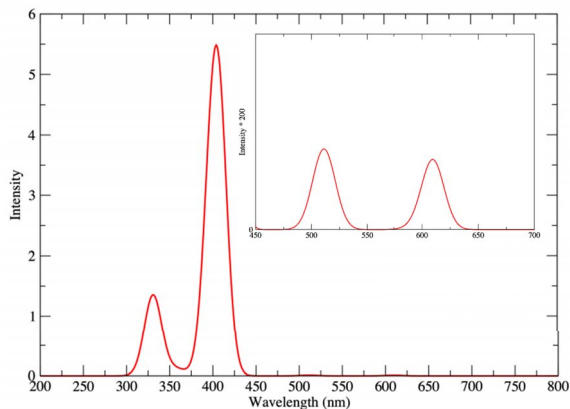


Figure 6. Theoretical absorption spectrum of **1**·**2PF₆** in CH_3CN .

low energy domain (Figure 6 inset) is governed by two π - π^* transitions centered on the porphyrin core at 512 and 510 nm respectively and by a charge transfer transition from the porphyrin to the acridinium core at 610 nm where the electron is delocalized over the two acridinium moieties. For this lowest excited singlet, two calculations were performed imposing a C_2 symmetry in order to preserve the delocalization and a broken symmetry. Already in the symmetric structure, the geometry underwent significant distortions upon relaxation. First, a flattening of the structures was observed resulting in the decrease of the dihedral angles between the fragments (porphyrin-phenyl angle = 59.9° and acridinium-phenyl angle = 77.2°) compared to ground state. In this C_2 optimized structure, this singlet emits at 693 nm thus corroborating the experimental data. Finally, breaking the symmetry leads to additional distortions and to localization of the electron in the excited state on one of the two acridiniums (Figure S37). This generates two minima separated by a very low barrier (302 cm^{-1}) between which the exciton freely oscillates, thus giving rise to an average symmetrical conformer.

6. Conclusion

A bisacridinium-Zn(II) porphyrin conjugate has been successfully synthesized in four steps using a novel acridinium benzaldehyde intermediate. Electrochemical characterization via cyclic voltammetry has revealed that the one-electron reduction of the

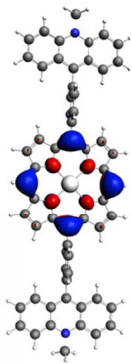
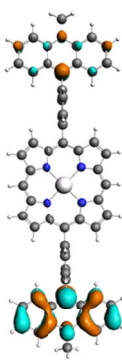
λ_{abs}	f_{osc}	%	Depleted orbital	Populated Orbital
610	$1.01 \cdot 10^{-2}$	100%		

Figure 7. Character of the singlet states generating the lowest energy absorption band in the absorption spectra of **1·2PF₆**.

two acridiniums occurs simultaneously, indicating limited communication between the two acridiniums. Furthermore, the observed two-electron oxidation of the porphyrin is supported by computational analysis showing two near degenerate HOMOs for the porphyrin. Comparison of the absorption features of the conjugate with the acridinium benzaldehyde intermediate and the Zn-bisphenyl porphyrin model confirms that the acridiniums are non-innocent moieties, with a complex interplay of porphyrin and acridinium centered transitions accounting for the apparent red-shift of both the Soret and the Q-bands of the porphyrin core, as shown by theoretical calculations. The almost complete quenching of the emission of both components in the conjugate was ascribed to an ultrafast photoinduced electron transfer process. Transient absorption analysis revealed the formation of a charge separated state within 0.3 ps, and its fast decay with a lifetime below 1 ps. In addition, an energy transfer process from the acridinium units to the porphyrin core was excluded. The interesting ultrafast photophysics of the conjugate opens new perspectives for the development of acridinium–porphyrin architectures.

Acknowledgements

We thank the European Union (H2020-MSCA-ITN grant “NOAH”, project ref. 765297) for financial support. Italian CNR (Project PHEEL) is also acknowledged.

Supplementary data

Supporting information for this article is available on the journal's website under <https://doi.org/10.5802/crchim.100> or from the author.

References

- [1] R. Paolesse, S. Nardis, D. Monti, M. Stefanelli, C. Di Natale, *Chem. Rev.*, 2017, **117**, 2517-2583.
- [2] M. Jurov, A. E. Schuckman, J. D. Batteas, C. M. Drain, *Coord. Chem. Rev.*, 2010, **254**, 2297-2310.
- [3] J. S. Lindsey, D. F. Bocian, *Acc. Chem. Res.*, 2011, **44**, 638-650.
- [4] M. Faustova, E. Nikolskaya, M. Sokol, M. Fomicheva, R. Petrov, N. Yabbarov, *ACS Appl. Bio Mater.*, 2020, **3**, 8146-8171.
- [5] I. Beletskaya, V. S. Tyurin, A. Y. Tsivadze, R. Guillard, C. Stern, *Chem. Rev.*, 2009, **109**, 1659-1713.
- [6] S. Durot, J. Taesch, V. Heitz, *Chem. Rev.*, 2014, **114**, 8542-8578.
- [7] W. Zhang, W. Lai, R. Cao, *Chem. Rev.*, 2017, **117**, 3717-3797.
- [8] C.-M. Che, V. K.-Y. Lo, C.-Y. Zhou, J.-S. Huang, *Chem. Soc. Rev.*, 2011, **40**, 1950-1975.
- [9] H.-P. Jacquot de Rouville, J. Hu, V. Heitz, *ChemPlusChem*, 2021, **86**, 110-129.
- [10] T. Mizutani, K. Wada, S. Kitagawa, *J. Am. Chem. Soc.*, 2001, **123**, 6459-6460.
- [11] K. Wada, T. Mizutani, H. Matsuoka, S. Kitagawa, *Chem. Eur. J.*, 2003, **9**, 2368-2380.
- [12] D. Kim, S. Lee, G. Gao, H. S. Kang, J. Ko, *J. Organomet. Chem.*, 2010, **695**, 111-119.
- [13] A. Chaudhary, S. P. Rath, *Chem. Eur. J.*, 2012, **18**, 7404-7417.
- [14] M. Tanaka, K. Ohkubo, C. P. Gros, R. Guillard, S. Fukuzumi, *J. Am. Chem. Soc.*, 2006, **128**, 14625-14633.
- [15] M. Tanaka, K. Ohkubo, C. P. Gros, R. Guillard, S. Fukuzumi, *ECS Trans.*, 2007, **2**, 167-176.
- [16] H. Kotani, K. Ohkubo, M. J. Crossley, S. Fukuzumi, *J. Am. Chem. Soc.*, 2011, **133**, 11092-11095.

- [17] J. S. Lindsey, *Acc. Chem. Res.*, 2010, **43**, 300-311.
- [18] H. Yi, L. Niu, S. Wang, T. Liu, A. K. Singh, A. Lei, *Org. Lett.*, 2017, **19**, 122-125.
- [19] L. A. Andronico, A. Quintavalla, M. Lombardo, M. Mirasoli, M. Guardigli, C. Trombini, A. Roda, *Chem. Eur. J.*, 2016, **22**, 18156-18168.
- [20] A. Nowak-Król, R. Plamont, G. Canard, J. A. Edzang, D. T. Gryko, T. S. Balaban, *Chem. Eur. J.*, 2015, **21**, 1488-1498.
- [21] N. W. Koper, S. A. Jonker, J. W. Verhoeven, C. Van Dijk, *Recl. Trav. Chim. Pays-Bas*, 1985, **104**, 296-302.
- [22] H. van Willigen, G. Jones, M. S. Farahat, *J. Phys. Chem.*, 1996, **100**, 3312-3316.
- [23] J. Fajer, D. C. Borg, A. Forman, D. Dolphin, R. H. Felton, *J. Am. Chem. Soc.*, 1970, **92**, 3451-3459.
- [24] S. Fukuzumi, K. Ohkubo, T. Suenobu, K. Kato, M. Fujitsuka, O. Ito, *J. Am. Chem. Soc.*, 2001, **123**, 8459-8467.
- [25] K. Ohkubo, K. Suga, K. Morikawa, S. Fukuzumi, *J. Am. Chem. Soc.*, 2003, **125**, 12850-12859.
- [26] A. Briš, P. Trošelj, D. Margetić, L. Flamigni, B. Ventura, *ChemPlusChem*, 2016, **81**, 985-994.
- [27] R. A. Marcus, *Angew. Chem. Int. Ed. Engl.*, 1993, **32**, 1111-1121.



MAPYRO: the French Fellowship of the Pyrrolic Macrocyclic Ring / *MAPYRO: la communauté française des macrocycles pyrroliques*

New fluorescent tetraphenylporphyrin-based dendrimers with alkene-linked fluorenyl antennae designed for oxygen sensitization

Dandan Yao^a, Limiao Shi^a, Zhipeng Sun^a, Mireille Blanchard-Desce^{*, b},
Olivier Mongin^{*, a}, Frédéric Paul^{*, a} and Christine O. Paul-Roth^{*, a}

^a Univ Rennes, INSA Rennes, CNRS, ISCR (Institut des Sciences Chimiques de Rennes) – UMR 6226, F-35000 Rennes, France

^b Université de Bordeaux, Institut des Sciences Moléculaires (CNRS UMR 5255), 33405 Talence, France

E-mails: ydd000@126.com (D. Yao), lmshi09@yahoo.com (L. Shi), sunzpciomp@126.com (Z. Sun), mireille.blanchard-desce@u-bordeaux.fr (M. Blanchard-Desce), olivier.mongin@univ-rennes1.fr (O. Mongin), frederic.paul@univ-rennes1.fr (F. Paul), christine.paul@univ-rennes1.fr, christine.paul@insa-rennes.fr (C. O. Paul-Roth)

Abstract. The design of porphyrin-based dendrimers featuring conjugated fluorenyl dendrons *via* alkene spacers allows evaluating the importance of the role of these spacers on the optical properties of interest. In the continuation of previous studies, a second-generation porphyrin-based dendrimer was synthesized and metalated by Zn(II) along with its known first-generation homologue. The targeted free-base porphyrin was obtained by repetitively cycling a Michaelis–Arbuzov reaction and a Horner–Wadsworth–Emmons reaction to construct the desired vinyl-containing dendrons. After metalation by Zn(II), *meso*-tetraphenylporphyrin-cored dendrimers with eight (**ZnTPP-D1**) and sixteen (**ZnTPP-D2**) fluorenyl arms at their periphery were eventually isolated. These species allow evaluating the influence of the central metal and of the 1,2-alkyne for 1,2-alkene exchange on fluorescence, oxygen photosensitization, and two-photon absorption. Such structure–property relationships are currently needed for the design of optimal dendrimeric photosensitizers allowing combined two-photon-based photodynamic therapy (2P-PDT) and imaging.

Keywords. Porphyrin, Fluorenyl, Fluorescence, Energy transfer, Double bond, Dendrimer, Photodynamic therapy.

Available online 30th July 2021

1. Introduction

There has been great interest in porphyrin systems because the peripheral substituents on the

macrocyclic core allows to significantly modulate the photophysical properties at will. Thus, light-harvesting compounds can be easily obtained by attaching four strongly absorbing energy-donor dendrons at the *meso* positions of the central porphyrin core which will play the role of peripheral

* Corresponding author.

“antenna” [1–3]. In this respect, Fréchet and coworkers [4–6] have reported porphyrin systems with fluorene-containing oligoether-type dendrons as efficient one- and two-photon light-harvesting units and demonstrated that such an “antenna effect” was facilitated in dendritic architectures *versus* linear architectures [5,6]. More recently, related star-shaped porphyrins with fully conjugated oligofluorene arms have also been reported by Bo and coworkers and shown to behave as a remarkable light-harvesting system [7–9].

In this context, we have previously reported the synthesis of porphyrin possessing four fluorenyl arms directly connected at the *meso*-positions. This compound (**TFP**; Figure 1a) [10,11] exhibited a high luminescence quantum yield (24%), demonstrating the good capacity of the fluorenyl units to enhance emission by increasing the radiative process [12]. Subsequently, we synthesized two series of substituted *meso*-porphyrin dendrimers with terminal fluorenyl arms, taking **TPP** as the central unit: (i) a non-conjugated family with flexible ether linkages [13–15] and, more recently, (ii) a conjugated family with rigid alkynyl linkages (Figure 1b) [16,17]. We could then show that these molecular architectures were promising models for the design of new biphotonic photosensitizers for theranostics, *i.e.*, allowing to perform photodynamic therapy [18,19] and fluorescence imaging after two-photon excitation [16,17]. Due to the practical advantages of two-photon excitation, this field has attracted attention and is rapidly expanding; several such porphyrin-based photosensitizers have been reported to date [20–26]. In order to gain additional insight about the potential of TPP-cored dendrimers such as **TPP-T1** or **TPP-T2** in this field, we have started systematically investigating the impact of various structural changes taking place in the peripheral light-harvesting antenna on the photophysical properties of these systems.

Given that 1,2-alkene spacers are known to promote electronic communication better than 1,2-alkyne ones [27], we recently started exploring the optical properties of related dendrimers featuring alkene linkages. However, this was exclusively done for the *first-generation* dendrimer **TPP-D1** (Figure 1c; $M = 2H$) resulting in a significant improvement in the linear and nonlinear optical properties *versus* **TPP-T1** [28]. This statement prompted us to test higher generation dendrimers of this kind.

Accordingly, we now report our efforts to isolate the *second-generation* dendrimer **TPP-D2** and the corresponding metalated species **ZnTPP-D1** and **ZnTPP-D2**. Subsequently, their linear and nonlinear optical properties of interest will be disclosed as well as evidence for the very efficient energy-transfer process taking place from the conjugated dendrons to the porphyrin core in these new species. These data will then be compared to those of their known alkyne-containing analogs (or **T** series; Figure 1b).

2. Results and discussion

2.1. Synthesis and characterization

This new family of dendrimers was prepared by the synthesis of the required dendrons (**D1-PhCHO** and **D2-PhCHO**), followed by their condensation with pyrrole to give the desired free-base porphyrins as intermediates, which were then metalated by Zn(II) to give the final dendrimers **ZnTPP-D1** and **ZnTPP-D2**.

2.1.1. Dendron synthesis

The synthesis of the two generations of vinyl-bridged aldehyde-terminated dendrons **D1-PhCHO** and **D2-PhCH** is described in Scheme 1. First, commercial 1-bromo-3,5-bis(methyl)benzene was halogenated with benzyl by *N*-bromosuccinimide (NBS) using azobis-isobutyronitrile (AIBN) as the radical initiator. Given that this bromination takes place usually non-selectively [29–32], the reaction conditions were optimized (temperature, time, and solvent). The resulting conditions mainly gave the desired dibrominated product along with mono- and tribrominated byproducts. The former byproduct could be isolated by chromatography (heptane), while the latter could not be fully separated from the targeted dibrominated product (ratio tri/di of 1/4 by 1H NMR). In the next step, this mixture containing 49% of the desired product was reacted directly with excess of $P(OEt)_3$ under reflux following a Michaelis–Arbuzov [29–31] protocol. The desired product **3** and its bromo-substituted byproduct were both formed and were subsequently separated by chromatography (Scheme 1). The unwanted byproduct could be easily eluted using CH_2Cl_2 , while the target product **3** was collected using ethyl acetate as a colorless oil in 83% yield. After a subsequent Horner–Wadsworth–Emmons (HWE) reaction [29–31], the compound **3**

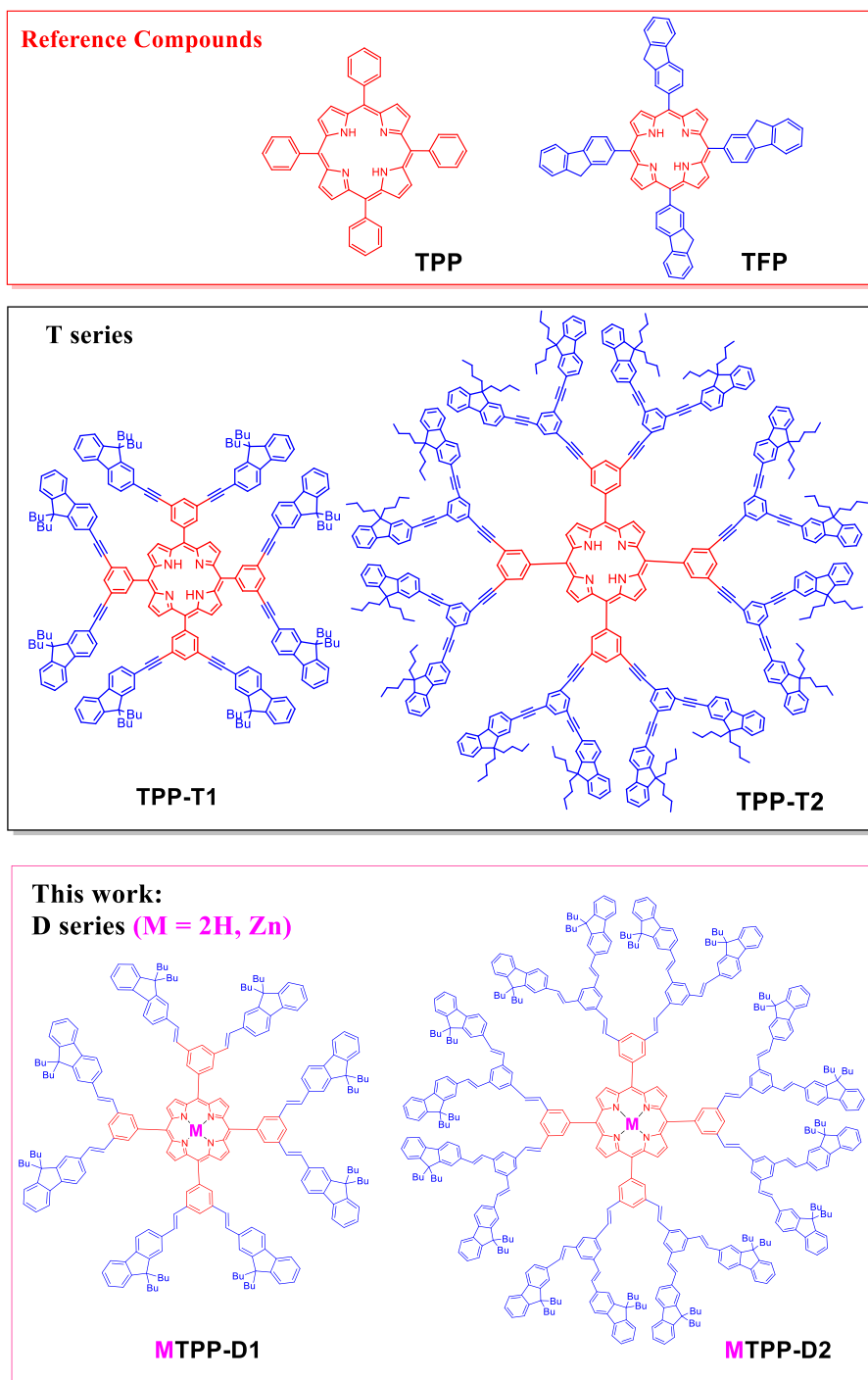
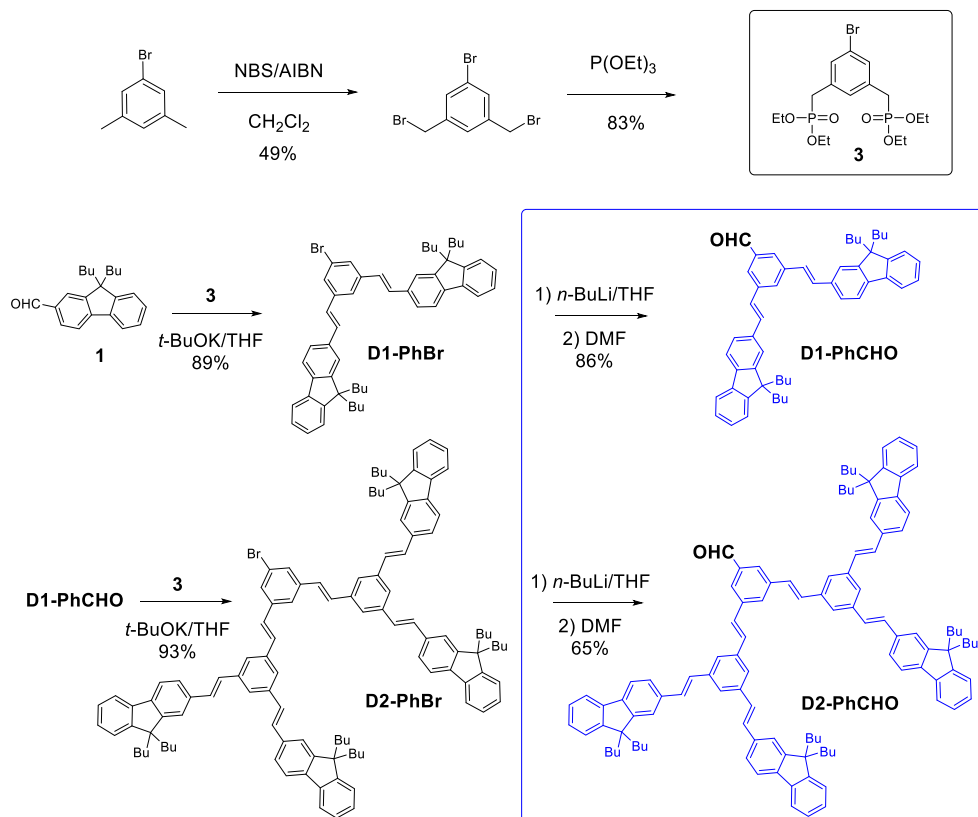


Figure 1. (a) Reference compounds; (b) previously reported alkyne-bridged free-base porphyrin dendrimers (**T series**) based on TPP (TPP-T1 and TPP-T2); (c) new porphyrin dendrimers (**D series**) based on TPP (MTPP-D1 and MTPP-D2; M = 2H, Zn).



Scheme 1. Synthetic routes for alkene-bridged dendrons **D1-PhCHO** [28] and **D2-PhCHO**.

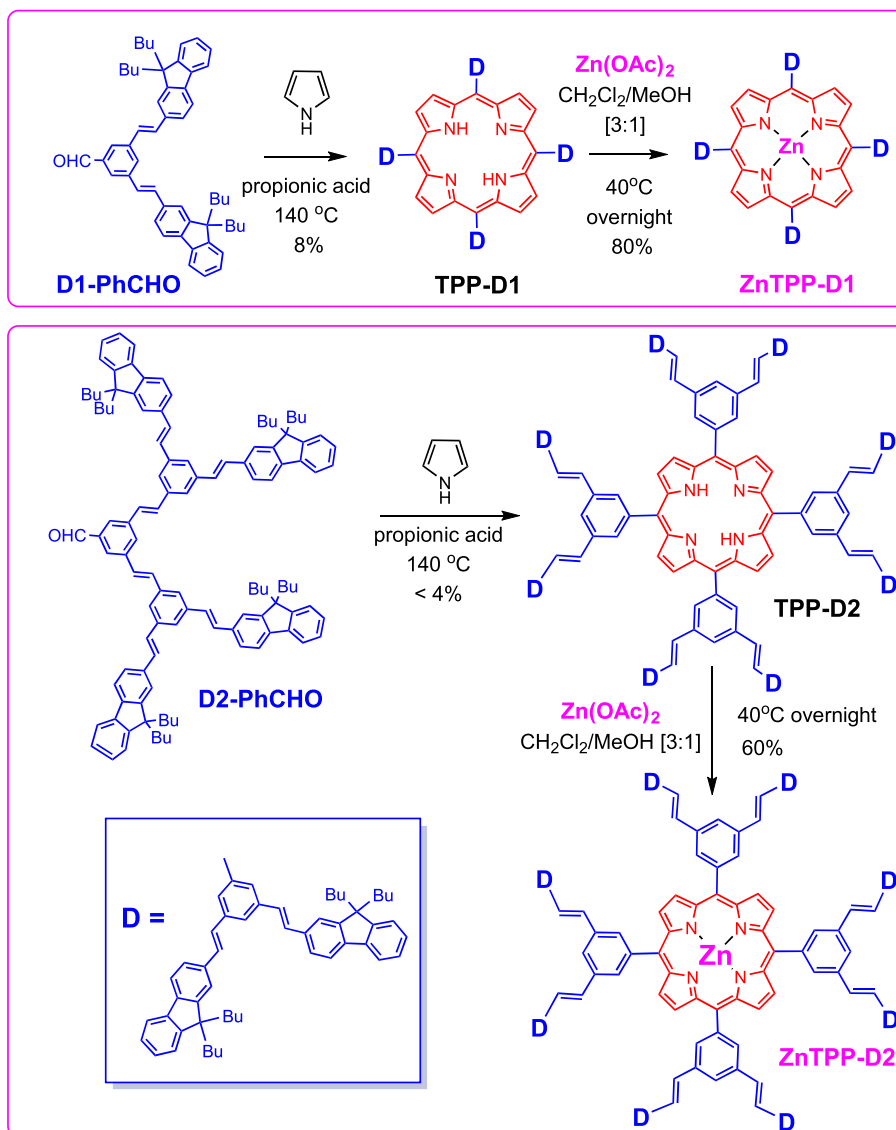
reacts with the previously prepared aldehyde **1** [16] in the presence of *t*-BuOK/THF to give the double-bonded precursor **D1-PhBr** in 89% yield. The aldehyde **D1-PhCHO** can then be obtained in two steps from this product in 86% yield. Repetition of the HWE reaction [29–31] between this new aldehyde and **3** gave access to the *second-generation* intermediate **D2-PhBr** in 93% yield, and subsequently to the corresponding **D2-PhCHO** dendron in 65% yield (Scheme 1).

2.1.2. Porphyrin synthesis

Two synthetic methods are most often used to synthesize porphyrins: the Adler–Longo [33,34] or the Lindsey reaction [35]. Both are efficient for synthesizing porphyrins substituted at their *meso* positions. Given that the *first-generation* dendrimer **TPP-D1** was previously isolated using the Adler–Longo approach [28], these reaction conditions were used again to synthesize **TPP-D2**. However, this compound could not be isolated in pure form even

after several purification attempts by chromatography and subsequent recrystallizations (CHCl₃ and MeOH), the yield of crude **TPP-D2** in the isolated solid being below 4%. Fortunately, all these porphyrin dendrimers have good solubilities in common organic solvents, allowing their easy metalation, and this approach provided a way to access the pure zinc complex from the mixture in the case of **ZnTPP-D2** (Scheme 2). Thus, the corresponding zinc complex **ZnTPP-D1** was formed at 40 °C overnight from **TPP-D2** using Zn(OAc)₂ in CH₂Cl₂/MeOH and isolated pure in 60% yield (Scheme 2). Using similar conditions for metalation, **ZnTPP-D1** was isolated in 80% yield from **TPP-D1**.

From a purely synthetic standpoint, the isolated yields in alkene-bridged dendrimers (**D**-type series; Figure 1c) were always lower than those of their alkyne-bridged analogs (**T**-type series; Figure 1b), although rigorously similar reaction conditions have been used (the isolated yields of **TPP-T1** and **TPP-T2** were 18% and 13%, respectively [16,17]), making the



Scheme 2. Synthesis of vinyl-bridged porphyrin dendrimers (**D** series) based on TPP-cored porphyrin (TPP-D1 and TPP-D2) and corresponding zinc(II) complexes (ZnTPP-D1 and ZnTPP-D2).

D-type series dendrimers more challenging to obtain *via* the Adler–Longo approach [16,17,36].

2.1.3. ¹H NMR analysis

The aldehyde dendrons **D1-PhCHO** and **D2-PhCHO**, and the corresponding dendrimers, *i.e.*, the free-base and metalated porphyrins **MTPP-D1** and **MTPP-D2**, were characterized by ¹H NMR analysis (Figures 2–4). Figure 2 shows the full ¹H NMR spectra of the dendrons compared to those of their analogs

with triple bonds (**T1-PhCHO** and **T2-PhCHO**). They all show three diagnostic signatures: (i) the aldehyde proton as a singlet, around 10 ppm; (ii) the aromatic protons located as multiplets, in region 7–8 ppm, belonging to protons of phenyl and fluorenyl, partially identified; (iii) four groups of alkyl protons H_{a,b,c,d} located at 0.5–2.1 ppm that are assigned to the *n*-butyl chains of fluorenyl. We can particularly notice that for the double-bonded dendrons **D1-PhCHO** and **D2-PhCHO**, we observe four additional

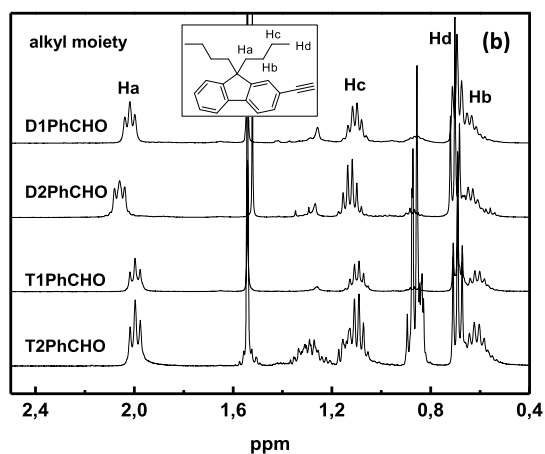
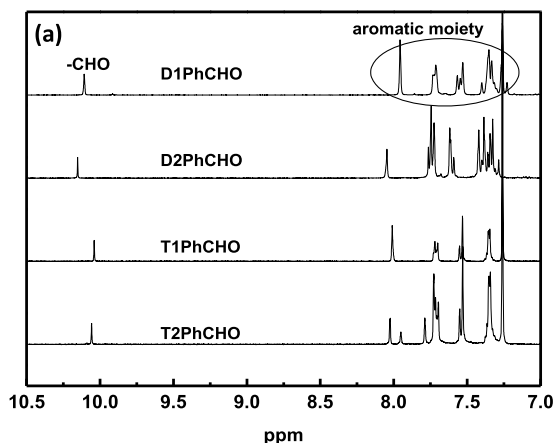


Figure 2. Aromatic (a) and Alkyl (b) moieties ^1H NMR spectra (400 MHz) of **D**-series dendrons **D1-PhCHO** and **D2-PhCHO** compared to reported **T**-series dendrons **T1-PhCHO** and **T2-PhCHO** in CDCl_3 [16,17].

alkene protons coming out as a broad peak around 7.18–7.40 ppm.

The full ^1H NMR spectra in CDCl_3 of the corresponding free-base porphyrin **TPP-D1** (Figure 3) shows four diagnostic signatures: (i) the β -pyrrolic protons of the porphyrin core (H_β) around 9 ppm, (ii) the aromatic protons around 7.3–8.4 ppm, (iii) the alkyl protons of the various butyl chains around 2.2–0.5 ppm, and (iv) the NH protons of porphyrin cavity around -2.6 ppm. For **TPP-D1**, as for reported **TPP-T1** and **TPP-T2** [16,17], we observe eight protons H_β of porphyrin ring located around 9 ppm. For aromatic and vinylic protons (around 7.2–8.4 ppm),

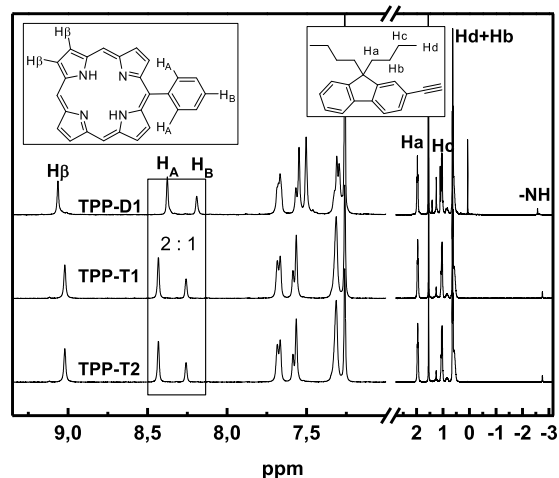


Figure 3. Full ^1H NMR spectra (400 MHz) of the free-base TPP-cored dendrimers **TPP-D1**, **TPP-T1**, and **TPP-T2** in CDCl_3 .

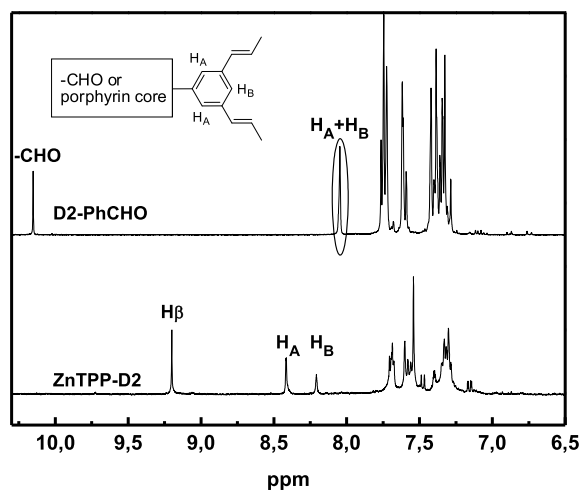


Figure 4. Partial ^1H NMR spectra (400 MHz) of the dendron **D2-PhCHO** and of the corresponding zinc(II) complex **ZnTPP-D2** in CDCl_3 .

only some of them can be easily assigned like H_A and H_B . Again, the vinyl protons of **TPP-D1** give rise to a broad peak around 7.2–7.3 ppm. For all these dendrimers, the *n*-butyl protons ($\text{H}_{\text{a,b,c,d}}$) are simply assigned to four groups of signals located at 0.5–2.1 ppm as for the corresponding dendrons. In contrast, for the larger dendrimer **TPP-D2**, a ^1H NMR spectrum with broad signals was obtained (see ESI)

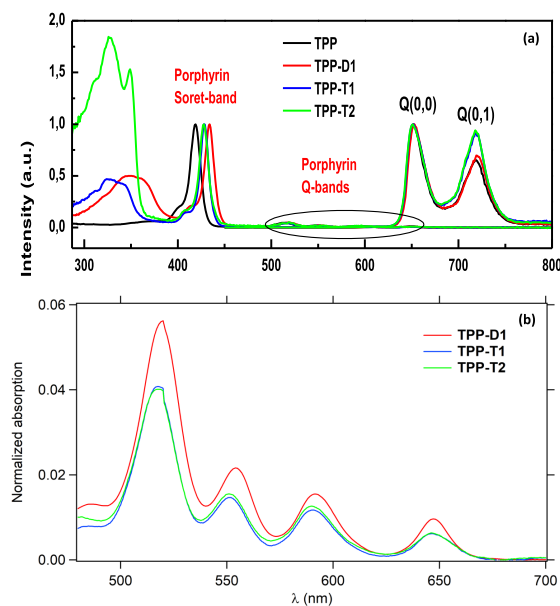


Figure 5. Normalized absorption and emission spectra of selected TPP-cored dendrimers (**TPP-D1**, **TPP-T1**, and **TPP-T2**) compared to reference **TPP** in toluene (a). Detail of the Q-bands of **TPP-D1**, **TPP-T1**, and **TPP-T2** (b).

and only for the corresponding zinc(II) complex **ZnTPP-D2** the spectrum was well resolved (Figure 4). Some characteristic signals are also readily identified; (i) eight protons H_{β} of porphyrin ring located around 9 ppm, (ii) H_A and H_B in the phenyl arms. However, most of the aromatic and vinylic protons overlap (7.2–8.4 ppm) because of the larger molecular structure.

2.2. Photophysical properties

UV-visible absorption and emission spectra, after excitation in the Soret band [37,38], were recorded for the isolated dendrimers at room temperature (Table 1 and Figures 5 and 6). The free-base tetraphenylporphyrin (**TPP**; Figure 1a) and the corresponding zinc complex (**ZnTPP**) were chosen as references compounds. Their two-photon oxygen-photosensitizing yields were subsequently evaluated and compared to those of their alkyne analogs (**TPP-T1** and **TPP-T2**) to analyze the impact of this structural modification (Tables 2–3).

For the free-base porphyrin series, all absorption spectra are typical of porphyrin derivatives with an

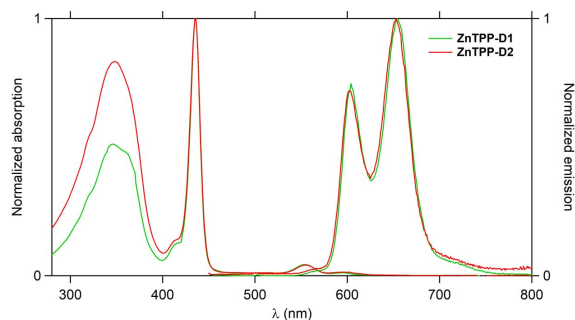


Figure 6. Absorption and emission spectra of **ZnTPP-D2** compared to **ZnTPP-D1** in CH_2Cl_2 at 20 °C.

intense Soret band around 430 nm and four Q-bands in the 520–650 nm range [37]. Compared to **TPP**, the dendrimers **TPP-D1**, **TPP-T1**, and **TPP-T2** present an additional absorption around 300–400 nm, corresponding to the conjugated fluorenyl dendrons. This band is almost of similar intensity for **TPP-D1** and **TPP-T1**, most likely in reason of their identical terminal fluorenyl number; however, a red shift is observed for **TPP-D1** compared to **TPP-T1**, likely due to the improved conjugation between core and arms in the former compound. Concerning the Soret band, the vinyl-bridged dendrimer **TPP-D1** presents also a larger red shift (15 nm) than its alkyne analog **TPP-T1** (9 nm) *versus* the Soret band of the reference **TPP**, which reflect the extension of the porphyrin π manifold [40] through conjugation with the peripheral arms at the *meso* positions.

The corresponding zinc complexes **ZnTPP-D1** and **ZnTPP-D2** exhibit characteristic changes in their electronic spectra compared to those of the corresponding free-base porphyrins **TPP-D1** and **TPP-D2** [37,41]. Only two Q-band absorption are now observed, around 552 nm and 635 nm, due to the symmetry change from D_{2h} to D_{4h} symmetry upon metalation and an intense Soret band around 435 nm (Table 1 and Figure 6). An additional broad band is also observed in UV range (346 nm) which corresponds to π – π^* absorption of the fluorenyl chromophores. This UV absorption is weaker for the *first-generation* zinc(II) complex (**ZnTPP-D1**) than for the higher generation dendrimer (**ZnTPP-D2**) due to the smaller number (eight *versus* sixteen) of fluorenyl groups present in the peripheral arms.

Upon excitation in their Soret band, all these compounds exhibit the characteristic porphyrin

Table 1. Photophysical properties of the new dendrimers **TPP-D1**, **ZnTPP-D1**, **ZnTPP-D2** compared to their alkynyl-bridged parents **TPP-T1** and **TPP-T2** and to **TPP** reference at 20 °C [16,17,36]

	Absorption ^a (nm)			Emission ^a		Quantum yield ^b Φ_F (%)
	Dendron	Soret band	Q-bands	Ex = Soret band Q(0,0)	Q(0,1)	
TPP	—	419	514, 548, 590, 649	652	719	11
ZnTPP	—	421	556, 603	603	650	3
TPP-D1	349	434	518, 552, 593, 649	652	719	13
ZnTPP-D1^c	346	436	554, 594	604	654	3
ZnTPP-D2^c	348	435	555, 595	602	652	6
TPP-T1	325	428	518, 552, 593, 649	652	719	12
TPP-T2	327, 349	428	518, 552, 593, 649	652	719	13

^aUnless precised, experiments were achieved in toluene (HPLC level) with the UV-visible absorption region from 287 to 800 nm and emission region from 450 to 800 nm.

^bUnless precised, experiments for fluorescence quantum yields were achieved in toluene (HPLC level) using TPP ($\Phi = 11\%$) as standard, by Soret-band excitation [12].

^cData obtained in CH₂Cl₂ (HPLC level).

Table 2. Two-photon absorption and brightness properties of **D** dendrimers and related **T** compounds in dichloromethane

Compound	Fluorenes/ porphyrin	$\lambda_{\text{TPA}}^{\text{max}}$ (nm)	σ_2^{max} (GM) ^a	$\Phi_F \cdot \sigma_2^{\text{max}}$ (GM) ^b	Two-photon brightness enhancement factor ^c
TPP	0	790	12 ^d	1.3	1
TPP-D1	8	790	280	36	28
ZnTPP-D1	8	790	260	8	6
ZnTPP-D2	16	810	450	27	20
TPP-T1	8	790	200	24	18
TPP-T2	16	790	290	38	29

^aIntrinsic TPA cross-sections measured in 10⁻⁴ M dichloromethane solutions by TPEF in the femtosecond regime; a fully quadratic dependence of the fluorescence intensity on the excitation power is observed and TPA responses are fully non-resonant.

^bMaximum two-photon brightness in dichloromethane.

^cEnhancement factor: $\Phi_F \sigma_2^{\text{max}}$ of the compound normalized to that of **TPP**.

^dData from lit [39].

emission peaks Q(0,0) and Q(0,1) [12,40]. After normalizing their emission spectra on their Q(0,0) peaks, these compounds exhibit two emission peaks at similar wavelengths, but with different intensities (Figure 5). Compared to **TPP**, the Q(0,1) band of all dendrimers does not change in intensity for **TPP-D1** but increases for **TPP-T1** and **TPP-T2**. The emission spectra of zinc(II) porphyrin complexes usually

consist of three sub-bands assigned to a vibronic progression from a Q state: Q(0,0), Q(0,1), and weak Q(0,2), the last one, near 720 nm being usually too weak to be observed [11]. Presently, for **ZnTPP-D1** and **ZnTPP-D2**, the emission spectra exhibit the two expected Q-bands around 603 nm and 653 nm (Figure 6), the blue shift of these bands compared to the corresponding free bases being ascribable to the

Table 3. Oxygen sensitization properties of double-bonded porphyrin dendrimers and related triple-bonded compounds

Compound	Φ_{Δ}^a (%)	$\Phi_{\Delta} \cdot \sigma_2^{\max}$ (GM) ^b	Two-photon excited oxygen sensitization enhancement factor ^c
TPP	60	7.2	1
TPP-D1	64	177	25
ZnTPP-D1	59	153	21
ZnTPP-D2	55	248	34
TPP-T1	59	118	16
TPP-T2	56	162	23

^aSinglet oxygen production quantum yield determined relative to **TPP** in dichloromethane (Φ_{Δ} [TPP] = 0.60).

^b $\Phi_{\Delta} \sigma_2^{\max}$: figure of merit of the two-photon excited singlet oxygen production in dichloromethane.

^cEnhancement factor: $\Phi_{\Delta} \sigma_2^{\max}$ of the compound normalized to that of **TPP**.

metal coordination. The quantum yields (Φ_F) were then measured for all these compounds (Table 1). While the free-base porphyrin dendrimers have similar quantum yields ($\Phi_F = 12$ –13%) than **TPP** ($\Phi_F = 11\%$), these values drop drastically (3–6%) when a metal like zinc(II) is introduced in the porphyrin cavity, as also observed for the reference **ZnTPP**.

The existence of an energy-transfer (ET) process from the peripheral 2-fluorenyl donors toward the central porphyrin acceptor core was subsequently studied. The emission spectra were measured from 450 to 800 nm, using two excitation wavelengths: the dendron absorption (325–351 nm) and the Soret-band absorption (419–434 nm). As expected, all dendrimers showed exclusive Q-band emission around 650–720 nm, in both cases, with no residual dendron emission (usually observed around 400 nm). This suggests that the peripheral fluorenyl groups transfer their energy very efficiently to the porphyrin core, given that any dendron emission is totally quenched (SI Figure S14). This very efficient energy transfer most likely corresponds to a so-called “through-bond” energy-transfer process (TBET) [42]. Thanks to this very efficient “antenna effect”, the dendron absorption band, when intense (as in **ZnTPP-D2**), might be efficiently used for exciting these compounds.

2.3. Two-photon absorption

As these dendrimers exhibit good fluorescence properties, their intrinsic two-photon absorption cross-

sections were determined by two-photon excited fluorescence (TPEF) in CH_2Cl_2 . Measurements were performed with 10^{-4} M solutions, using a mode-locked Ti:sapphire laser delivering femtosecond pulses, following the experimental protocol described by Xu and Webb [43]. A fully quadratic dependence of the fluorescence intensity on the excitation power was observed for each sample at all the wavelengths of the spectra (790–920 nm), indicating that the cross-sections determined are only due to TPA. A significant increase of their TPA cross-sections compared to that of **TPP** (12 GM at 790 nm) was observed for all porphyrins possessing fluorenyl dendrons (Table 2 and Figure 7). Comparison between the free-base dendrimers **TPP-D1** and **TPP-T1** reveals that replacing triple bonds with double bonds in the peripheral dendrons leads to a significant increase of the TPA cross-sections.

The zinc complexes of the **D**-type series (**ZnTPP-D1** and **ZnTPP-D2**) also exhibit high TPA cross-sections ($\sigma_2 = 260$ and 450 GM, respectively) at 790 nm, **ZnTPP-D2** being the best two-photon absorber of the series of compounds presently investigated. From the comparison between **TPP-D1** and **ZnTPP-D1**, metalation by Zn(II) does not result in a significant change in cross-section at this wavelength and induces a slight decrease of σ_2 at higher wavelengths compared to the corresponding free-base porphyrin. This statement suggests that the cross-section of the missing **TPP-D2** free-base porphyrin would be similar or slightly above that of **ZnTPP-D2**

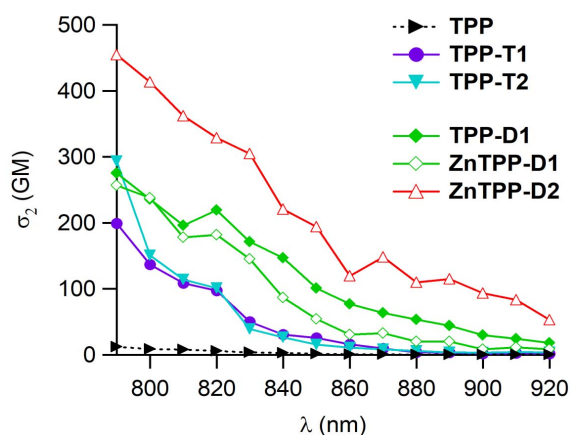


Figure 7. Two-photon excitation spectra of **D** dendrimers **TPP-D1**, **ZnTPP-D1**, and **ZnTPP-D2** and comparison with related **T** compounds **TPP-T1**, **TPP-T2**, and reference **TPP** in dichloromethane.

in the 790–920 nm range. In this respect, the clear enhancement of σ_2 observed for **ZnTPP-D2** relative to **ZnTPP-D1** is particularly remarkable. First, it reveals a more pronounced structural difference in two-photon cross-sections for the **D**-type series than for the **T**-type series, in favor of the largest dendrimers. Then it suggests that the free-base dendrimer **TPP-D2** would be a better two-photon absorber than its **TPP-T2** analog in the investigated wavelength range.

The two-photon brightness ($\sigma_2 \cdot \Phi_F$) is a figure of merit allowing the evaluation of the potential of two-photon absorbers for fluorescence imaging. For the zinc complexes, any change in σ_2 is combined with a strong decrease in Φ_F leading to a decrease of this figure of merit for **ZnTPP-D1** relative to that of its free-base analog **TPP-D1**, which is the highest of the compound presently discussed. The **ZnTPP-D2** dendrimer still exhibits an interesting two-photon brightness which is enhanced more than 20 times compared to **TPP** used as reference. Among free-base porphyrins, the two-photon brightness of **TPP-D1** is also significantly higher than that of its analog **TPP-T1**, revealing the positive impact of replacing triple bond by double bonds in the peripheral dendrons for imaging purposes.

The oxygen-photosensitizing properties of these dendrimers were also studied. Their quantum yields of singlet oxygen generation (Φ_Δ) were determined

and compared to those of analogous **T** dendrimers and **TPP** used as reference (Table 3). All these dendrimers exhibit values comprised between 0.55 and 0.64, comparable to that of reference **TPP** (0.60). Interestingly, the free-base dendrimer **TPP-D1** shows the highest value $\Phi_\Delta = 64\%$, whereas the two zinc complexes **ZnTPP-D1** and **ZnTPP-D2** show the lowest ones (59% and 55%, respectively). As previously noticed for **T**-type dendrimers [16,17,36], the increase in fluorescence quantum yield of the new free-base dendrimer **TPP-D1** relative to **TPP** is not obtained at the expense of the singlet oxygen production.

In combination with the notable increase of the TPA cross-sections of the dendrimer **TPP-D1** compared to its **TPP-T1** analog, significant enhancements of the figure of merit for the two-photon excited oxygen sensitization ($\Phi_\Delta \cdot \sigma_2^{\text{max}} = 177 \text{ GM}$) can be achieved. For the zinc complexes, this value goes up to 153 GM for **ZnTPP-D1** and even to 248 GM for larger **ZnTPP-D2**. The free-base **TPP-D1** dendrimer exhibits a clearly higher enhancement factor than its **T**-type analog, in relation with its higher σ_2 and its slightly increased Φ_Δ . This compound, easy to synthesize, appears therefore particularly promising for two-photon photodynamic therapy, and, considering its TPEF properties, also for theranostic applications provided it can be made water-soluble by proper functionalization. It should be emphasized that other porphyrin-based systems with more efficient conjugation between the sub-chromophoric units have often been shown to exhibit higher TPA cross-sections, but these are generally accompanied by strong modifications of their other photophysical properties such as the red shift of their linear absorption range [24,44–51], which somewhat limits their interest for theranostics. Indeed, most often these highly efficient two-photon absorbers exhibit a modest to negligible fluorescence or some interfering residual one-photon absorption above 800 nm, which leads to the loss of the 3D resolution. In contrast, the dendrimers presently reported, with a more restricted π -conjugation between the dendrons and the porphyrin core,¹ exhibit an improved

¹There is a large dihedral angle between the *meso*-aryl substituent and the macrocycle, which is more than 60° in the case of **TPP**, see [52].

trade-off [16,17,36,53] between intrinsic TPA, fluorescence, and photosensitizing properties.

3. Experimental section

3.1. General

Unless otherwise stated, all solvents used in reactions were distilled using common purification protocols [54], except DMF and $^i\text{Pr}_2\text{NH}$, which were dried on molecular sieves (3 Å). All chromatographic separations were effected on silica gel (40–60 μ , 60 Å). ^1H and ^{13}C NMR spectra were recorded on BRUKER Ascend 400 and 500 at 298 K. The chemical shifts are referenced to internal tetramethylsilane. High-resolution mass spectra were recorded on Bruker MicrOTOF-Q II in ESI positive mode in dried solvent at CRMPO in Rennes. Reagents were purchased from commercial suppliers and used as received. Element analyses were collected on a Microanalyser Flash EA1112. UV-visible absorption and photoluminescence spectroscopy measurements for all porphyrin dendrimers in solution were performed on Edinburg FLS920 Fluorimeter (Xe900) and BIO-TEK instrument UVIKON XL spectrometer at room temperature. Toluene and dichloromethane for spectral analysis were HPLC grade.

3.2. Dendron synthesis and characterization

The two dendrons **D1-PhCHO** and **D2-PhCHO** were obtained after a multistep synthesis from the brominated 1-bromo-3,5-xylene precursors and the corresponding 2-fluorenylaldehyde *via* Horner-Wadsworth–Emmons reactions followed by carbonylation using butyllithium and DMF.

1-bromo-3,5-bis(bromomethyl)benzene. Commercial 1-bromo-3,5-xylene (5.0 g, 3.67 mL, 27.02 mmol, 1 eq) was added into CH_2Cl_2 (100 mL, distilled), together with NBS (9.6 g, 54.04 mmol, 2 eq) and AIBN (220 mg, 1.35 mmol, 0.05 eq). The mixture was stirred for 30 min at room temperature, and then refluxed for 30 h. Then cooled in ice-water bath and filtered, washing residue with heptane. The solvents were evaporated and the residue was further purified by chromatography (heptane), collecting the target product (4.56 g, 49% yield) admixed with 1-bromo-3-bromomethyl-5-methylbenzene (20%) as white powder, as well as pure 1-bromo-3-bromomethyl-

5-methylbenzene (3.55 g) and 1-bromo-3-(bromomethyl)-5-(dibromomethyl)benzene (1.4 g). ^1H NMR (400 MHz, CDCl_3 , ppm): δ 7.47 (s, 2H), 7.34 (s, 1H), 4.41 (s, 4H).

Tetraethyl (5-bromo-1,3-phenylene)bis (methylene)diphosphonate (3). In a flask, the previously isolated [4:1] mixture of 1-bromo-3,5-bromomethyl-benzene and 1-bromo-3-bromomethyl-5-methylbenzene (2.4 g, 7 mmol, 1 eq) and $\text{P}(\text{OEt})_3$ (2.4 mL, 14 mmol, 2 eq) were added, respectively. The mixture was refluxed for 4 h at 140 °C. The excess of $\text{P}(\text{OEt})_3$ was removed under reduced pressure. Then the title product was purified by chromatography using CH_2Cl_2 to remove other byproducts and then collected by ethyl acetate, giving a colorless oil (2.66 g, 83% yield). ^1H NMR (400 MHz, CDCl_3 , ppm): δ 7.34 (s, 2H), 7.16 (s, 1H), 4.07–4.00 (m, 8H), 3.08 (d, $J = 22.0$ Hz, 4H), 1.26 (t, $J = 7.0$ Hz, 12 H).

Intermediate D1-PhBr. In a Schlenk tube, fluorenylaldehyde **1** (1.69 g, 5.51 mmol, 2.2 eq) and previously obtained **3** (1.15 g, 2.51 mmol, 1 eq) were added, then THF (100 mL, dried) was injected. After cooling the Schlenk with an ice-water bath (0 °C), *t*-BuOK (1.20 g, 10.69 mmol, 4.4 eq) was added under Argon and the reaction was kept stirring for 1 h at 0 °C. The bath was removed, a saturated NH_4Cl solution (aq) added and the resulting solution extracted with ethyl acetate. After evaporating the solvents, it was further purified by chromatography (CH_2Cl_2 /heptane [1:10]), giving **D1-PhBr** as a white powder (1.7 g, 89% yield). ^1H NMR (400 MHz, CDCl_3 , ppm): δ 7.71 (d, $J = 7.6$ Hz, 4H), 7.61 (s, 1H), 7.60 (s, 2H), 7.52 (d, $J = 8.4$ Hz, 2H), 7.50 (s, 2H), 7.37–7.31 (m, 6H), 7.27 (d, $J = 16.0$ Hz, 2H), 7.12 (d, $J = 16.4$ Hz, 2H), 2.01 (t, $J = 8.0$ Hz, 8H), 1.15–1.06 (m, 8 H), 0.71–0.58 (m, 20H).

Dendron D1-PhCHO. In a Schlenk tube, **D1-PhBr** (720 mg, 0.94 mmol, 1 eq) was dissolved in THF (60 mL) and *n*-BuLi (0.59 mL, 0.94 mmol, 1.6 M, 1 eq) was added dropwise at –78 °C during 15 min. The reaction was stirred for additional 40 min at low temperature. Then DMF (1 mL, dried) was added and stirring was continued for 1 h at –78 °C. The bath was removed, a saturated NH_4Cl solution (aq) added and the resulting solution extracted with ethyl acetate. After evaporating the solvents, it was further purified by chromatography (CH_2Cl_2 /heptane [1:5]), giving **D1-PhCHO** as a light-yellow powder (580 mg, 86% yield).

^1H NMR (400 MHz, CDCl_3 , ppm): δ 10.11 (s, 1H), 7.96 (s, 3H), 7.73–7.71 (m, 4H), 7.56 (d, $J = 8.0$ Hz, 2H), 7.53 (s, 2H), 7.40–7.23 (m, 10H), 2.02 (t, $J = 8.0$ Hz, 8H), 1.15–1.06 (m, 8 H), 0.71–0.56 (m, 20H). HRMS-ESI: m/z calcd for $\text{C}_{53}\text{H}_{58}\text{O}$: 710.44822 $[\text{M}]^+$; found 710.4481.

Intermediate D2-PhBr. This synthesis is a classical procedure similar to that previously used for **D1-PhBr**. The purification was completed by chromatography (heptane/ CH_2Cl_2 [10:1]), providing **D2-PhBr** as a white powder (93% yield). ^1H NMR (400 MHz, CDCl_3 , ppm): δ 7.72–7.71 (m, 10H), 7.64 (s, 7H), 7.57 (d, $J = 8.0$ Hz, 4H), 7.55 (s, 4H), 7.37–7.31 (m, 16H), 7.30–7.18 (m, 8H), 2.03 (t, $J = 8.0$ Hz, 16H), 1.16–1.07 (m, 16 H), 0.72–0.57 (m, 40H).

Dendron D2-PhCHO. This synthesis is a classical procedure similar to that previously used for **D1-PhCHO**. The purification was completed by chromatography (heptane/ CH_2Cl_2 [5:1]), providing **D2-PhCHO** as a yellow powder (65% yield). ^1H NMR (400 MHz, CD_2Cl_2 , ppm): δ 10.15 (s, 1H), 8.05 (s, 3H), 7.76–7.73 (m, 13H), 7.62–7.59 (m, 8H), 7.42–7.29 (m, 25H), 2.06 (t, $J = 8.0$ Hz, 16H), 1.17–1.08 (m, 16 H), 0.72–0.54 (m, 40H). HRMS-ESI: m/z calcd for $\text{C}_{115}\text{H}_{122}\text{O}$: 1518.94902 $[\text{M}]^+$; found 1518.9487.

3.3. Porphyrin synthesis and characterization

Reference porphyrins **TPP**, **TPP-T1**, and **TPP-T2** were synthesized as described earlier by our group [32,40]. The generation G1 dendrimer **TPP-D1** was obtained under Adler–Longo conditions as described earlier (8% yield) [28].

ZnTPP-D1. The free-base porphyrin **TPP-D1** reacts with excess of $\text{Zn}(\text{OAc})_2$ in [3:1] mixture of CH_2Cl_2 and MeOH at 40 °C overnight. After evaporating the solvents, **ZnTPP-D1** was purified by chromatography (petroleum ether/ CH_2Cl_2 [5:1]) and after evaporation of the volatiles was obtained as a pink powder (80% yield). ^1H NMR (400 MHz, CD_2Cl_2 , ppm): δ 9.20 (s, 8H), 8.42 (s, 8H), 8.21 (s, 4H), 7.71–7.68 (m, 32H), 7.60–7.54 (m, 60H), 7.48 (d, $J = 8.4$ Hz, 8H), 7.42–7.27 (m, 80H), 7.15 (dd, $J_1 = 8.4$ Hz, $J_2 = 2.4$ Hz, 4H), 2.01 (t, $J = 7.2$ Hz, 64H), 1.12–1.01 (m, 64H), 0.65–0.51 (m, 160H) [28]. ^{13}C NMR (125 MHz, CDCl_3 , ppm): δ 151.3, 151.0, 143.0, 141.2, 140.8, 136.3, 136.1, 132.0, 130.7, 127.6, 127.1, 126.8, 125.8, 124.0, 122.8, 120.8, 119.9, 119.7, 54.9, 40.3, 25.9, 23.1,

13.8. HRMS MALDI: m/z calcd for $\text{C}_{228}\text{H}_{236}\text{N}_4\text{Zn}$: 3093.7876 $[\text{M}]^+$; found 3093.782.

Dendrimer TPP-D2. The mixture of **D2-PhCHO** (250 mg, 0.16 mmol, 1 eq) and propionic acid (4 mL) was heated to 120 °C. After pyrrole (0.01 mL, 0.16 mmol, 1 eq) in propionic acid (1 mL) was added into the mixture dropwise, the reaction was kept refluxing for 5.5 h. After cooling to room temperature, MeOH was then added to the reaction mixture and the precipitate was filtered. The residue could be purified by chromatography (petroleum ether/ CH_2Cl_2 [5:1]) as a red powder (10 mg, 4% yield). ^1H NMR (400 MHz, CD_2Cl_2 , ppm): δ 9.10 (broad s, 8H), 8.50 (s, 8H), 8.20–7.10 (large signals, 188H), 2.01 (large s, 64H), 1.00 (m, 64H), 0.60–0.50 (m, 160H).

ZnTPP-D2. Previous crude mixture **TPP-D2** (10 mg, 1.6×10^{-6} mol, 1 eq) reacts with excess of $\text{Zn}(\text{OAc})_2$ (3 mg, 1.6×10^{-5} mol, 10 eq) in a [3:1] mixture of CH_2Cl_2 and MeOH (1 mL) at 40 °C overnight. After evaporating the solvents, the Zn complex **ZnTPP-D2** could be isolated by chromatography (petroleum ether/ CH_2Cl_2 [5:1]), as a pink powder (60% yield). ^1H NMR (400 MHz, CD_2Cl_2 , ppm): δ 9.20 (s, 8H), 8.42 (s, 8H), 8.21 (s, 4H), 7.71–7.68 (m, 32H), 7.60–7.54 (m, 60H), 7.48 (d, $J = 8.4$ Hz, 8H), 7.42–7.27 (m, 80H), 7.15 (dd, $J_1 = 8.4$ Hz, $J_2 = 2.4$ Hz, 4H), 2.01 (t, $J = 7.2$ Hz, 64H), 1.12–1.01 (m, 64H), 0.65–0.51 (m, 160H).

3.4. Spectroscopic measurements

All measurements have been performed with freshly prepared air-equilibrated solutions at room temperature (298 K). Fluorescence measurements were performed on dilute solutions (*ca.* 10^{-6} M, optical density < 0.1) contained in standard 1 cm quartz cuvettes. Fully corrected emission spectra were obtained, for each compound, under excitation at the wavelength of the absorption maximum, with $A_{\lambda\text{ex}} < 0.1$ to minimize internal absorption.

Measurements of singlet oxygen quantum yield (Φ_Δ). Measurements were performed on a Fluorolog-3 (Horiba Jobin Yvon), using a 450 W Xenon lamp. The emission at 1272 nm was detected using a liquid nitrogen-cooled Ge-detector model (EO-817L, North Coast Scientific Co). Singlet oxygen quantum yields Φ_Δ were determined in dichloromethane solutions, using tetraphenylporphyrin (**TPP**) in dichloromethane as reference solution (Φ_Δ [TPP]

= 0.60) and were estimated from $^1\text{O}_2$ luminescence at 1272 nm.

Two-Photon Absorption Experiments. To span the 790–920 nm range, a Nd:YLF-pumped Ti:sapphire oscillator (Chameleon Ultra, Coherent) was used generating 140 fs pulses at a 80 MHz rate. The excitation power is controlled using neutral density filters of varying optical density mounted in a computer-controlled filter wheel. After five-fold expansion through two achromatic doublets, the laser beam is focused by a microscope objective (10 \times , NA 0.25, Olympus, Japan) into a standard 1 cm absorption cuvette containing the sample. The applied average laser power arriving at the sample is typically between 0.5 and 40 mW, leading to a time-averaged light flux in the focal volume on the order of 0.1–10 mW/mm². The fluorescence from the sample is collected in epifluorescence mode, through the microscope objective, and reflected by a dichroic mirror (Chroma Technology Corporation, USA; “blue” filter set: 675dcxru; “red” filter set: 780dxcr). This makes it possible to avoid the inner filter effects related to the high dye concentrations used (10⁻⁴ M) by focusing the laser near the cuvette window. Residual excitation light is removed using a barrier filter (Chroma Technology; “blue”: e650–2p, “red”: e750sp–2p). The fluorescence is coupled into a 600 μm multimode fiber by an achromatic doublet. The fiber is connected to a compact CCD-based spectrometer (BTC112-E, B&W Tek, USA), which measures the two-photon excited emission spectrum. The emission spectra are corrected for the wavelength dependence of the detection efficiency using correction factors established through the measurement of reference compounds having known fluorescence emission spectra. Briefly, the setup allows for the recording of corrected fluorescence emission spectra under multiphoton excitation at variable excitation power and wavelength. TPA cross-sections (σ_2) were determined from the two-photon excited fluorescence (TPEF) cross-sections ($\sigma_2 \cdot \Phi_F$) and the fluorescence emission quantum yield (Φ_F). TPEF cross-sections of 10⁻⁴ M CH₂Cl₂ solutions were measured relative to fluorescein in 0.01 M aqueous NaOH using the well-established method described by Xu and Webb [39,43] and the appropriate solvent-related refractive index corrections [55]. The quadratic dependence of the fluorescence intensity on the exci-

tation power was checked for each sample and all wavelengths.

4. Conclusions

We report here the synthesis, characterization, and a photochemical study of two new zinc(II) complexes of **TPP**-based dendritic chromophores possessing 8 to 12 fluorenyl groups at their periphery (**ZnTPP-D1** and **ZnTPP-D2**). The corresponding free-base porphyrins are analogs of related dendrimers in which we have now replaced the alkyne linkages (**T** series) by *E*-alkene ones (**D** series) at their periphery (Scheme 1). While **TPP-D2** could not be isolated pure, metalation of this free base by Zn(II) provided a convenient mean to selectively access a representative of the higher generation dendrimer (**ZnTPP-D2**). Comparison with previously gathered data indicate that the optical properties of these dendrimers exhibit an obvious dependence on the dendrimer structure, *E*-alkene linkers being clearly better than 1,2-alkyne ones for enhancing the photo-physical properties of interest (luminescence, 2PA cross-section, and sensitization yields) for performing 2P-PDT and fluorescence imaging. Comparison between **TPP-D1** and **ZnTPP-D1** also reveals that metalation does not drastically affect the two-photon absorption cross-section nor improve the oxygen-sensitizing efficiency of these dendrimers.

Acknowledgments

The authors acknowledge China Scholarship Council (CSC) for PhD funding (DY, LS, and XZ). This project was supported by the departmental committees CD35, CD28, and CD29 of the “*Ligue contre le Cancer du Grand-Ouest*.”

Supplementary data

Supporting information for this article is available on the journal's website under <https://doi.org/10.5802/crchim.99> or from the author.

References

- [1] R. J. Abraham, G. E. Hawkes, M. F. Hudson, K. M. Smith, *J. Chem. Soc., Perkin. Trans. II*, 1975, 204-211.
- [2] H. N. Fonda, J. V. Gilbert, R. A. Cormier, J. R. Sprague, K. Kamioka, J. S. Connolly, *J. Phys. Chem.*, 1993, **97**, 7024-7033.

- [3] A. Toeibs, N. Haeberle, *Justus Liebigs Ann. Chem.*, 1968, **718**, 183-187.
- [4] E. M. Harth, S. Hecht, B. Helms, E. E. Malmstrom, J. M. Fréchet, C. J. Hawker, *J. Am. Chem. Soc.*, 2002, **124**, 3926-3938.
- [5] W. R. Dichtel, J. M. Serin, C. Edde, J. M. Fréchet, *J. Am. Chem. Soc.*, 2004, **126**, 5380-5381.
- [6] M. A. Oar, J. M. Serin, J. M. Fréchet, *Chem. Mater.*, 2006, **18**, 3682-3692.
- [7] B. Li, J. Li, Y. Fu, Z. Bo, *J. Am. Chem. Soc.*, 2004, **126**, 3430-3431.
- [8] B. Li, X. Xu, M. Sun, Y. Fu, G. Yu, Y. Liu, Z. Bo, *Macromolecules*, 2006, **39**, 456-461.
- [9] M. Sun, Z. Bo, *J. Polym. Sci.: Part A: Polym. Chem.*, 2006, **45**, 111-124.
- [10] C. O. Paul-Roth, G. Simonneaux, *Tetrahedron Lett.*, 2006, **47**, 3275-3278.
- [11] C. O. Paul-Roth, G. Simonneaux, *C. R. Acad. Sci. Ser. IIb: Chim.*, 2006, **9**, 1277-1286.
- [12] C. Paul-Roth, G. Williams, J. Letessier, G. Simonneaux, *Tetrahedron Lett.*, 2007, **48**, 4317-4322.
- [13] S. Drouet, C. Paul-Roth, G. Simonneaux, *Tetrahedron*, 2009, **65**, 2975-2981.
- [14] S. Drouet, C. O. Paul-Roth, *Tetrahedron*, 2009, **65**, 10693-10700.
- [15] A. Merhi, S. Drouet, N. Kerisit, C. O. Paul-Roth, *Tetrahedron*, 2012, **68**, 7901-7910.
- [16] D. Yao, V. Hugues, M. Blanchard-Desce, O. Mongin, C. O. Paul-Roth, F. Paul, *New J. Chem.*, 2015, **39**, 7730-7733.
- [17] D. Yao, X. Zhang, O. Mongin, F. Paul, C. O. Paul-Roth, *Chem. Eur. J.*, 2016, **22**, 5583-5597.
- [18] L. B. Josefsen, R. W. Boyle, *Theranostics*, 2012, **2**, 916-966.
- [19] P.-C. Lo, M. S. Rodriguez-Morgade, R. K. Pandey, D. K. P. Ng, T. Torres, F. Dumoulin, *Chem. Soc. Rev.*, 2020, **49**, 1041-1056.
- [20] Z. Sun, L.-P. Zhang, F. Wu, Y. Zhao, *Adv. Funct. Mater.*, 2017, **27**, article no. 1704079.
- [21] F. Bolze, S. Jenni, A. Sour, V. Heitz, *Chem. Commun.*, 2017, **53**, 12857-12877.
- [22] M. Khurana, H. A. Collins, A. Karotki, H. L. Anderson, D. T. Cramb, B. C. Wilson, *Photochem. Photobiol.*, 2007, **83**, 1441-1448.
- [23] J. Schmitt, S. Jenni, A. Sour, V. Heitz, F. Bolze, A. Pallier, C. S. Bonnet, É. Tóth, B. Ventura, *Bioconjug. Chem.*, 2018, **29**, 3726-3738.
- [24] J. R. Starkey, E. M. Pascucci, M. A. Drobizhev, A. Elliott, A. K. Rebane, *Biochim. Biophys. Acta*, 2013, **1830**, 4594-4603.
- [25] H. A. Collins, M. Khurana, E. H. Moriyama, A. Mariampillai, E. Dahlstedt, M. Balaz, M. K. Kuimova, M. Drobizhev, V. X. D. Yang, D. Phillips, A. Rebane, B. C. Wilson, H. L. Anderson, *Nat. Photonics*, 2008, **2**, 420-424.
- [26] L. Shi, C. Nguyen, M. Daurat, A. C. Dhieb, W. Smirani, M. Blanchard-Desce, M. Gary-Bobo, O. Mongin, C. Paul-Roth, F. Paul, *Chem. Commun.*, 2019, **55**, 12231-12234.
- [27] F. Paul, C. Lapinte, *Coord. Chem. Rev.*, 1998, **178/180**, 431-480.
- [28] D. Yao, X. Zhang, S. Abid, L. Shi, M. Blanchard-Desce, O. Mongin, F. Paul, C. O. Paul-Roth, *New J. Chem.*, 2018, **42**, 395-401.
- [29] L. Rigamonti, B. Babgi, M. P. Cifuentes, R. L. Roberts, S. Petrie, R. Stranger, S. Righetto, A. Teshome, I. Asselberghs, K. Clays, M. G. Humphrey, *Inorg. Chem.*, 2009, **48**, 3562-3572.
- [30] S. Yao, H.-Y. Ahn, X. Wang, J. Fu, E. W. Van Stryland, D. J. Hagan, K. D. Belfield, *J. Org. Chem.*, 2010, **75**, 3965-3974.
- [31] G. Mehta, P. Sarma, *Tetrahedron Lett.*, 2002, **43**, 9343-9346.
- [32] O. Hassan Omar, F. Babudri, G. M. Farinola, F. Naso, A. Operamolla, *Eur. J. Org. Chem.*, 2011, 529-537.
- [33] A. D. Adler, F. R. Longo, J. D. Finarelli, J. Assour, L. Korsakoff, *J. Org. Chem.*, 1967, **32**, 476-476.
- [34] A. D. Adler, F. R. Longo, W. Shergalis, *J. Am. Chem. Soc.*, 1964, **86**, 3145-3149.
- [35] J. S. Lindsey, I. C. Schreiman, H. C. Hsu, P. C. Kearney, A. M. Marguerettaz, *J. Org. Chem.*, 1987, **52**, 827-836.
- [36] D. Yao, X. Zhang, A. Triadon, N. Richey, O. Mongin, M. Blanchard-Desce, F. Paul, C. O. Paul-Roth, *Chem. Eur. J.*, 2017, **23**, 2635-2647.
- [37] M. Gouterman, *J. Mol. Spectrosc.*, 1961, **6**, 138-163.
- [38] E. Austin, M. Gouterman, *Bioinorg. Chem.*, 1978, **9**, 281-298.
- [39] N. S. Makarov, M. Drobizhev, A. Rebane, *Opt. Exp.*, 2008, **16**, 4029-4047.
- [40] M. Gouterman, *The Porphyrins*, vol. 3, Academic Press, New-York, 1978.
- [41] J. Griffiths, *Colour and Constitution of Organic Molecules*, Academic Press Inc., London, 1976.
- [42] D. Cao, L. Zhu, Z. Liu, W. Lin, *J. Photochem. Photobiol. C: Photochem. Rev.*, 2020, **44**, article no. 100371.
- [43] C. Xu, W. W. Webb, *J. Opt. Soc. Am. B*, 1996, **13**, 481-491.
- [44] M. Drobizhev, Y. Stepanenko, Y. Dzenis, A. Karotki, A. Rebane, P. N. Taylor, H. L. Anderson, *J. Am. Chem. Soc.*, 2004, **126**, 15352-15353.
- [45] D. Y. Kim, T. K. Ahn, J. H. Kwon, D. Kim, T. Ikeue, N. Aratani, A. Osuka, M. Shigeiwa, S. Maeda, *J. Phys. Chem. A*, 2005, **109**, 2996-2999.
- [46] M. Drobizhev, Y. Stepanenko, Y. Dzenis, A. Karotki, A. Rebane, P. N. Taylor, H. L. Anderson, *J. Phys. Chem. B*, 2005, **109**, 7223-7236.
- [47] T. K. Ahn, K. S. Kim, D. Y. Kim, S. B. Noh, N. Aratani, C. Ikeda, A. Osuka, D. Kim, *J. Am. Chem. Soc.*, 2006, **128**, 1700-1704.
- [48] K. Ogawa, H. Hasegawa, Y. Inaba, Y. Kobuke, H. Inouye, Y. Kanemitsu, E. Kohno, T. Hirano, S.-I. Ogura, I. Okura, *J. Med. Chem.*, 2006, **49**, 2276-2283.
- [49] S. Achelle, P. Couleaud, P. Baldeck, M.-P. Teulade-Fichou, P. Maillard, *Eur. J. Org. Chem.*, 2011, **2011**, 1271-1279.
- [50] F. Hammerer, S. Achelle, P. Baldeck, P. Maillard, M.-P. Teulade-Fichou, *J. Phys. Chem. A*, 2011, **115**, 6503-6508.
- [51] M. Pawlicki, M. Morisue, N. K. S. Davis, D. G. McLean, J. E. Haley, E. Beuerman, M. Drobizhev, A. Rebane, A. L. Thompson, S. I. Pascu, G. Accorsi, N. Armaroli, H. L. Anderson, *Chem. Sci.*, 2012, **3**, 1541-1547.
- [52] S. J. Silvers, A. Tulinsky, *J. Am. Chem. Soc.*, 1967, **89**, 3331-3337.
- [53] O. Mongin, V. Hugues, M. Blanchard-Desce, A. Merhi, S. Drouet, D. Yao, C. Paul-Roth, *Chem. Phys. Lett.*, 2015, **625**, 151-156.
- [54] D. D. Perrin, W. L. F. Armarego, *Purification of Laboratory Chemicals*, 3rd ed., Pergamon Press, Oxford, 1988.
- [55] M. H. V. Werts, N. Nerambourg, D. Pélégry, Y. Le Grand, M. Blanchard-Desce, *Photochem. Photobiol. Sci.*, 2005, **4**, 531-538.



MAPYRO: the French Fellowship of the Pyrrolic Macrocyclic Ring / *MAPYRO: la communauté française des macrocycles pyrroliques*

Here's looking at the reduction of noninnocent copper corroles *via* anion induced electron transfer

W. Ryan Osterloh^{Ⓜ a}, Yuanyuan Fang^{Ⓜ a}, Nicolas Desbois^{Ⓜ b}, Mario L. Naitana^{Ⓜ b}, Stéphane Brandès^{Ⓜ b}, Sandrine Pacquelet^b, Claude P. Gros^{Ⓜ *, b} and Karl M. Kadish^{Ⓜ *, a}

^a Department of Chemistry, University of Houston, Houston, Texas 77204-5003, USA

^b Université Bourgogne Franche-Comté, ICMUB (UMR CNRS 6302), 9 Avenue Alain Savary, BP 47870, 21078 Dijon, Cedex, France

E-mails: osterloh91@gmail.com (W. Ryan Osterloh), fangyy1019@yahoo.com (Y. Fang), Nicolas.Desbois@u-bourgogne.fr (N. Desbois), mario.naitana83@gmail.com (M. L. Naitana), Stephane.Brandes@u-bourgogne.fr (S. Brandès), Sandrine.Pacquelet@u-bourgogne.fr (S. Pacquelet), claude.gros@u-bourgogne.fr (C. P. Gros), kadish@central.uh.edu (K. M. Kadish)

Abstract. The synthesis, electrochemical and spectroscopic characterization of five copper triarylcorroles bearing one, two or three *meso*-nitroaryl substituents is reported. Redox potentials and spectroscopic properties of the neutral Cu(II) corrole cation radicals and singly reduced form of the complexes are reported in CH₂Cl₂ and the ability of the initial noninnocent derivatives to be chemically reduced *via* anion induced electron transfer (AIET) is explored using cyanide (CN⁻) or fluoride (F⁻) anions in the form of tetra-*n*-butylammonium salts. UV-visible spectra of the singly reduced corroles and the species generated after addition of CN⁻ or F⁻ to solutions of the neutral compounds are identical, thus confirming the AIET event in these systems. This result, when combined with the facile electrochemical reduction, provides strong indirect evidence for the presence of noninnocence in these systems.

Keywords. Corroles, Anion induced electron transfer, Noninnocent, Electrochemistry, Spectroelectrochemistry.

Available online 30th July 2021

1. Introduction

Numerous free-base and transition metal triarylcorroles bearing different *meso*- and β -substituents have been synthesized [1,2] and electrochemically examined [3], with particular emphasis being placed on elucidating the electronic configuration of those metal complexes which are known to act as air-stable

radicals [4–8]. In 2010, Pierloot *et al.* [9] presented *ab initio* evidence for a noninnocent corrole ligand in the case of copper corroles, and since that time there have been many reports characterizing neutral copper corroles as having a reduced divalent central metal ion (Cu^{II}) and an oxidized macrocyclic ligand in its cation radical form (Cor^{•2-}) [5–7,10–14]. Evidence for this assignment has involved a wide variety of approaches, including structural analysis, spectroscopic measurements and electrochemical criteria to assess the noninnocent behavior of

* Corresponding authors.

the corrole in question and a concise summary of what has been published in this area was recently reviewed by Ganguly and Ghosh [15]. In our own work we have suggested an electrochemical litmus test for evaluating the innocence or noninnocence of transition-metal corroles [3,5,10,11,13,16–19], and suggested that the presence of a facile reduction at potentials more positive than -0.20 V *versus* SCE (Saturated Calomel Electrode) could be used as one electrochemical diagnostic criterion to establish ligand and noninnocence in these systems.

Our recent studies on the electrochemistry of tetrapyrrole macrocycles has focused in part on cobalt corroles [16–19], some of which possessed redox-active *meso*-nitrophenyl groups [16,17] where ligand noninnocence or innocence was shown to be governed by the number and type of axial ligands bound to the formal cobalt(III) central metal ion. In one of these studies [19], we reported the effect of anions on the spectroscopic and electrochemical properties of noninnocent cobalt corroles and noted that the addition of cyanide anions (CN^-) to solution led to the stepwise formation of a five- and six-coordinate cobalt(III) complex with an innocent corrole macrocyclic ligand, while the addition of other anions, such as fluoride (F^-), led to a chemical reduction of the noninnocent corrole ligand giving an anionic $[\text{Cor}^{3-}\text{Co}^{\text{II}}]^-$ product. The reaction with F^- was rationalized by the known ability of strong Lewis basic anions to reduce or form a solvent caged radical pair with certain π -acids (i.e. ligands with a low lying LUMO or SOMO-1) *via* anion induced electron transfer (AIET) [20–22].

There remains little doubt surrounding the assignment of ligand noninnocence in the case of copper corroles which are isolated as four-coordinate species and do not undergo axial ligation in solution and these $[\text{Cor}^{\bullet 2-}\text{Cu}^{\text{II}}]$ systems therefore serve as ideal metallocorroles to explore the ability of AIET to occur in aprotic media. This is examined in the current study which reports synthesis and characterization of the five copper corroles (1–5) in Scheme 1, with one aim of this study being to elucidate the prevailing electrochemical and spectroscopic behavior of copper nitroaryl corroles in CH_2Cl_2 and the other to explore the possible reduction of these open-shell complexes by cyanide or fluoride anions added to solution in the form of tetra-*n*-butylammonium salts, TBACN or TBAF.

2. Experimental section

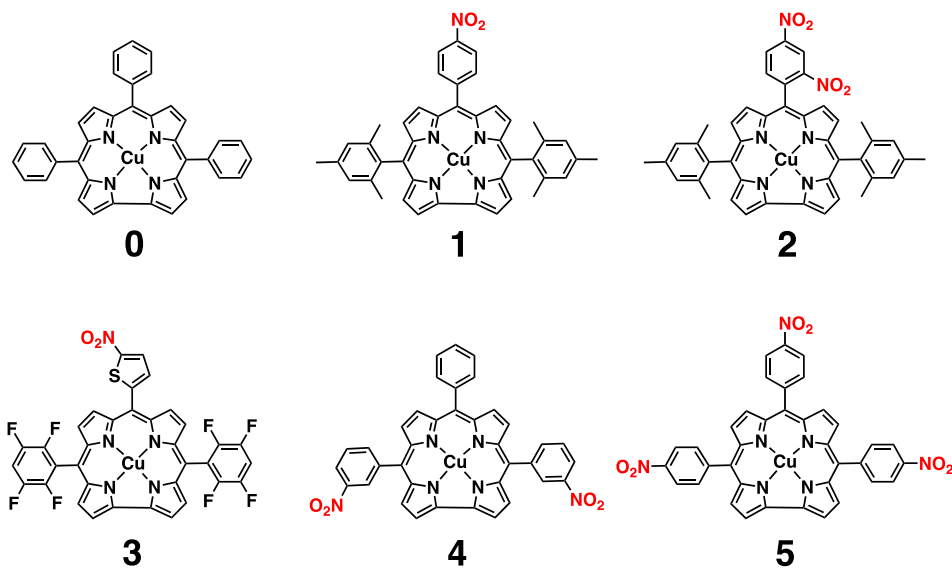
2.1. Material and instrumentation

All chemicals and solvents were of the highest electrochemical grade available and were used without further purification. NMR solvents were purchased from Eurisotope. DriSolve anhydrous dichloromethane (CH_2Cl_2 , $\geq 99.8\%$) was purchased from Sigma Chemical Co. Tetra-*n*-butyl-ammonium perchlorate (TBAP, $\geq 99.0\%$), 95.0% tetra-*n*-butyl-ammonium cyanide (TBACN) and 98% tetra-*n*-butyl-ammonium fluoride hydrate (TBAF) were purchased from Sigma Chemical Co. and stored in a desiccator until used. Copper corrole **0** (see Scheme 1) was synthesized and characterized according to literature procedures [23].

^1H NMR spectra were recorded on a Bruker Avance NEO 500 spectrometer operating at 500 MHz and available at the PACSMUB-WPCM technological platform, which relies on the “Institut de Chimie Moléculaire de l’Université de Bourgogne” and SATT SAYENS “TM”, a Burgundy University private subsidiary. All NMR shift values are expressed in ppm. ^1H NMR spectra were calibrated using the residual peak of chloroform at 7.26 ppm and ^{19}F NMR spectra were calibrated with an internal reference (CFCl_3).

UV–visible spectra of the synthesized compounds were recorded on a Varian Cary 50 or Hewlett-Packard model 8453 diode array spectrophotometer. Quartz cells with optical path lengths of 10 mm were used. ESI mass spectra were recorded on a LTQ Orbitrap XL (THERMO) instrument for HR-MS spectra and on an AmaZon SL (Bruker) instrument for the LRMS spectra or on a Bruker Microflex LRF MALDI Tandem TOF mass spectrometer using dithranol as the matrix.

Thin-layer UV–vis spectroelectrochemical measurements were made using a commercially available thin-layer cell from Pine Instruments Inc. which had a platinum honeycomb working electrode consisting of 19 Pt-coated channels with each channel being 0.50 mm in diameter and a center-to-center distance of 0.75 mm. Potentials were applied and monitored with an EG&G PAR Model 173 potentiostat/galvanostat. High-purity argon from Matheson Trigas was used to deoxygenate the solution and a stream of inert gas was kept over the solution during each spectroelectrochemical experiment.



Scheme 1. Structures and numbering of the investigated copper triarylcorroles 1–5 and the reference compound 0.

Electrochemical measurements were performed at 298 K using an EG&G Princeton Applied Research (PAR) Model 173 potentiostat/galvanostat, paired with a EG&G PAR Model 175 universal programmer and a Houston Instruments Omnigraphic 2000 XY Plotter. The three electrode system used for cyclic voltammetric measurements consisted of a glassy carbon working electrode, a platinum counter electrode and a saturated calomel reference electrode (SCE) which was separated from the bulk of the solution by a fritted glass bridge of low porosity. The bridge was purchased from Gamry Instruments and contained the solvent/supporting electrolyte mixture.

2.2. Synthesis of 5,15-dimesityl-10-(2,4-dinitrophenyl)corrole, (Mes)₂(2,4-(NO₂)₂Ph)CorH₃

In a round bottom flask, 5-mesityldipyrromethane (396.5 mg, 1.5 mmol) and 2,4-dinitrobenzaldehyde (147 mg, 0.75 mmol) were dissolved in 150 mL of CH₃OH. Afterwards a solution of 3.8 mL of HCl_{aq} (36%w) in 75 mL of water was added and the crude material was stirred at room temperature for 2 h. The mixture was extracted with 80 mL of CHCl₃ after which the organic phase was washed twice with 80 mL of water, dried on sodium sulfate, filtered

and then diluted with 250 mL of CHCl₃. *p*-Chloranil (369 mg, 1.5 mmol) was added and the mixture was stirred overnight at room temperature. The reaction mixture was evaporated to dryness and chromatographed on silica gel using a CHCl₃-heptane (2:1, v:v) eluent. Yield 160.2 mg (0.23 mmol, 31%). UV-vis (CH₂Cl₂) λ_{max} [nm, ε × 10³ (M⁻¹·cm⁻¹): 406 (106.2), 421 (86.9), 569 (20.5), 599 (14.8). ¹H NMR (500 MHz, CDCl₃), δ (ppm): 9.17 (d, ⁴J = 2.5 Hz, 1H, H_{Ph}), 8.88 (d, ³J = 4.5 Hz, 2H, H_β), 8.72 (d, ³J = 8.0 Hz, 1H, H_{Ph}), 8.50 (d, ³J = 5.0 Hz, 2H, H_β), 8.44 (d, ³J = 8.0 Hz, 1H, H_{Ph}), 8.32 (d, ³J = 4.5 Hz, 2H, H_β), 8.21 (d, ³J = 4.5 Hz, 2H, H_β), 7.27–7.25 (s, 4H, mesityl, overlapped with CHCl₃ deuterated solvent residual signal), 2.59 (s, 6H, CH₃), 1.94 (s, 6H, CH₃), 1.89 (s, 6H, CH₃). LRMS (MALDI/TOF) [M+H]⁺: 701.13 (exp.), 701.29 (calcd). HRMS (ESI) [M+H]⁺: 701.2882 (exp.), 701.2871 (calcd). See Figures S1 and S2 for ¹H NMR and ESI-MS data.

2.3. General synthetic procedures for copper corroles

2.3.1. Protocol A

Corrole (0.091 mmol) and Cu(acac)₂ (191.0 mg, 0.73 mmol, 8.0 eq) were dissolved in dichloromethane (9 mL) and triethylamine (0.3 mmol). The mixture was stirred at room temperature for 20 min

and then vacuum dried. The residue was purified by column chromatography as described below.

2.3.2. Protocol B

Corrole (0.041 mmol) and $\text{CuOAc}_2 \cdot \text{H}_2\text{O}$ (66.4 mg, 0.33 mmol, 8.0 eq) were dissolved in dichloromethane (5 mL) and methanol (20 mL). The mixture was stirred at room temperature until the color changed to yellow-brown, after which the temperature was increased to 75 °C for 5 h. After evaporating to dryness, the residue was purified by column chromatography as described below.

2.4. $(\text{Mes})_2(4\text{-NO}_2\text{Ph})\text{CorCu}$ (**1**)

This compound was synthesized following *Protocol B* starting from 30.0 mg of free base corrole [24]. Purification was carried out on a silica gel column using a CH_2Cl_2 /heptane (1:1, v:v) eluent. The synthesis of corrole **1** followed a modified synthetic procedure reported in the literature [25]. Yield: 31.2 mg (0.044 mmol, 95%). UV-vis (CH_2Cl_2) λ_{max} [nm, $\epsilon \times 10^3$ ($\text{M}^{-1} \cdot \text{cm}^{-1}$)]: 396 (67.9), 537 (7.9), 597 (4.7). ^1H NMR (500 MHz, CDCl_3), δ (ppm): 8.36 (d, $^3J = 8.0$ Hz, 2H, H_{Ph}), 7.99 (m, 2H, H_{β}), 7.77 (d, $^3J = 8.0$ Hz, 2H, H_{Ph}), 7.36 (d, $^3J = 4.0$ Hz, 2H, H_{β}), 7.21 (m, 2H, H_{β}), 7.03 (m, 6H, H_{β} , H_{Mes}), 2.40 (s, 6H), 2.06 (s, 12H). LRMS (MALDI/TOF) $[\text{M}]^{+\bullet}$: 715.17 (exp.), 715.20 (calcd). See Figures S3 and S4 for ^1H NMR and ESI-MS data.

2.5. $(\text{Mes})_2(2,4\text{-}(\text{NO}_2)_2\text{Ph})\text{CorCu}$ (**2**)

This compound was synthesized following *Protocol B* starting from 30.5 mg of free base corrole (**Mes**)₂(2,4-(NO₂)₂Ph)CorH₃. Purification was carried out on a silica gel column using a CH_2Cl_2 /heptane (1:1, v:v) eluent. Yield: 31.0 mg (0.0041 mmol, 94%). UV-vis (CH_2Cl_2) λ_{max} [nm, $\epsilon \times 10^3$ ($\text{M}^{-1} \cdot \text{cm}^{-1}$)]: 397 (91.8), 601 (5.6). ^1H NMR (500 MHz, CDCl_3), δ (ppm): 8.99 (d, $^4J = 2.0$ Hz, 1H, H_{Ph}), 8.58 (d, $^3J = 8.0$ Hz, 1H, H_{Ph}), 8.05 (m, 2H, H_{β}), 7.86 (d, $^3J = 8.0$ Hz, 1H, H_{Ph}), 7.36 (d, $^3J = 4.0$ Hz, 2H, H_{β}), 7.23 (m, 2H, H_{β}), 7.04 (s, 2H, H_{Mes}), 7.03 (s, 2H, H_{Mes}), 6.82 (d, $^3J = 4.5$ Hz, 2H, H_{β}), 2.40 (s, 6H, CH_3), 2.07 (s, 6H, CH_3), 2.05 (s, 6H, CH_3). LRMS (MALDI/TOF) $[\text{M}]^{+\bullet}$: 760.20 (exp.), 760.19 (calcd). HRMS (ESI) $[\text{M}]^{+\bullet}$: 760.1887 (exp.), 760.1854 (calcd), $[\text{M}+\text{Na}]^{+\bullet}$: 783.1753 (exp.), 783.1752 (calcd). See Figures S5 and S6 for ^1H NMR and ESI-MS data.

2.6. $(2,3,4,5\text{-F}_4\text{Ph})_2(2\text{-NO}_2\text{thiophene})\text{CorCu}$ (**3**)

This compound was synthesized following *Protocol B* starting from 30.2 mg of free base corrole [26–28]. Purification was carried out on a silica gel column using a CH_2Cl_2 /heptane (1:1, v:v) eluent. Yield: 30.3 mg (0.0039 mmol, 93%). UV-vis (CH_2Cl_2) λ_{max} [nm, $\epsilon \times 10^3$ ($\text{M}^{-1} \cdot \text{cm}^{-1}$)]: 405 (73.2). ^1H NMR (500 MHz, CDCl_3), δ (ppm): 7.97 (d, $^3J = 4.0$ Hz, 1H, H_{thio}), 7.93 (d, $^3J = 4.0$ Hz, 2H, H_{β}), 7.43 (d, $^3J = 4.5$ Hz, 2H, H_{β}), 7.40 (d, $^3J = 4.5$ Hz, 2H, H_{β}), 7.36 (d, $^3J = 4.0$ Hz, 1H, H_{thio}), 7.31–7.26 (m, 4H, H_{Ph} , H_{β}). ^{19}F NMR (470 MHz, CDCl_3), δ (ppm): –137.55 to –137.57 (m, 8F). LRMS (MALDI/TOF) $[\text{M}]^{+\bullet}$: 780.98 (exp.), 780.99 (calcd). HRMS (ESI) $[\text{M}]^{+\bullet}$: 780.9899 (exp.), 780.9875 (calcd). See Figures S7 and S8 for ^1H NMR, ^{19}F NMR and ESI-MS data.

2.7. $(3\text{-NO}_2\text{Ph})_2(\text{Ph})\text{CorCu}$ (**4**)

This compound was synthesized following *Protocol B* starting from 30.0 mg of free base corrole [29]. Purification was carried out on a silica gel column using a CH_2Cl_2 /heptane (2:1, v:v) eluent. Synthesis of corrole **4** has already been reported in the literature [29]. Yield: 17.3 mg (0.026 mmol, 52%). UV-vis (CH_2Cl_2) λ_{max} [nm, $\epsilon \times 10^3$ ($\text{M}^{-1} \cdot \text{cm}^{-1}$)]: 407 (80.6), 541 (6.3), 625 (4.3). ^1H NMR (500 MHz, CDCl_3), δ (ppm): 8.59 (m, 2H, H_{Ph}), 8.44 (d, $^3J = 8.0$ Hz, 2H, H_{Ph}), 8.05 (d, $^3J = 8.0$ Hz, 2H, H_{Ph}), 7.89 (m, 2H, H_{β}), 7.69 (t, $^3J = 8.0$ Hz, 2H, H_{Ph}), 7.60 (m, 3H, H_{Ph}), 7.54 (d, $^3J = 5.0$ Hz, 2H, H_{β}), 7.47 (m, 2H, H_{Ph}), 7.27 (d, $^3J = 4.5$ Hz, 2H, H_{β}), 7.26 (m, 2H, H_{β}). LRMS (MALDI/TOF) $[\text{M}]^{+\bullet}$: 676.06 (exp.), 676.09 (calcd). See Figures S9 and S10 for ^1H NMR and ESI-MS data.

2.8. $(4\text{-NO}_2\text{Ph})_3\text{CorCu}$ (**5**)

This compound was synthesized following *Protocol A* starting from 60.0 mg of free base corrole [30]. The purification process consisted of a silica gel column using neat CH_2Cl_2 as the eluent. Synthesis of corrole **5** has already been reported in the literature [31]. Yield: 30.0 mg (0.042 mmol, 46%). UV-vis (CH_2Cl_2) λ_{max} [nm, $\epsilon \times 10^3$ ($\text{M}^{-1} \cdot \text{cm}^{-1}$)]: 420 (37.5), 540 (5.0), 627 (3.5). ^1H NMR (500 MHz, CDCl_3), δ (ppm): 8.37 (m, 6H, H_{Ph}), 8.00 (m, 2H, H_{β}), 7.92 (d, $^3J = 8.5$ Hz, 4H, H_{Ph}), 7.83 (d, $^3J = 8.5$ Hz, 2H, H_{Ph}), 7.59 (d, $^3J = 4.5$ Hz, 2H, H_{β}), 7.31 (m, 2H, H_{β}), 7.19 (d, $^3J = 4.5$ Hz,

Table 1. Half-wave potentials (*V versus SCE*) of copper triarylcorroles **0–5** in CH₂Cl₂ containing 0.1 M TBAP

Cpd	<i>E</i> _{1/2} (<i>V versus SCE</i>)				<i>i</i> _{pc} ^{R2} / <i>i</i> _{pc} ^{R1} ^a	Ref.
	2nd Ox	1st Ox	1st Red	2nd Red (#e)		
0	1.46 ^c	0.78	−0.19	−1.94 (1) ^b	—	[10]
1	1.40 ^c	0.80	−0.16	−1.16 (1)	0.95	t.w
2	1.43 ^c	0.83	−0.09	−0.92 (1)	1.00	t.w
3	1.57 ^c	1.08	0.19	−1.00 (1)	1.00	t.w
4	1.46 ^c	0.88	−0.08	−1.13 (2)	1.95	t.w
5	1.44	0.95	0.02	−1.10 (3)	2.94	t.w

Structures of the compounds are given in Scheme 1.

^a *i*_{pc}^{R2}/*i*_{pc}^{R1} = ratio of cathodic peak current for 2nd Red (at the *meso*-nitroaryl group) over that of the first 1st Red (at the conjugated macrocycle).

^b Obtained in CH₂Cl₂/0.1 M TBAP at −60 °C.

^c Peak potential of irreversible process at scan rate of 0.1 V/s. t.w = this work.

2H, H_β). LRMS (MALDI/TOF) [M]⁺: 721.06 (exp.), 721.08 (calcd). See Figures S11 and S12 for ¹H NMR and ESI-MS data.

3. Results and discussion

3.1. Electrochemistry

Each copper corrole was electrochemically examined in CH₂Cl₂ containing 0.1 M TBAP at room temperature. Examples of cyclic voltammograms for **1–5** are given in Figure 1 and half-wave potentials are summarized in Table 1 which also includes data for the parent copper triphenylcorrole (**0** in Scheme 1) under the same solution conditions [10].

As seen in Figure 1, the nitroaryl corroles **1–5** exhibit two reversible reductions and at least one reversible oxidation while the parent compound **0** exhibits only one reversible reduction and one reversible oxidation within the solvent potential window. Half-wave potentials for the first reduction of the corroles are located between 0.19 and −0.19 *V versus SCE* and are assigned to occur at the conjugated macrocycle as given in (1).



This assignment of electron transfer site is consistent with earlier assignments for numerous copper [5,11–13,32] and other noninnocent

metallocorroles [5,15–19,33,34] and fits with the Kadish electrochemical diagnostic criterion [18] that noninnocent macrocycles will undergo a facile reduction in nonaqueous media (*vide supra*). As seen in Figure 1 and Table 1, the most facile one-electron addition occurs for **3** (*E*_{1/2} = 0.19 V), consistent with the electron withdrawing properties of both the *meso*-nitrothiophene group and the two *meso*-tetrafluorophenyl substituents while corrole **1** bearing two mesityl and one *para*-nitrophenyl *meso*-group exhibits the most difficult ligand centered reduction of the investigated nitroaryl corroles at *E*_{1/2} = −0.16 V. All of the nitroarylcorroles are easier to reduce than the parent compound, **0** (*E*_{1/2} = −0.19 V), an expected result due to the highly electron-withdrawing NO₂ substituent.

The second reduction of compounds **1–5** ranges from *E*_{1/2} = −1.16 (for **1**) to −0.92 V (for **2**) and these values can be compared to −1.94 V for the second reduction of corrole **0** when the measurement was carried out at −60 °C [10]. This large difference in potential for the second reduction of the five copper corroles bearing one or more nitroaryl substituents is consistent with a change in the site of electron transfer, from π -ring centered in the case of **0** to the electroactive *meso*-nitroaryl ring(s) in the case of compounds **1–5**. This assignment of electron transfer site in **1–5** is consistent with

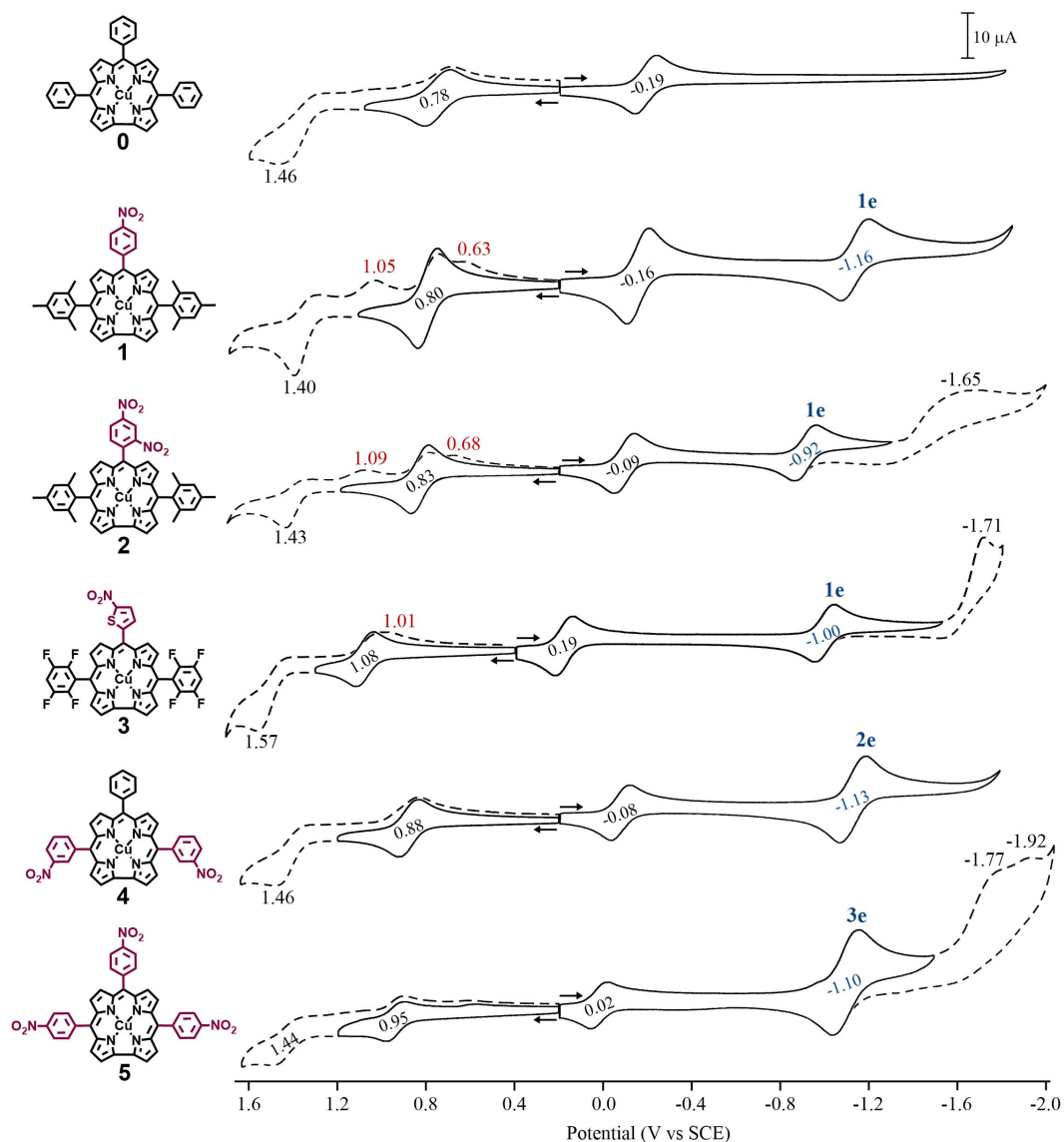


Figure 1. Cyclic voltammograms of copper corroles **1–5** in CH_2Cl_2 containing 0.1 M TBAP. Scan rate = 0.1 V/s. Potentials for the *meso*-nitroaryl reduction are shown in blue, the number of electrons transferred in the second reduction step is indicated above the half-wave potential and peak potentials for chemically generated products formed after oxidation are given in red.

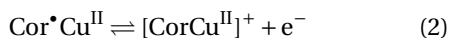
the known electrochemistry of nitrobenzene [35], which is reduced in two steps, the first being reversible and located at $E_{1/2} = -1.08$ V versus SCE in CH_2Cl_2 [36]. The half-wave potential for the second reduction of **1** ($E_{1/2} = -1.16$ V) is close to that of free nitrobenzene while the second reversible reduction of corroles **2** ($E_{1/2} = -0.92$ V) and **3** ($E_{1/2} = -1.00$ V) are located at potentials close to reported

$E_{1/2}$ values in nonaqueous media for reduction of *m*-dinitrobenzene [37] and 2-nitrothiophene [38], respectively. Additional evidence for reduction of the nitroaryl groups is given by $i_{\text{pc}}^{\text{R}2}/i_{\text{pc}}^{\text{R}1}$, defined as the ratio of cathodic peak current (i_{pc}) for the second electroreduction over the i_{pc} value for the first reduction of the same compound. As seen in Table 1, this ratio is approximately 1.0 for compounds **1–3**,

2.0 for compound **4**, and 3.0 for compound **5**, values consistent with the number of nitroaryl substituents on the examined corrole and indicating a single one-electron reduction of this group in each case. Reductions occurring at the *meso*-NO₂Ph groups of iron [39,40], cobalt [16,17,19,40] and copper [31] corroles have previously been reported while similar *meso*-substituent-centered reductions have also been shown to occur for porphyrins bearing *meso*-nitrophenyl groups [40,41].

As mentioned above, nitrobenzene [35] and nitrothiophene [38] are both characterized by two reductions in nonaqueous media, the second of which is irreversible. The same is seen for the copper corroles **2**, **3** and **5** in CH₂Cl₂ (Figure 1) where the second and third reductions are assigned to occur at the *meso*-nitroaryl group. It is worth noting that the copper corrole **2** bearing both a *ortho*- and *para*-NO₂ substituent on one *meso*-phenyl ring of the compound displays only a single one-electron reduction at -0.97 V while *m*-dinitrobenzene displays two closely spaced reversible reductions [37,42] located at -0.90 and -1.25 V *versus* SCE when measured in acetonitrile containing tetra-*n*-propylammonium perchlorate [37].

The first oxidation of corroles **1–5** is reversible and located at potentials ranging from 0.80 to 1.08 V *versus* SCE. On the basis of literature assignments for compound **0** and related copper corroles [5,10–12,43], this process in the current study is assigned as a ligand-centered oxidation, resulting in a cationic product with a divalent Cu^{II} metal center and a doubly oxidized corrole macrocycle according to (2).



A plot of the first oxidation potential *versus* the first reduction potential for compounds **0–5** in CH₂Cl₂ containing 0.1 M TBAP is shown in Figure 2 and reveals a characteristic of these noninnocent corrole systems. The plot in the figure is linear with a high correlation coefficient of $R^2 = 0.985$, thus suggesting that the site of both electroreduction and electrooxidation remains the same throughout the series of compounds, and supporting the assignments given in (1) and (2). Inductive effects of *meso*-substituents on corroles, porphyrins and related macrocycles are known to govern redox potentials [3, 19,41,44–48] and it was expected that a linear plot would be obtained between the two redox potentials

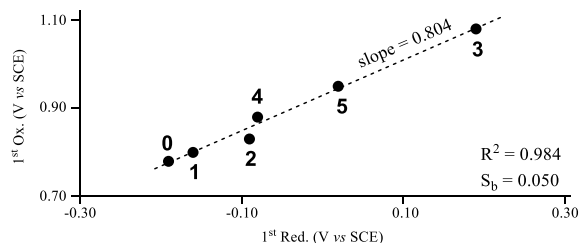


Figure 2. Plots of $E_{1/2}$ for first oxidation *versus* $E_{1/2}$ for first reduction of corroles **0–5** in CH₂Cl₂ containing 0.1 M TBAP.

in Figure 2 (assuming that the sites of electron transfer remain the same throughout the series); however the magnitude of the slope in the plot of Figure 2 provides insight into how the electron withdrawing substituents influence differently the oxidation and reduction potentials of noninnocent corroles in the currently investigated series of compounds. As seen in the figure, the slope of the linear regression analysis is 0.804 with a standard error (or deviation) of the slope (S_b) of 0.050. The obtained slope of less than 1.0 indicates that reduction of the noninnocent copper triarylcorroles (or the LUMO/SOMO-1) is more affected by electron withdrawing substituents on the *meso*-aryl groups than is the oxidation (or HOMO energies) by a factor of ~ 1.25 .

Each investigated corrole also undergoes a second oxidation which is irreversible for **1–4** and located at an anodic peak potential (E_{pa}) between 1.40 and 1.57 V (see Figure 1). A chemical reaction follows this electron transfer and leads to a new electrooxidation product which is reduced at potentials between $E_{pc} = 1.01$ and 1.05 V for **1–3** on the reverse scan. Interestingly, corrole **5** displays a reversible second oxidation at $E_{1/2} = 1.44$ V indicating the absence of a coupled chemical reaction on the cyclic voltammetry timescale, but plots of E_{pc} values for this process in compounds **1–5** *versus* $E_{1/2}$ for the first reduction or first oxidation are linear, suggesting that the site of the second electron abstraction does not change in the series of investigated corroles.

3.2. Electrochemical or chemical reduction via anion induced electron transfer (AIET)

To characterize the one-electron reduction product(s) of **1–5**, thin-layer UV-vis spectroelectrochem-

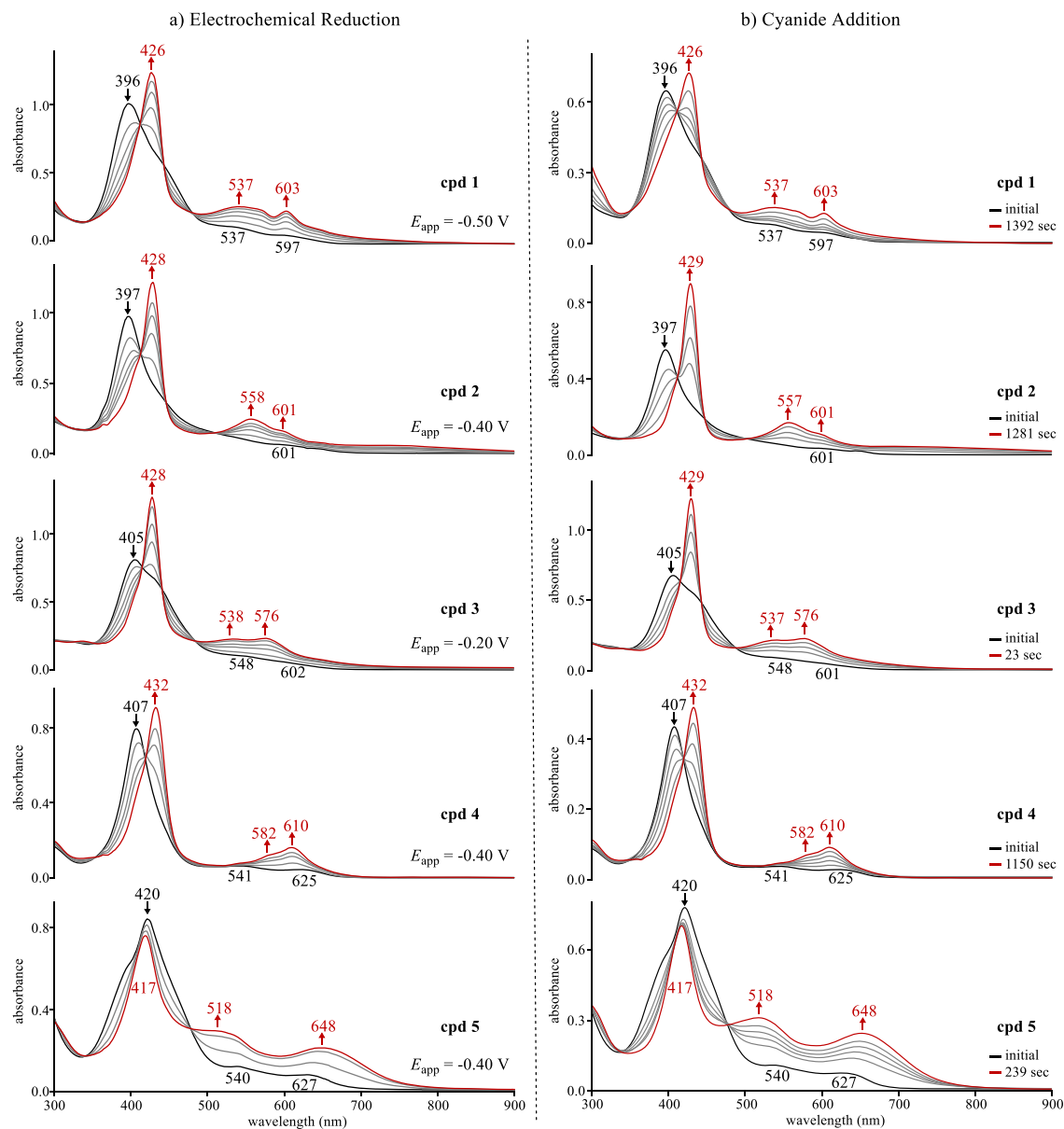


Figure 3. UV-vis spectral changes for compounds 1–5 (a) during an applied reducing potential ($\sim 10^{-4}$ M) in CH_2Cl_2 containing 0.1 M TBAP and (b) upon addition of TBACN (0.02 M) to $\sim 10^{-5}$ M corrole in CH_2Cl_2 where the changes were recorded as a function of time.

ical studies were carried out in CH_2Cl_2 containing 0.1 M TBAP. The spectral changes obtained under the influence of an applied reducing potential in the thin layer cell are presented in Figure 3a and the data for the neutral and singly reduced corroles in the CH_2Cl_2 solvent containing 0.1 M TBAP are summarized in Table 2.

The neutral corroles 1–5 have a well-defined Soret band located between 396 and 420 nm and broad ill-defined Q-bands as seen in Figure 3a. Similar spectra have been reported for **0** under the same solution conditions [5,10]. Upon reduction of corroles 1–4, the Soret band at decreases in intensity as a new red-shifted Soret band of higher intensity grows in at

Table 2. UV-vis spectral data of neutral and singly reduced copper corroles **0–5** in CH₂Cl₂ containing 0.1 M TBAP

Cpd	λ_{\max} , nm ($\epsilon \times 10^{-4} \text{ M}^{-1} \cdot \text{cm}^{-1}$)						Ref.
	Neutral			Singly reduced			
	Soret	Q-Band(s)		Soret	Q-Band(s)		
0	410 (7.2)	540 (0.4)	633 (0.2)	432 (9.0)	578 (1.3)	607 (1.8)	[10]
1	396 (6.8)	537 (0.8)	597 (0.5)	426 (8.5)	537 (1.8)	603 (1.6)	t.w
2	397 (9.2)		601 (0.6)	428 (11.9)	558 (2.4)	601 (1.6)	t.w
3	405 (7.3)	548 (0.9)	602 (0.6)	428 (11.6)	538 (1.9)	576 (2.0)	t.w
4	407 (8.1)	541 (0.6)	625 (0.4)	432 (8.3)	582 (1.2)	610 (1.5)	t.w
5	420 (3.8)	540 (0.5)	627 (0.4)	417 (3.4)	518 (1.3)	648 (1.0)	t.w

Structures of the compounds are given in Scheme 1.

t.w = this work.

426–432 nm along with two new Q-bands located at 537–582 nm and 576 to 610 nm. There are no near-IR bands characteristic of a corrole π -anion radical and the spectral changes in Figure 3a for **1–4** are consistent with (1) which specifies generation of [CorCu^{II}]⁻, a compound which possesses an intact conjugated macrocycle (i.e. Cor³⁻).

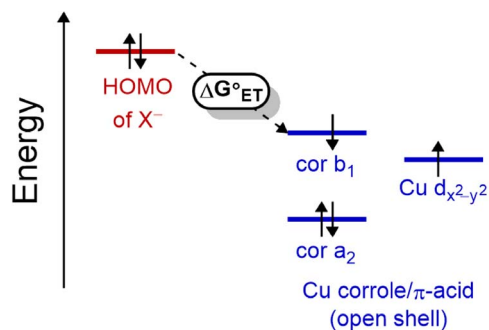
Copper corrole **5** exhibits slightly different behavior upon electroreduction. As seen in Figure 3a, the Soret band of **5** shifts by only 3 nm to higher energy wavelengths while the corresponding band for compounds **1–4** shifts by 23–31 nm to the red after reduction. Singly reduced **5** also has two broad and intense Q-bands at 518 and 648 nm, a spectral pattern quite different than is seen for singly reduced **0–4**. This difference between the UV-vis spectrum of singly reduced **5** and the singly reduced corroles [10,12,13]) might result from a change in the site of electron transfer, but the plot in Figure 2 does not lend credence to this explanation. Nonetheless, the final spectrum of singly reduced **5** possesses broad Q-bands in the visible region which appear similar to hyperporphyrin-type spectra reported for peripherally protonated free base tris(*p*-aminophenyl)corrole isomers [49], a phenomenon which might arise from a mesomeric effect of the *para*-nitro substituents which is known to enhance delocalization of the conjugated π electrons, thus stabilizing the single negative charge on the molecule *via* resonance [50–52].

The effect of cyanide anions (CN⁻) on UV-vis spectra of the copper corroles was also exam-

ined and the time dependent spectral changes observed upon addition of an aliquot to give a 0.02 M TBACN/CH₂Cl₂ solution of **1–5** ($\sim 10^{-5}$ M) is shown in Figure 3b. In each case, the spectral changes seen upon the addition of CN⁻ are strikingly similar to what is seen for the same corroles under the application of an applied reducing potential (Figure 3a). Moreover, the final spectrum of each corrole after electrochemical or chemical conversion to its monoanionic form are identical to each other, thus providing clear evidence for the ability of cyanide anions to reduce the open-shell noninnocent Cor[•]Cu^{II} to a [CorCu^{II}]⁻ product according to (1) *via* anion induced electron transfer (AIET).

The time elapsed for conversion of the neutral copper corrole to its final chemically reduced form ranged from 23 s for corrole **3** to 1392 s for compound **1**. Moreover, a monotonic increase in the elapsed time needed to complete the AIET processes was observed with decrease in the first reduction potential of the compound (i.e. a more negative $E_{1/2}$ value). This trend is consistent with the thermodynamically driven electron transfer (ET) event from the HOMO of cyanide anion to the LUMO/SOMO-1 of the corrole “ π -acid” complex [20–22] where the relative energies of the corrole LUMO/SOMO-1 are indirectly determined by the first reduction potential.

A simple diagram for this AIET process is given in Scheme 2, where the HOMO of the anion, in this case cyanide, lies at an energy level well above that of the open-shell copper corrole orbitals as detailed by



Scheme 2. Schematic energy diagram for the HOMOs of anions (X^-) and the LUMO/SOMO-1 of the open-shell copper corrole depicting thermal electron transfer (ET).

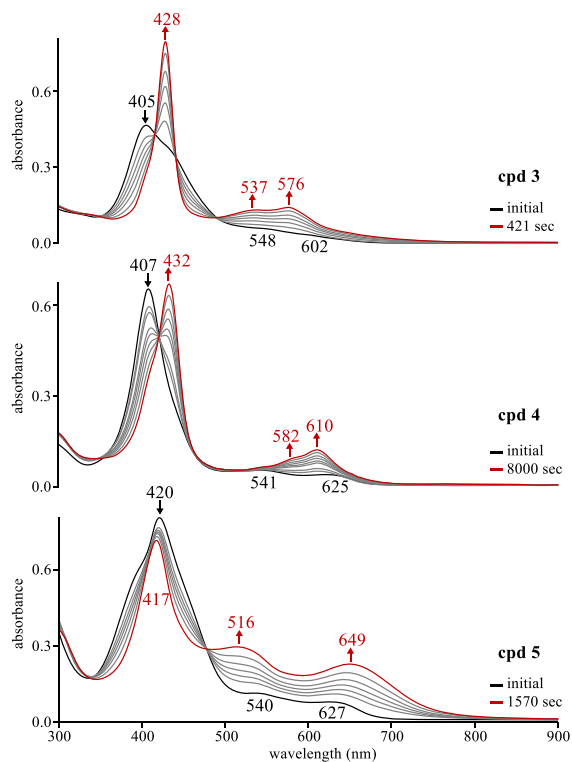


Figure 4. UV-vis spectral changes for compounds 3–5 upon addition of TBAF (0.05 M) to $\sim 10^{-5}$ M corrole in CH_2Cl_2 where the changes are recorded as a function of time.

Ghosh, Solomon and coworkers [6] as well as Nocera and coworkers [53].

Like in the case of cyanide anion, F^- has also been shown to reduce π -acids [22] and was pre-

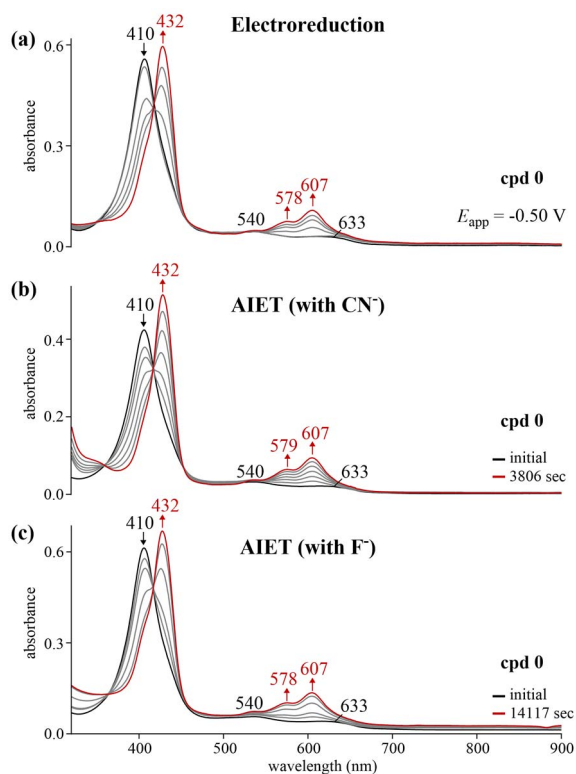


Figure 5. UV-vis spectral changes for reference corrole 0 (a) during an applied reducing potential ($\sim 10^{-4}$ M) in CH_2Cl_2 containing 0.1 M TBAP, (b) upon addition of TBACN (0.02 M) to $\sim 10^{-5}$ M corrole in CH_2Cl_2 and (c) upon addition of TBAF (0.5 M) to $\sim 10^{-5}$ M corrole in CH_2Cl_2 where the changes are recorded as a function of time.

viously shown to reduce noninnocent cobalt corroles [19]. Thus, the ability of fluoride anions to reduce open-shell noninnocent copper corroles by the addition of TBAF to solution was also investigated in the current study. As seen in Figure 4, the addition of TBAF (0.05 M) to a CH_2Cl_2 solution of corroles 3–5 led to exactly the same pattern of spectral changes as seen for either electroreduction in a thin layer cell or chemical reduction via CN^- (Figure 3). However, The time to complete reduction of these corroles by anion induced electron transfer was slower with F^- than with CN^- and this is shown by a comparison of the data for compounds 3–5 in Figure 3 with that which was observed in Figure 4 where the rates decreased by a fac-

tor of ~18 to 6.5 depending upon the substitution pattern.

Identical UV-visible were also observed for the electrochemically and chemically reduced parent compound **0** (Figure 5) but the time for reduction by anion induced electron transfer was slower for F⁻ than CN⁻ despite the ten-fold increase in the concentration of fluoride as compared to cyanide.

4. Conclusion

The mounting evidence for the ability of Lewis basic anions to reduce noninnocent corroles as described in the current study on copper corroles and also in our previous report for cobalt corroles [19] suggests that the occurrence of an anion induced electron transfer (AIET) event in aprotic media can serve as an additional probe for provisionally assigning the non-innocence or innocence of metalloporphyrins, particularly where there is a more cryptic noninnocent behavior as in the case of silver corrole derivatives [4,5].

Conflicts of interest

The authors declare no competing financial interest.

Acknowledgements

This work was supported by the Robert A. Welch Foundation (KMK, Grant E-680), the CNRS (UMR UB-CNRS 6302) and the “Université Bourgogne Franche-Comté”, and the “Conseil Régional de Bourgogne” through the Plan d’Actions Régional pour l’Innovation (PARI II CDEA) and the European Union through the PO FEDER-FSE Bourgogne 2014/2020 (*via* the CoMICS program, Chemistry of Molecular Interactions: Catalysis & Sensors and the ISITE CO₂DECIN). The authors warmly thank Dr. Valentin Quesneau and Dr. Léo Bucher for the preparation of some free-base corroles.

Supplementary data

¹H NMR of corroles **1–5** and ¹⁹F NMR of **3**. LRMS (ESI) spectra of corroles **1–5** and HRMS (ESI) spectra of **2** and **3**. ¹H NMR of (Mes)₂(2,4-(NO₂)₂Ph)CorH₃ and LRMS and HRMS (ESI) for (Mes)₂(2,4-(NO₂)₂Ph)CorH₃.

Supporting information for this article is available on the journal’s website under <https://doi.org/10.5802/crchim.95> or from the author.

References

- [1] J. F. B. Barata, M. G. P. M. S. Neves, M. A. F. Faustino, A. C. Tomé, J. A. S. Cavaleiro, *Chem. Rev.*, 2017, **117**, 3192-3253.
- [2] S. Nardis, F. Mandoj, M. Stefanelli, R. Paolesse, *Coord. Chem. Rev.*, 2019, **388**, 360-405.
- [3] Y. Fang, Z. Ou, K. M. Kadish, *Chem. Rev.*, 2017, **117**, 3377-3419.
- [4] A. Ghosh, *Chem. Rev.*, 2017, **117**, 3798-3881.
- [5] K. E. Thomas, H. Vazquez-Lima, Y. Fang, Y. Song, K. J. Gagnon, C. M. Beavers, K. M. Kadish, A. Ghosh, *Chem. Eur. J.*, 2015, **21**, 16839-16847.
- [6] H. Lim, K. E. Thomas, B. Hedman, K. O. Hodgson, A. Ghosh, E. I. Solomon, *Inorg. Chem.*, 2019, **58**, 6722-6730.
- [7] A. Ghosh, T. Wondimagegn, A. B. J. Parusel, *J. Am. Chem. Soc.*, 2000, **122**, 5100-5104.
- [8] D. Shimizu, A. Osuka, *Chem. Sci.*, 2018, **9**, 1408-1423.
- [9] K. Pierloot, H. Zhao, S. Vancoillie, *Inorg. Chem.*, 2010, **49**, 10316-10329.
- [10] Z. Ou, J. Shao, H. Zhao, K. Ohkubo, I. H. Wasbotten, S. Fukuzumi, A. Ghosh, K. M. Kadish, *J. Porphyr. Phthalocyanines*, 2004, **08**, 1236-1247.
- [11] L. Ye, Z. Ou, Y. Fang, Y. Song, B. Li, R. Liu, K. M. Kadish, *J. Porphyr. Phthalocyanines*, 2016, **20**, 753-765.
- [12] F. Wu, J. Xu, H. Gao, C. Li, S. Xu, H. Uno, Y. Xu, Y. Zhao, Z. Shen, *Chem. Commun.*, 2021, **57**, 383-386.
- [13] P. Yadav, M. Sankar, X. Ke, L. Cong, K. M. Kadish, *Dalton Trans.*, 2017, **46**, 10014-10022.
- [14] A. Alemayehu, J. Conradie, A. Ghosh, *Eur. J. Inorg. Chem.*, 2011, **2011**, 1857-1864.
- [15] S. Ganguly, A. Ghosh, *Acc. Chem. Res.*, 2019, **52**, 2003-2014.
- [16] X. Jiang, M. L. Naitana, N. Desbois, V. Quesneau, S. Brandès, Y. Rousselin, W. Shan, W. R. Osterloh, V. Blondeau-Patissier, C. P. Gros, K. M. Kadish, *Inorg. Chem.*, 2018, **57**, 1226-1241.
- [17] X. Jiang, W. Shan, N. Desbois, V. Quesneau, S. Brandès, E. V. Caemelbecke, W. R. Osterloh, V. Blondeau-Patissier, C. P. Gros, K. M. Kadish, *New J. Chem.*, 2018, **42**, 8220-8229.
- [18] W. R. Osterloh, N. Desbois, V. Quesneau, S. Brandès, P. Fleurat-Lessard, Y. Fang, V. Blondeau-Patissier, R. Paolesse, C. P. Gros, K. M. Kadish, *Inorg. Chem.*, 2020, **59**, 8562-8579.
- [19] W. R. Osterloh, V. Quesneau, N. Desbois, S. Brandès, W. Shan, V. Blondeau-Patissier, R. Paolesse, C. P. Gros, K. M. Kadish, *Inorg. Chem.*, 2020, **59**, 595-611.
- [20] S. Guha, S. Saha, *J. Am. Chem. Soc.*, 2010, **132**, 17674-17677.
- [21] G. Aragay, A. Frontera, V. Lloveras, J. Vidal-Gancedo, P. Ballester, *J. Am. Chem. Soc.*, 2013, **135**, 2620-2627.
- [22] S. Saha, *Acc. Chem. Res.*, 2018, **51**, 2225-2236.
- [23] I. H. Wasbotten, T. Wondimagegn, A. Ghosh, *J. Am. Chem. Soc.*, 2002, **124**, 8104-8116.
- [24] D. T. Gryko, K. Jadach, *J. Org. Chem.*, 2001, **66**, 4267-4275.
- [25] T. H. Ngo, W. Van Rossom, W. Dehaen, W. Maes, *Org. Biomol. Chem.*, 2009, **7**, 439-443.
- [26] S. Kappler-Gratias, L. Bucher, N. Desbois, Y. Rousselin, K. Bystricky, C. P. Gros, F. Gallardo, *RSC Med. Chem.*, 2020, **11**, 783-801.

- [27] C. Gros, F. Gallardo, N. Desbois, "Preparation of Corrole Compounds and Methods of Use Thereof for Treating Poxvirus Infection", 2019, *PCT Int. Appl.* WO2019105940A1.
- [28] C. Gros, F. Gallardo, N. Desbois, "Preparation of Corrole Compounds and Methods of Use Thereof for Treating Human Cytomegalovirus Infections", 2019, *PCT Int. Appl.* WO2019105928A1.
- [29] M. Li, Y. Niu, W. Zhu, J. Mack, G. Fomo, T. Nyokong, X. Liang, *Dyes Pigments*, 2017, **137**, 523-531.
- [30] R. Paolesse, S. Nardis, F. Sagone, R. G. Khoury, *J. Org. Chem.*, 2001, **66**, 550-556.
- [31] D. Bhattacharya, P. Singh, S. Sarkar, *Inorg. Chim. Acta*, 2010, **363**, 4313-4318.
- [32] H. Lei, H. Fang, Y. Han, W. Lai, X. Fu, R. Cao, *ACS Catal.*, 2015, **5**, 5145-5153.
- [33] S. Ganguly, J. Conradie, J. Bendix, K. J. Gagnon, L. J. McCormick, A. Ghosh, *J. Phys. Chem. A*, 2017, **121**, 9589-9598.
- [34] V. Quesneau, W. Shan, N. Desbois, S. Brandès, Y. Roussetin, M. Vanotti, V. Blondeau-Patissier, M. Naitana, P. Fleurat-Lessard, E. Van Caemelbecke, K. M. Kadish, C. P. Gros, *Eur. J. Inorg. Chem.*, 2018, **2018**, 4265-4277.
- [35] T. Kitagawa, T. P. Layloff, R. N. Adams, *Anal. Chem.*, 1963, **35**, 1086-1087.
- [36] K. M. Kadish, E. Wenbo, P. J. Santic, Z. Ou, J. Shao, K. Ohkubo, S. Fukuzumi, L. J. Govenlock, J. A. McDonald, A. C. Try, Z.-L. Cai, J. R. Reimers, M. J. Crossley, *J. Phys. Chem. B*, 2007, **111**, 8762-8774.
- [37] D. H. Geske, J. L. Ragle, M. A. Bambenek, A. L. Balch, *J. Am. Chem. Soc.*, 1964, **86**, 987-1002.
- [38] I. M. Sosonkin, G. N. Strogov, T. K. Ponomareva, A. N. Domarev, A. A. Glushkova, G. N. Freidlin, *Chem. Heterocycl. Comp.*, 1981, **17**, 137-140.
- [39] S. Nardis, M. Stefanelli, P. Mohite, G. Pomarico, L. Tortora, M. Manowong, P. Chen, K. M. Kadish, F. R. Fronczek, G. T. McCandless, K. M. Smith, R. Paolesse, *Inorg. Chem.*, 2012, **51**, 3910-3920.
- [40] Y. Fang, X. Jiang, Z. Ou, C. Michelin, N. Desbois, C. P. Gros, K. M. Kadish, *J. Porphy. Phthalocyanines*, 2014, **18**, 832-841.
- [41] A. Ghosh, I. Halvorsen, H. J. Nilsen, E. Steene, T. Wondim-agegn, R. Lie, E. van Caemelbecke, N. Guo, Z. Ou, K. M. Kadish, *J. Phys. Chem. B*, 2001, **105**, 8120-8124.
- [42] M. Mohammad, A. Y. Khan, M. Afzal, A. Nisa, R. Ahmed, *Aust. J. Chem.*, 1974, **27**, 2495-2498.
- [43] K. M. Kadish, V. A. Adamian, E. Van Caemelbecke, E. Gueletii, S. Will, C. Erben, E. Vogel, *J. Am. Chem. Soc.*, 1998, **120**, 11986-11993.
- [44] K. M. Kadish, M. M. Morrison, *J. Am. Chem. Soc.*, 1976, **98**, 3326-3328.
- [45] K. M. Kadish, M. M. Morrison, *Inorg. Chem.*, 1976, **15**, 980-982.
- [46] K. M. Kadish, M. M. Morrison, *Bioinorg. Chem.*, 1977, **7**, 107-115.
- [47] K. M. Kadish, E. Van Caemelbecke, G. Royal, "Electrochemistry of metalloporphyrins in nonaqueous media", in *The Porphyrin Handbook* (K. M. Kadish, K. M. Smith, R. Guillard, eds.), vol. 8, Academic Press, Burlington, MA, 2000, 1-97.
- [48] A. Ghosh, E. Steene, *J. Inorg. Biochem.*, 2002, **91**, 423-436.
- [49] I. K. Thomassen, A. Ghosh, *ACS Omega*, 2020, **5**, 9023-9030.
- [50] C. Hansch, A. Leo, R. W. Taft, *Chem. Rev.*, 1991, **91**, 165-195.
- [51] O. Exner, T. M. Krygowski, *Chem. Soc. Rev.*, 1996, **25**, 71-75.
- [52] E. V. A. D. A. Dougherty, "Experiments related to thermodynamics and kinetics", in *Modern Physical Organic Chemistry*, University Science Books, Mill Valley, California, 2006, 421-488.
- [53] C. M. Lemon, M. Huynh, A. G. Maher, B. L. Anderson, E. D. Bloch, D. C. Powers, D. G. Nocera, *Angew. Chem. Int. Ed.*, 2016, **55**, 2176-2180.



MAPYRO: the French Fellowship of the Pyrrolic Macrocyclic Ring / MAPYRO: la communauté française des macrocycles pyrroliques

In vitro toxicity and photodynamic properties of porphyrinoids bearing imidazolium salts and N-heterocyclic carbene gold(I) complexes

Clémence Rose^a, Laure Lichon^b, Morgane Daurat^c, Sébastien Clément^{® a}, Magali Gary-Bobo^{® b} and Sébastien Richeter^{®*, a}

^a ICGM, Univ Montpellier, CNRS, ENSCM, Montpellier, France

^b IBMM, Univ Montpellier, CNRS, ENSCM, Montpellier, France

^c NanoMedSyn, 15 avenue Charles Flahault, 34093, Montpellier, France

E-mails: clemence.rose@universite-paris-saclay.fr (C. Rose),

laure.lichon@umontpellier.fr (L. Lichon), m.daurat@nanomedsyn.com (M. Daurat),

sebastien.clement1@umontpellier.fr (S. Clément), magali.gary-bobo@inserm.fr

(M. Gary-Bobo), sebastien.richeter@umontpellier.fr (S. Richeter)

Abstract. Porphyrins bearing imidazolium salts were synthesized and used as N-heterocyclic carbene (NHC) precursors for the preparation of gold(I) complexes. The dark toxicity and phototoxicity of the obtained compounds were investigated *in vitro* on MCF-7 breast cancer cells. The obtained data showed that porphyrins equipped with imidazolium salts are non-toxic in the dark and present interesting photodynamic properties. On the contrary, corresponding NHC-gold(I) complexes are not suitable photosensitizers for photodynamic therapy (PDT) applications. Their dark toxicity strongly depends on the nature of the linker between the porphyrin core and the NHC. This work was extended to the synthesis of a pyropheophorbide *a* derivative with a pendant imidazolium group for PDT applications using excitation wavelengths of 450 nm, 545 nm, and importantly of 650 nm.

Keywords. Porphyrinoids, N-heterocyclic carbenes, Gold complexes, Photodynamic therapy, Biocompatibility, Cancer cells.

Available online 17th August 2021

1. Introduction

In the field of cancer therapy, photodynamic therapy (PDT) represents an interesting alternative approach besides chemotherapy, radiotherapy and surgery for

some types of cancer, notably skin cancer or tumors accessible to light (directly or thanks to optical fiber) [1–4]. It relies in using a photosensitizer (PS), which is activated by light and able to generate reactive oxygen species (ROS) and singlet oxygen (¹O₂). It implies that the PS in its singlet excited state (¹PS) can reach its triplet state (³PS) through intersystem crossing (ISC, ¹PS → ³PS). Then, energy transfer from the ³PS with ground state molecular oxygen in its

* Corresponding author.

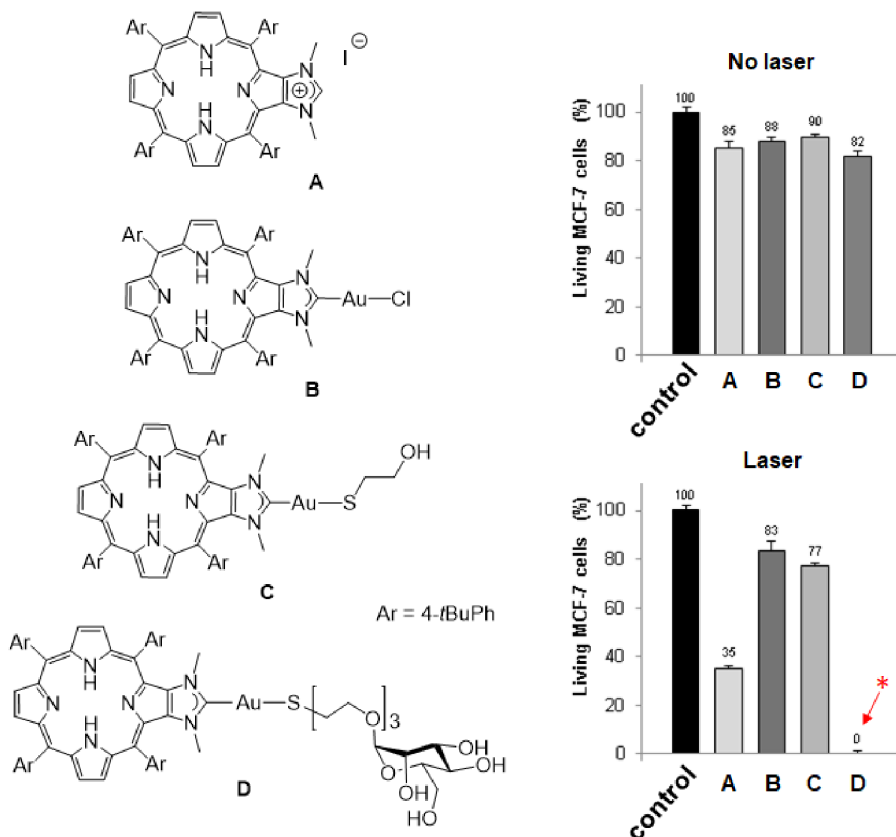
triplet state $^3\text{O}_2$ leads to the generation of $^1\text{O}_2$ (PDT of type 2). Alternatively, electron transfer processes involving the ^3PS lead to the formation of ROS and cytotoxic free radicals (PDT of type 1). Ultimately, these strong oxidizing agents may lead to the death of cancer cells through necrotic and apoptotic mechanisms [5–9]. The important aspect of PDT is that only cells containing PS and irradiated with visible light are susceptible to be destroyed. To date, porphyrinoids (including porphyrins, chlorins, phthalocyanines) are among the best performing PS for PDT because of their inherent chemical stability and suitable photophysical properties [10–13]. These tetrapyrrolic aromatic compounds strongly absorb light in the visible region and, more importantly, they are efficient PS to generate $^1\text{O}_2$. For example, the $^1\text{O}_2$ quantum yield of 5,10,15,20-*meso*-tetraphenylporphyrin (H_2TPP) in toluene is $\Phi_\Delta = 68\%$ [14]. Of course, there are some important drawbacks like their poor water solubility or their lack of selective accumulation in cancer cells, but these drawbacks may be circumvented by appropriate functionalization of the porphyrin core [15–17]. Interestingly, some porphyrins were functionalized with peripheral ligands allowing the coordination of metal ions at their periphery [18]. Some of the obtained complexes found relevant applications in the field of PDT [19]. For example, porphyrins functionalized with peripheral platinum(II) or ruthenium(II) complexes were used for dual chemo- and phototherapy [20–32]. Platinum(II) complexes have anticancer activity and also, significantly improve the photodynamic effect by promoting the generation of $^1\text{O}_2$ through a heavy atom effect [20–28]. Ruthenium(II) complexes were also reported for dual chemo- and phototherapy [29–32]. Moreover, some ruthenium(II) complexes proved to be efficient PS for two-photon excitation [33–35]. Although gold(I) complexes are promising candidates to develop new metallodrugs for cancer therapy, examples of porphyrinoids bearing peripheral gold(I) complexes for combined chemo- and phototherapy are relatively scarce. Gold(I) complexes of porphyrins functionalized with peripheral phosphine ligands were synthesized and biological studies showed that these compounds present rather low cytotoxicity [36]. However, water-soluble complexes of this type proved to be efficient PS for PDT. N-heterocyclic carbenes (NHC) are phosphine analogs and are attractive ligands to design new metallo-

drugs. During the last decade, we reported the synthesis of several porphyrin derivatives equipped with peripheral NHC-metal complexes [37–41], including gold(I) complexes [42–45]. The photodynamic properties of imidazolium salt **A** and gold(I) complexes **B–D** depicted in Scheme 1 were investigated and we observed the important role played by the ligand *trans* to the NHC [45]. Indeed, the excellent photodynamic properties observed for the PS **D** functionalized with mannose are due to active targeting of cancer cells overexpressing mannose receptors at their surface. We also observed that imidazolium salt **A** is an efficient PS for PDT, while gold(I) complex **B** and **C** are inefficient for chemo- and phototherapy. The aim of this study is to draw more detailed conclusions about the potential of porphyrins equipped with peripheral NHC-gold(I) complexes for dual chemo- and phototherapy. For this purpose, we report here the synthesis and the biological properties of porphyrins bearing imidazolium salts and NHC-gold(I) complexes at their periphery.

2. Results and discussion

2.1. Synthesis of porphyrins *meso*-functionalized with imidazolium salts

Imidazolium salts are routinely used as NHC precursors. NHC could be generated upon deprotonation of an imidazolium salt with a base and trapped with a metal cation such as Ag^+ or Au^+ , for example. We first investigated compounds with imidazolium salts directly N-linked to one *meso* position of a porphyrin core. The first imidazolium salt, namely free-base porphyrin **3**, was obtained in a three-step procedure starting from the porphyrin **1** previously described in [46]. The reaction of porphyrin **1** with imidazole and NaH in DMF (140 °C) afforded porphyrin **2** in 72% yield after column chromatography [46]. Then, demetalation of porphyrin **2** in acidic conditions followed by methylation of the peripheral imidazole group with CH_3I afforded porphyrin **3** in an overall yield of 77% after purification (Scheme 2). The ^1H NMR spectrum of porphyrin **3** showed the expected signal of the imidazolium proton H^2 at $\delta = 10.44$ ppm and the signal of the two inner NH protons at $\delta = -2.95$ ppm. High-resolution ESI-TOF mass spectrometry (positive mode) featured the expected molecular mass peak at $m/z = 647.2926$ Da

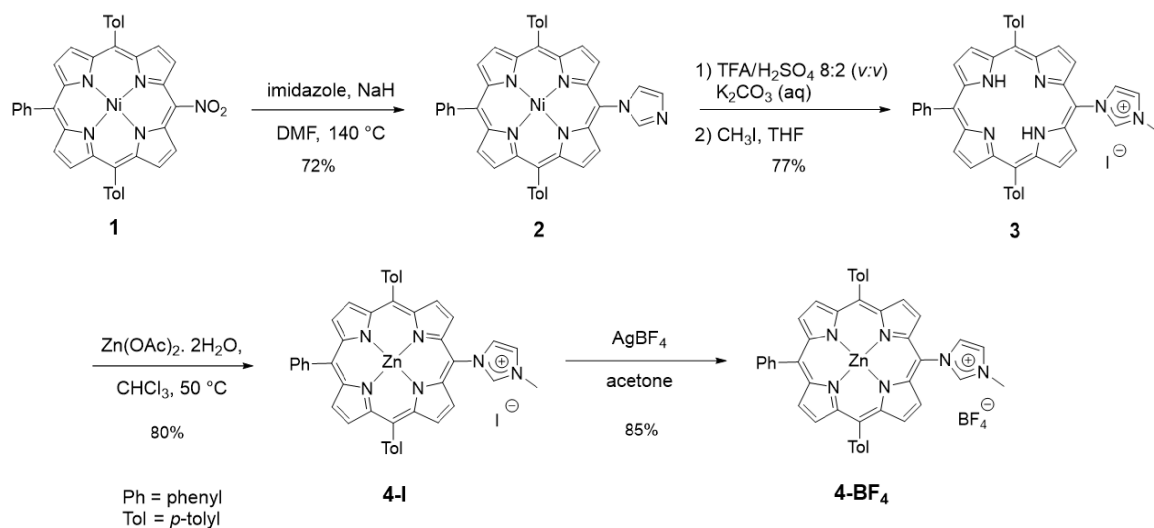


Scheme 1. Left: Structures of compounds A–D. Right: Cytotoxic (no laser) and photodynamic effect (laser) of imidazolium salt A and gold(I) complexes B–D. The cells were incubated or not (control experiment in black) with 10 μM of PS for 4 h and then, submitted or not to laser irradiation ($\lambda = 405 \text{ nm}$, $18.75 \text{ J}\cdot\text{cm}^{-2}$, 10 min). Cells were allowed to grow for two days and cell viability was quantified with MTT assay. Data are mean values standard deviation from three independent experiments. *No living cells detected [45].

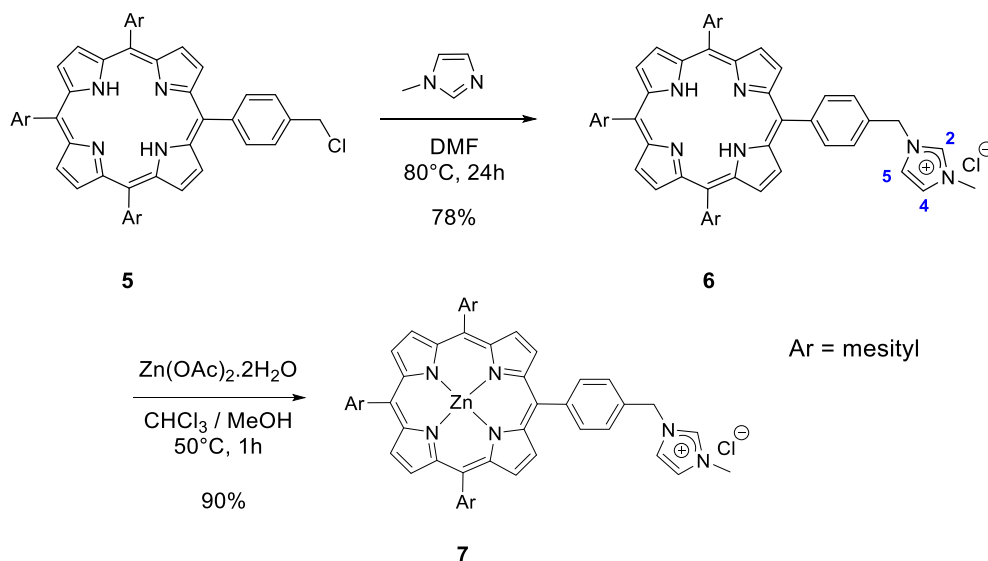
with an isotopically resolved profile in agreement with the calculated distribution for the monocationic species $[\text{M}-\text{I}]^+$ (calcd $m/z = 647.2918 \text{ Da}$). The iodide counter-ion was observed by ESI-TOF mass spectrometry (negative mode) at $m/z = 126.91 \text{ Da}$. Porphyrin 3 was then metalated with $\text{Zn}(\text{OAc})_2 \cdot 2\text{H}_2\text{O}$ to obtain the corresponding zinc(II) porphyrin 4-I in 80% yield. Metal insertion within the porphyrin core was confirmed by ^1H NMR, UV-visible absorption spectroscopy and mass spectrometry (see ESI). To avoid the presence of iodide in the coordination sphere of gold(I) complexes, iodide was substituted by tetrafluoroborate, which is a non-coordinating anion. For this purpose, reaction of porphyrin 4-I with AgBF_4 in acetone in the dark gave porphyrin

4-BF₄ in 85% yield after column chromatography. Tetrafluoroborate anion was observed by ^{19}F NMR spectroscopy with the two expected signals at $\delta = -149.20$ and -149.26 ppm (caused by the two boron isotopes ^{10}B and ^{11}B , respectively) and by mass spectrometry (negative mode).

Then, we synthesized imidazolium-based porphyrin compounds with a spacer between the *meso* position of the porphyrin core and the imidazolium salt. For this purpose, free-base porphyrin 5 was used as starting material. The synthesis of this compound is described in [47]. Nucleophilic substitution on the chlorine atom of porphyrin 5 with 1-methylimidazole in DMF (80 °C) afforded porphyrin 6 in 78% yield (Scheme 3). The ^1H NMR spectrum



Scheme 2. Synthesis of porphyrins **3**, **4-I** and **4-BF₄**.

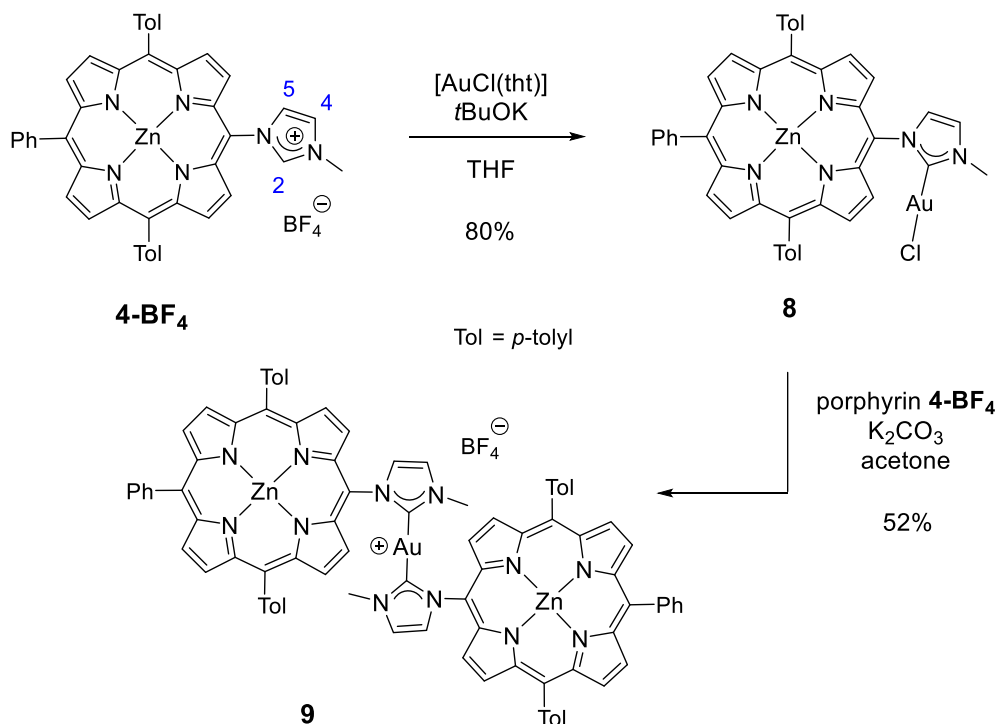


Scheme 3. Synthesis of the porphyrins **6** and **7**.

of the porphyrin **6** clearly showed the expected signal of the imidazolium proton H² at $\delta = 11.17$ ppm. The signals of imidazolium protons H⁴ and H⁵ were also observed as apparent triplets at $\delta = 7.45$ and 7.31 ppm. Porphyrin **7** was obtained in 90% yield by reacting free-base porphyrin **6** with Zn(OAc)₂ · 2H₂O.

2.2. Synthesis of gold(I) complexes

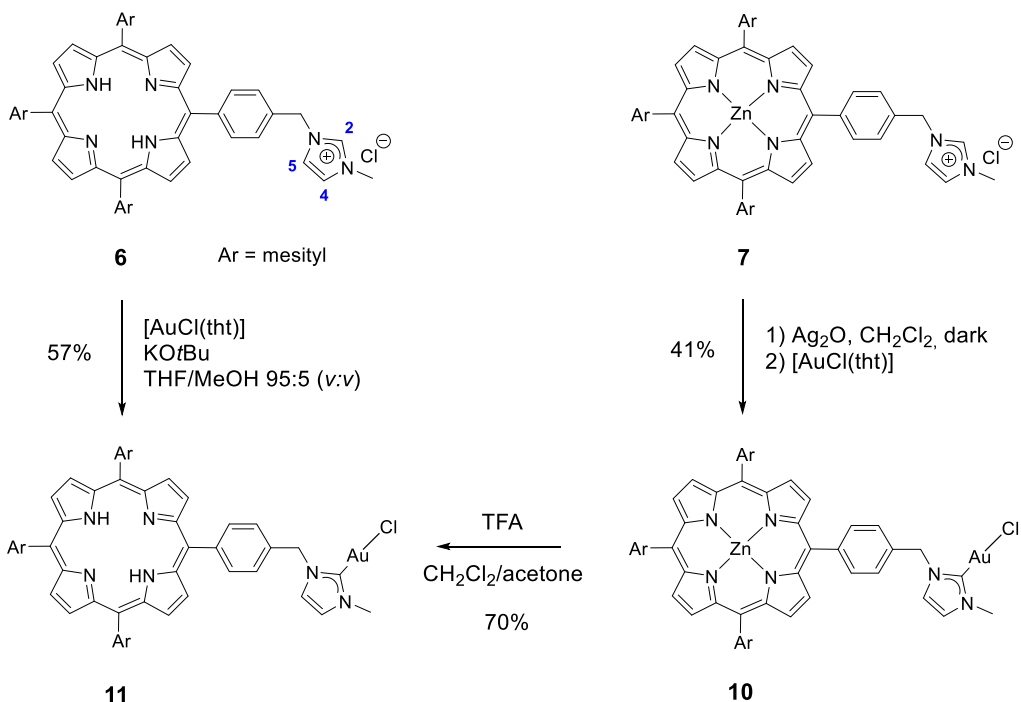
NHC-gold(I) complexes can be synthesized following different procedures. For example, complex **8** was synthesized in one step by reacting porphyrin **4-BF₄** with [AuCl(tht)] (tht = tetrahydrothiophene) in the presence of *t*BuOK in dry THF. The mono(NHC)-gold(I) complex **8** was obtained in 80% yield after column chromatography and recrystallization



Scheme 4. Synthesis of gold(I) complexes **8** and **9**.

(Scheme 4). The absence of signal corresponding to the imidazolium proton H² in the ¹H NMR spectrum of complex **8** confirmed the formation of the C_{NHC}-Au(I) bond. Imidazolium protons H⁴ and H⁵ are shifted upfield by $\Delta\delta \sim 0.40$ ppm as a consequence of the formation of the C_{NHC}-Au(I) bond. The signal of the C_{NHC} bound to Au^I was observed at $\delta = 175.1$ ppm in the ¹³C{¹H} NMR spectrum of complex **8**. This chemical shift is in good agreement with those reported in literature for [(NHC)AuCl] complexes [48,49]. Complex **9** was prepared in one step according to the reaction conditions reported by Richeter [42–45]. The deprotonation of the porphyrin **4-BF₄** with K₂CO₃ in acetone in the presence of one equivalent of the complex **8** afforded the homoleptic complex **9** in 52% yield after column chromatography (Scheme 4). High-resolution ESI-TOF mass spectrometry (positive mode) featured the expected molecular mass peak at $m/z = 1617.3612$ Da with an isotopically resolved profile in good agreement with the calculated distribution of the monocationic species [ZnP-Au-ZnP]⁺ (calcd $m/z = 1617.3610$ Da). NMR spectroscopy also con-

firmed the formation of the complex **9**. Notably, in the ¹³C{¹H} NMR spectrum, the signal of the C_{NHC} bound to Au^I was observed at $\delta = 188.8$ ppm, a chemical shift in good agreement with those reported in literature for homoleptic monocationic complexes [(NHC)Au^I(NHC)]⁺ [48,49]. The ¹H NMR spectra of complexes **8** and **9** are displayed in Figure 1. Interestingly, in both cases, four separated doublets were observed for the *ortho* and *meta* protons of the tolyl groups. This can be explained by the restricted rotation of the C_{meso}-N_{NHC} bond due to the presence of the sterically demanding NHC-gold(I) complexes. As a consequence, different chemical environments are experienced by the *meso* aryl protons. The N-Me protons signal of complex **9** at $\delta = 2.04$ ppm is significantly shielded ($\delta = 4.23$ ppm for complex **8**) indicating that the N-Me group of one porphyrin sits on top of the second porphyrin ring and is exposed to its ring current. Finally, the two gold(I) complexes were characterized by diffusion-ordered spectroscopy (DOSY) ¹H NMR. As expected, the diffusion coefficient of **9** (1.15×10^{-10} m²·s⁻¹) is lower compared to **8** (1.54×10^{-10} m²·s⁻¹) because it contains two porphyrins.



Scheme 5. Synthesis of gold(I) complexes **10** and **11**.

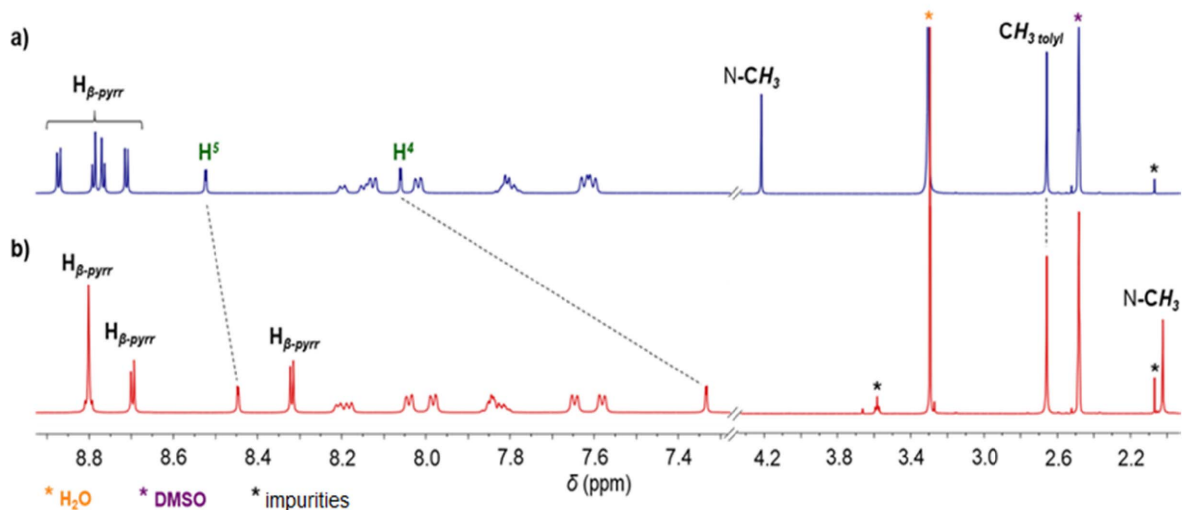


Figure 1. ¹H NMR spectra (400 MHz, DMSO-*d*₆, 298 K) of gold(I) complexes **8** (a) and **9** (b).

Gold(I) complex **10** was prepared following a strategy that is widely used for the synthesis of NHC gold(I) complexes: the reaction of the porphyrin **7** with 1 equation of Ag₂O in dichloromethane afforded the corresponding silver(I) complex which was not

isolated and used straightforward for the transmetalation reaction with [AuCl(tht)]. The corresponding gold(I) complex **10** was obtained in 41% yield after column chromatography and recrystallization (Scheme 5). The absence of signal for proton H² in

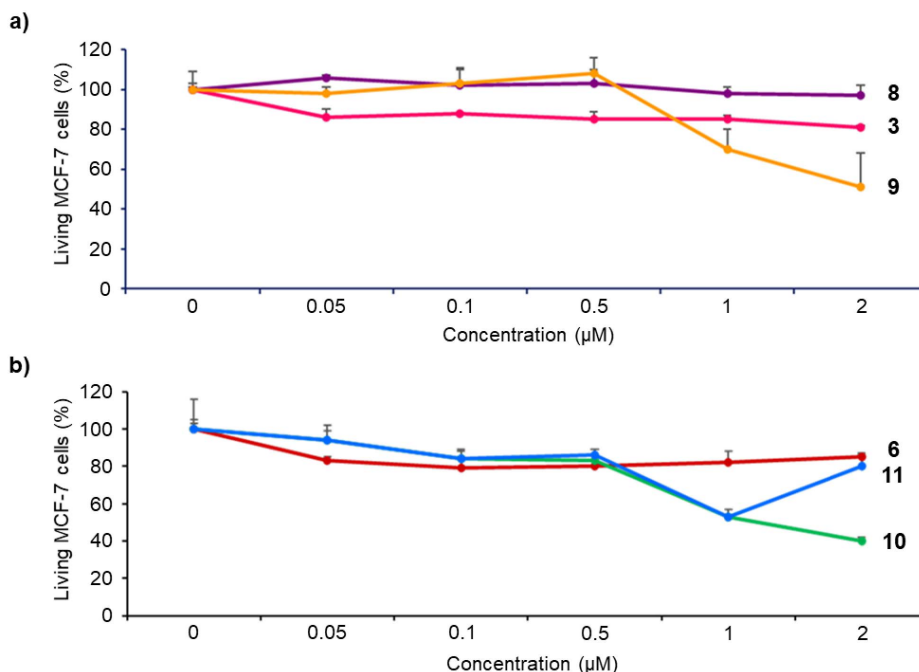


Figure 2. Cytotoxicity of imidazolium salts **3** and **6**, and their corresponding gold(I) complexes **8–11** on MCF-7 cancer cells. The cells were incubated without (control) or with 0.05, 0.1, 0.5, 1 or 2 μM of the different compounds for 72 h. Cell viability was quantified with MTT assay. Data are mean values standard deviation from three independent experiments.

the ^1H NMR spectrum of complex **10** and the signal of the C_{NHC} bound to Au^{I} observed by $^{13}\text{C}\{^1\text{H}\}$ NMR spectroscopy at $\delta = 172.3$ ppm confirmed the formation of the expected gold(I) complex. Gold(I) complex **11** containing a free-base porphyrin could not be synthesized following a similar strategy because silver(I) may be complexed by the porphyrin core. However, gold(I) complex **11** could be obtained by two different pathways. First, it is possible to remove the zinc(II) by treating the complex **10** with a TFA/ CH_2Cl_2 mixture. These acidic conditions do not degrade the peripheral gold(I) complex as it was previously shown by us with analogous complexes [45]. Complex **11** was obtained in 70% yield after neutralization with NaHCO_3 and column chromatography. It is also possible to react free-base porphyrin **6** with one equivalent of $[\text{AuCl}(\text{tht})]$ with *t*BuOK, in a THF/MeOH mixture in the dark to obtain the corresponding complex gold(I) complex **11** in 57% yield after column chromatography (Scheme 5). The formation of complex **11** was first confirmed by ^1H NMR spectroscopy and the disappearance of the signal at

$\delta = 11.17$ ppm corresponding to the imidazolium proton H^2 . In its $^{13}\text{C}\{^1\text{H}\}$ NMR spectrum, the carbene signal observed at $\delta = 172.5$ ppm demonstrated the formation of the $\text{C}_{\text{NHC}}\text{-Au(I)}$ bond.

2.3. Cytotoxicity and phototoxicity studies

Biological properties of NHC-based gold(I) complexes have been extensively reported in literature [50–62]. The cytotoxicity of imidazolium salts and gold(I) complexes on MCF-7 breast cancer cells was first investigated. For this purpose, MCF-7 cancer cells were incubated for 72 h in the dark with each compound at different concentrations varying from 0.05 to 2 μM . After 72 h, MTT assay (3-(4,5-dimethylthiazol-2-yl)-2,5-diphenyltetrazolium bromide) was performed to establish the cell viability and the results obtained are summarized in Figure 2. Free-base porphyrins **3** and **6** containing imidazolium salts are rather non-toxic up to 2 μM with less than 15% cell death irrespective of the presence or not of a linker between the porphyrin core and

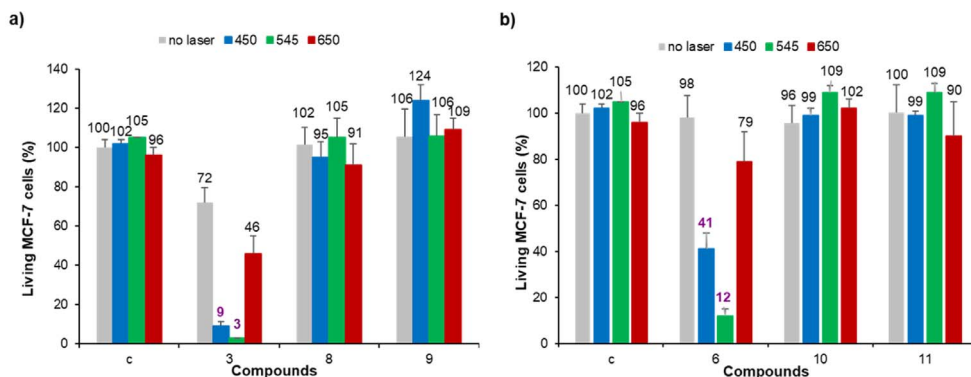


Figure 3. Photodynamic effect of imidazolium salts **3** and **6**, and their corresponding gold(I) complexes **8-11** on MCF-7 cancer cells. The cells were incubated with 0.5 μM of each compound for 24 h and then submitted to laser irradiation at $\lambda = 450, 545$ or 650 nm for 10 min. Cells are allowed to grow for 48 h and cell viability was quantified with MTT assay.

the NHC. In contrast, gold(I) complexes' cytotoxicity strongly depends on the presence or not of a linker between the porphyrin core and the NHC. Indeed, complex **8** without linker between the porphyrin core and the NHC is not cytotoxic at 2 μM . On the contrary, complex **10** with the *meso*-benzylic linker between the porphyrin core and the NHC shows a significant cytotoxicity with 60% cell death at 2 μM . Therefore, the closer are the porphyrin core and the NHC gold(I) complex, the lower is the observed cytotoxicity. This is in agreement with the low cytotoxicity observed for complex **B** (Scheme 1) where NHC ligand is fused to the porphyrin core. Compound **9** is a cationic bis(NHC) gold(I) complex and it seems that the positive charge tends to increase the observed cytotoxicity since ~50% cell death was observed at 2 μM . Compared to complex **10**, cytotoxicity of the corresponding gold(I) complex **11** including a free-base porphyrin is similar to a concentration up to 1 μM . The lower cytotoxicity observed for complex **11** at a concentration of 2 μM may be attributed to its low solubility in the cell culture medium.

Photodynamic properties of the different compounds were then investigated at 0.5 μM since no or moderate cytotoxicity was observed at this concentration. MCF-7 cancer cells were incubated with the different PS for 24 h and submitted to laser irradiation at $\lambda = 450, 545$ or 650 nm for 10 min. The results obtained after MTT assay to estimate cell viability are gathered in Figure 3. As can be seen in this fig-

ure, none of the gold(I) complexes showed significant photodynamic effect whatever the irradiation wavelength. This is in agreement with our previous finding that gold(I) complexes without any specific targeting agent are not suitable PS for PDT, although their $^1\text{O}_2$ quantum yields may be improved through heavy atom effect [45]. On the contrary, both imidazolium salts **3** and **6** induced important cell death under laser irradiation at $\lambda = 450$ and 545 nm. The best photodynamic effect was observed for imidazolium salt **6** at 0.5 μM which induced ~86% cell death after 10 min of irradiation at $\lambda = 545$ nm.¹ The good solubility of imidazolium salts in aqueous media and the fact that these cationic species can strongly interact with the negatively charged cancer cell membranes can explain the observed enhanced photodynamic activity compared to the corresponding gold(I) complex. Nevertheless, photodynamic activity of both imidazolium salts **3** and **6** is weaker under irradiation at $\lambda = 650$ nm since less than ~19–26% cell death was observed (see footnote 1). This prompted us to investigate the functionalization of pyropheophorbide *a* with imidazole and imidazolium groups and their use for PDT applications.

¹The values of photo-induced cell death are related to the non-irradiated cells in the same experiment to fairly describe the PDT efficiency, i.e. the cell death induced by light excitation only.

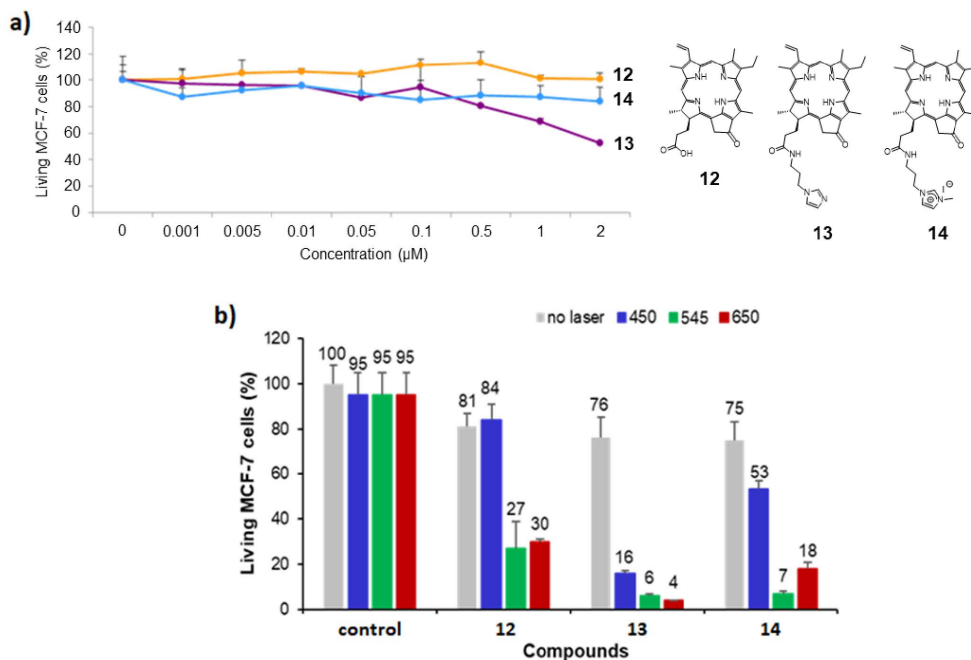


Figure 5. (a) Cytotoxic effect of chlorin derivatives **12–14** on MCF-7 cancer cells. The cells were incubated without (control) or with different concentrations of compounds **12–14** for 72 h. Cell viability was quantified with MTT assay. Data are mean values standard deviation from three independent experiments. (b) Photodynamic effect of the chlorin derivatives **12–14** under irradiation at $\lambda = 450$ nm (left), 545 nm (middle) and 650 nm (right). MCF-7 cancer cells were incubated with 0.5 μM of each chlorin for 24 h and then submitted to laser irradiation for 10 min. Cells were allowed to grow for 48 h and the living MCF-7 cells were quantified with MTT assay.

The cytotoxicity studies of chlorin derivatives **12–14** on MCF-7 breast cancer cells are summarized in Figure 5a and revealed that pyropheophorbide *a* **12** and imidazolium salt **14** were not cytotoxic on MCF-7 cells because they induce less than 10% cell death at a concentration of 2 μM . On the contrary, imidazole **13** exhibits significant cytotoxicity at 1 μM , with more than 30% cell death (~45% cell death at 2 μM). According to these results, photodynamic activity of chlorin derivatives **12–14** was evaluated with PS concentration of 0.5 μM under irradiation at $\lambda = 450, 545$ and 650 nm. The obtained data are summarized in Figure 5b. Upon irradiation at $\lambda = 450$ nm, only imidazole **13** exhibited a strong photodynamic effect by inducing 60% cell death. Imidazolium salt **14** revealed a slightly phototoxic activity with 22% cell death, whereas pyropheophorbide *a* **12** was not phototoxic at all (Figure 5b, left). Upon irradiation at $\lambda = 545$ and 650 nm, all chlorin derivatives **12–14** turned out to be phototoxic (Figure 5b, middle and right).

The significant phototoxicity of the three chlorins observed upon irradiation at $\lambda = 650$ nm constitutes the noteworthy result in this study, since synthetic imidazolium salts **3** and **6** induced less than ~19–26% cell death upon irradiation at $\lambda = 650$ nm (Figure 3). Chlorin derivatives **12, 13** and **14**, induced 51%, 72% and 57% cell death, respectively, and turned out to be better photosensitizers upon irradiation with red light (see footnote 1).

3. Conclusion

Porphyryns bearing imidazolium salts were used as NHC precursors for the synthesis of gold(I) complexes with the aim to combine their cytotoxicity with PDT. This study shows that porphyryns conjugated with NHC-gold(I) complexes are metallo-drugs possessing anticancer properties, as long as the NHC ligand is not directly bonded to the porphyrin core: a spacer is probably needed to keep away

the NHC-gold(I) complex from the bulky porphyrin core. Although heavy atom effect may be beneficial to improve $^1\text{O}_2$ production, these porphyrins conjugated with gold(I) complexes are not suitable PS for PDT. Additional functionalization with targeting agents is necessary to ensure active targeting of the cancer cells and simultaneously better solubility in aqueous media [68–70]. By contrast, the corresponding porphyrins equipped with imidazolium salt moieties are suitable PS for PDT and this effect is attributed to the positive charges of the imidazolium cations, which are known to ensure strong interactions with negatively charged cancer cell membranes. These cationic porphyrins can induce significant cell death upon laser irradiation at 450 and 545 nm, but not at 650 nm. To improve light absorption and photodynamic effect at 650 nm, pyropheophorbide *a* derivatives equipped with pendant imidazole/imidazolium groups were synthesized. These hemisynthetic compounds proved to be efficient PS for PDT at 650 nm.

4. Experimental section

4.1. Materials and instruments

Reactions needing inert atmosphere were performed under argon using oven-dried glassware and Schlenk techniques. Dry THF was obtained by a PureSolve MD5 solvent purification system from Innovative Technology. Dry DMF was purchased from Sigma-Aldrich. Dry CH_2Cl_2 and THF were obtained by a PureSolve MD5 solvent purification system from Innovative Technology. Gold(I) complex $[\text{AuCl}(\text{tht})]$ (tht = tetrahydrothiophene) was prepared according to the procedure described in literature [71]. Pyrrole (>99%) was purchased from TCI and distilled under reduced pressure before use. Imidazole (99.5%), iodomethane (99%) and zinc(II) acetate dihydrate (>98%) were purchased from Sigma-Aldrich. Silver tetrafluoroborate (99%) and hydrogen tetrachloroaurate(III) trihydrate ACS 99.99%, Au 49.0% min was used as starting material and purchased from Alfa Aesar. TLC were carried out on Merck DC Kieselgel 60 F-254 aluminum sheets and spots were visualized with UV-lamp ($\lambda = 254/365$ nm) if necessary. Preparative purifications were performed by silica gel flash column chromatography (Merck 40–60 μM). NMR spectroscopy and MS spectrometry were performed at the Laboratoire de Mesures Physiques

(LMP) of the University of Montpellier (UM). NMR spectra were recorded on Bruker 400 MHz Avance III HD or 600 MHz Avance III spectrometers at 298K. DMSO- d_6 , CD_2Cl_2 and CD_3OD were used as received (purchased from Eurisotop, France). ^1H and $^{13}\text{C}\{^1\text{H}\}$ NMR spectra were calibrated to TMS on the basis of the relative chemical shift of the residual non-deuterated solvent as an internal standard. Chemical shifts (δ) are expressed in ppm from the residual non-deuterated solvent signal and coupling constants values (nJ) are expressed in Hz. Abbreviations used for NMR spectra are as follows: s, singlet; d, doublet; t, triplet; m, multiplet. Mass spectra (HRMS) were recorded on ESI-TOF Q instruments in positive/negative modes. UV-visible absorption spectra were recorded at 25 °C on a JASCO V-650 spectrophotometer in 10 mm quartz cells (Hellma). Molar extinction coefficients ϵ ($\text{L}\cdot\text{mol}^{-1}\cdot\text{cm}^{-1}$) are expressed as $\log \epsilon$.

4.2. Synthesis and characterization of the different compounds

4.2.1. Porphyrin 1

The synthesis and characterization data of the porphyrin **1** were reported in [46].

4.2.2. Porphyrin 2

Porphyrin **1** (150 mg, 0.225 mmol, 1.0 eq) and imidazole (150 mg, 2.25 mmol, 10 eq) were dissolved in dry DMF (11 mL). The solution was purged under Argon atmosphere for 10 min. NaH (60% in suspension in oil, 85 mg, 2.22 mmol, 10 eq) was added and the reaction mixture was stirred at room temperature for 30 min. Then, the reaction mixture was stirred at 140 °C for 1 h. After cooling at room temperature, CH_2Cl_2 (150 mL) was added and the organic phase was washed (distilled H_2O), dried (MgSO_4) and concentrated. The residue was purified by column chromatography (SiO_2 , eluent from CH_2Cl_2 to $\text{CH}_2\text{Cl}_2/\text{MeOH}$ (98:2)) to give the porphyrin **2** in 72% yield (112 mg). **^1H NMR (400 MHz, CD_2Cl_2 , 298 K):** δ 8.86 (d, $^3J_{\text{H-H}} = 5.0$ Hz, 2H, $\text{H}_{\text{pyrrole}}$), 8.84–8.76 (m 4H, $\text{H}_{\text{pyrrole}}$), 8.66 (d, $^3J_{\text{H-H}} = 5.0$ Hz, 2H, $\text{H}_{\text{pyrrole}}$), 8.37 (s, 1H, H^2), 8.05 (s, 1H, H^5), 8.02 (dd, $^3J_{\text{H-H}} = 7.8$ Hz, $^4J_{\text{H-H}} = 1.6$ Hz, H_o), 7.90 (d, $^3J_{\text{H-H}} = 8.0$ Hz, 4H, H_a), 7.79–7.64 (m, 3H, H_m), 7.52 (m, 5H, H_b and H^4), 2.65 (s, 6H, $\text{CH}_{3\text{tolyl}}$). **$^{13}\text{C}\{^1\text{H}\}$ NMR (150.9 MHz, CD_2Cl_2 ,**

298, K): δ 144.4, 144.2, 143.7, 142.4, 141.1, 138.5, 137.9, 134.2, 134.2, 134.1 133.2, 133.2, 129.1, 128.7, 128.5, 128.2, 127.5, 121.2, 120.9, 112.8, 21.7 (CH₃tolyl) ppm. **UV-visible (DMSO):** $\lambda_{\max}(\log \epsilon)$: 414 (5.39), 526 (4.26) nm. **MALDI-TOF⁺ MS:** calcd for C₄₃H₃₀N₆Ni: 689.2, found 689.2.

4.2.3. Porphyrin 3

Porphyrin **2** (125 mg, 0.18 mmol, 1.0 eq) was dissolved in a TFA/H₂SO₄ 4:1 (v:v) mixture and the reaction was stirred for 45 min at room temperature. Then, the mixture was poured into ice and water and neutralized by K₂CO₃(s). The organic phase was extracted with CH₂Cl₂, dried (MgSO₄), and concentrated. The residue was purified by column chromatography (SiO₂, eluent CH₂Cl₂). Recrystallization from CH₂Cl₂/*n*-hexane afforded the free base corresponding porphyrin in 87% yield (100 mg). Then, the obtained compound (90 mg, 0.14 mmol, 1.0 eq) was dissolved in dry THF (25 mL) and CH₃I (2.2 mL, excess) was added. The reaction was stirred at 40 °C for 18 h under argon. Recrystallization from CH₂Cl₂/*n*-hexane afforded the porphyrin **3** as a purple solid in 89% yield (98 mg).

¹H NMR (400 MHz, CD₂Cl₂, 298 K): δ 10.44 (t, ³J_{H-H} = 1.7 Hz, 1H, H²), 9.06–8.98 (m, 5H, H_{pyrrole} and H⁵), 8.90–8.86 (m, 4H, H_{pyrrole}), 8.40 (t, ³J_{H-H} and ⁴J_{H-H} = 1.7 Hz, 1H, H⁴), 8.24–8.19 (m, 2H, H_o), 8.11 (d, ³J_{H-H} = 7.3 Hz, 4H, H_a), 7.92–7.82 (m, 3H, H_m and H_p), 7.68 (d, ³J_{H-H} = 7.3 Hz, 4H, H_b), 4.31 (s, 3H, N-CH₃), 2.69 (s, 6H, CH₃tolyl), –2.95 (s, 2H, NH) ppm. **¹³C{¹H} NMR (150.9 MHz, DMSO-*d*₆, 298 K):** δ 142.5, 140.9, 137.9, 137.5, 134.4, 139.3, 134.3, 134.2, 132.7, 131.9, 130.2, 128.5, 128.2, 128.0, 127.1, 123.3, 123.1, 121.9, 108.7, 36.8 (NCH₃), 21.2 (CH₃tolyl) ppm. **UV-visible (DMSO):** $\lambda_{\max}(\log \epsilon)$ = 413 (5.32), 525 (4.19), 615 (3.37) nm. **HR ESI-MS (positive mode):** calcd for C₄₄H₃₅N₆⁺: 647.2918, found: 647.2926. **ESI-MS (negative mode):** calcd for I[–]: 126.91, found: 126.96.

4.2.4. Porphyrin 4-I

Porphyrin **3** (50 mg, 0.065 mmol, 1.0 eq) was dissolved in CHCl₃(5.5 mL). A solution of Zn(OAc)₂ · 2H₂O (19.8 mg, 0.090 mmol, 1.4 eq) in MeOH (1.5 mL) was added and the reaction was stirred at 50 °C for 1 h. After evaporation of the solvent, recrystallization from CH₂Cl₂/*n*-hexane afforded the porphyrin **4-I** in 80% yield (44 mg). **¹H NMR (400 MHz, DMSO-*d*₆, 298 K):** δ 10.40–10.36

(br s, 1H, H²), 8.95 (t, ³J_{H-H} and ⁴J_{H-H} = 1.8 Hz, 1H, H⁵), 8.92 (s, 4H, H_{pyrrole}), 8.86–8.78 (m, 4H, H_{pyrrole}), 8.38 (t, ³J_{H-H} and ⁴J_{H-H} = 1.8 Hz, 1H, H⁴), 8.22–8.14 (m, 2H, H_o), 8.10–8.02 (m, 4H, H_a), 7.88–7.76 (m, 3H, H_m and H_p), 7.64 (d, ³J_{H-H} = 7.4 Hz, 4H, H_b), 4.30 (s, 3H, N-CH₃), 2.68 (s, 6H, CH₃tolyl) ppm. **¹³C{¹H} NMR (150.9 MHz, DMSO-*d*₆, 298 K):** δ 150.6, 150.1, 149.5, 146.9, 142.2, 142.2, 139.1 137.1, 134.3, 134.2, 134.1, 132.7, 133.7, 132.7, 132.3, 130.4, 128.0, 127.9, 127.6, 127.5, 126.8, 123.4, 123.0, 122.2, 108.9, 36.8 (N-CH₃), 21.2 (CH₃tolyl) ppm. **UV-visible (DMSO):** $\lambda_{\max}(\log \epsilon)$ = 426 (5.37), 516 (3.42), 599 (3.60) nm. **ESI-MS (positive mode):** calcd for C₄₄H₃₃N₆Zn⁺: 709.21, found: 709.28. **ESI-MS (negative mode):** calcd for I[–]: 126.91, found: 126.96.

4.2.5. Porphyrin 4-BF₄

Porphyrin **4-I** (160 mg, 0.19 mmol, 1.0 eq) was dissolved in acetone (50 mL). Then, a solution of AgBF₄ (39.5 mg, 0.20 mmol, 1.1 eq) in acetone (2.5 mL) was added dropwise and the reaction mixture was stirred for 1 h under argon at room temperature in the dark. After evaporation, the crude product was purified by column chromatography (SiO₂, eluent from CH₂Cl₂ to CH₂Cl₂/MeOH 95:5, (v:v)). Recrystallization from CH₂Cl₂/*n*-hexane afforded the porphyrin **4-BF₄** in 85% yield (125 mg). **¹H NMR (400 MHz, DMSO-*d*₆, 298 K):** δ 10.39 (br dd, 1H, H²), 8.95 (t, ³J_{H-H} and ⁴J_{H-H} = 1.8 Hz, 1H, H⁵), 8.91 (s, 4H, H_{pyrrole}), 8.84–8.76 (m, 4H, H_{pyrrole}), 8.37 (t, ³J_{H-H} and ⁴J_{H-H} = 1.8 Hz, 1H, H⁴), 8.21–8.15 (m, 2H, H_o), 8.08–8.03 (m, 4H, H_a), 7.83–7.79 (m, 3H, H_m and H_p), 7.63 (d, ³J_{H-H} = 7.4 Hz, 4H, H_b), 4.30 (s, 3H, N-CH₃), 2.68 (s, 6H, CH₃tolyl) ppm. **¹³C{¹H} NMR (150.9 MHz, DMSO-*d*₆, 298 K):** δ 150.6, 150.1, 149.5, 146.9, 142.2, 142.2, 139.1 137.1, 134.3, 134.2, 134.1, 132.7, 133.7, 132.7, 132.3, 130.4, 128.0, 127.9, 127.6, 127.5, 126.8, 123.4, 123.0, 122.2, 108.9, 36.8 (N-CH₃), 21.2 (CH₃tolyl) ppm. **¹⁹F (400 MHz, DMSO-*d*₆, 298 K):** δ –149.26 (s), –149.20 (s) ppm. **UV-visible (CH₂Cl₂):** $\lambda_{\max}(\log \epsilon)$ = 420 (5.79), 518 (3.18), 548 (4.40) nm. **ESI-MS (positive mode):** calcd for C₄₄H₃₃N₆Zn⁺: 709.21, found: 709.28. **ESI-MS (negative mode):** calcd for BF₄[–]: 87.00, found: 86.98.

4.2.6. Porphyrin 5

The synthesis and characterization data of the porphyrin **5** were reported in [47].

4.2.7. Porphyrin 6

Porphyrin **5** (160 mg, 0.2 mmol, 1.0 eq) was dissolved in dry DMF (15 mL) and 1-methylimidazole (1.1 mL, 100 eq) was added. The solution was stirred at 80 °C for 24 h under argon atmosphere. Alkylation completion was monitored by TLC. Once finished, the solvent was evaporated under reduced pressure. Recrystallization from CH₂Cl₂/*n*-hexane gave the porphyrin **6** in 78% yield (138 mg). **¹H NMR (400 MHz, CD₂Cl₂, 298 K):** δ 11.17 (br s, 1H, H²), 8.76 (d, ³J_{H-H} = 4.8 Hz, 2H, H_{pyrrole}), 8.67 (d, ³J_{H-H} = 4.8 Hz, 2H, H_{pyrrole}), 8.63 (br s, 4H, H_{pyrrole}), 8.28 (d, ³J_{H-H} = 8.0 Hz, 2H, H_o), 7.86 (d, ³J_{H-H} = 8.0 Hz, 2H, H_m), 7.45 (t, ³J_{H-H} and ⁴J_{H-H} = 1.8 Hz, 1H, H⁵), 7.31 (dd, ³J_{H-H} and ⁴J_{H-H} = 1.8 Hz, 1H, H⁴), 7.29 (broad s, 6H, H_{mes meta}), 5.94 (s, 2H, CH₂), 4.16 (s, 3H, N-CH₃), 2.61 (s, 9H, CH_{3 mes para}), 1.83–1.86 (2s, 18H, CH_{3 mes ortho}), –2.62 (s, 2H, NH) ppm. **¹³C{¹H} NMR (150.9 MHz, CD₂Cl₂, 298 K):** δ 143.9, 139.9, 139.8, 138.7, 138.6, 138.5, 135.8, 133.3, 128.3, 127.9, 123.9, 122.4, 121.0, 118.6, 118.6, 118.4, 22.0, 21.9, 21.7 ppm. **UV-visible (CH₂Cl₂):** λ_{max}(log ε) = 418 (5.41), 515 (4.05), 548 (3.55), 590 (3.52), 648 (3.31) nm. **HR ESI-MS (positive mode):** calcd for C₅₈H₅₅N₆⁺: 835.4488, found: 835.4494.

4.2.8. Porphyrin 7

Porphyrin **6** (110 mg, 0.126 mmol, 1.0 eq) was dissolved in CHCl₃ (12 mL). A solution of Zn(OAc)₂ · 2H₂O (41.6 mg, 0.189 mmol, 1.5 eq) in MeOH (2.6 mL) was added and the solution was stirred at 50 °C for 1 h. Then, the solvent was evaporated under reduced pressure. Recrystallization from CH₂Cl₂/*n*-hexane afforded the porphyrin **7** in 90% yield (106 mg). **¹H NMR (400 MHz, DMSO-*d*₆, 298 K):** δ 9.46 (t, ⁴J_{H-H} = 1.7 Hz, 1H, H²), 8.64 (d, ³J_{H-H} = 4.6 Hz, 2H, H_{pyrrole}), 8.56 (d, ³J_{H-H} = 4.6 Hz, 2H, H_{pyrrole}), 8.54–8.50 (m, 4H, H_{pyrrole}), 8.22 (d, ³J_{H-H} = 8.1 Hz, 2H, H_o), 8.07 (t, ³J_{H-H} and ⁴J_{H-H} = 1.7 Hz, 1H, H⁵), 7.87 (t, ³J_{H-H} and ⁴J_{H-H} = 1.7 Hz, 1H, H⁴), 7.77 (d, ³J_{H-H} = 8.1 Hz, 2H, H_m), 7.30 (broad s, 6H, H_{mes meta}), 5.78 (s, 2H, CH₂), 3.98 (s, 3H, N-CH₃), 2.57 (s, 9H, CH_{3 mes para}), 1.78, 1.77, 1.75 (3s, 18H, CH_{3 mes ortho}) ppm. **¹³C{¹H} NMR (150.9 MHz, DMSO-*d*₆, 298 K):** δ 149.0, 149.0, 148.9, 148.8, 143.2, 139.1, 139.0, 138.4, 138.4, 137.1, 136.9, 136.8, 134.6, 133.9, 131.5, 130.5, 130.0, 127.6, 126.2, 124.2, 122.8, 118.4, 117.7, 51.9, (–CH₂), 36.0 (N-CH₃), 21.6, 21.5,

21.0 (CH_{3 ortho}, CH_{3 para}) ppm. **UV-visible (CH₂Cl₂):** λ_{max}(log ε) = 420 (5.63), 549 (4.22) nm. **HR ESI-MS (positive mode):** calcd for C₅₈H₅₃N₆Zn⁺: 897.3623, found: 897.3632.

4.2.9. Gold(I) complex 8

Porphyrin **4-BF₄** (60 mg, 0.075 mmol, 1.0 eq) and [AuCl(tht)] (26.5 mg, 0.083 mmol, 1.1 eq) were dissolved in dry THF (6.3 mL). A solution of *t*BuOK (9.3 mg, 0.083 mmol, 1.1 eq) in THF/MeOH (2.3 mL/10 drops) was added dropwise and the reaction mixture was stirred at room temperature under argon for 18 h. After evaporation, the crude was purified by column chromatography (SiO₂, eluent CH₂Cl₂). Recrystallization from CH₂Cl₂/*n*-hexane gave the gold(I) complex **8** as a dark pink solid in 80% yield (72 mg).

¹H NMR (600 MHz, DMSO-*d*₆, 298 K): δ 8.87 (d, ³J_{H-H} = 4.6 Hz, 2H, H_{pyrrole}), 8.80–8.76 (m, 4H, H_{pyrrole}), 8.71 (d, ³J_{H-H} = 4.6 Hz, 2H, H_{pyrrole}), 8.52 (d, ³J_{H-H} = 1.9 Hz, 1H, H⁵), 8.21–8.11 (m, 4H, H_o), 8.06 (d, ³J_{H-H} = 1.9 Hz, 1H, H⁴), 8.02 (dd, ³J_{H-H} = 7.3 Hz and ⁴J_{H-H} = 2.1 Hz, 2H, H_a), 7.82–7.78 (m, 3H, H_m and H_p), 7.64–7.58 (m, 4H, H_b), 4.23 (s, 3H, N-CH₃), 2.67 (s, 6H, CH_{3 tolyl}) ppm. **¹³C{¹H} NMR (150.9 MHz, DMSO-*d*₆, 298 K):** δ 175.1 (C_{NHC}), 150.2, 150.0, 149.3, 148.1, 142.4, 139.3, 136.9, 134.15, 134.1, 134.0, 133.0, 132.1, 131.9, 130.2, 128.4, 127.3, 126.6, 122.4, 121.5, 121.2, 113.7, 38.1 (CH_{3 tolyl}), 21.1 (N-CH₃) ppm. **¹H DOSY NMR (600 MHz, CD₂Cl₂, 298 K):** 1.54 × 10^{–10} m²·s^{–1}. **UV-visible (CH₂Cl₂):** λ_{max}(log ε) = 420 (5.75), 548 (4.38) nm. **HR ESI-MS (positive mode):** calcd for C₄₄H₃₂AuClN₆Zn: 946.1911, found: 946.1923.

4.2.10. Gold(I) complex 9

Complex **8** (45 mg, 0.048 mmol, 1.0 eq) and porphyrin **4-BF₄** (34.6 mg, 0.044 mmol, 0.90 eq) were dissolved in acetone/MeOH (18 mL/0.5 mL). Then, K₂CO₃ (6.7 mg, 0.048 mmol, 1.0 eq) was added and the reaction mixture was stirred at room temperature for 16 h under argon in the dark. After evaporation, the crude was purified by column chromatography (SiO₂, eluent from CH₂Cl₂ to CH₂Cl₂/MeOH 95:5 (v:v)). Recrystallization from CH₂Cl₂/*n*-hexane afforded the gold(I) complex **9** in 52% yield (40 mg).

¹H NMR (600 MHz, DMSO-*d*₆, 298 K): δ 8.80 (s, 8H, H_{pyrrole}), 8.70 (d, 4H, ³J_{H-H} = 4.5 Hz, H_{pyrrole}), 8.45 (d, ³J_{H-H} = 1.8 Hz, 2H, H⁵), 8.32 (d,

$^3J_{\text{H-H}} = 4.5$ Hz, 4H, H_{pyrrole}), 8.22–8.17 (m, 4H, H_{O}), 8.04 and 7.98 (2dd AB system, $^3J_{\text{H-H}} = 7.7$ and 2.0 Hz, each 4H, H_{a}), 7.89–7.79 (m, 6H, H_{m} and H_{p}), 7.65 and 7.58 (2dd AB system, $^3J_{\text{H-H}} = 7.7$ and 2.0 Hz, each 4H, H_{b}), 7.34 (d, $^3J_{\text{H-H}} = 1.8$ Hz, 2H, H^4), 2.68 (s, 12H, $\text{CH}_3_{\text{tolyl}}$), 2.04 (s, 6H, N- CH_3) ppm. **$^{13}\text{C}\{^1\text{H}\}$ NMR (150.9 MHz, DMSO- d_6 , 298 K):** δ 188.8 (C_{NHC}), 150.2, 150.0, 149.8, 149.5, 147.6, 142.3, 139.2, 136.9, 134.1, 134.0, 133.9, 132.7, 132.3, 132.0, 129.7, 128.3, 127.7, 127.4, 126.7, 122.4, 121.5, 113.6, 35.1 ($\text{CH}_3_{\text{tolyl}}$), 21.0 (N- CH_3) ppm. **^1H DOSY NMR (600 MHz, CD_2Cl_2 , 298 K):** $1.15 \times 10^{-10} \text{m}^2 \cdot \text{s}^{-1}$. **UV-visible (CH_2Cl_2):** $\lambda_{\text{max}}(\log \epsilon) = 420$ (5.75), 548 (4.38) nm. **High-resolution ESI-MS (positive mode):** calcd for $\text{C}_{88}\text{H}_{32}\text{Au}_2\text{N}_{12}\text{Zn}_2^+$: 1617.3610, found: 1617.3612. **HR ESI-MS (negative mode):** calcd for BF_4^- : 87.00, found: 86.98.

4.2.11. Gold(I) complex 10

Porphyrin **7** (40 mg, 0.043 mmol, 1.0 eq) was dissolved in dry CH_2Cl_2 (10 mL). Then, Ag_2O (9.9 mg, 0.043 mmol, 1.0 eq) was added and the reaction mixture was vigorously stirred at room temperature under argon protected from light. After 16 h, $[\text{AuCl}(\text{tht})]$ (13.7 mg, 0.043 mmol, 1.0 eq) was added and the mixture was stirred for 18 h under the same conditions. The solvent was evaporated under reduced pressure and the crude compound was purified by column chromatography (SiO_2 , eluent CH_2Cl_2). Recrystallization from $\text{CH}_2\text{Cl}_2/n$ -hexane gave the gold(I) complex **10** as a red-purple solid in 41% yield (20 mg). **^1H NMR (400 MHz, CD_2Cl_2 , 298 K):** δ 8.84 (d, $^3J_{\text{H-H}} = 4.6$ Hz, 2H, H_{pyrrole}), 8.73 (d, $^3J_{\text{H-H}} = 4.6$ Hz, 2H, H_{pyrrole}), 8.69 (d, $^3J_{\text{H-H}} = 1.2$ Hz, 4H, H_{pyrrole}), 8.23 (d, $^3J_{\text{H-H}} = 8.0$ Hz, 2H, H_{O}), 7.69 (d, $^3J_{\text{H-H}} = 8.0$ Hz, 2H, H_{m}), 7.29 (broad s, 6H, $H_{\text{mes meta}}$), 7.26 (d, $^3J_{\text{H-H}} = 2.0$ Hz, 1H, H^5), 7.13 (d, $^3J_{\text{H-H}} = 2.0$ Hz, 1H, H^4), 5.74 (s, 2H, CH_2), 3.96 (s, 3H, N- CH_3), 2.62 (s, 9H, $\text{CH}_3_{\text{mes para}}$), 1.84–1.82 (2s, 18H, $\text{CH}_3_{\text{mes ortho}}$) ppm. **$^{13}\text{C}\{^1\text{H}\}$ NMR (150.9 MHz, CD_2Cl_2 , 298 K):** δ 172.3 (C_{NHC}), 150.4, 150.4, 150.3, 150.2, 143.8, 139.7, 139.6, 139.5, 139.4, 138.1, 135.4, 135.3, 138.4, 135.6, 135.5, 132.4, 131.6, 131.5, 131.1, 128.1, 126.5, 123.2, 121.4, 119.7, 119.4, 119.3, 55.5 (CH_2), 38.9 (N- CH_3), 22.0, 21.9, 21.7 ($\text{CH}_3_{\text{mes ortho}}$, $\text{CH}_3_{\text{mes para}}$) ppm. **UV-visible (CH_2Cl_2):** $\lambda_{\text{max}}(\log \epsilon) = 420$ (5.75), 549 (4.36) nm. **MALDI-TOF $^+$ MS:** calcd for $\text{C}_{64}\text{H}_{55}\text{Au}_4\text{N}_{12}\text{Cl}_4$: 1128.29, found 1128.30.

4.2.12. Gold(I) complex 11

Procedure A. Porphyrin **6** (40 mg, 0.043 mmol, 1.0 eq) was dissolved in dry THF (10.5 mL). Then, $[\text{AuCl}(\text{tht})]$ (15.4 mg, mmol, 1.1 eq) was added and the mixture was degassed with argon for 10 min. $t\text{BuOK}$ (6 mg, mmol, 1.1 eq) was dissolved in MeOH (0.5 mL) and added dropwise to the reaction mixture, which was stirred at room temperature for 18 h under argon in the dark. Then, the solvent was evaporated under reduced pressure and the residue was purified by column chromatography (SiO_2 , eluent CH_2Cl_2). Recrystallization from $\text{CH}_2\text{Cl}_2/n$ -hexane afforded the gold(I) complex **11** as a purple solid in 57% yield (28 mg). **Procedure B.** Porphyrin **10** (30 mg, 0.027 mmol) was dissolved in acetone (12 mL) under argon. Then, a $\text{CH}_2\text{Cl}_2/\text{TFA}$ 4:1 mixture (6 mL) was slowly added and the reaction mixture was stirred for 30 min. After neutralization with NaHCO_3 , the solvent was evaporated and the residue purified by column chromatography (SiO_2 , eluent CH_2Cl_2). Recrystallization from $\text{CH}_2\text{Cl}_2/n$ -hexane afforded the gold(I) complex **11** as a purple solid in 70% yield (20 mg). **^1H NMR (400 MHz, CD_2Cl_2 , 298 K):** δ 8.77 (d, $^3J_{\text{H-H}} = 4.8$ Hz, 2H, H_{pyrrole}), 8.67 (d, $^3J_{\text{H-H}} = 4.8$ Hz, 2H, H_{pyrrole}), 8.63 (s, 4H, H_{pyrrole}), 8.22 (d, $^3J_{\text{H-H}} = 8.0$ Hz, 2H, H_{O}), 7.69 (d, $^3J_{\text{H-H}} = 8.0$ Hz, 2H, H_{m}), 7.29 (s, 6H, $H_{\text{mes meta}}$), 7.24 (d, $^3J_{\text{H-H}} = 1.9$ Hz, 1H, H^5), 7.12 (d, 1H, $^3J_{\text{H-H}} = 1.9$ Hz, H^4), 5.73 (s, 2H, CH_2), 3.95 (s, 3H, N- CH_3), 2.61 (s, 9H, $\text{CH}_3_{\text{mes para}}$), 1.86–1.84 (2s, 18H, $\text{CH}_3_{\text{mes ortho}}$), -2.62 (s, 2H, NH) ppm. **$^{13}\text{C}\{^1\text{H}\}$ NMR (150.9 MHz, CD_2Cl_2 , 298 K):** δ 172.5 (C_{NHC}), 143.0, 139.9, 138.9, 138.8, 138.6, 138.4, 135.6, 135.5, 128.3, 126.7, 123.2, 121.4, 118.8, 118.6, 118.4, 55.5 (CH_2), 39.0 (N- CH_3), 21.9 (2s, $\text{CH}_3_{\text{mes ortho}}$), 21.7 ($\text{CH}_3_{\text{mes para}}$) ppm. **UV-visible (CH_2Cl_2):** $\lambda_{\text{max}}(\log \epsilon) = 418$ (5.65), 514 (4.28), 548 (3.80), 590 (3.75), 647 (3.55) nm. **MALDI-TOF $^+$ MS:** calcd for $\text{C}_{64}\text{H}_{55}\text{Au}_4\text{N}_{12}\text{Cl}_4$: 1066.38, found 1066.40.

4.2.13. Pyropheophorbide a 12

The synthesis and characterization data of **pyropheophorbide a 12** were reported in [63–66].

4.2.14. Chlorin 13

Pyropheophorbide **a 12** (62 mg, 0.12 mmol, 1.0 eq), 1-(3-aminopropyl)imidazole (18.6 μL , 0.16 mmol, 1.4 eq) and 4-DMAP (18.4 mg, 0.15 mmol, 1.3 eq) were dissolved in dry CH_2Cl_2 (4.0 mL). DCC

(31.1 mg, 0.15 mmol, 1.3 eq) was portionwise added at 0 °C under argon atmosphere. The reaction mixture was stirred at room temperature for 3 h in the dark. The reaction was monitored by TLC. Once finished, H₂O (4.0 mL) was added and the mixture was stirred for 15 min. Then, organic phase was extracted with CH₂Cl₂, washed (distilled H₂O), dried (MgSO₄) and concentrated. The residue was dissolved in a minimum amount of CH₂Cl₂ and refrigerated overnight. The crude was then filtered, washed with cold CH₂Cl₂, and the filtrate was concentrated (the operation was reiterated twice). Recrystallization from CH₂Cl₂/*n*-hexane afforded the chlorin **13** as a dark green solid in 46% yield (34 mg). **¹H NMR (400 MHz, CD₂Cl₂, 298 K):** δ 9.44, 9.41, 8.64 (each s, each 1H, 5, 10 and 20-H), 8.04 (dd, ³J_{H-H} = 17.8, 11.6 Hz, 1H, 3¹), 7.18 (br dd, 1H, H_d), 6.81 (br dd, ³J_{H-H} = 1.3 Hz and ⁴J_{H-H} = 1.3 Hz, 1H, H_f), 6.62 (br dd, ³J_{H-H} = 1.3 Hz and ⁴J_{H-H} = 1.3 Hz, 1H, H_e), 6.34–6.16 (m, 2H, 3²), 5.24 and 5.06 (2d AB system, ²J_{H-H} = 19.8 Hz, each 1H, 13²), 4.58–4.51, 4.39–4.36 (each m, each 1H, 17 and 18), 3.75–3.69 (m, 2H, 8¹), 3.59–3.49 (m, 2H, H_c), 3.65, 3.43, 3.26 (each s, each 3H, 2¹, 7¹ and 12¹), 2.89–2.72, 2.66–2.42, 2.25–2.17 and 1.95–1.80 (each m, each 2H, 17¹, 17², H_a and H_b), 1.81 (d, ³J_{H-H} = 7.3 Hz, 3H, 18¹), 1.67 (t, ³J_{H-H} = 7.6 Hz, 4H, 8²), –1.79 (s, 2H, NH) ppm. **UV-visible (CH₂Cl₂):** λ_{max}(log ε) = 412 (4.57), 508 (3.88), 538 (3.82), 609 (3.75), 667 (4.13) nm. **MALDI-TOF⁺ MS:** calcd for C₃₉H₄₃N₇O₂ 642.35, found 642.30.

4.2.15. Chlorin **14**

Chlorin **13** (30 mg, 0.047 mmol, 1.0 eq) was dissolved in dry THF (6.0 mL) and CH₃I (290 μL, 4.7 mmol, 100 eq) was added. The solution was stirred at 40 °C for two days under argon atmosphere and protected from light. The reaction was monitored by TLC. After evaporation of the solvent, recrystallization from CH₂Cl₂/*n*-hexane afforded the monocationic chlorin **14** as a black solid in 52% yield (19 mg). **¹H NMR (400 MHz, (CD₂Cl₂/CD₃OD 9:1 (v:v), 298 K):** δ 9.50, 9.37, 8.72 (each s, each 1H, 5, 10 and 20-H), 9.26 (br s, 1H, H_d), 8.04 (dd, ³J_{H-H} = 17.9, 11.5 Hz, 1H, 3¹), 7.04, 6.98 (each br s, each 1H, H_e and H_f), 6.31 and 6.18 (2d AB system, ²J_{H-H} = 19.8 Hz, each 1H, 3²), 5.32 and 5.07 (2 d AB system, ²J_{H-H} = 19.2 Hz, each 1H, 13²), 4.70–4.64 and 4.33–4.28 (each m, each 1H, 17 and 18), 3.79 (s, 3H, H_g), 3.62 and 3.23 (each s, each

3H), 3.00–2.91 (m, 2H, H_a), 2.71–2.56 and 2.43–2.32 (each m, each 3H, 17¹, 17² and H_b), 1.81 (d, ³J_{H-H} = 7.4 Hz, 1H, 18¹), 1.69 (t, ³J_{H-H} = 7.6 Hz, 4H, 8²), –1.75 (s, 2H, NH) ppm. **¹³C{¹H} NMR (150.9 MHz, (CD₂Cl₂/CD₃OD 9:1 (v:v), 298 K):** δ 197.1 (C=O), 174.4, 173.1, 161.8, 155.6, 151.1, 149.4, 145.6, 142.1, 138.1, 137.3, 136.7 (2s), 136.1, 132.8, 130.8, 129.6, 128.6, 123.5, 122.9, 122.7, 104.4, 97.1, 94.5, 52.5, 50.5, 49.6, 48.8, 47.7, 37.0, 35.7, 34.4, 33.6, 31.0, 29.9, 26.2, 25.6, 23.5, 19.9, 17.7, 12.5, 12.2, 11.5 ppm. **UV-visible (CH₂Cl₂):** λ_{max}(log ε) = 413 (4.67), 509 (3.75), 540 (3.67), 610 (3.61), 668 (4.28) nm. **HR ESI-MS (positive mode):** calcd for C₄₀H₄₆N₇O₂⁺ 656.3708 found 656.3694. **HR ESI-MS (negative mode):** calcd for I[–]: 126.9050 found: 126.9046.

4.3. Biological studies

Cell culture. Human breast cancer cells (MCF-7) were purchased from ATCC (American Type Culture Collection, Manassas, VA). Cells were cultured in Dulbecco's Modified Eagle's Medium (DMEM-F12) supplemented with 10% fetal bovine serum and 1% penicillin–streptomycin. Cells were allowed to grow in humidified atmosphere at 37 °C under 5% CO₂.

4.3.1. Cytotoxicity study in the dark

MCF-7 cells were seeded into 96-well plates at 5000 cells per well in 200 μL culture medium and allowed to grow for 24 h. Increasing concentrations (from 0 to 2 μM) of compounds were incubated in culture medium of MCF-7 cells during 72 h. Then, a MTT assay was performed to evaluate the toxicity. Briefly, cells were incubated for 4 h with 0.5 mg·mL^{–1} of MTT (3-(4,5-dimethylthiazol-2-yl)-2,5-diphenyltetrazolium bromide; Promega) in media. The MTT/media solution was then removed, and the precipitated crystals were dissolved in EtOH/DMSO (1:1). The solution absorbance was read with a microplate reader at 540 nm.

4.3.2. PDT experiments

For 450 nm and 545 nm *in vitro* phototoxicity, 1000 cells by well were plated in a 384-well plates, in 50 μL of culture medium. Twelve hours after seeding, compounds were added on cells at a concentration of 0.5 μM for 24 h. After this incubation, cells were submitted (or not) to laser irradiation for 10 min with the Leica DM IRB at 450 nm (4.6 J·cm^{–2}) or 545 nm

($19.5 \text{ J}\cdot\text{cm}^{-2}$). The laser beam was focussed by a microscope objective lens (magnification $\times 4$). Two days after irradiation, an MTT assay was performed to measure the cell viability. For 650 nm *in vitro* phototoxicity, 5000 cells by well were plated in a 96-well plates, in $100 \mu\text{L}$ of culture medium. Twelve hours after seeding, compounds were added on cells at a concentration of $0.5 \mu\text{M}$ for 24 h. Then, cells were submitted (or not) to laser irradiation with a red laser at 650 nm for 10 min ($18.75 \text{ J}\cdot\text{cm}^{-2}$). Two days after irradiation, an MTT assay was performed to evaluate the cell viability.

Acknowledgments

The authors are grateful to the University of Montpellier, the CNRS and the French Ministry of Research for financial support. SR is also grateful for financial support from the Région Languedoc-Roussillon (Research Grant Chercheur(se)s d'Avenir – 2015-005984) and the FEDER Program (Fonds Européen de Développement Régional).

Supplementary data

Supporting information for this article is available on the journal's website under <https://doi.org/10.5802/crchim.98> or from the author.

References

- [1] T. J. Dougherty, C. J. Gomer, B. W. Henderson, G. Jori, D. Kessel, M. Korbelik, J. Moan, Q. Peng, *J. Natl. Cancer Inst.*, 1998, **90**, 889-905.
- [2] P. Jichlinski, H.-J. Leisinger, *Urol. Res.*, 2001, **29**, 396-405.
- [3] S. B. Brown, E. A. Brown, I. Walker, *Lancet Oncol.*, 2004, **5**, 497-508.
- [4] M. Ethirajan, Y. Chen, P. Joshi, R. K. Pandey, *Chem. Soc. Rev.*, 2011, **40**, 340-362.
- [5] B. W. Henderson, T. J. Dougherty, *Photochem. Photobiol.*, 1992, **55**, 145-157.
- [6] I. J. MacDonald, T. J. Dougherty, *J. Porphy. Phthalocyanines*, 2001, **5**, 105-129.
- [7] D. E. J. G. J. Dolmans, D. Fukumura, R. K. Jain, *Nat. Rev. Cancer*, 2003, **3**, 380-387.
- [8] E. Skovsen, J. W. Snyder, J. D. C. Lambert, P. R. Ogilby, *J. Phys. Chem. B*, 2005, **109**, 8570-8573.
- [9] A. E. O'Connor, W. M. Gallagher, A. T. Byrne, *Photochem. Photobiol.*, 2009, **85**, 1053-1074.
- [10] R. Bonnett, *Chem. Soc. Rev.*, 1995, **24**, 19-33.
- [11] E. D. Sternberg, D. Dolphin, C. Brückner, *Tetrahedron*, 1998, **54**, 4151-4202.
- [12] M. Ethirajan, N. J. Patel, R. K. Panda, "19 Porphyrin-Based Multifunctional Agents for Tumor-Imaging and Photodynamic Therapy (PDT)", in *Handbook of Porphyrin Science* (K. M. Kadish, K. M. Smith, R. Guilard, eds.), vol. 4, World Scientific, Singapore, 2010, 249-323.
- [13] P. M. Antoni, A. Naik, I. Albert, R. Rubbiani, S. Gupta, P. Ruiz-Sanchez, P. Munikorn, J. M. Mateos, V. Luginbuehl, P. Thamyongkit, U. Ziegler, G. Gasser, G. Jeschke, B. Spingler, *Chem. Eur. J.*, 2015, **21**, 1179-1183.
- [14] E. Zenkevich, E. Sagun, V. Knyukshto, A. Shulga, A. Mironov, O. Efremova, R. Bonnett, S. P. Songea, M. Kasem, *J. Photochem. Photobiol. B*, 1996, **33**, 171-180.
- [15] Z. Chen, W. Lu, C. Garcia-Prieto, P. Huang, *J. Bioenerg. Biomembr.*, 2007, **39**, 267-274.
- [16] C. Moylan, E. M. Scanlan, M. O. Senge, *Curr. Med. Chem.*, 2015, **22**, 2238-2348.
- [17] S. Singh, A. Aggarwal, N. V. S. D. K. Bhupathiraju, G. Arianna, K. Tiwari, C. M. Drain, *Chem. Rev.*, 2015, **115**, 10261-10306.
- [18] S. Richeter, C. Jeandon, J.-P. Gisselbrecht, R. Ruppert, in *Handbook of Porphyrin Science* (K. M. Kadish, K. M. Smith, R. Guilard, eds.), vol. 3, World Scientific, Singapore, 2010, 429-483.
- [19] J.-F. Longevial, C. Clément, J. A. Wytko, R. Ruppert, J. Weiss, S. Richeter, *Chem. Eur. J.*, 2018, **24**, 15442-15460.
- [20] H. Brunner, K.-M. Schellerer, B. Treittinger, *Inorg. Chim. Acta*, 1997, **264**, 67-79.
- [21] C. Lottner, K.-C. Bart, G. Bernhardt, H. Brunner, *J. Med. Chem.*, 2002, **45**, 2064-2078.
- [22] H. Brunner, K.-M. Schellerer, *Inorg. Chim. Acta*, 2003, **350**, 39-48.
- [23] C. Lottner, R. Knuechel, G. Bernhardt, H. Brunner, *Cancer Lett.*, 2004, **203**, 171-180.
- [24] C. Lottner, R. Knuechel, G. Bernhardt, H. Brunner, *Cancer Lett.*, 2004, **2015**, 167-177.
- [25] C. Lottner, K.-C. Bart, G. Bernhardt, H. Brunner, *J. Med. Chem.*, 2002, **45**, 2079-2089.
- [26] H. Brunner, N. Gruber, *Inorg. Chim. Acta*, 2004, **357**, 4423-4451.
- [27] A. Naik, R. Rubbiani, G. Gasser, B. Spingler, *Angew. Chem. Int. Ed.*, 2014, **53**, 6938-6941.
- [28] T. T. Tasso, T. M. Tsubone, M. S. Baptista, L. M. Mattiazzi, T. V. Acunha, B. A. Iglesias, *Dalton Trans.*, 2017, **46**, 11037-11045.
- [29] J. Onuki, A. V. Ribas, M. H. G. Medeiros, K. Araki, H. E. Toma, L. H. Catalani, P. Di Mascio, *Photochem. Photobiol.*, 1996, **63**, 272-277.
- [30] F. Schmitt, P. Govindaswamy, G. Süß-Fink, W. H. Ang, P. J. Dyson, L. Juillerat-Jeanneret, B. Therien, *J. Med. Chem.*, 2008, **51**, 1811-1816.
- [31] F. Schmitt, P. P. Govindaswamy, O. Zava, G. Süß-Fink, L. Juillerat-Jeanneret, B. Therien, *J. Biol. Inorg. Chem.*, 2009, **14**, 101-109.
- [32] F. Schmitt, N. P. E. Barry, L. Juillerat-Jeanneret, B. Therien, *Bioorg. Med. Chem. Lett.*, 2012, **22**, 178-180.
- [33] N. Sheng, D. Liu, J. Wu, B. Gu, Z. Wang, Y. Cui, *Dyes Pigm.*, 2015, **119**, 116-121.
- [34] J. X. Zhang, K.-L. Wong, W.-K. Wong, N.-K. Mak, D. W. J. Kwong, H.-L. Tam, *Org. Biomol. Chem.*, 2011, **9**, 6004-6010.
- [35] H. Ke, W. Ma, H. Wang, G. Cheng, H. Yuan, W.-K. Wong, D. W. J.

- Kwong, H.-L. Tam, K.-W. Cheah, C.-F. Chan, K.-L. Wong, *J. Lumin.*, 2014, **154**, 356-361.
- [36] S. Tasan, C. Licona, P.-E. Doulain, C. Michelin, C. P. Gros, P. Le Gendre, P. D. Harvey, C. Paul, C. Gaidon, E. Bodio, *J. Biol. Inorg. Chem.*, 2015, **20**, 143-154.
- [37] S. Richeter, A. Hadj-Aïssa, C. Taffin, A. van der Lee, D. Leclercq, *Chem. Commun.*, 2007, 2148-2150.
- [38] J.-F. Lefebvre, M. Lo, D. Leclercq, S. Richeter, *Chem. Commun.*, 2011, **47**, 2976-2978.
- [39] J.-F. Lefebvre, M. Lo, J.-P. Gisselbrecht, O. Coulembier, S. Clément, S. Richeter, *Chem. Eur. J.*, 2013, **19**, 15652-15660.
- [40] M. Abdelhameed, P.-L. Karsenti, A. Langlois, J.-F. Lefebvre, S. Richeter, R. Ruppert, P. D. Harvey, *Chem. Eur. J.*, 2014, **20**, 12988-13001.
- [41] J.-F. Lefebvre, J.-F. Longevial, K. Molvinger, S. Clément, S. Richeter, *C. R. Chim.*, 2016, **19**, 94-102.
- [42] J.-F. Longevial, A. Langlois, A. Buisson, C. H. Devillers, S. Clément, A. van der Lee, P. D. Harvey, S. Richeter, *Organometallics*, 2016, **35**, 663-672.
- [43] C. Rose, A. Lebrun, S. Clément, S. Richeter, *Chem. Commun.*, 2018, **54**, 9603-9606.
- [44] J.-F. Longevial, M. Lo, A. Lebrun, D. Laurencin, S. Clément, S. Richeter, *Dalton Trans.*, 2020, **49**, 7005-7014.
- [45] J.-F. Longevial, K. El Cheick, D. Aggad, A. Lebrun, A. van der Lee, F. Tielens, S. Clément, A. Morère, M. Garcia, M. Gary-Bobo, S. Richeter, *Chem. Eur. J.*, 2017, **23**, 14017-14026.
- [46] C. H. Devillers, S. Hebié, D. Lucas, H. Cattey, S. Clément, S. Richeter, *J. Org. Chem.*, 2014, **79**, 6424-6434.
- [47] J. S. Lindsey, S. Prathapan, T. E. Johnson, R. W. Wagner, *Tetrahedron*, 1994, **50**, 8941-8968.
- [48] S. Gaillard, A. M. Z. Slawin, A. T. Bonura, E. D. Stevens, S. P. Nolan, *Organometallics*, 2010, **29**, 394-402.
- [49] D. Marchione, M. A. Izquierdo, G. Bistoni, R. W. A. Havenith, A. Macchioni, D. Zuccaccia, F. Tarantelli, L. Belpassi, *Chem. Eur. J.*, 2017, **23**, 2722-2728.
- [50] M. Baker, P. J. Barnard, S. J. Berners-Price, S. K. Brayshaw, J. L. Hickey, B. W. Skelton, A. H. White, *Dalton Trans.*, 2006, 3708-3715.
- [51] J. L. Hickey, R. A. Ruhayel, P. J. Barnard, M. V. Baker, S. J. Berners-Price, A. Filipovska, *J. Am. Chem. Soc.*, 2008, **130**, 12570-12571.
- [52] R. Rubbiani, I. Kitanovic, H. Alborzinia, S. Can, A. Kitanovic, L. A. Onambebe, M. Stefanopoulou, Y. Geldmacher, W. S. Sheldrick, G. Wolber, A. Prokop, S. Wölfl, I. Ott, *J. Med. Chem.*, 2010, **53**, 8608-8618.
- [53] R. Rubbiani, S. Can, I. Kitanovic, H. Alborzinia, M. Stefanopoulou, M. Kokoschka, S. Monchgesang, W. S. Sheldrick, S. Wölfl, I. Ott, *J. Med. Chem.*, 2011, **54**, 8646-8657.
- [54] A. Gautier, F. Cisnetti, *Metallomics*, 2012, **4**, 23-32.
- [55] T. Zou, C. T. Lum, S. S.-Y. Chui, C.-M. Che, *Angew. Chem. Int. Ed.*, 2013, **52**, 2930-2933.
- [56] R. Rubbiani, E. Schuh, A. Meyer, J. Lemke, J. Wimberg, N. Metzler-Nolte, F. Meyer, F. Mohr, I. Ott, *Med. Chem. Commun.*, 2013, **4**, 942-948.
- [57] B. Bertrand, L. Stefan, M. Pirrotta, D. Monchaud, E. Bodio, P. Richard, P. Le Gendre, E. Warmerdam, M. H. de Jager, G. M. Groothuis, M. Picquet, A. Casini, *Inorg. Chem.*, 2014, **53**, 2296-2303.
- [58] R. Rubbiani, L. Salassa, A. de Almeida, A. Casini, I. Ott, *Chem. Med. Chem.*, 2014, **9**, 1205-1210.
- [59] P. Holenya, S. Can, R. Rubbiani, H. Alborzinia, A. Junger, X. Cheng, I. Ott, S. Wölfl, *Metallomics*, 2014, **6**, 1591-1601.
- [60] R. W.-Y. Sun, M. Zhang, D. Li, Z.-F. Zhang, H. Cai, M. Li, Y.-J. Xian, S. W. Ng, A. S.-T. Wong, *Chem. Eur. J.*, 2015, **21**, 18534-18538.
- [61] C. Schmidt, B. Karge, R. Misgeld, A. Prokop, R. Franke, M. Brönstrup, I. Ott, *Chem. Eur. J.*, 2017, **23**, 1869-1880.
- [62] B. Dominelli, J. D. G. Correia, F. E. Kuehn, *J. Organomet. Chem.*, 2018, **866**, 153-164.
- [63] K. M. Smith, D. A. Goff, D. J. Simpson, *J. Am. Chem. Soc.*, 1985, **107**, 4946-4954.
- [64] H. Tamiaki, M. Amakawa, Y. Shimono, R. Tanikaga, A. R. Holzwarth, K. Schaffner, *Photochem. Photobiol.*, 1996, **63**, 92-99.
- [65] H. Tamiaki, K. Fukai, H. Shimazu, S. Shoji, *Photochem. Photobiol.*, 2014, **90**, 121-128.
- [66] M. Chevrier, A. Fattori, L. Lasser, C. Kotras, C. Rose, M. Cangiotti, D. Beljonne, A. Mehdi, M. Surin, R. Lazzaroni, P. Dubois, M. F. Ottaviani, S. Richeter, J. Bouclé, S. Clément, *Molecules*, 2020, **25**, article no. 198.
- [67] G.-I. Sengge, N. Badraa, Y. K. Shim, *J. Porphyr. Phthalocyanines*, 2009, **13**, 818-822.
- [68] M. V. Baker, P. J. Barnard, S. J. Berners-Price, S. K. Brayshaw, J. L. Hickey, B. W. Skelton, A. H. White, *J. Organomet. Chem.*, 2005, **690**, 5625-5635.
- [69] J. Weaver, S. Gaillard, C. Toye, S. Macpherson, S. P. Nolan, A. Riches, *Chem. Eur. J.*, 2011, **17**, 6620-6624.
- [70] B. Bertrand, A. de Almeida, E. P. M. van der Burgt, M. Picquet, A. Citta, A. Folda, M. P. Rigobello, P. Le Gendre, E. Bodio, A. Casini, *Eur. J. Inorg. Chem.*, 2014, 4532-4536.
- [71] R. Usón, A. Laguna, M. Laguna, D. A. Briggs, H. H. Murray, J. P. Flacker Jr., *Inorg Synth.*, 1989, **26**, 85-91.



MAPYRO: the French Fellowship of the Pyrrolic Macrocyclic Ring / *MAPYRO: la communauté française des macrocycles pyrroliques*

Imbroglia at a photoredox-iron-porphyrin catalyst dyad for the photocatalytic CO₂ reduction

Adelais Trapali^{ⓑ a}, Philipp Gotico^{ⓑ b}, Christian Herrero^{ⓑ c}, Minh-Huong Ha-Thi^{ⓑ b},
Thomas Pino^{ⓑ b}, Winfried Leibl^{ⓑ d}, Georgios Charalambidis^{ⓑ *, a},
Athanasios Coutsolelos^{ⓑ *, a}, Zakaria Halime^{ⓑ *, c} and Ally Aukauloo^{ⓑ *, c, d}

^a Laboratory of Bioinorganic Chemistry, Chemistry Department, University of Crete, PO Box 2208, 71003 Heraklion, Crete, Greece

^b Université Paris-Saclay, CNRS, Institut des Sciences Moléculaires d'Orsay (ISMO), 91405, Orsay, France

^c Université Paris-Saclay, CNRS, Institut de Chimie Moléculaire et des Matériaux d'Orsay (ICMMO), 91405, Orsay, France

^d Université Paris-Saclay, CEA, Institute for Integrative Biology of the Cell (I2BC), 91198, Gif-sur-Yvette, France

E-mails: atrapali@uoc.gr (A. Trapali), philipp.gotico@universite-paris-saclay.fr (P. Gotico), christian.herrero@u-psud.fr (C. Herrero), minh-huong-ha-thi@universite-paris-saclay.fr (M.-H. Ha-Thi), thomas.pino@universite-paris-saclay.fr (T. Pino), winfried.leibl@cea.fr (W. Leibl), gcharal@uoc.gr (G. Charalambidis), acoutsol@uoc.gr (A. Coutsolelos), zakaria.halime@universite-paris-saclay (Z. Halime), ally.aukauloo@universite-paris-saclay (A. Aukauloo)

Abstract. We have covalently connected the ruthenium trisbipyridine complex (**bpyRu**) as a photoredox module to an iron porphyrin catalyst (**porFe**) through an amido function for investigating the synergistic action to power the photocatalytic CO₂ reduction. The electrochemical studies of the **porFe-bpyRu** dyad did not show any marked effect on the redox properties of the constitutive units. However, the photophysical properties of the **porFe-bpyRu** dyad point to the complete extinction of the photoredox module that undergoes ultrafast quenching processes with the **porFe** acolyte, the unavoidable dilemma in this type of molecular assemblies. Nevertheless, when exogenous **bpyRu** and a sacrificial electron donor were added to this dyad, we found that it exhibits much higher turnover number and selectivity towards CO₂ photocatalytic reduction to CO than with the iron porphyrin analogue (**porFe**). Comprehensive analyses of the data suggest that this catalytic enhancement displayed by the dyad can be attributed to an interesting electron relay role played by the appended **bpyRu** moiety.

Keywords. Supramolecular dyad, Iron porphyrins, Carbon dioxide reduction, Photocatalysis, Flash photolysis.

Available online 17th August 2021

* Corresponding authors.

1. Introduction

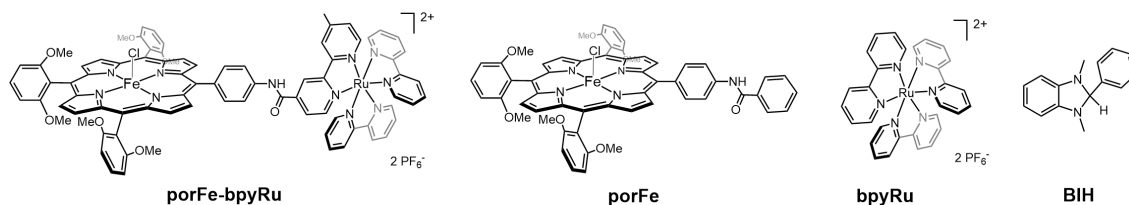
The photo-synthesis of reduced forms of carbon from CO₂ holds the promise to set us on track to mitigate the alarming anthropogenic amount of CO₂ we are dumping into our biosphere from the massive use of fossil fuels [1,2]. Blueprints of this strategy are directly provided by photosynthesis and cellular respiration that have enabled the development of energy infrastructures for solar energy harnessing and its storage in chemical compounds [3]. The efficient capture of sunlight, its conversion into a chemical potential and coupled to oxidative and reductive catalytic processes are the elemental steps that must be synchronized and optimized.

Since the early reports in the 80s on homogeneous photocatalytic systems for CO₂ reduction based on transition metals [4,5], a multitude of electron donor (ED)/photosensitizer (PS)/catalyst (Cat) combinations have been reported to reduce CO₂ in organic and aqueous media [6–11]. In the scheme of photocatalytic CO₂ reduction, the PS mediates the transfer of electrons from the ED to the Cat, but utilizes photons to drive the otherwise endergonic electron transfer steps. In a simple multicomponent approach, the three components can be simply mixed in solution and the kinetics of the electron transfer steps are expected to be diffusion-limited without kinetic advantage for a particular interaction. An alternative approach to overcome this diffusion limit and favor productive reaction steps consists of covalently attaching the PS and the Cat in a PS–Cat dyad to promote fast electron transfer from the PS to the Cat [12–15].

We and others have demonstrated that iron-porphyrins are one of the best performing homogeneous catalysts for the electrocatalytic reduction of CO₂ [16–19]. Their electrocatalytic properties such as overpotential, turnover number (TON) and turnover frequency (TOF) can be further improved by introducing substituents on the porphyrin macrocycle such as electron withdrawing or donating groups, proton relays, hydrogen bond donors or electrostatic groups [10,11,20–24]. When associated with a PS in a multicomponent system, iron-porphyrins were also recently shown to catalyze the photoreduction of CO₂ to CO [25–27], and even further to methane in some conditions [28,29]. However, to the best of our knowledge, there are no reported supramolecular

dyads consisting of an iron porphyrin catalyst and any photosensitizer [30]. This is in part due to the fact that the high absorption coefficient of the porphyrin catalyst across the visible region, overlaps and sometimes overwhelms the light-absorption role of the photosensitizer, leading to short-lived, and therefore non-productive, excited states. As such, for most multicomponent systems, there is a common trend of employing huge differences in the concentration of the iron porphyrin catalyst (μM range) and the photosensitizer (mM range). This piqued our curiosity to examine if a photoredox-iron-porphyrin catalyst design may lead to a new reactivity pattern.

In this work, we report the synthesis and characterization of a molecular assembly **porFe-bpyRu** composed of an iron porphyrin as catalyst covalently attached to a ruthenium trisbipyridine, the photosensitizer, through an amide linker (Scheme 1). Methoxy groups were introduced on the porphyrin as electron donating groups to enhance the nucleophilic character of the iron center and promote CO₂ reduction [16]. The electrochemical and photophysical properties of the **porFe-bpyRu** dyad were systematically compared with iron porphyrin (**porFe**) and ruthenium trisbipyridine (**bpyRu**) reference compounds. The electrochemical data indicate that the amide linkage does not promote strong electronic communication between the Cat and the PS, keeping the independent redox properties of the constitutive modules intact. Laser flash photolysis studies demonstrated that upon excitation of the photosensitizer in the dyad, an efficient energy transfer occurs towards the porphyrin catalyst, leading to a very fast quenching (<20 ns) due to the presence of the Fe metal, thereby shutting off the possibility for the light activation of the catalytic unit. In the presence of an electron donor, an immediate dark electron transfer is observed in the catalyst (**porFe-bpyRu** or **porFe**) forming Fe(II) species from Fe(III). For an independent mixture of the PS/PS–Cat and a reversible electron donor, a light induced charge shift leading to the reduced Fe(I) species was evidenced. Accordingly, upon exciting an exogenous **bpyRu** added to the **porFe-bpyRu**/electron donor mixture, a photo-induced electron transfer was observed from the exogenous Ru(I) photoreductant to the Fe(II) species, consequently forming the two-electron reduced form Fe(I). More interestingly, under continuous irradiation in the presence



Scheme 1. Structures and abbreviation of the **porFe-bpyRu** supramolecular complex and the corresponding model complexes **porFe** and **bpyRu** and the electron donors **BIH** and **Asc**.

of dimethylphenylbenzimidazole (**BIH**) as sacrificial electron donor, the **porFe-bpyRu** dyad displayed a surprisingly higher photocatalytic activity and CO₂-to-CO selectivity compared to the referenced iron porphyrin (**porFe**). Comprehensive photophysical and electrochemical studies pinpoint to the fact that despite the extinction of the photophysical properties of the photosensitizer in the supramolecular dyad, its appendage to the **porFe** was beneficial inasmuch as it acts as an electron reservoir next to the catalytic unit that promotes the formation of the catalytically active species at minimal thermodynamic cost.

2. Experimental section

2.1. General procedure

Proton and carbon nuclear magnetic resonance (¹H and ¹³C NMR) spectra were recorded at room temperature on Bruker Advance spectrometers. The electrospray ionization mass spectrometry (ESI-HRMS) experiments were performed on TSQ (Thermo Scientific, 2009) with an ESI⁺ method. Ground state absorption spectra were measured on a Specord spectrophotometer (Analytik Jena). EPR spectra were recorded at 40 K on a Bruker ELEXSYS 500 spectrometer equipped with a Bruker ER 4116DM X band resonator, an Oxford Instrument continuous flow ESR 900 cryostat, and an Oxford ITC 503 temperature control system. Cyclic voltammetry measurements were performed in an electrochemical cell composed of a glassy carbon (3 mm diameter) working electrode, Ag/AgNO₃ (10⁻² M) reference electrode, and a platinum wire counter electrode with tetrabutylammonium hexafluorophosphate (TBAP) as supporting electrolyte. Scan rate was chosen at 100 mV/s and a CH Instruments potentiostat workstation was utilized to control the applied voltages

and to measure resulting current. Ferrocene was used as an internal reference and the potentials are converted to NHE [31]. Spectroelectrochemical measurements were performed in a thin-layer quartz cuvette cell using a platinum honeycomb electrode (PINE Research) and a Pt wire reference electrode. Nanosecond transient absorption measurements were performed on a home-built set-up which has been described in detail previously [32] and a commercial Edinburgh Instruments LP920 Laser Flash Photolysis Spectrometer system. Photocatalytic experiments were performed in a 41.5 mL vial containing 6.5 mL CO₂-saturated DMF/H₂O (9:1 v/v) + 2 μM catalyst + 50 μM photosensitizer + 50 mM electron donor. A SugarCUBE high intensity LED fiber optic illuminator was utilized with a blue light output centered at 463 nm with a full width at half maximum (FWHM) characteristic of about 50 nm, adjusted to produce 9.5 mW·cm⁻². The reaction vessel is connected in line with a micro gas chromatography Inficon system to analyze the products of the reaction.

2.2. Synthesis and characterization

2.2.1. Synthesis of 1,3-dimethoxybenzene (**1**)

Potassium bicarbonate, K₂CO₃ (6.28 g, 45 mmol) and methyl iodide CH₃I (2.6 mL, 41.4 mmol) are added simultaneously and dropwise to a stirred solution of resorcinol (2.00 g, 18 mmol) in anhydrous acetone, at 0 °C under Ar atmosphere. The reaction mixture is stirred at room temperature for 12 h. Once reaction reached completion, the volatiles are evaporated under reduced pressure and 30 mL of H₂O are added to the residue. The crude product mixture is extracted with ethyl acetate (3 × 30 mL) and the combined organic layers are dried over Na₂SO₄. After evaporation of the solvent, the obtained residue is purified via silica column chromatography (hexane/ethyl acetate (5:1 v/v)) to give

1,3-dimethoxybenzene as a light-yellow oil (1.92 g, 13.9 mmol, 77%). ^1H NMR (500 MHz, CDCl_3): δ = 7.19 (t, J = 8.2 Hz, 1H), 6.52 (d, J = 2.4 Hz, 1H), 6.51 (d, J = 2.4 Hz, 1H), 6.47 (t, J = 2.4 Hz, 1H), 3.8 (s, 6H).

2.2.2. Synthesis of 2,6-dimethoxybenzaldehyde (**2**)

1,3-dimethoxybenzene (1.4 mL, 1.51 g, 10.9 mmol) is dissolved in 50 mL of dry THF, under N_2 and the resulting solution is purged with N_2 for at least 20 min. Afterwards, under vigorous stirring, *n*-BuLi (8.2 mL, 86.8 mmol) is added dropwise at 0 °C and once the addition is completed, the reaction mixture is stirred at room temperature for 2 h under N_2 atmosphere. Then, dry DMF (2.1 mL, 27 mmol) is added to the solution and the mixture is stirred for an additional 2 h. After 2 h, 20 mL of H_2O are added and extractions with ethyl acetate (3 \times 30 mL) are carried out. The collected organic layers are dried over Na_2SO_4 and evaporated under vacuum to obtain a yellowish oily residue. The desired product was recrystallized from hexane (15 mL) and collected as a light brown solid (1.26 g, 7.6 mmol, 70%). ^1H NMR (500 MHz, CDCl_3): δ = 10.51 (s, 1H), 7.45 (t, J = 8.5 Hz, 1H), 6.58 (d, J = 8.5 Hz, 2H) 3.90 (s, 6H).

2.2.3. Synthesis of 5-(4-nitrophenyl)-10,15,20-tris-(2,6-dimethoxyphenyl)-21H, 23H porphyrin (**3**)

2,6-dimethoxybenzaldehyde (0.75 g, 4.5 mmol) and 4-nitrobenzaldehyde (0.23 g, 1.5 mmol) are dissolved in 600 mL of CHCl_3 and the resulting solution is subsequently purged with N_2 for at least 30 min under vigorous stirring. Then, pyrrole (0.42 mL, 6 mmol) is added dropwise in the absence of light and the reaction mixture is purged with N_2 for an additional period of 10 min, before BF_3OEt_2 (233 μL , 1.88 mmol) is added. After the addition of BF_3OEt_2 , the reaction mixture is stirred in the dark at room temperature for 3 h under N_2 atmosphere. Then, DDQ (1.36 g, 6 mmol) is added to the solution and it stirred for 2 h at room temperature. The resulting crude product mixture is subsequently filtered through silica pad and then is purified via silica column chromatography (CH_2Cl_2 /hexane 4:1 (v/v)). However, only a small percentage of the desired porphyrin can be obtained clean. Given that, without any further purification, the 148 mg of the crude mixture was then used for the synthesis of 5-(4-aminophenyl)-10,15,20-tris-(2,6-dimethoxyphenyl)-21H, 23H porphyrin (**4**). ^1H NMR (500 MHz, CDCl_3): δ = 8.77 (d, J = 4.7 Hz, 2H),

8.72 (s, 4H), 8.64 (d, J = 4.7 Hz, 2H), 8.59 (d, J = 8.7 Hz, 2H), 8.39 (d, J = 8.7 Hz, 2H), 7.71 (m, 3H), 6.99 (m, 6H), 3.53 (s, 6H), 3.51 (s, 12H), -2.57 (s, 2H). ^{13}C NMR (75 MHz, CDCl_3): δ = 160.7, 150.1, 147.5, 135.3, 130.3, 121.7, 120.0, 119.8, 115.53, 112.2, 111.9, 104.3, 104.3, 56.2. UV/Vis (CH_2Cl_2): λ_{max} (ϵ , $\text{mM}^{-1}\cdot\text{cm}^{-1}$) = 419 (262.5), 514 (16.6), 550 (5.5), 590 (5.3), 644 (2.5).

2.2.4. Synthesis of 5-(4-aminophenyl)-10,15,20-tris-(2,6-dimethoxyphenyl)-21H, 23H porphyrin (**4**)

To a stirred solution of the isomeric mixture of porphyrin derivative (**3**) (148 mg) in DCM (15 mL), 2.5 mL of conc. HCl and $\text{SnCl}_2\cdot 2\text{H}_2\text{O}$ (0.2 g, 0.89 mmol) are added at 0 °C and the mixture is heated to 70 °C for at least 20 h. The progress of the reaction is monitored by thin layer chromatography (TLC, SiO_2 , CH_2Cl_2 /MeOH (99:1 v/v)). Upon reaction completion, 50 mL of DCM are transferred to the solution and it is left stirring for 15 min. Afterwards, the organic phase is collected, quenched with sat. aqueous solution of NaHCO_3 and washed thoroughly with H_2O . Then, the obtained organic layer is dried over Na_2SO_4 and evaporated until dryness. Porphyrin (**4**) is obtained as a purple solid after silica column chromatography (DCM/EtOH (98:2 v/v)) purification (67.4 mg, 0.083 mmol, overall yield of two steps 5.5%). ^1H NMR (500 MHz, CDCl_3): δ = 8.77 (d, J = 4.7 Hz, 2H), 8.72 (s, 4H), 8.64 (d, J = 4.7 Hz, 2H), 8.59 (d, J = 8.7 Hz, 2H), 8.39 (d, J = 8.7 Hz, 2H), 7.71 (m, 3H), 6.99 (m, 6H), 3.53 (s, 6H), 3.51 (s, 12H), -2.57 (s, 2H). ^{13}C NMR (75 MHz, CDCl_3): δ = 160.7, 150.1, 147.5, 135.3, 130.3, 121.7, 120.0, 119.8, 115.53, 112.2, 111.9, 104.3, 104.3, 56.2. UV/Vis (CH_2Cl_2): λ_{max} (ϵ , $\text{mM}^{-1}\cdot\text{cm}^{-1}$) = 419 (262.5), 514 (16.6), 550 (5.5), 590 (5.3), 644 (2.5).

2.2.5. Synthesis of 4'-methyl-4-carboxy-2,2'-bipyridine (**5**)

4,4-dimethyl-2,2'-bipyridine (1.1 g, 6 mmol) is dissolved in 65 mL of 1,4-dioxane and SeO_2 (800 mg, 7.2 mmol) is added. The resulting solution is stirred and heated to reflux for 24 h. After 24 h, the hot solution is passed through a short pad of celite to remove the elemental Se that is formed during the reaction. The filtrate once it is cooled down to room temperature, it is evaporated under reduced pressure. The obtained yellow residue is dissolved in 40 mL of EtOH and under vigorous stirring, 10 mL of aqueous solution of AgNO_3 (1.1 g, 6.6 mmol) is added in

the absence of light. Then, over a period of 30 min, 25 mL of aqueous solution of 1 M NaOH are added dropwise and the reaction mixture is stirred for 15 h at room temperature. Afterwards, the solution is concentrated under vacuum and the formed precipitate is filtered and washed first with 1.3 M NaOH (2 × 15 mL) and then with 15 mL of H₂O. The filtrate is collected and extracted with DCM (4 × 30 mL). Next, the pH of the collected basic aqueous layer is adjusted to pH = 3.5 by the addition of 4.0 N HCl/CH₃COOH (1:1 v/v). Upon acidification, the precipitation of a pink solid is observed and the mixture is kept at -10 °C for an additional period of 20 h for further precipitation. The precipitate is filtered and dried at 90 °C for 12 h. Finally, the crude mixture is purified via a Soxhlet extractor apparatus using anhydrous acetone as the eluent for 3 days. 4'-methyl-4-carboxy-2,2'-bipyridine is obtained as a light-yellow solid (255 mg, 1.19 mmol, 20%). ¹H NMR (500 MHz, DMSO-*d*₆): δ = 13.89 (br s, 1H), 8.85 (br d, *J* = 4.9 Hz, 1H), 8.82 (br s, 1H), 8.57 (br d, *J* = 4.9 Hz, 1H), 8.27 (br s, 1H), 7.85 (dd, *J* = 4.8 Hz, *J* = 1.4 Hz, 1H), 7.33 (br d, *J* = 4.8 Hz, 1H), 2.43 (s, 3H).

2.2.6. Synthesis of *cis*-bis(2,2'-bipyridine)dichlororuthenium(II) (Ru(bpy)₂Cl₂) (6)

2,2'-bipyridine (0.331 g, 2.1 mmol), 10 mL of dry DMF, RuCl₃ (0.200 g, 0.96 mmol) and LiCl (0.290 g, 6.75 mmol) are transferred into a two-neck round bottom flask and the resulting dark purple solution is heated to reflux overnight. After cooling down to room temperature, the formed orange precipitate is filtered and washed thoroughly first with acetone and then with H₂O. Finally, it is washed with diethyl ether and hexane. Ru(bpy)₂Cl₂ is obtained as a dark purple solid (0.160 g, 0.33 mmol, 34%). ¹H NMR (500 MHz, DMSO-*d*₆): δ = 9.97 (br d, *J* = 4.6 Hz, 2H), 8.64 (br d, *J* = 7.9 Hz, 2H), 8.49 (br d, *J* = 7.8 Hz, 2H); 8.06 (m, 2H), 7.76 (m, 2H), 7.68 (m, 2H), 7.51 (br d, *J* = 4.9 Hz, 2H), 7.10 (m, 2H).

2.2.7. Synthesis of compound 7

In a schlenk tube, compound 5 (48 mg, 0.224 mmol) is dissolved in 9 mL of SOCl₂ and the resulting stirring solution is heated up to 78 °C under N₂ for 2 h. In the next step, SOCl₂ is evaporated under reduced pressure and to the remaining residue 15 mL of dry THF is added. Then, porphyrin (4) (60 mg, 0.074 mmol) and anhydrous Et₃N are

transferred to the solution under N₂. The reaction mixture is heated up to 50 °C for 20 h. Once the reaction reaches completion, the volatiles are removed under vacuum and the crude solid is purified via column chromatography (SiO₂, DCM/MeOH (99:1 v/v)) affording derivative (7) as a purple solid (73 mg, 0.073 mmol, 98%). ¹H NMR (500 MHz, CDCl₃): δ = 8.94 (s, 1H), 8.93 (s, 1H), 8.78 (d, *J* = 4.7 Hz, 2H), 8.76 (s, 1H), 8.74 (d, *J* = 4.7 Hz, 2H), 8.71 (m, 4H), 8.61 (m, 1H), 8.36 (m, 1H), 8.21 (d, *J* = 8.5 Hz, 2H), 8.07 (d, *J* = 8.3 Hz, 2H), 8.01 (dd, *J*₁ = 4.8 Hz, *J*₂ = 1.9 Hz, 1H), 7.70 (t, *J* = 8.5 Hz, 3H), 7.23 (m, 1H), 6.99 (m, 6H), 3.52 (s, 6H), 3.50 (s, 12H), 2.53 (s, 3H), -2.59 (s, 2H). ¹³C NMR (75 MHz, CDCl₃): δ = 164.2, 160.7, 157.4, 155.1, 150.6, 149.2, 148.8, 143.3, 139.5, 137.1, 135.2, 131.9, 130.2, 125.6, 122.5, 122.2, 120.1, 119.9, 118.6, 118.1, 117.5, 111.7, 111.0, 104.3, 56.2, 21.4. UV/Vis (CH₂Cl₂): λ_{max} (ε, mM⁻¹·cm⁻¹) = 419 (382.9), 513 (16.5), 546 (5.4), 589 (4.9), 645 (2.5).

2.2.8. Synthesis of compound 8

To a stirring solution of porphyrin derivative (4) (45 mg, 0.06 mmol) in dry THF, benzoyl chloride (50 μL, 0.38 mmol) and 70 μL of dry Et₃N are added. The mixture is heated up to 70 °C for 12 h under N₂ atm. Afterwards, THF and Et₃N are evaporated under reduced pressure and the reaction product mixture is purified by column chromatography (SiO₂, CH₂Cl₂/EtOH (99.7/0.3 v/v)). The desired product is afforded as a purple solid (40 mg, 0.043 mmol, 73%). ¹H NMR (500 MHz, CDCl₃): δ = 8.76 (d, *J* = 4.7 Hz, 2H), 8.72 (m, 6H), 8.14 (d, *J* = 8.4 Hz, 2H), 8.12 (s, 1H), 7.98 (m, 2H), 7.92 (d, *J* = 8.4 Hz, 2H), 7.69 (m, 3H), 7.58 (m, 1H), 7.52 (m, 2H), 6.98 (m, 6H), 3.51 (s, 6H), 3.49 (s, 12H), -2.53 (br s, 2H). ¹³C NMR (75 MHz, CDCl₃): δ = 166.1, 160.7, 139.0, 137.4, 135.1, 132.0, 130.1, 129.0, 127.3, 126.4, 120.3, 120.0, 118.2, 111.6, 110.9, 104.3, 56.2. UV/Vis (CH₃CN): λ_{max} (ε, mM⁻¹·cm⁻¹) = 415 (401.1), 511 (17.3), 544 (6.0), 588 (5.1), 644 (2.8).

2.2.9. Synthesis of compound 9

In a two-neck round bottom flask, porphyrin (7) (60 mg, 0.06 mmol) is dissolved in 38 mL of CH₃COOH and the stirring solution is purged with N₂ for 15 min at room temperature. After degassing, Ru(bpy)₂Cl₂ (57.6 mg, 0.12 mmol) is transferred to the flask and the reaction mixture is heated to reflux for 12 h under N₂. Then CH₃COOH is evaporated

under reduced pressure and the obtained orange red-dish residue is washed with H₂O (5 × 20 mL). Then, the crude residue is purified by column chromatography (SiO₂, CH₃CN/H₂O/KNO_{3(sat)} (30:2:1 v/v)). Afterwards, the counter anions of Ru^{II} are exchanged with PF₆⁻ anions. More specifically, the dyad is dissolved in the minimum amount of CH₃CN and to the resulting solution, a saturated solution of NH₄PF₆ in MeOH is added. Then, H₂O was added slowly. Upon addition of H₂O, the precipitation of a brown-purple solid is observed. The precipitate is subsequently filtered and washed thoroughly with H₂O to remove the excess of the NH₄PF₆ salt giving porphyrin derivative (**9**) as an orange-purple solid (21 mg, 0.012 mmol, 20%). ¹H NMR (500 MHz, (CD₃)₂CO): δ = 10.50 (br s, 1H), 9.43 (s, 1H), 8.98 (s, 1H), 8.76 (s, 1H), 8.76 (s, 4H), 8.73 (s, 4H), 8.64 (br s, 2H), 8.39 (br s, 2H), 8.26 (d, *J* = 8.2 Hz, 2H), 8.16–8.09 (m, 2H), 8.03–7.95 (m, 5H), 7.84 (br d, *J* = 5.6 Hz, 1H), 7.79 (t, *J* = 8.6 Hz, 3H), 7.57–7.49 (m, 4H), 7.45 (d, *J* = 5.4 Hz, 1H), 7.14 (d, *J* = 8.6 Hz, 6H), 3.52 (s, 18H), 2.61 (s, 3H), –2.50 (s, 2H). ¹³C NMR (75 MHz, (CD₃)₂CO): δ = 163.3, 161.3, 159.0, 157.8, 157.1, 153.2, 152.5, 152.4, 151.7, 151.6, 144.2, 139.3, 138.9, 138.7, 135.5, 131.4, 129.9, 128.6, 126.7, 126.3, 125.1, 125.0, 122.9, 120.0, 199.7, 119.4, 118.9, 113.0, 112.6, 104.9, 56.1, 21.2. UV/Vis (CH₃CN): λ_{max} (ε, mM⁻¹·cm⁻¹) = 288 (87.8), 415 (413.5), 476 (22.9), 510 (24.2), 544 (9.3), 587 (6.7), 642 (4.1).

2.2.10. Synthesis of *porFe-bpyRu*

FeBr₂ (0.088 g, 0.41 mmol) and derivate (**9**) (0.023 g, 0.014 mmol) are dissolved in 5 mL of dry and degassed THF. The reaction mixture is kept under stirring and heated at 50 °C for 12 h under Ar. The progress of the reaction is monitored by absorption spectroscopy. Once the reaction is completed, THF is evaporated under reduced pressure. The remaining solid is dissolved in 20 mL of DCM and treated with 4N HCl (3 × 15 mL). The organic layers are combined, washed with H₂O (3 × 15 mL) and dried over Na₂SO₄. The crude product is purified via silica column chromatography (CH₃CN/H₂O/KNO_{3(sat)} (30:2:1 v/v)). Then, the counter anions of Ru^{II} were exchanged with PF₆⁻ anions, as described previously for the synthesis of compound **9**. The final compound is given as an orange-purple solid (18 mg, 0.010 mmol, 71%). **UV/Vis (CH₃CN)**: λ_{max} (ε, mM⁻¹·cm⁻¹) = 288 (83.0), 377 (59.4), 417 (95.8), 465 (27.7), 505 (17.9), 576 (5.3), 655 (4.1), 689 (4.3). **ESI-HRMS**: m/z calculated for

a chemical formula C₈₂H₆₅ClFeN₁₁O₇Ru²⁺ [M]²⁺ = 754.1543, found 754.1580.

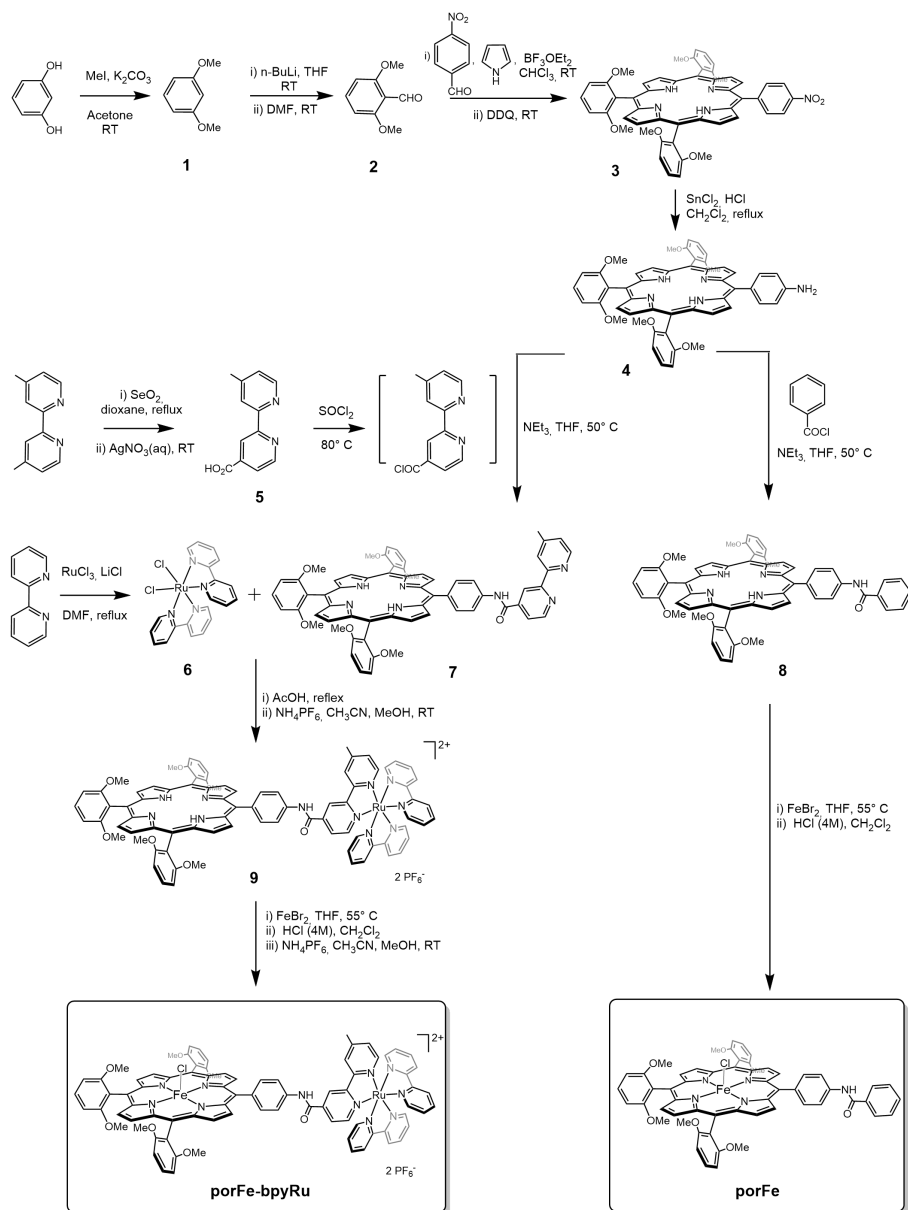
2.2.11. Synthesis of *porFe*

To a solution of FeBr₂ (0.272 g, 1.27 mmol) in 5 mL of dry and degassed THF, porphyrin (**7**) (0.037 g, 0.041 mmol) is added and the mixture of the reaction and heated at 55 °C for 12 h under Ar. After reaction reaches completion, THF is evaporated and the residue is dissolved in 20 mL of DCM. Then, 15 mL of 4N HCl is added. The organic phase is collected and extracted for additional two times with 4N HCl (2 × 15 mL). Finally, the organic layers are collected, washed with H₂O (3 × 15 mL) and dried over Na₂SO₄. **PorFe** is afforded as an orange-purple solid after column chromatography (SiO₂, CH₂Cl₂/MeOH (99:1 v/v)) purification (24 mg, 0.024 mmol, 58%). **UV/Vis (CH₂Cl₂)**: λ_{max} (ε, mM⁻¹·cm⁻¹) = 274 (31.6), 341 (32.0), 417 (87.2), 499 (11.2), 506 (11.0), 577 (5.4), 640 (3.0). **ESI-HRMS**: m/z calculated for a chemical formula C₅₇H₄₅FeN₅O₇ [M-Cl]⁺ = 967.2619, found 967.2664.

3. Results and discussion

3.1. Synthesis

As shown in Scheme 2, dyad **porFe-bpyRu** and iron-porphyrin **porFe** share the same porphyrin platform **4**. This synthetic intermediate was prepared in an acid-catalyzed condensation of four pyrroles, one *para*-nitrobenzaldehyde and three di-*ortho*-methoxybenzaldehyde (**2**) followed by an oxidation of the obtained macrocycle using dichloro-5,6-dicyano-*p*-benzoquinone (DDQ), then by a reduction of the nitro group into amino using tin chloride in acidic conditions. Aldehyde **2** was obtained in two steps from resorcinol by first methylating the hydroxy groups and then a lithium-mediated formylation reaction of the aromatic carbon in position 2 takes places. The coupling between porphyrin **4** and one of the bipyridines of the **bpyRu** moiety was performed using modified bipyridine **5** bearing a carboxyl group in position 4 that was prepared by a SeO₂ oxidation of one of the methyl groups in the 4,4'-dimethyl-2,2'-bipyridyl. After an activation of the carboxyl group using thionyl chloride, **5** reacts with the aniline group in porphyrin **4** to yield the amide-bridged porphyrin-bipyridine



Scheme 2. Synthesis of the **porFe-bpyRu** supramolecular complex and the corresponding reference complex **porFe**.

ligand **7**. The bipyridine in **7** can displace the two chlorides of the dichlorobis(bipyridine)ruthenium **6** to form the porphyrin-bpyRu complex (**9**) that leads, after complexation of the iron, to the aimed dyad **porFe-bpyRu**. Reference iron-porphyrin **porFe** was prepared using a similar synthetic scheme and by replacing the bipyridine **5** with benzoyl chloride.

3.2. Electrochemical characterization

Cyclic voltammetry (CV) of model compound **porFe** in argon-degassed dimethylformamide (DMF) containing 100 mM of tetra-*N*-butylammonium hexafluorophosphate (TBAP) shows three reversible redox waves corresponding to the formal Fe(III/II), Fe(II/I), and Fe(I/0) couples (Figure 1(a), Table 1).

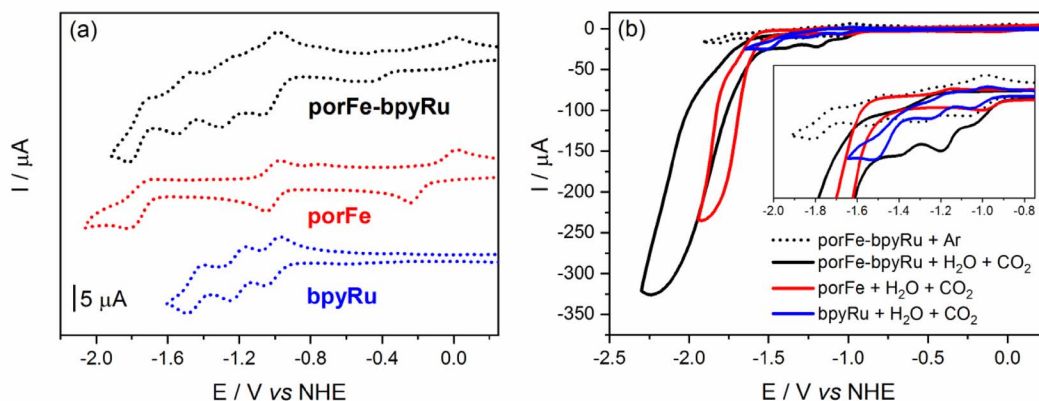


Figure 1. Cyclic voltammograms (CV) of the supramolecular and reference complexes at concentrations of 0.5 mM in dimethylformamide with 100 mM tetra-*N*-butylammonium hexafluorophosphate (a) under Ar and (b) under CO₂ and 5.5 mM H₂O. Inset in (b) shows magnification of the onset of catalysis.

Table 1. Electrochemical potentials of the formal redox couples involved in the supramolecular and reference complexes, referenced *vs* NHE in dimethylformamide with 100 mM tetra-*N*-butylammonium hexafluorophosphate

Complex	Fe(III/II)	Fe(II/I)	Fe(I/0)	Ru(II/I)	Ru(I/0)	Ru(0/-I)
porFe-bpyRu	-0.23	-1.03	-1.77	-1.03	-1.27	-1.51
porFe	-0.12	-1.02	-1.76	—	—	—
bpyRu	—	—	—	-1.01	-1.21	-1.45

As expected, due to the presence of the methoxyl groups, these three waves are shifted to more negative potentials compared to those of the previously reported non-functionalized iron-tetraphenylporphyrin (FeTPP) [18]. Three successive reduction waves are also observed for **bpyRu** complex which were previously reported to be mainly centered on the bipyridine ligands [33]. The CV of **porFe-bpyRu** displays a combination of the **porFe** and **bpyRu** reduction waves. A noticeable anodic shift of about 100 mV is observed for the Fe(III/II) couple in the dyad compared to the reference complex but no significant shifts are observed for the Fe(II/I) and Fe(I/0) redox couples. Similarly, the bpy-based reduction waves of the Ru moiety in the dyad showed minimal anodic shifts of around 5 mV. These are all indicative that the amide linker does not establish a strong electronic communication between the two moieties. The redox couples Fe(II/I) and Ru(II/I) overlap in the dyad as a two-electron reduction wave, which is indicative that the one-electron reduced form of

the PS can reduce both the Fe(II) and Fe(III) states of the catalyst in the dyad with thermodynamic driving force of 0 and -800 meV, respectively. However, this same photoreductant would have an uphill penalty of +760 meV to reduce the iron-porphyrin moiety to its catalytically active Fe(0) form.

When the CVs were performed under a CO₂ atmosphere and in presence of water as a proton source (Figure 1(b)), **porFe** and **porFe-bpyRu** displayed a typical catalytic current corresponding to CO₂ reduction at the last reduction wave (Fe(I/0) redox couple) with a significantly higher current intensity in the case of **porFe-bpyRu**. More interestingly, the onset potential of catalysis started at a significantly more positive potential in the dyad (Figure 1(b) inset), almost at the Fe(II/I) and Ru(II/I) waves with a smaller current intensity increase preceding a much higher current observed after -1.5 V. A control experiment with **bpyRu** in the same conditions shows minimal current intensity increase and only at the third bpy-reduction wave, confirming that the iron-porphyrin

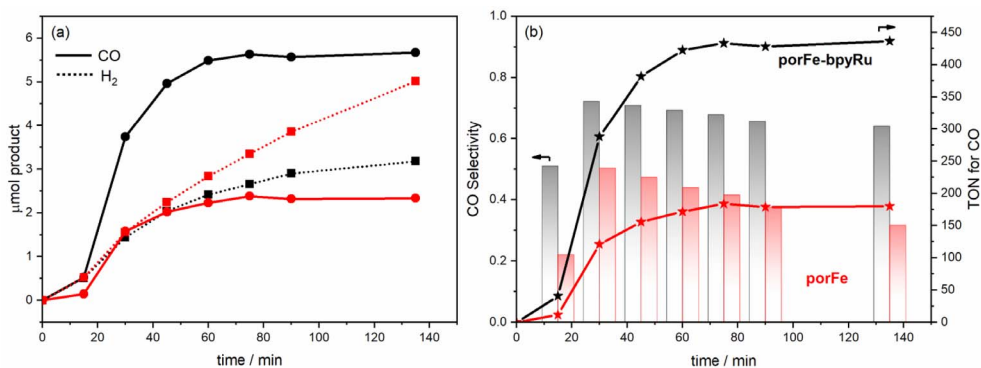


Figure 2. (a) Photocatalytic curves for the production of CO (solid lines) and H₂ (dotted lines) during the irradiation of the following in CO₂-saturated DMF/H₂O (9:1 v/v): 2 μM **porFe-bpyRu** + 50 μM **bpyRu** + 50 mM **BIH** (black); 2 μM **porFe** + 50 μM **bpyRu** + 50 mM **BIH** (red). (b) Comparison of the photocatalytic performance in terms of selectivity towards CO production (columns) and turnover numbers (TON).

Table 2. Summary of photocatalytic activities showing the production of CO and H₂ after irradiation for 135 min of a CO₂-saturated DMF/H₂O (9:1 v/v) solution containing the photosensitizer–catalyst system investigated in this study

Photosensitizer	Catalyst	μmol CO	μmol H ₂	TON CO	TON H ₂	Selectivity _{CO}
2 μM porFe-bpyRu	—	n.d.	n.d.	—	—	—
2 μM porFe-bpyRu	50 μM bpyRu	5.7	3.2	436	244	64%
2 μM porFe	50 μM bpyRu	2.3	5.0	180	386	32%
2 μM porFe	—	n.d.	n.d.	—	—	—
—	50 μM bpyRu	1.4	0.5	4.5	1.6	74%

n.d. = not detectable.

catalyst is responsible for the observed catalytic wave in the **porFe-bpyRu** dyad. The early onset potential for the first catalytic regime of the dyad takes place right after the electro-generation of the Fe(I) species that is accompanied concomitantly with addition of one electron on the bipyridine holding the PS and the Cat. This proposal is based on the fact that the bridging bipyridine is chemically modified with a C-terminated amido group and is under the influence of two metallic cations, rendering it the privilege locus for the addition of an electron as compare to the other two bipyridine ligands. This species can therefore be looked at as an Fe(I) coupled to an anion radical species that can trigger the catalytic activity.

3.3. Photocatalytic evaluation

Motivated by the promising results from the electrochemical measurements, we undertook the eval-

uation of the photocatalytic performance of the supramolecular dyad toward CO₂ reduction. An initial experiment was performed by irradiating with a blue LED source a solution containing 2 μM **porFe-bpyRu** as photo-catalyst and 50 mM **BIH** as sacrificial electron donor in DMF/H₂O (9:1 v/v). Unfortunately, the gas chromatography analysis of the reaction vessel headspace was not able to detect any gas product. Similarly, no detectable products were observed for a solution containing only 2 μM **porFe** and 50 mM **BIH**. In the same conditions but in a bimolecular configuration using 2 μM **porFe** as catalyst and 50 μM **bpyRu** as PS, the reaction produces 5.0 μmol of H₂ as the major product and 2.3 μmol of CO (Figure 2(a), Table 2). However, in a hybrid configuration where exogenous **bpyRu** (50 μM) in combination with 2 μM **porFe-bpyRu** were used, 5.7 μmol CO and 3.2 μmol H₂ were produced after 135 min of irradiation (Figure 2(a), Table 2). To ascertain that the

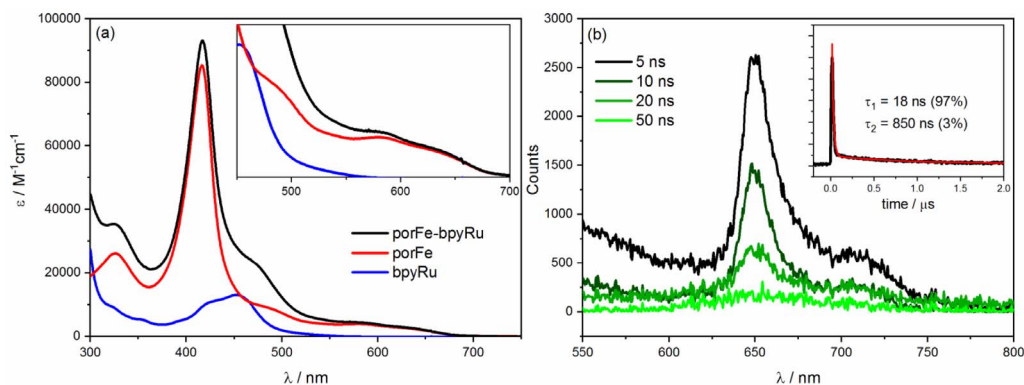


Figure 3. (a) Absorption spectra of the supramolecular **porFe-bpyRu** dyad in comparison with the reference complexes in ACN/H₂O (6:4 v/v). Inset shows magnification of the Q bands region. (b) Transient emission spectra of **porFe-bpyRu** in DMF upon laser excitation at 460 nm. Inset shows kinetics at 650 nm revealing emission lifetime of 18 ns. Similar transient emission was recorded in ACN/H₂O (Figure S2).

photocatalytic activity comes mainly from the dyad, a control experiment was performed with 50 μM of **bpyRu** and in absence of the dyad. Under these conditions, much smaller amounts of CO (1.4 μmol) and H₂ (0.5 μmol) are produced (Figure S1), possibly due the minor CO₂ reduction activity of the Ru bis-bipyridyl, a degradation product of **bpyRu** that was shown to form in absence of the electron acceptor, in this case the Cat, and exhibit some CO₂ reduction activity [34–36]. In the same catalytic conditions, the **porFe-bpyRu** dyad displays a higher selectivity (~64%) for CO production (Figure 2(b)) during the course of photocatalysis, while in the case of **porFe** the selectivity was below 40%. This improved selectivity exhibited by the supramolecular **porFe-bpyRu** dyad also translates in a significantly higher TON of ~440 compared to that obtained with the **porFe** as catalyst (TON = 180). Even though the **porFe-bpyRu** dyad didn't fulfill the initially intended photo-catalyst role, it surprisingly improves the selectivity and TON when used as a catalyst in presence of exogenous PS.

3.4. Photophysical and mechanistic analyses

The intriguing and peculiar photocatalytic performance of the **porFe-bpyRu** dyad merited further photophysical investigation. The absorption spectrum of the dyad (Figure 3(a)) consists of combination of spectral features of the mononuclear complexes **porFe** and **bpyRu**: a Soret band at 417 nm and Q bands at 490, 585, and 635 nm characteristic of the

iron porphyrin catalyst and the ³MLCT band of Ru PS as broad shoulder at 460 nm. The absence of significant spectral changes between the **porFe-bpyRu** dyad and the mixture of **porFe** and **bpyRu** confirm the previous observation that the amide linkage does not alter the electronic properties of the individual components in the ground state. Upon excitation at 460 nm to excite mainly the Ru PS (a similar excitation domain of the blue LED lamp employed in the photocatalytic experiments), only emission from the **porFe** could be detected (Figure 3(b); narrow band at 650 nm with a shoulder at 700 nm). The absence of emission from the Ru excited state, expected as a broad band at 610 nm, is indicative of ultrafast quenching of the Ru excited state. As expected, the lifetime of the **porFe** fluorescence is shorter than the time resolution (20 ns) of the ns laser flash photolysis apparatus. No transient absorption peaks were observed (even at the shortest time scale of the experiment) indicating the absence of any long-lived excited triplet Ru species. These observations are attributed to (a) an efficient energy transfer from the excited singlet Ru species to singlet porphyrin, which is then significantly quenched due to the presence of the heavy Fe metal center, and (b) competing photon absorption (~50%) between the PS and the Cat.

Upon addition of sodium ascorbate (Asc) as a reversible electron donor for the photophysical measurements, a noticeable red shift in the Soret band (416 nm → 428 nm) of the ground state spectrum of **porFe-bpyRu** was observed in Ar-saturated

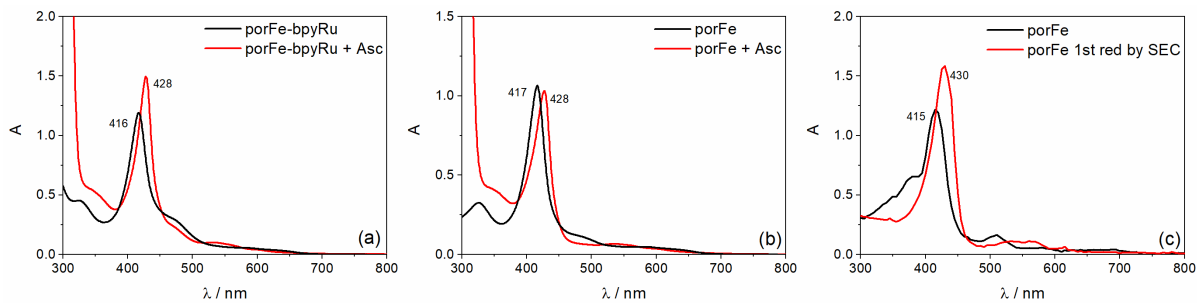


Figure 4. UV-Vis spectral changes when **Asc** is added to a solution of (a) **porFe-bpyRu** or (b) **porFe** in Ar-saturated ACN/H₂O (6:4 v/v) and its similarity to (c) the spectral evolution during the 1st reduction Fe^{III} → Fe^{II} of **porFe** in ACN using spectroelectrochemistry, SEC (more details in Figure S3).

ACN/H₂O solutions (Figure 4(a)). A similar shift was observed for the reference **porFe** catalyst (Figure 4(b)), indicating that there is a dark chemical reaction occurring between the **Asc** and the catalyst. Spectroelectrochemical measurement on the reference complex **porFe** shows a similar characteristic red-shift of the Soret band for the Fe(II) species (Figures 4(c) and S3–S4) which indicates that the observed red shift of the Soret band is due to the reduction of Fe(III) to Fe(II). A similar reduction of Fe(III) is occurring when **BIH** was used as sacrificial electron donor. The electron paramagnetic resonance (EPR) spectra of **porFe-bpyRu** (Figure S5) shows the disappearance of the high spin Fe(III) signal upon addition of the electron donor in the dark. We also investigated the photophysical properties of the singly reduced Fe(II) state of **porFe-bpyRu** upon excitation at 460 nm. Here too, no transient absorption peaks were observed. Hence, revealing again an efficient quenching of any excited states. Accordingly, the absence of long-lived excited species and the lack of light-induced electron transfer processes leading to reduced species for redox reactions, explain why the **porFe-bpyRu** dyad in the presence of **BIH** did not show any photocatalytic CO₂ reduction activity under continuous illumination. Therefore, these results highlight that linking the **bpyRu** PS and **porFe** catalyst through the single amido function was disadvantageous in the scenario of eliminating the diffusion control limits in the photo-driven electron transfer processes and catalysis. Reasons behind this in our particular case probably originate from the competition for photon absorption between the catalyst and the photosensitizer, a mismatch of emission and absorption properties of both constitutive

chromophores and finally the short distance between the two modules which promote an efficient energy transfer and quenching of the excited states.

As it turns out, the photoredox-catalyst molecular dyad did not lead to the expected photo-induced charge separation and charge accumulation towards the catalyst. We then pursue the photophysical investigation by the addition of an exogenous ruthenium (II) trisbipyridine photosensitizer (**bpyRu**) together with **Asc** a reversible electron donor considering the **porFe-bpyRu** as basically a dyad with an extinct photosensitizer unit but with a functioning **porFe** catalyst unit. In this configuration, photo-induced electron transfer steps are observed as summarized in Figures 5(a)–(c). At short time domain (0–100 ns in Figure 5(a)), upon laser excitation at 460 nm and formation of the excited state Ru* (bleaching of Ru(II) MLCT at 450 nm), there is a simultaneous formation of the one-electron reduced form of the PS, formal Ru(I) species, characterized by an absorption at 520 nm, and oxidized Asc⁺ (absorbing at 360 nm). Global fitting of the kinetic traces with a triexponential function [$a_1 \exp(-t/\tau_1) + a_2 \exp(-t/\tau_2) + a_3 \exp(-t/\tau_3) + c$] gave satisfactory fits (Figure 5(d)). This first photo-induced electron transfer event (Ru(II) + Asc → Ru(I) + Asc⁺) occurs with an apparent time constant of 26 ns with 100 mM **Asc**. In the proceeding time scale (100 ns to 60 μs in Figure 5(b)), the Ru(I) species decays to give a new spectral feature at 458 nm, corresponding to the reduction from the Fe(II) to Fe(I) oxidation state of the porphyrin catalyst moiety of the **porFe-bpyRu** dyad. This is confirmed by two control experiments: (a) similar transient absorption changes are observed for the solution containing the reference complexes

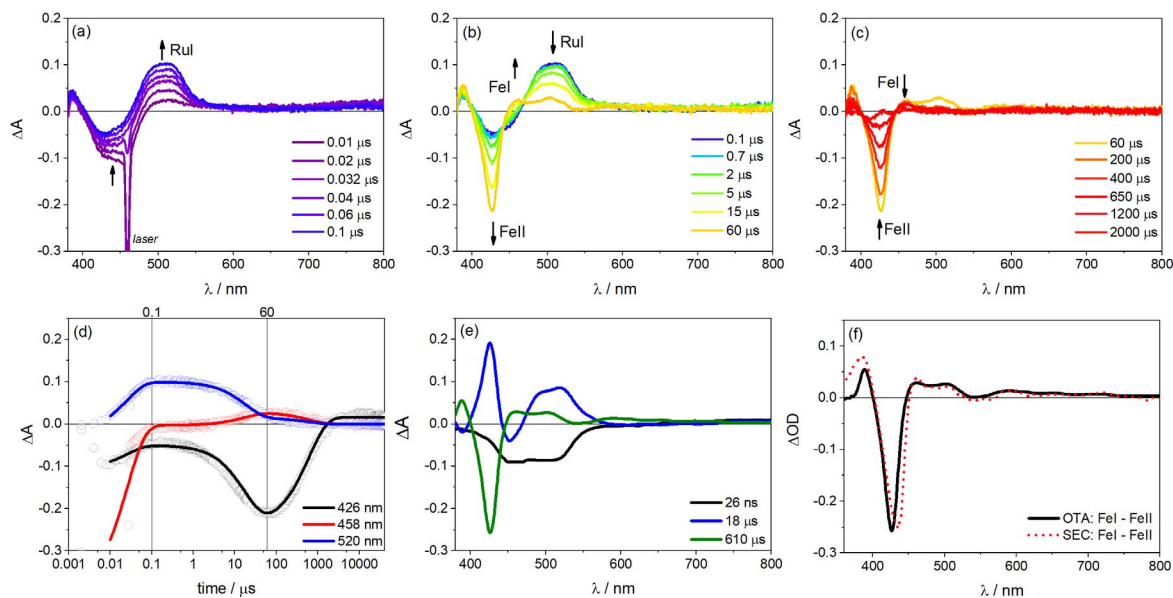


Figure 5. (a–c) Optical transient absorption (OTA) spectra in three time domains showing the spectral evolution of each species during single flash photolysis of a solution containing 13 μM **porFe-bpyRu** dyad, 31 μM **bpyRu**, and 100 mM **Asc** in ACN/H₂O (6:4 v/v) (laser excitation at 460 nm, 10 mJ per pulse). (d) Globally-fitted transient kinetics at some wavelengths with fitting parameters used to plot the (e) decay-associated difference spectra. (f) Comparison of the OTA decay spectra corresponding to (Fe(I)–Fe(II)) with that obtained from spectroelectrochemistry (SEC) in Figure S3 (in the absence of H₂O).

porFe, **bpyRu** and **Asc** in the similar time window (Figure S6) and (b) a similar differential spectrum is observed during spectroelectrochemical measurement of the reference complex **porFe** when going from the Fe(II) to the Fe(I) oxidation states (Figures 5(e), (f) and S3). This second electron transfer event ($\text{Ru(I)} + \text{Fe(II)} \rightarrow \text{Ru(II)} + \text{Fe(I)}$) occurs with a diffusion-limited second order rate constant of $7.9 \times 10^9 \text{ M}^{-1}\cdot\text{s}^{-1}$ estimated from the apparent time constant of 18 μs and formation of 7.1 μM Fe(I). Finally, at longer time scale ($>60 \mu\text{s}$ in Figure 5(c)), this Fe(I) species decays back to the Fe(II) state after charge recombination with oxidized $\text{Asc}^{\cdot+}$ ($\text{Fe(I)} + \text{Asc}^{\cdot+} \rightarrow \text{Fe(II)} + \text{Asc}$) with a time constant of 610 μs .

These photophysical investigations have shown that when the **porFe-bpyRu** dyad is assimilated as only the catalyst in the presence of exogenous ruthenium (II) trisbipyridine photosensitizer and a sacrificial electron donor, three electrons can be accumulated on the catalyst to form the Fe(I)–Ru(II) species: one electron coming from a dark reaction with the electron donor and two electrons coming from the photo-induced Ru(I) reductant. These

first three electron transfer events are similarly envisioned as the initial steps in the proposed photocatalytic cycle in Figure 6. However, from the CV of **porFe** catalyst (Figure 1(b)) it is clear that the Fe(0) oxidation state must be reached before the catalytic reduction of CO₂ can proceed. With this thermodynamic constraint, the Ru(I) photo-reductant faces an uphill thermodynamic penalty of +760 meV to proceed. An alternative route may come from the non-innocent reducing radical BI[•] resulting from the first electron donor step of BIH ($E = -1.39 \text{ V vs NHE}$ [37]) ensuing a less positive $\Delta G \sim +370 \text{ meV}$ for this reaction), as we and others have previously reported [38–40]. However, an interesting feature of the **porFe-bpyRu** dyad is the possibility for the appended ruthenium (II) trisbipyridine to act as an electron reservoir, as suggested by the earlier onset of catalysis (Figure 1(b)) occurring at a potential corresponding to the Fe(II/I) and Ru(II/I) couples. Since there is only a minimal driving force for the exogenous Ru(I) photo-reductant to reduce the appended Ru moiety in the dyad ($\Delta G \sim +20 \text{ meV}$), we hypothesize that this occurs to form a Fe(I)–Ru(I) state of the dyad:

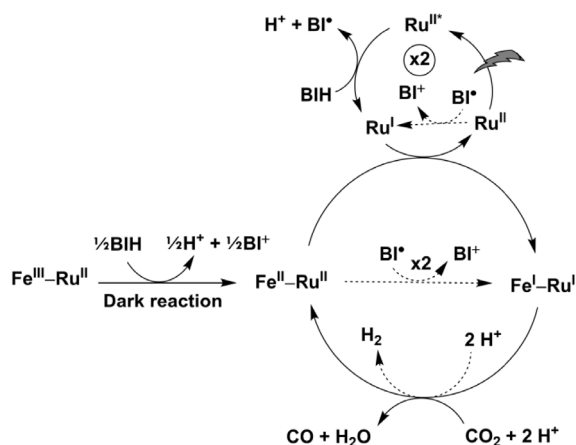


Figure 6. Proposed photocatalytic cycle involving the supramolecular **porFe-bpyRu** dyad and exogenous **bpyRu** PS with BIH as sacrificial electron donor. Dashed arrows show competing minor pathways.

$\text{Fe(I)-Ru(II)} + \text{Ru(I)} \rightarrow \text{Fe(I)-Ru(I)} + \text{Ru(II)}$. The formal Fe(I)-Ru(I) state can then be regarded as an Fe(I) species backed up by an additional electron with the same reducing power probably delocalized on the bipyridine extending onto the porphyrin macrocycle. Such a reduced species may then start the two-electron activation of CO_2 at a lower overpotential than the classic Fe(0) active form. The lower thermodynamic penalty along this route can account for the higher performances of the **porFe-bpyRu** dyad, in terms of TON and CO selectivity, than the **porFe** catalyst in the presence of the same amount of exogenous ruthenium (II) trisbipyridine as photosensitizer. As a consequence, even though the **bpyRu** photoredox unit in the **porFe-bpyRu** dyad is shut down due to fast deleterious energy transfer processes, it assists in lowering the overpotential for CO_2 reduction by acting as a reservoir for providing an extra reducing power to ignite the catalysis at the formal Fe(I) state of the catalyst.

4. Conclusion

We have synthesized a new photoredox-catalyst couple, the **porFe-bpyRu**, where a ruthenium (II) trisbipyridine photosensitizer **bpyRu** is covalently attached to an iron porphyrin catalyst **porFe** through an amide linker. We found that this molecular dyad

did not lead to the expected photo-induced charge separation and charge accumulation towards the catalyst due to a non-productive quenching of the excited state of the photosensitizer by energy transfer to the catalyst. A comparative electrochemical study points to a change in the electrocatalytic pattern of the **porFe-bpyRu** dyad compared to the **porFe** catalyst. Indeed, for the **porFe**, the catalytic wave is observed at the Fe(0) state while for the **porFe-bpyRu** dyad, a catalytic wave starts at the formal Ru(I)-Fe(I) species at some 700 mV lower overpotential than the **porFe** catalyst. This species can be best described as a formal Fe(I) species at the catalyst in interaction with a radical anion on the bipyridine ligand holding the **porFe**. Interestingly though, in presence of exogenous **bpyRu** photosensitizer, the **porFe-bpyRu** dyad presents a significant enhancement of the turnover number and CO_2 -to-CO selectivity of the catalysis compared to the **porFe** catalyst analogue under the same photocatalytic conditions. Reasons behind this probably come from the role of the **bpyRu** unit in the **porFe-bpyRu** dyad that acts an electron reservoir to power the photocatalytic activity. DFT calculations are underway to provide more insights in the functioning of such dyad.

Acknowledgements

This work has been supported by the French National Research Agency (ANR-19-CE05-0020-02, LOCO). We thank CNRS, CEA Saclay, LABEX CHARMMAT, ICMMO and University Paris-Saclay for the financial support. This research was also funded by the General Secretariat for Research and Technology (GSRT) and Hellenic Foundation for Research and Innovation (HFRI; project code: 508). In addition, this research has been co-financed by the European Commission's Seventh Framework Program (FP7/2007-2013) under grant agreement no. 229927 (FP7-REGPOT-2008-1, Project BIO-SOLENUTI).

Supplementary data

Supporting information for this article is available on the journal's website under <https://doi.org/10.5802/crchim.104> or from the author.

It contains transient emission, transient absorption, EPR, spectroelectrochemistry, NMR and ESI-HRMS spectra.

References

- [1] G. A. Olah, *Angew. Chem. Int. Ed.*, 2005, **44**, 2636-2639.
- [2] H. B. Gray, *Nat. Chem.*, 2009, **1**, article no. 7.
- [3] J. Barber, M. D. Archer, "Photosynthesis and photoconversion", in *Molecular to Global Photosynthesis* (J. Barber, ed.), Imperial College Press, London, 2004, 1-44.
- [4] J.-M. Lehn, R. Ziessel, *Proc. Natl. Acad. Sci. USA*, 1982, **79**, 701-704.
- [5] J. L. Grant, K. Goswami, L. O. Spreer, J. W. Otvos, M. Calvin, *J. Chem. Soc. Dalton Trans.*, 1987, 2105-2109.
- [6] B. Kumar, M. Llorente, J. Froehlich, T. Dang, A. Sathrum, C. P. Kubiak, *Annu. Rev. Phys. Chem.*, 2012, **63**, 541-569.
- [7] N. Elgrishi, M. B. Chambers, X. Wang, M. Fontecave, *Chem. Soc. Rev.*, 2017, **46**, 761-796.
- [8] A. Rosas-Hernández, C. Steinlechner, H. Junge, M. Beller, *Top. Curr. Chem.*, 2017, **376**, article no. 1.
- [9] F. Wang, *ChemSusChem*, 2017, **10**, 4393-4402.
- [10] H. Takeda, C. Cometto, O. Ishitani, M. Robert, *ACS Catal.*, 2017, **7**, 70-88.
- [11] K. E. Dalle, J. Warnan, J. J. Leung, B. Reuillard, I. S. Karmel, E. Reisner, *Chem. Rev.*, 2019, **119**, 2752-2875.
- [12] B. Gholamkhass, H. Mametsuka, K. Koike, T. Tanabe, M. Furue, O. Ishitani, *Inorg. Chem.*, 2005, **44**, 2326-2336.
- [13] Y. Tamaki, T. Morimoto, K. Koike, O. Ishitani, *Proc. Natl. Acad. Sci. USA*, 2012, **109**, 15673-15678.
- [14] C. Herrero, A. Quaranta, S. El Ghachtouli, B. Vauzeilles, W. Leibl, A. Aukauloo, *Phys. Chem. Chem. Phys.*, 2014, **16**, 12067-12072.
- [15] Y. Kuramochi, Y. Fujisawa, A. Satake, *J. Am. Chem. Soc.*, 2020, **142**, 705-709.
- [16] C. Costentin, S. Drouet, M. Robert, J.-M. Savéant, *Science*, 2012, **338**, 90-94.
- [17] I. Azcarate, C. Costentin, M. Robert, J.-M. Savéant, *J. Am. Chem. Soc.*, 2016, **138**, 16639-16644.
- [18] A. Khadhraoui, P. Gotico, B. Boitrel, W. Leibl, Z. Halime, A. Aukauloo, *Chem. Commun.*, 2018, **54**, 11630-11633.
- [19] P. Gotico, B. Boitrel, R. Guillot, M. Sircoglou, A. Quaranta, Z. Halime, W. Leibl, A. Aukauloo, *Angew. Chem. Int. Ed.*, 2019, **58**, 4504-4509.
- [20] P. Gotico, Z. Halime, A. Aukauloo, *Dalton Trans.*, 2020, **49**, 2381-2396.
- [21] F. Franco, C. Rettenmaier, H. S. Jeon, B. Roldan Cuenya, *Chem. Soc. Rev.*, 2020, **49**, 6884-6946.
- [22] A. W. Nichols, C. W. Machan, *Front. Chem.*, 2019, **7**, article no. 397.
- [23] Y. Matsubara, *ACS Energy Lett.*, 2019, **4**, 1999-2004.
- [24] F. Franco, S. Fernández, J. Lloret-Fillol, *Curr. Opin. Electrochem.*, 2019, **15**, 109-117.
- [25] J. Grodkowski, D. Behar, P. Neta, P. Hambright, *J. Phys. Chem. A*, 1997, **101**, 248-254.
- [26] J. Bonin, M. Chaussemier, M. Robert, M. Routier, *ChemCatChem*, 2014, **6**, 3200-3207.
- [27] J. Bonin, M. Robert, M. Routier, *J. Am. Chem. Soc.*, 2014, **136**, 16768-16771.
- [28] H. Rao, L. C. Schmidt, J. Bonin, M. Robert, *Nature*, 2017, **548**, 74-77.
- [29] H. Rao, C.-H. Lim, J. Bonin, G. M. Miyake, M. Robert, *J. Am. Chem. Soc.*, 2018, **140**, 17830-17834.
- [30] Y. Tamaki, O. Ishitani, *ACS Catal.*, 2017, **7**, 3394-3409.
- [31] V. V. Pavlishchuk, A. W. Addison, *Inorg. Chim. Acta*, 2000, **298**, 97-102.
- [32] S. Mendes Marinho, M.-H. Ha-Thi, V.-T. Pham, A. Quaranta, T. Pino, C. Lefumeux, T. Chamailé, W. Leibl, A. Aukauloo, *Angew. Chem. Int. Ed.*, 2017, **56**, 15936-15940.
- [33] K. Kalyanasundaram, *Coord. Chem. Rev.*, 1982, **46**, 159-244.
- [34] J. Hawecker, J.-M. Lehn, R. Ziessel, *Helv. Chim. Acta*, 1986, **69**, 1990-2012.
- [35] A. Nakada, K. Koike, T. Nakashima, T. Morimoto, O. Ishitani, *Inorg. Chem.*, 2015, **54**, 1800-1807.
- [36] J.-M. Lehn, R. Ziessel, *J. Organomet. Chem.*, 1990, **382**, 157-173.
- [37] X.-Q. Zhu, M.-T. Zhang, A. Yu, C.-H. Wang, J.-P. Cheng, *J. Am. Chem. Soc.*, 2008, **130**, 2501-2516.
- [38] P. Gotico, A. Del Vecchio, D. Audisio, A. Quaranta, Z. Halime, W. Leibl, A. Aukauloo, *ChemPhotoChem*, 2018, **2**, 715-719.
- [39] P. Gotico, T.-T. Tran, A. Baron, B. Vauzeilles, C. Lefumeux, M.-H. Ha-Thi, T. Pino, Z. Halime, A. Quaranta, W. Leibl, A. Aukauloo, *ChemPhotoChem*, 2021, **5**, 654-664.
- [40] Y. Tamaki, K. Koike, T. Morimoto, O. Ishitani, *J. Catal.*, 2013, **304**, 22-28.



MAPYRO: the French Fellowship of the Pyrrolic Macrocyclic Ring / *MAPYRO: la communauté française des macrocycles pyrroliques*

Design and synthesis of charged porphyrin dimers for polyoxometalate recognition

Raphaël Lamare^{Ⓢ a}, Romain Ruppert^{Ⓢ a}, Mourad Elhabiri^{Ⓢ b}, Gilles Ulrich^{Ⓢ c},
Laurent Ruhlmann^{Ⓢ *, a} and Jean Weiss^{Ⓢ *, a}

^a Institut de Chimie de Strasbourg, UMR 7177 CNRS-Université de Strasbourg,
4 rue Blaise Pascal, 67000 Strasbourg, France

^b Equipe Chimie Bioorganique et Médicinale, Laboratoire d'Innovation Moléculaire et
Applications (LIMA), UMR7042, CNRS-Unistra-UHA, European School of Chemistry,
Polymers and Materials (ECPM), 25, rue Becquerel, 67087 Strasbourg, France

^c ICPEES - Institut de Chimie et Procédés pour l'Énergie, l'Environnement et la Santé,
ECPM, 25 rue Becquerel, 67087 Strasbourg, France

E-mails: raphael.lamare@etu.unistra.fr (R. Lamare), rruppert@unistra.fr (R. Ruppert),
elhabiri@unistra.fr (M. Elhabiri), gulrich@unistra.fr (G. Ulrich), lruhlmann@unistra.fr
(L. Ruhlmann), jweiss@unistra.fr (J. Weiss)

Abstract. A series of porphyrin dimers have been prepared and characterized in order to form inclusion complexes with Lindqvist-type polyoxometallates. The synthesis of the porphyrin dimer has been optimized and can serve general purposes. The formation of inclusion complexes has been monitored using spectroscopic methods and moderate affinities with $\log K_{\text{assoc}}$ varying from 2.6 to 4.2 have been determined and the parameters governing the formation of the complexes have been examined.

Keywords. Porphyrins, Polyoxometalates, Molecular recognition, Fluorescence quenching, Host-guest chemistry.

Available online 17th August 2021

1. Introduction

Polyoxometalates (POMs) have been widely studied in photovoltaic applications and in the design of electroactive materials despite their absorption in the 200–400 nm region that is a significant drawback regarding their efficiency. This inconvenience has been mostly circumvented by the use of sensitizers, that

absorbs in the visible region, able to transfer electrons to POMs. Among these sensitizers, porphyrins that offer the advantages of strong absorption coefficients in the visible domain have been used in efficient, but rather undefined, assemblies generated by polymerization at the surface of electrodes [1,2]. Discrete species can be prepared by several covalent methods. In polyoxomolybdates [3–6] and polyoxovanadates [7], replacing one or several peripheral hydroxyl groups by alkoxy groups of a linker already connected to a porphyrin unit has proven to

* Corresponding authors.

be efficient on several occasions, leading to scaffolds with photocatalytic activity. In the case of polyoxotungstates, it is also possible to substitute an oxo-group by a transition metal ion that will coordinate a peripheral ligand introduced on a porphyrin [8]. Coordination chemistry has been employed taking advantage of the Lewis acidity of metal ions incorporated in the porphyrin core [9,10], however, due to the highly negative charge of the POMs, electrostatic interactions have emerged as an efficient self-assembly driving force in the field of porphyrin/POM hybrids [11–13]. Despite their performances in photo-induced processes, materials built on electrostatic interactions are structurally poorly defined [14–16] which limits the scope of optimization based on molecular properties. Well-defined species provide information on interactions at the molecular scale and a reliable insight on the performance of the resulting molecular materials.

2. Results and discussion

Supramolecular chemistry and its toolbox of non-covalent interactions combined with host–guest principles of molecular recognition provide tools for the design of hosts adapted for the binding of diversely shaped polyoxomolybdates. In an attempt to provide a rational approach to the formation of well-defined porphyrin/POM hybrids, charged bis-porphyrinic receptors have been synthesized and used in binding studies of Lindqvist-type POMs. The design of pre-organized porphyrin dimers able to develop controlled interactions with polyoxometalates is described hereafter. In order to introduce charges on the porphyrin dimers, two options were possible and are summarized in Figure 1. Introduction of charges at the position marked in green ($X = N^+$) *via* nucleophilic addition of a pyridine group on a porphyrin radical cation, obtained by chemical or electrochemical oxidation of a triarylporphyrin, failed for mechanistic reasons [17], and thus the introduction of charges in the positions marked in red ($Y = N^+$) has been developed (Figure 1).

Two main synthetic methods have been developed. The first dealt with the stepwise functionalization of the linker and the formation of the series of compounds represented in Scheme 1.

The yields of porphyrins **3**, **4**, **5** and **6** have been optimized through the testing of a variety of solvents

at room temperature and reflux. It must be noted that some loss of compound occurs during the anion exchange that follows the quaternization of the pyridine group. The porphyrins **3**, **4**, **5** and **6** can be involved as alkylating agent for a second quaternization of either **1** or **2** in refluxing THF over 30 h to lead to the bis-porphyrins **7**, **8**, **9**, **10** represented in Figure 2.

The same series of compounds can be obtained by the second approach that consists in reacting an excess of the porphyrins **1** or **2** with the appropriate α, α' -dibromoxylene in refluxing THF. This direct method afforded the doubly charged bis-porphyrins **7**, **8**, **9** and **10** in 46%, 38%, 46% and 32% yield, respectively. Although all the bis-porphyrins were intended to form tweezers in which the two porphyrins are facing each other, all characterization methods suggested that the compounds adopt an extended conformation in solution, as shown, for example, by the ^1H NMR spectrum of **7** in DMSO (Figure 3). In this spectrum, no anisotropic shielding of the porphyrin protons due to stacking is observed and all signals appear at chemical shifts typical of independent porphyrins.

Primary modelling has been performed using Spartan (MM2) for 9Zn_2 and three different template guests, namely 4,4'-bipyridine, 4,4'-dipyridylacetylene, and 4-(*p*-phenyl-4-pyridyl)-pyridine, to evaluate the most favourable size for a guest in the hypothetical zinc(II) complexes. The structure calculated for 4,4'-dipyridylacetylene as a guest is depicted in Figure 4. The series of calculated structures suggested that in a cofacial conformation of the two porphyrins, an energy minimum should be reached for a distance somewhere between 11 and 14 Å for 9Zn_2 although all structures have proven to be quite flexible. For this reason, the choice of POM guest for this study rested on a Lindqvist-type entity in which the distance between terminal oxygen atoms is 8 Å (X-ray diffraction) [18]. The inclusion of Lindqvist POM ($[\text{Mo}_6\text{O}_{19}]^{2-}$) in bis-porphyrins has been investigated by various methods. UV-visible absorption titrations were judged not suitable due to the absence of noticeable spectral variations upon addition of guest. However, fluorescence quenching experiment and excited state lifetime measurements on the porphyrin dimers and electrochemistry provided insightful information on the recognition process.

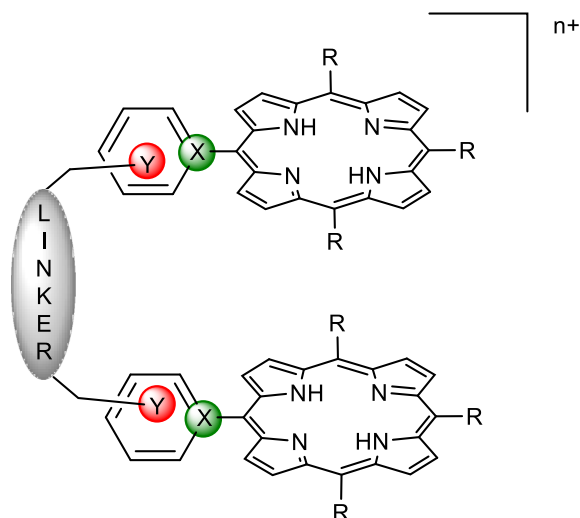
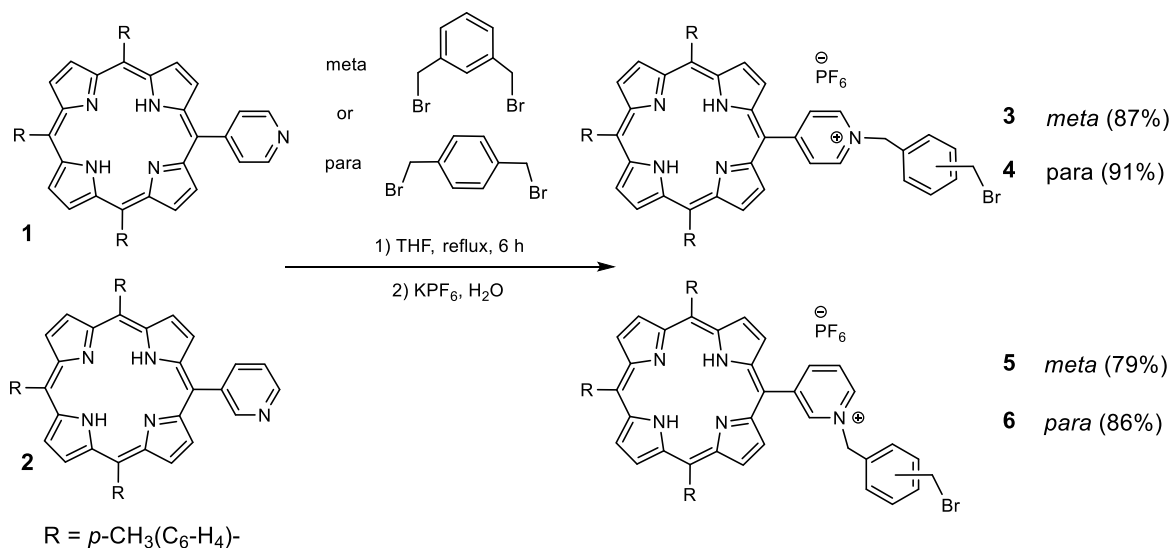


Figure 1. Targeted charged bis-porphyrins and two possible charge localizations (X or Y = tetravalent N).



Scheme 1. Synthesis of bis-porphyrin precursors 3–6.

3. Fluorescence quenching titrations

Fluorescence quenching experiments have been performed on hosts **3–6** and **7–10** to determine the highest association constant. For the strongest porphyrin/POM association, excited state lifetime measurements have been performed. Figure 5(a) represents a typical evolution of the porphyrin emission observed during the titration of **9** (6.43×10^{-6} M)

with [Mo₆O₁₉][(n-Bu)₄N]₂ (1.76×10^{-2} M). Monitoring the decrease of the intensity for both emission bands centred at 652 and 712 nm upon addition of the POM guest lead to the plot in Figure 5(b) which confirms that the emission decrease at 652 nm is not the sole result of dilution. The same trend is observed for the band at 712 nm. The analysis of these data using the Specfit program yielded an association constant *K* with a log value of 4.20 ± 0.03

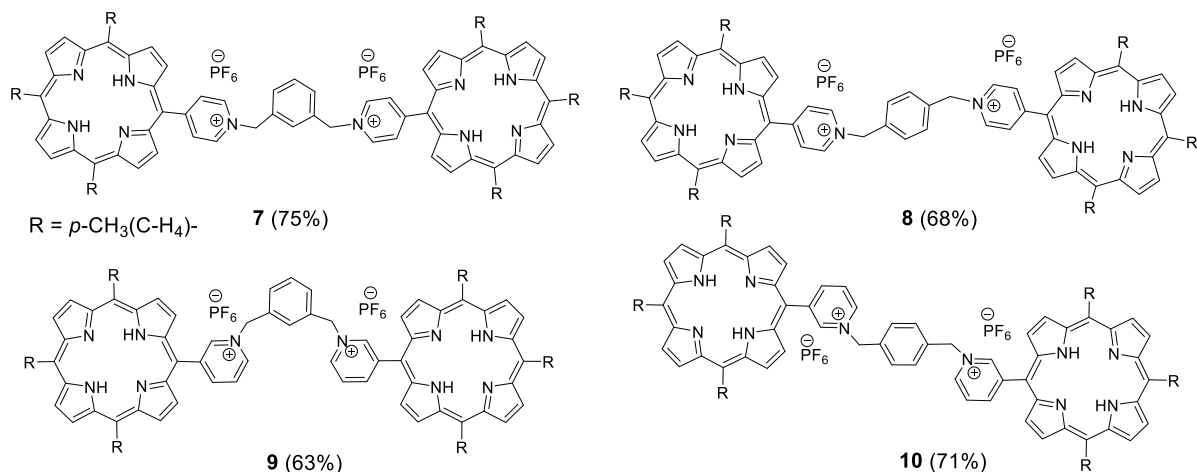


Figure 2. Series of doubly charged porphyrin dimers obtained by stepwise quaternization.

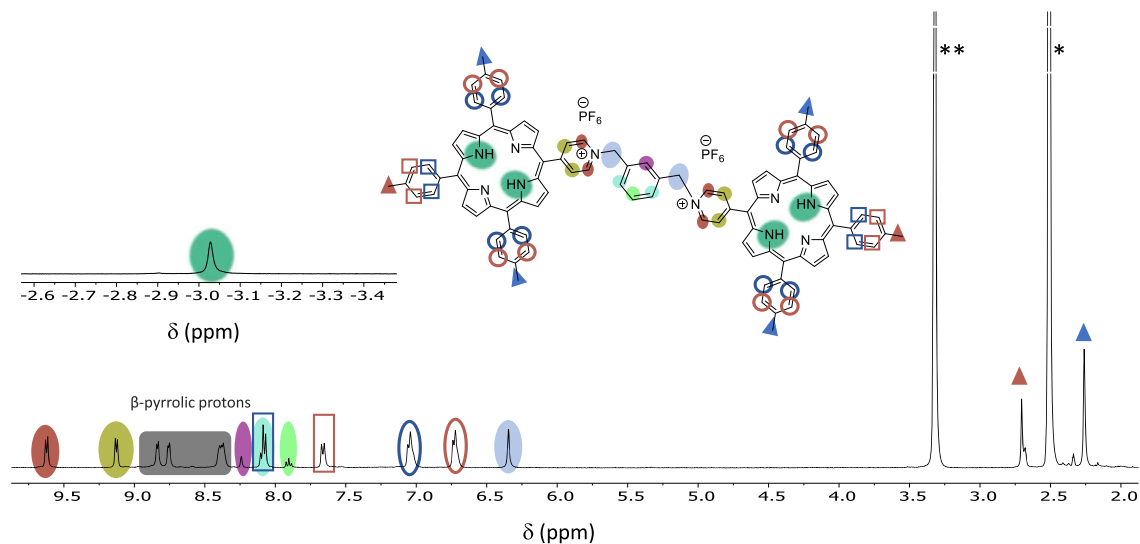


Figure 3. ¹H NMR of **7** at 300 MHz in DMSO-*d*₆ (298 K). (*) Residual non deuterated solvent and (**) H₂O.

for a complex **9**-POM with a 1:1 stoichiometry. The corresponding Job plot is available in the supporting information (Figure S51), and the distribution curve (Figure S46 in the ESI) shows that a maximum of 95% of host-guest complex is formed in the presence of large excess of POM (ca. 340 eq).

The behaviour of **9** has been compared with the behaviour of a single porphyrin derivative such as **6**, and, interestingly, the fluorescence quenching seems globally more efficient in the case of the single porphyrin **6** (Figure 6). The residual emission observed

at the end of the titration is indeed probably due to free porphyrin **6** because of the experimental conditions for which only about 65% of **6**-POM complex is formed (Figure S47 in the ESI). In addition, the monitoring of the decrease clearly suggests that the association process is less efficient than in the case of the dimer ($\log K = 2.4 \pm 0.1$ for **6**-POM versus $\log K = 4.20 \pm 0.03$ for **9**-POM as determined by Specfit). Thus, a reasonable hypothesis is that the single porphyrin **6** has more degrees of freedom and is able to establish some close contact with the POM for efficient excited

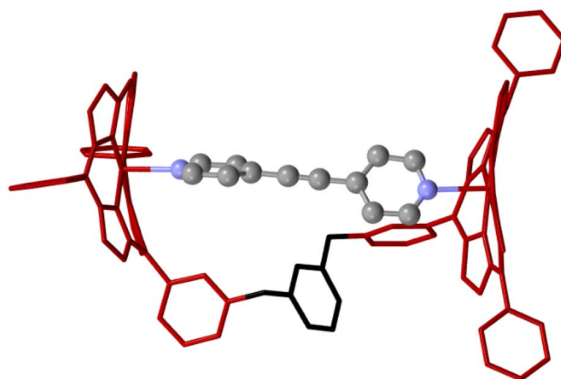


Figure 4. Artificially folded calculated structure of a coordination complex of 9Zn_2 with 4,4'-dipyridylacetylene. Colour code: Burgundy = porphyrin, black = spacer, ball and stick = guest.

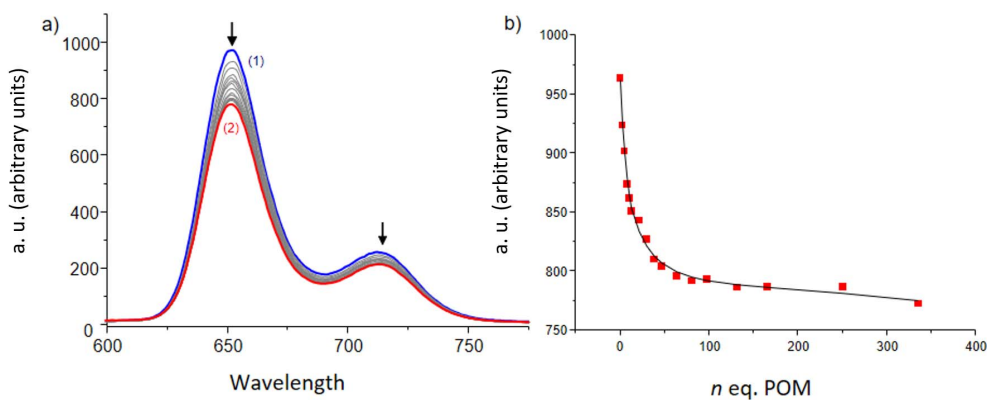


Figure 5. (a) Fluorescence titration of **9** with $[\text{Mo}_6\text{O}_{19}][(\text{n-Bu})_4\text{N}]_2$. Solvent: DME, $T = 25.0\text{ }^\circ\text{C}$, $\lambda_{\text{ex}} = 517\text{ nm}$, emission and excitation slits 15/20 nm, (1) $[\mathbf{9}] = 6.43 \times 10^{-6}\text{ M}$; (2) $[\text{POM}]/[\mathbf{9}] = 340$. (b) Monitoring of the emission intensity at 652 nm as a function of the number of $[\text{Mo}_6\text{O}_{19}][(\text{n-Bu})_4\text{N}]_2$ equivalents. The absorption spectra are not corrected from dilution effects.

Table 1. Solvent DME, $T = 25.0\text{ }^\circ\text{C}$, $\lambda_{\text{ex}} = 517 (\pm 1)\text{ nm}$, (error) equal to 1σ (standard deviation)

Compound	Porphyrin 3	Bis-por 7	Porphyrin 4	Bis-por 8	Porphyrin 5	Bis-por 9	Porphyrin 6	Bis-por 10
$\log K(\sigma)$	2.8(1)	2.7(1)	2.7(1)	3.3(1)	2.8(1)	4.20(3)	2.4(1)	2.6(2)

state quenching whereas, in the dimer, the presence of the spacer introduces some restraints preventing both porphyrins from getting in close contact with the POM guest or forcing only one of the porphyrin to be quenched by the POM guest thus explaining the significant residual of emission **9**-POM (Figure S46 in the ESI). It should be noted that for all single porphyrin derivatives, stoichiometry has been difficult

to assign due to the level of error in the data and the weakness of most association constants and the latter have been determined for a 1/1 stoichiometry for comparison. A summary of the association constants is displayed in Table 1.

The association constants with the single porphyrin species are all in the same range and, as expected, rather weak. Among the bis-porphyrin

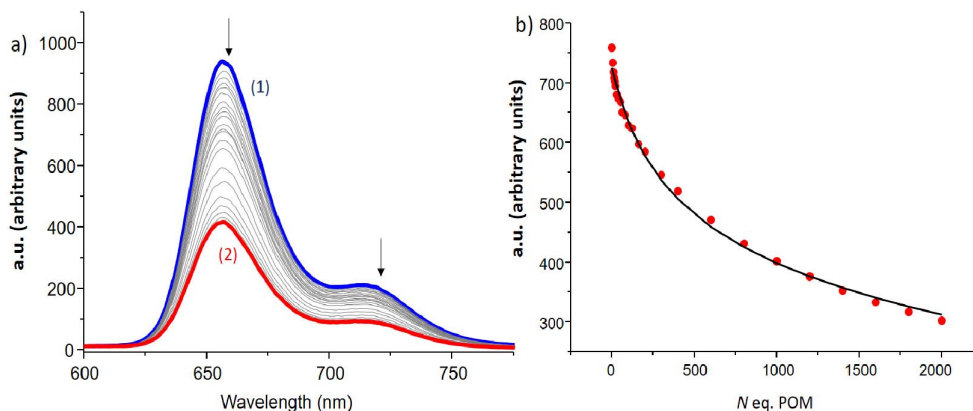


Figure 6. (a) Fluorescence titration of **6** with $[\text{Mo}_6\text{O}_{19}][(\text{n-Bu})_4\text{N}]_2$. Solvent: DMF, $T = 25.0\text{ }^\circ\text{C}$, $\lambda_{\text{ex}} = 517\text{ nm}$, emission and excitation slits 15/20 nm, (1) $[\mathbf{6}] = 4.39 \times 10^{-6}\text{ M}$; (2) $[\text{POM}]/[\mathbf{6}] = 2000$. (b) Monitoring of the emission intensity at 657 nm as a function of the number of equivalents $[\text{Mo}_6\text{O}_{19}][(\text{n-Bu})_4\text{N}]_2$. The emission spectra are not corrected from dilution effects.

receptors, **9** emerges being by far the best receptor for a Lindqvist-type guest. Although the SpartanTM model suggest an ideal porphyrin–porphyrin distance in the 11 to 14 Å range that is too large for the terminal oxygen atoms spacing in a Lindqvist-type polyoxometalate, the difference in stability may be explained by a stronger interaction of the oxygen atoms with the *m*-pyridinium charges in **9**. A better wrapping of the porphyrins around the POM would release two PF_6^- anions and the corresponding entropy gain could account for the 2 orders of magnitude enhancement of the association. In comparison, for a similar positioning of the pyridinium charges in **10**, the longer spacer must still allow a stronger and thus more organized interaction of the counter anions with the host–guest complex. As a result of the binding studies described above, the **9**:POM species has been selected to investigate the properties of the porphyrin/POM scaffolds.

4. Electrochemistry and photophysical properties of **9**:POM species

The binary complex **9**-POM has been selected to determine the nature of both the interactions and the quenching observed in solution. As shown by the series of voltammograms in Figure 7, the trace of the bis-porphyrin reduction is unaffected by the addition of POM in the millimolar concentration range. This

observation suggests the absence of electronic interactions between the host and the guest in the ground state, confirming the absence of spectral changes that hampered an easy determination of the association constants by UV–Vis means. The values of the redox couples observed in Figure 7 allow prediction of the energy levels involved in a photo-induced electron transfer in any porphyrin/POM donor/acceptor scaffold.

The two modes of quenching, static and dynamic, are represented in Figure 8, together with the associated energy diagram of the oxidative quenching of the porphyrin excited state. In a static quenching process, the fluorescence decrease is caused by the lesser number of fluorescent chromophores when the quencher is present that transduces in a lower fluorescence quantum yield but the kinetic constants associated to the relaxation of the excited state remain unchanged. As a result, the excited state lifetime does not vary upon changes in the concentration of the quencher, which is typical of the formation of a non-fluorescent host–guest complex [19]. When the quenching results from a dynamic process, the rising of a new deactivation pathway affects the relaxation of the excited state and both the fluorescence quantum yield and the lifetime of the excited state vary upon the quencher concentration changes [20].

As shown in the Figure 9, neither the profile nor the time scale of the decay show any alteration upon the addition of POM to the fluorescent dimer **9**.

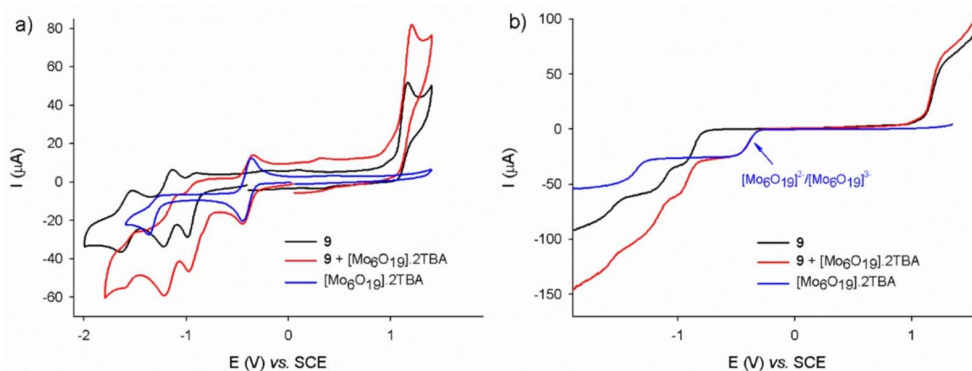


Figure 7. (a) Cyclic voltammogram of the porphyrin dimer **9** (black trace), of $[[\text{Mo}_6\text{O}_{19}][(\text{n-Bu})_4\text{N}]_2]$ (blue trace) and a mixture of **9** + $[[\text{Mo}_6\text{O}_{19}][(\text{n-Bu})_4\text{N}]_2]$ (red trace), conditions: DMF 0.1 M NBu_4PF_6 , $[\mathbf{9}] = [[\text{Mo}_6\text{O}_{19}][(\text{n-Bu})_4\text{N}]_2] = 0.80$ mM. Scan rate: $\nu = 100$ $\text{mV}\cdot\text{s}^{-1}$. (b) Corresponding stationary voltamperometry: $\nu = 10$ $\text{mV}\cdot\text{s}^{-1}$, working electrode: glassy carbon ($d = 3$ mm), internal reference: Fc (not shown).

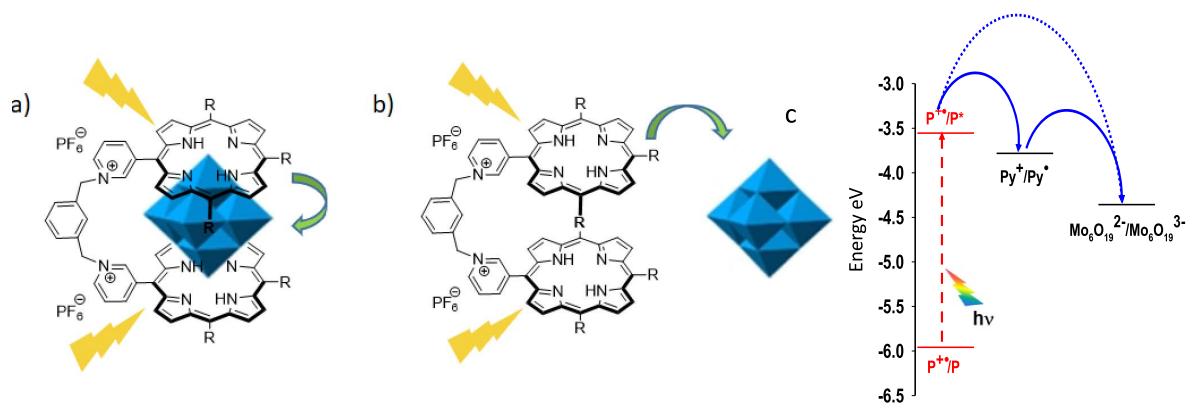


Figure 8. Idealized representation of the oxidative (a) static fluorescence quenching and (b) dynamic fluorescence quenching of porphyrins in the dimer **9** by a Lindqvist-type polyoxometalate; (c) energy diagram of the subsequent electron transfer. P = porphyrin.

Table 2. Lifetime values for dimer **9** as a function of $[[\text{Mo}_6\text{O}_{19}][(\text{Bu}_4\text{N})_2]$ equivalents (10% error margin)

POM equivalents	0	2.5	5	18	36	72	184	368
Lifetime (ns)	10.1	9.94	9.77	9.51	9.27	9.53	9.86	9.80

Table 2 summarizes the small changes (average: 6%) observed for the lifetime of **9** which are assigned to small dilution effects and largely within the standard errors (10%).

These results clearly show that the partial fluorescence extinction is caused by the formation of a host–guest complex between **9** and the POM in their ground state and not by a dynamic process or an electron transfer in the excited state.

5. Conclusion

In this work, several dicationic bis-porphyrins have been prepared as receptors for polyoxometalate anions. The receptors show various positioning and spacing of their positive charge and, to the one exception of **9**, only moderate affinities for a Lindqvist-type polyoxometalate. As a result, it is fair to assume that electrostatic interactions taken for granted

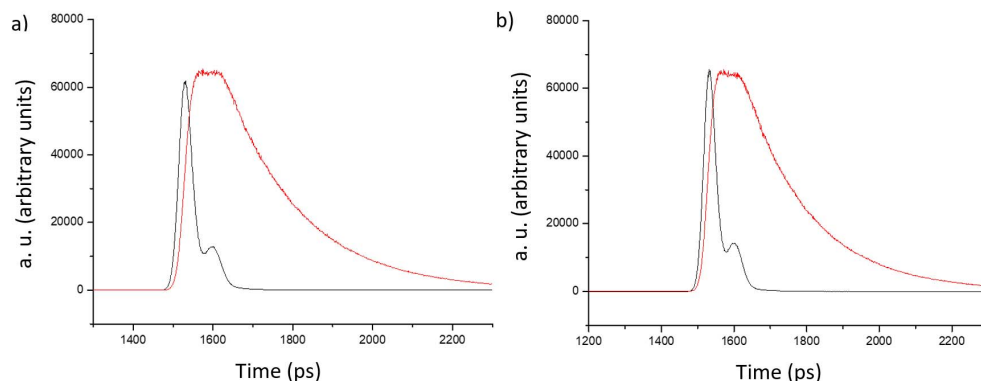


Figure 9. Excitation pulse (black trace) and decay of the fluorescing species (red trace): (a) dimer **9**, (b) dimer **9** and 368 equivalents of $[\text{Mo}_6\text{O}_{19}][(\text{n-Bu})_4\text{N}]_2$. Solvent DME, $T = 25.0\text{ }^\circ\text{C}$, $\lambda_{\text{ex}} = 517\text{ nm}$, $[\mathbf{9}] = 6.43 \times 10^{-6}\text{ M}$.

in most self-assembling methods for the formation of porphyrin-POM scaffolds are subject to geometric requirements. Thus without the knowledge of the precise structure of the porphyrin-POM assembly, the rationalization of the behaviour and the structure/properties relationships remains difficult, if not unreliable. In the case of the most stable host-guest complex **9-POM**, it has been shown that a quenching of the excited state of the bis-porphyrin is due to the formation of a host-guest complex because the lifetime of the fluorescent species itself remains unaffected. To rationalize all parameters, receptors with different spacers and the use of charged metalloporphyrins instead of free bases needs to be performed. At the moment, the investigation of the affinities of all other porphyrin dimers described in this work for variously shaped POMs such as Keggin and Anderson is in progress in order to extract parameters relevant to the host-guest interactions.

6. Experimental section

6.1. General methods

Dichloromethane used for reactions or column chromatography was distilled from calcium hydride. Tetrahydrofuran and toluene were distilled over sodium/benzophenone ketyl under argon. All other commercially available reagents and solvents were used without further purification. Bases (K_3PO_4 , K_2CO_3 , Cs_2CO_3 and Na_2CO_3) were oven-dried at $100\text{ }^\circ\text{C}$. Analytical thin layer chromatography (TLC) was carried out on silica gel 60 F_{254} (Merck) and

column chromatography was performed with silica gel or alumina from Merck (alumina oxide 60 standardized or silica gel 60, $0.04\text{--}0.063\text{ }\mu\text{m}$). Nuclear magnetic resonance spectra were recorded on Bruker Avance spectrometers at 300, 400, 500 or 600 MHz. The chemical shifts are given in parts-per-million (ppm) on the delta scale. The solvent peak was used as reference value: for ^1H NMR: $\text{CDCl}_3 = 7.26\text{ ppm}$, $\text{DMSO-}d_6 = 2.50\text{ ppm}$, for ^{13}C NMR: $\text{CDCl}_3 = 77.23\text{ ppm}$, $\text{DMSO-}d_6 = 39.52\text{ ppm}$. The data are presented as follows: chemical shift, multiplicity (s = singlet, d = doublet, t = triplet, q = quartet, hept = heptuplet, m = multiplet), coupling constant (J/Hz) and the integration. Mass spectra were obtained by ESI-TOF or MALDI-TOF (337 nm nitrogen laser for desorption, dithranol used as matrix) experiments. High resolution mass spectra (HRMS) data were recorded on a microTOF spectrometer equipped with orthogonal electrospray interface (ESI). The ions (m/z) were analyzed on a Bruker Daltonics microTOF for ESI and a Bruker Autoflex II TOF-TOF for MALDI. The parent ions, $[\text{M}+\text{H}]^+$, $[\text{M}+\text{K}]^+$, $[\text{M}+\text{Na}]^+$ or $[\text{M}^{n+}]$ are given. UV-visible spectra were recorded on a Cary 5000 UV/vis/NIR double-beam spectrometer in dichloromethane, chloroform or DMF. Molar extinction coefficients were determined for samples with analyte concentrations ranging from 5×10^{-6} to $5 \times 10^{-5}\text{ mol}\cdot\text{L}^{-1}$.

Binding studies were carried out with spectroscopic grade DMF (Carlo Erba, 99.9% for spectroscopy). To prevent any photochemical degradation, all solutions were protected from daylight expo-

sure. All stock solutions were prepared using a Mettler Toledo XA105 Dual Range (0.01/0.1 mg–41/120 g) to weigh samples, and complete dissolution in DMF was achieved using an ultrasonic bath. The concentrations of stock solutions of the receptors and substrates were calculated by the quantitative dissolution of solid samples in DMF.

Luminescence titrations were carried out on solutions of dimers and monomers with absorbances lower than 0.1. The titrations of 2 mL of dimer or monomer with $[\text{Mo}_6\text{O}_{19}][(\text{Bu}_4\text{N})_2]$ ($[\text{Dimers}] = 6.43 \times 10^{-6}$ M and $[\text{Monomers}] = 4.39 \times 10^{-6}$ M) were carried out in a 1 cm Hellma quartz optical cell by the addition of known microvolumes of solutions of $[\text{Mo}_6\text{O}_{19}][(\text{Bu}_4\text{N})_2]$ with an Eppendorf Research plus. The excitation wavelengths were set at 517 or 559 nm. The luminescence spectra were recorded from 550 to 800 nm on a PerkinElmer LS-50B instrument maintained at 25 °C. The slit widths were set between 15 and 20 nm for the emission. Luminescence titrations were conducted under precise and identical experimental conditions.

The spectrophotometric titration of **9** with $[\text{Mo}_6\text{O}_{19}][(\text{Bu}_4\text{N})_2]$ (**9**) = 1.76×10^{-2} M) was carried out in a 1 cm Hellma quartz optical cell by the addition of known microvolumes of solutions of $[\text{Mo}_6\text{O}_{19}][(\text{Bu}_4\text{N})_2]$ with an Eppendorf Research plus. Special care was taken to ensure that complete equilibration was attained. The corresponding UV-Vis spectra were recorded from 300 to 800 nm on a Cary 5000 (Agilent) spectrophotometer maintained at 25 °C.

The spectrophotometric data were analyzed with Specfit [21] program that adjusts the absorptivities and the stability constants of the species formed at equilibrium. Specfit uses factor analysis to reduce the absorbance matrix and to extract the eigenvalues prior to the multi-wavelength fit of the reduced data set according to the Marquardt algorithm [22,23].

6.2. General procedure for the single porphyrin derivatives **3–6** (GPI)

A mixture of porphyrin **1** or **2** and the α, α' -dibromom-xylene corresponding in THF (15 mL) was refluxed for 6 h under argon atmosphere. Water was added to the reaction mixture. The organic layer was separated, and the aqueous layer was extracted with CH_2Cl_2 (20 mL). The organic layer was washed with

water, dried over Na_2SO_4 and the solvent removed under vacuum. The crude product was recrystallized three times (addition of saturated KPF_6 aqueous solution to acetone solution). The precipitate was filtered, washed with water and solubilized in acetone. The acetone was then removed under vacuum.

6.2.1. Porphyrin **3**

Prepared following the **GPI** and using α, α' -dibromo-m-xylene (160 mg, 1.60 mmol, 20 eq) and porphyrin **1** (50 mg, 0.08 mmol, 1 eq). The crude product was purified by silica gel column chromatography (CH_2Cl_2) and gradually ending with $\text{CH}_2\text{Cl}_2/\text{Acetone}$ (9/1). The compound **3** (73 mg, 0.071 mmol, 87%) was obtained as a purple solid. ^1H NMR (500 MHz, Acetone- d_6): δ 9.73 (d, $J = 6.6$ Hz, 2H, H-*ortho*-py $^+$), 9.16 (d, $J = 6.6$ Hz, 2H, H-*meta*-py $^+$), 9.03–8.84 (m, 8H, H- β -pyrrolic), 8.23–8.06 (m, 6H, H-tolyl), 7.93 (s, 1H), 7.81 (dt, $J = 7.0, 2.0$ Hz, 1H), 7.68 (d, $J = 7.7$ Hz, 6H, H-tolyl), 7.65–7.59 (m, 2H), 6.43 (s, 2H, Py $^+$ -CH $_2$ -Ar), 4.81 (d, $J = 5.5$ Hz, 2H, Ar-CH $_2$ -Br), 2.72 (s, 9H, -CH $_3$), -2.72 (s, 2H, free base). ^{13}C NMR (11 MHz, Acetone- d_6) δ 161.1, 145.4, 144.3, 139.2, 139.1, 139.0, 135.4, 134.8, 134.4, 130.6, 129.2, 129.1, 128.7, 128.7, 128.7, 123.7, 123.7, 122.5, 122.5, 113.1, 64.3, 27.6, 21.7. ^{31}P NMR (203 MHz, Acetone- d_6) δ -144.0 (hept, $J = 711.7$ Hz). ^{19}F NMR (471 MHz, Acetone- d_6) δ -72.6 (d, $J = 711.7$ Hz). UV-Vis (DMF): λ (ϵ) = 419 (223000), 516 (12700), 552 (7700), 591 (5700), 647 nm ($4100 \text{ M}^{-1}\cdot\text{cm}^{-1}$). ESI-TOF: $m/z = 840.27$ Calcd for $\text{C}_{54}\text{H}_{43}\text{N}_5\text{Br}$ ($[\text{M}^+]$): 840.27. TLC (silica) R_f : 0.25 ($\text{CH}_2\text{Cl}_2/\text{Acetone}$ 9/1).

6.2.2. Porphyrin **4**

Prepared following the **GPI** and using α, α' -dibromo-m-xylene (160 mg, 1.60 mmol, 20 eq) and porphyrin **1** (50 mg, 0.08 mmol, 1 eq). The crude product was purified by silica gel column chromatography (CH_2Cl_2) and gradually ending with $\text{CH}_2\text{Cl}_2/\text{Acetone}$ (9/1). The compound **4** (76 mg, 0.073 mmol, 91%) was obtained as a purple solid. ^1H NMR (400 MHz, Acetone- d_6): δ 9.72 (d, $J = 6.8$ Hz, 2H, H-*ortho*-py $^+$), 9.16 (d, $J = 6.8$ Hz, 2H, H-*meta*-py $^+$), 9.03–8.95 (m, 4H, H- β -pyrrolic), 8.91 (q, $J = 4.9$ Hz, 4H, H- β -pyrrolic), 8.17–8.06 (m, 6H, H-tolyl), 7.94 (d, $J = 8.0$ Hz, 2H), 7.75 (d, $J = 8.0$ Hz, 2H), 7.69–7.59 (m, 6H, H-tolyl), 6.43 (s, 2H, Py $^+$ -CH $_2$ -Ar), 4.78 (s, 2H, Ar-CH $_2$ -Br), 2.70 (s, 6H, -CH $_3$), 2.69 (s, 3H, -CH $_3$), -2.73 (s, 2H, free base). ^{13}C NMR (126 MHz,

Acetone- d_6): δ -72.5 (d, J = 707.7 Hz). ^{31}P NMR (121 MHz, Acetone- d_6): δ -144.2 (hept, J = 707.7 Hz). ^{19}F NMR (282 MHz, Acetone- d_6): δ 160.9, 144.2, 141.2, 139.5, 138.8, 135.2, 134.5, 134.5, 131.3, 131.0, 128.5, 128.5, 123.4, 122.3, 113.0, 65.0, 33.4, 27.5, 21.5. UV-Vis (DMF): λ (ϵ) = 421 (314000), 518 (19000), 556 (11800), 592 (7300), 649 nm (6600 $\text{M}^{-1}\cdot\text{cm}^{-1}$). HRMS, ESI-TOF: m/z = 840.2685 Calcd for $\text{C}_{54}\text{H}_{43}\text{BrN}_5^+$ ($[\text{M}^+]$): 840.2696. TLC R_f : 0.24 ($\text{CH}_2\text{Cl}_2/\text{Acetone}$ 9/1).

6.2.3. Porphyrin 5

Prepared following the **GP1** and using α, α' -dibromo-*m*-xylene (160 mg, 1.60 mmol, 20 eq) and porphyrin **2** (50 mg, 0.08 mmol, 1 eq). The crude product was purified by silica gel column chromatography (CH_2Cl_2) and gradually ending with $\text{CH}_2\text{Cl}_2/\text{Acetone}$ (9/1). The compound **5** (68 mg, 0.065 mmol, 79%) was obtained as a purple solid. ^1H NMR (400 MHz, Acetone- d_6): δ 10.21 (m, 1H, H-py $^+$), 9.79 (dt, J = 6.2, 1.5 Hz, 1H, H-py $^+$), 9.60 (dt, J = 8.0, 1.5 Hz, 1H, H-py $^+$), 9.04–8.88 (m, 8H, H- β -pyrrolic), 8.81 (dd, J = 8.1, 6.2 Hz, 1H, H-py $^+$), 8.18–8.07 (m, 2H, H-tolyl), 7.97 (br s, 1H) 7.83 (dd, J = 7.6, 1.6 Hz, 1H), 7.70–7.61 (m, 7H, H-tolyl), 7.58–7.55 (m, 1H, H3), 6.45 (s, 2H, Py $^+$ -CH $_2$ -Ar), 4.68 (s, 2H, Ar-CH $_2$ -Br), 2.71 (s, 3H, -CH $_3$), 2.70 (s, 6H, -CH $_3$), -2.78 (s, 2H, free base). ^{13}C NMR (126 MHz, Acetone- d_6): δ 150.1, 148.1, 145.2, 144.0, 140.8, 139.5, 139.5, 138.8, 135.2, 131.5, 130.9, 130.9, 130.2, 128.5, 128.5, 128.3, 123.1, 122.1, 110.6, 65.7, 33.5, 21.5. ^{31}P NMR (121 MHz, Acetone- d_6): δ -144.3 (hept, J = 707.5 Hz). ^{19}F NMR (282 MHz, Acetone- d_6): δ -72.60 (d, J = 707.5 Hz). UV-Vis (DMF): λ (ϵ) = 422 (312000), 517 (18000), 552 (8900), 591 (6400), 649 nm (5700 $\text{M}^{-1}\cdot\text{cm}^{-1}$). HRMS, ESI-TOF: m/z = 840.2658 Calcd for $\text{C}_{54}\text{H}_{43}\text{BrN}_5^+$ ($[\text{M}^+]$): 840.2696. TLC R_f : 0.19 ($\text{CH}_2\text{Cl}_2/\text{Acetone}$ 9/1).

6.2.4. Porphyrin 6

Prepared following the **GP1** and using α, α' -dibromo-*p*-xylene (160 mg, 1.60 mmol, 20 eq) and porphyrin **2** (50 mg, 0.08 mmol, 1 eq). The crude product was purified by silica gel column chromatography (CH_2Cl_2) and gradually ending with $\text{CH}_2\text{Cl}_2/\text{Acetone}$ (9/1). The compound **6** (72 mg, 0.07 mmol, 86%) was obtained as a purple solid. ^1H NMR (400 MHz, Acetone- d_6): δ 10.19 (s, 1H, H-py $^+$), 9.79 (d, J = 6.2 Hz, 1H, H-py $^+$), 9.59 (d, J = 7.9 Hz, 1H, H-py $^+$), 9.10–8.87 (m, 8H, H- β -pyrrolic), 8.80 (dd,

J = 7.9, 6.2 Hz, 1H, H-py $^+$), 8.21–8.06 (m, 6H, H-tolyl), 7.86 (d, J = 8.1 Hz, 2H), 7.74–7.58 (m, 8H, H-tolyl), 6.44 (s, 2H, Py $^+$ -CH $_2$ -Ar), 4.69 (s, 2H, Ar-CH $_2$ -Br), 2.71 (s, 6H, -CH $_3$), 2.71 (s, 3H, -CH $_3$), -2.78 (s, 2H, free base). ^{13}C NMR (126 MHz, Acetone- d_6): δ 50.1, 148.2, 145.2, 139.5, 138.8, 135.2, 134.7, 131.2, 130.8, 128.5, 128.5, 128.3, 123.1, 122.1, 65.6, 33.3, 21.5. ^{31}P NMR (121 MHz, Acetone- d_6): δ -141.3 (hept, J = 707.5 Hz). ^{19}F NMR (282 MHz, Acetone- d_6): δ -72.6 (d, J = 707.5 Hz). UV-Vis (DMF): λ (ϵ) = 422 (314000), 517 (17500), 552 (8500), 591 (6000), 649 nm (5200 $\text{M}^{-1}\cdot\text{cm}^{-1}$). HRMS, ESI-TOF: m/z = 840.2644 Calcd for $\text{C}_{54}\text{H}_{43}\text{BrN}_5^+$ ($[\text{M}^+]$): 840.2696. TLC R_f : 0.23 ($\text{CH}_2\text{Cl}_2/\text{Acetone}$ 9/1).

6.3. General procedure for the bis-porphyrin 7–10 (GP2)

6.3.1. Method A

A mixture of monomeric porphyrin and porphyrins **1** or **2** in THF (5 mL) was refluxed for 30 h under argon atmosphere. Water was added to the reaction mixture. The organic layer was separated, and the aqueous layer was extracted with CH_2Cl_2 (20 mL). The organic layer was washed with water, dried over Na_2SO_4 and the solvent removed under vacuum. The crude product was recrystallized three times (addition of saturated KPF $_6$ aqueous solution to acetone solution). The precipitate was filtered, washed with water and solubilized in acetone. The acetone was removed under vacuum.

6.3.2. Method B

A mixture of porphyrin **1** or **2** and the α, α' -dibromo-*xylene* corresponding in THF (15 mL) was refluxed for 38 h under argon atmosphere. Water was added to the reaction mixture. The organic layer was separated, and the aqueous layer was extracted with CH_2Cl_2 (20 mL). The organic layer was washed with water, dried over Na_2SO_4 and the solvent removed under vacuum. The crude product was recrystallized three times (addition of saturated KPF $_6$ aqueous solution to acetone solution). The precipitate was filtered, washed with water and solubilized in acetone. The acetone was removed under vacuum.

6.3.3. Bis-porphyrin 7

Prepared following the **GP2** and using monomeric systems (61 mg, 0.062 mmol, 1 eq) (Method A) or

α, α' -Dibromo-*m*-xylene (18 mg, 0.062 mmol, 1 eq) (Method B) and porphyrin **1** (204 mg, 0.31 mmol, 5 eq). The crude product was purified by silica gel column chromatography (CH_2Cl_2) and gradually ending with a solution of KPF_6 (27 mM) in acetone. The compound **7** (80 mg, 0.047 mmol, 75%, Method A) or (49 mg, 0.029 mmol, 46%, Method B) was obtained as a purple solid. ^1H NMR (500 MHz, $\text{DMSO}-d_6$): δ 9.62 (d, $J = 6.0$ Hz, 4H, H-*ortho*-py $^+$), 9.12 (d, $J = 6.0$ Hz, 4H, H-*meta*-py $^+$), 8.83 (d, $J = 4.5$ Hz, 4H, H- β -pyrrolic), 8.74 (d, $J = 4.5$ Hz, 4H, H- β -pyrrolic), 8.38 (d, $J = 4.7$ Hz, 4H, H- β -pyrrolic), 8.35 (d, $J = 4.7$ Hz, 4H, H- β -pyrrolic), 8.24 (s, 1H), 8.12–8.02 (m, 6H, H-*ortho*-tolyl), 7.89 (d, $J = 7.7$ Hz, 1H), 7.65 (d, $J = 7.4$ Hz, 4H, H-*meta*-tolyl), 7.01 (d, $J = 7.3$ Hz, 8H, H-*ortho*-tolyl), 6.69 (d, $J = 7.3$ Hz, 8H, H-*meta*-tolyl), 6.33 (s, 4H, $-\text{CH}_2-$), 2.69 (s, 6H, $-\text{CH}_3$), 2.24 (s, 12H, $-\text{CH}_3$), -3.06 (s, 4H, free base). ^{13}C NMR (126 MHz, $\text{DMSO}-d_6$): δ 158.5, 143.4, 138.1, 137.6, 137.3, 136.7, 135.5, 134.2, 133.4, 132.8, 131.0, 130.4, 129.7, 127.7, 126.9, 121.7, 120.3, 112.4, 63.1, 21.1, 20.6. ^{31}P NMR (121 MHz, $\text{DMSO}-d_6$): δ -144.2 (hept, $J = 711.3$ Hz). ^{19}F NMR (282 MHz, $\text{DMSO}-d_6$): δ -70.1 (d, $J = 711.3$ Hz). UV-Vis (DMF): λ (ϵ) = 419 (198000), 516 (11300), 552 (6300), 591 (4500), 648 nm ($3700 \text{ M}^{-1} \cdot \text{cm}^{-1}$). ESI-TOF: $m/z = 709.83$ Calcd for $\text{C}_{100}\text{H}_{78}\text{N}_{10}^{2+}$ ($[\text{M}^{2+}]$): 709.32. TLC R_f : 0.26 (solution of KPF_6 (27 mM) in Acetone).

6.3.4. Bis-porphyrin **8**

Prepared following the **GP2** and using monomeric systems (61 mg, 0.062 mmol, 1 eq) (Method A) or α, α' -Dibromo-*p*-xylene (18 mg, 0.062 mmol, 1 eq) (Method B) and porphyrin **1** (204 mg, 0.31 mmol, 5 eq). The crude product was purified by silica gel column chromatography (CH_2Cl_2) and gradually ending with a solution of KPF_6 (27 mM in acetone). The compound **8** (72 mg, 0.042 mmol, 68%, Method A) or (40 mg, 0.024 mmol, 38%, Method B) was obtained as a purple solid. ^1H NMR (400 MHz, $\text{DMSO}-d_6$): δ 9.66 (d, $J = 6.2$ Hz, 4H, H-*ortho*-py $^+$), 9.12 (d, $J = 6.2$ Hz, 4H, H-*meta*-py $^+$), 9.06–8.99 (m, 4H, H- β -pyrrolic), 8.97–8.92 (m, 4H, H- β -pyrrolic), 8.90–8.81 (m, 8H, H- β -pyrrolic), 8.11 (s, 4H, H-aryl), 8.10–8.04 (m, 12H, H-*ortho*-tolyl), 7.65 (d, $J = 7.8$ Hz, 8H, H-*meta*-tolyl), 7.61 (d, $J = 7.8$ Hz, 4H, H-*meta*-tolyl), 6.28 (s, 4H, $-\text{CH}_2-$), 2.68 (s, 6H, $-\text{CH}_3$), 2.64 (s, 12H, $-\text{CH}_3$), -2.89 (s, 4H, free base). ^{13}C NMR (126 MHz, $\text{DMSO}-d_6$): δ 158.8, 143.8, 138.5, 138.2, 138.2, 138.1, 138.0, 136.5,

135.9, 134.6, 133.7, 130.8, 128.2, 122.5, 121.4, 113.1, 111.1, 69.0, 30.1, 21.6, 21.5. ^{31}P NMR (121 MHz, $\text{DMSO}-d_6$): δ -141.27 (hept, $J = 711.3$ Hz). ^{19}F NMR (282 MHz, $\text{DMSO}-d_6$): δ -70.14 (d, $J = 711.3$ Hz). UV-Vis (DMF): λ (ϵ) = 422 (354000), 518 (37600), 556 (29200), 592 (22400), 650 nm ($19300 \text{ M}^{-1} \cdot \text{cm}^{-1}$). HR-ESI-TOF: $m/z = 709.8236$ Calcd for $\text{C}_{100}\text{H}_{78}\text{N}_{10}^{2+}$ ($[\text{M}^{2+}]$): 709.8216. TLC R_f : 0.31 (solution of KPF_6 (5 mM) in Acetone).

6.3.5. Bis-porphyrin **9**

Prepared following the **GP2** and using monomeric systems (61 mg, 0.062 mmol, 1 eq) (Method A) or α, α' -Dibromo-*m*-xylene (18 mg, 0.062 mmol, 1 eq) (Method B) and porphyrin **2** (204 mg, 0.31 mmol, 5 eq). The crude product was purified by silica gel column chromatography (CH_2Cl_2) and gradually ending with a solution of KPF_6 (27 mM in acetone). The compound **9** (67 mg, 0.039 mmol, 63%, Method A) or (51 mg, 0.030 mmol, 48%, Method B) was obtained as a purple solid. ^1H NMR (400 MHz, $\text{DMSO}-d_6$): δ 10.19 (s, 2H, H-py $^+$), 9.62 (d, $J = 6.5$ Hz, 2H, H-py $^+$), 9.38 (d, $J = 7.9$ Hz, 2H, 2H, H-py $^+$), 8.89–8.79 (m, 8H, H- β -pyrrolic), 8.75–8.65 (m, 8H, H- β -pyrrolic), 8.54 (dd, $J = 7.9, 6.5$ Hz, 2H, H-py $^+$), 8.13–8.05 (m, 4H, H-tolyl), 8.01 (s, 1H), 7.86 (d, $J = 7.7$ Hz, 2H), 7.80 (d, $J = 7.3$ Hz, 4H, H-tolyl), 7.71 (t, $J = 7.7$ Hz, 1H), 7.69–7.59 (m, 8H, H-tolyl), 7.40 (d, $J = 7.3$ Hz, 4H, H-tolyl), 7.22 (d, $J = 7.8$ Hz, 4H, H-tolyl), 6.21 (s, 4H, $-\text{CH}_2-$), 2.68 (s, 6H, $-\text{CH}_3$), 2.49 (s, 12H, $-\text{CH}_3$), -3.01 (s, 4H, free base). ^{13}C NMR (126 MHz, $\text{DMSO}-d_6$): δ 1148.9, 147.0, 144.4, 141.6, 138.1, 137.8, 137.7, 137.6, 137.4, 135.4, 134.2, 134.0, 133.9, 133.8, 130.5, 130.2, 130.2, 130.2, 129.3, 127.8, 127.7, 127.6, 127.6, 127.4, 127.0, 121.7, 120.6, 110.2, 104.9, 55.9, 32.2, 29.6, 21.1, 20.9. ^{31}P NMR (121 MHz, $\text{DMSO}-d_6$): δ -144.2 (hept, $J = 711.3$ Hz). ^{19}F NMR (282 MHz, $\text{DMSO}-d_6$): δ -70.1 (d, $J = 711.3$ Hz). UV-Vis (DMF): λ (ϵ) = 422 (154000), 516 (9800), 552 (4700), 590 (3600), 647 nm ($2500 \text{ M}^{-1} \cdot \text{cm}^{-1}$). HR-ESI-TOF: $m/z = 709.8220$ Calcd for $\text{C}_{100}\text{H}_{78}\text{N}_{10}^{2+}$ ($[\text{M}^{2+}]$): 709.8216. TLC R_f : 0.21 (solution of KPF_6 (5 mM) in Acetone).

6.3.6. Bis-porphyrin **10**

Prepared following the **GP10** and using monomeric systems (61 mg, 0.062 mmol, 1 eq) (Method A) or α, α' -Dibromo-*p*-xylene (18 mg, 0.062 mmol, 1 eq) (Method B) and porphyrin **2** (204 mg,

0.31 mmol, 5 eq). The crude product was purified by silica gel column chromatography (CH₂Cl₂) and gradually ending with a solution of KPF₆ (27 mM in acetone). The compound **10** (76 mg, 0.044 mmol, 71%, Method A) or (34 mg, 0.020 mmol, 32%, Method B) was obtained as a purple solid. ¹H NMR (500 MHz, DMSO-*d*₆): δ 10.26 (s, 2H, H-py⁺), 9.71 (d, *J* = 6.3 Hz, 2H, H-py⁺), 9.39 (d, *J* = 7.9 Hz, 2H, H-py⁺), 8.88–8.82 (m, 8H, H-β-pyrrolic), 8.77–8.69 (m, 8H, H-β-pyrrolic), 8.64 (dd, *J* = 7.9, 6.3 Hz, 2H, H-py⁺), 8.15–8.04 (m, 4H, H-tolyl), 7.91 (s, 4H, H-aryl), 7.83 (d, *J* = 7.7 Hz, 4H, H-tolyl), 7.70–7.58 (m, 8H, H-tolyl), 7.34 (d, *J* = 7.7 Hz, 4H, H-tolyl), 7.15 (d, *J* = 7.7 Hz, 4H, H-tolyl), 6.17 (s, 4H, –CH₂–), 2.68 (s, 6H, –CH₃), 2.41 (s, 12H, –CH₃), –2.97 (s, 4H, free base). ¹³C NMR (126 MHz, DMSO-*d*₆): δ 162.3, 148.7, 147.0, 144.4, 141.6, 138.1, 137.8, 137.6, 137.3, 135.7, 134.2, 134.0, 133.8, 133.8, 129.8, 127.7, 127.5, 127.4, 127.2, 121.7, 120.7, 110.3, 63.3, 55.8, 35.8, 30.8, 21.1, 20.8. ³¹P NMR (121 MHz, DMSO-*d*₆): δ –144.2 (hept, *J* = 711.3 Hz). ¹⁹F NMR (282 MHz, DMSO-*d*₆): δ –70.1 (d, *J* = 711.3 Hz). UV-Vis (DMF): λ (ε) = 420 (101000), 516 (8500), 552 (5900), 590 (4800), 649 nm (4200 M⁻¹·cm⁻¹). HR-ESI-TOF: *m/z* = 709.3229 Calcd for C₁₀₀H₇₈N₁₀²⁺ ([M²⁺]): 709.3200. TLC *R*_f: 0.28 (solution of KPF₆ (5 mM) in acetone).

Acknowledgments

The authors are grateful to the University of Strasbourg and the CNRS for constant financial support. RL gratefully acknowledges the Région Grand-Est and the Fondation Recherche en Chimie for a PhD fellowship. The authors declare no conflicts of interest.

Supplementary data

Supporting information for this article is available on the journal's website under <https://doi.org/10.5802/crchim.105> or from the author.

References

- [1] I. Azcarate, Z. Huo, R. Farha, M. Goldmann, H. Xu, B. Hasenknopf, E. Lacôte, L. Ruhlmann, *Chem. Eur. J.*, 2015, **21**, 8271-8280.
- [2] J. Hao, A. Giraudeau, Z. Ping, L. Ruhlmann, *Langmuir*, 2008, **24**, 1600-1603.
- [3] Q. Chen, D. P. Goshorn, C. P. Scholes, X. L. Tan, J. Zubieta, *J. Am. Chem. Soc.*, 1992, **114**, 4667-4681.
- [4] W. H. Knoth, R. L. Harlow, *J. Am. Chem. Soc.*, 1981, **103**, 4265-4266.
- [5] K. J. Elliott, A. Harriman, L. Le Pleux, Y. Pellegrin, E. Blart, C. R. Mayer, F. Odobel, *Phys. Chem. Chem. Phys.*, 2009, **11**, 8767-8773.
- [6] F. Odobel, M. Séverac, Y. Pellegrin, E. Blart, C. Fosse, C. Cannizzo, C. R. Mayer, K. J. Elliott, A. Harriman, *Chem.–Eur. J.*, 2009, **15**, 3130-3138.
- [7] Y. Zhu, Y. Huang, Q. Li, D. Zang, J. Gu, Y. Tang, Y. Wei, *Inorg. Chem.*, 2020, **59**, 2575-2583.
- [8] D. Schaming, C. Costa-Coquelard, I. Lampre, S. Sorgues, M. Erard, X. Liu, J. Liu, L. Sun, J. Canny, R. Thouvenot, L. Ruhlmann, *Inorg. Chim. Acta*, 2010, **363**, 2185-2192.
- [9] A. Yokoyama, K. Ohkubo, T. Ishizuka, T. Kojima, S. Fukuzumi, *Dalton Trans.*, 2012, **41**, 10006-10013.
- [10] C. Li, N. Mizuno, K. Yamaguchi, K. Suzuki, *J. Am. Chem. Soc.*, 2019, **141**, 7687-7692.
- [11] C. Costa-Coquelard, S. Sorgues, L. Ruhlmann, *J. Phys. Chem. A*, 2010, **114**, 6394-6400.
- [12] S.-Q. Liu, J.-Q. Xu, H.-R. Sun, D.-M. Li, *Inorg. Chim. Acta*, 2000, **306**, 87-93.
- [13] I. Ahmed, R. Farha, M. Goldmann, L. Ruhlmann, *Chem. Commun.*, 2013, **49**, 496-498.
- [14] C. Li, K.-M. Park, H.-J. Kim, *Inorg. Chem. Commun.*, 2015, **60**, 8-11.
- [15] Z. Shi, Y. Zhou, L. Zhang, C. Mu, H. Ren, D. ul Hassan, D. Yang, H. M. Asif, *RSC Adv.*, 2014, **4**, 50277-50284.
- [16] G. Bazzan, W. Smith, L. C. Francesconi, C. M. Drain, *Langmuir*, 2008, **24**, 3244-3249.
- [17] R. Lamare, L. Ruhlmann, R. Ruppert, J. Weiss, *J. Porphy. Phthalocyanines*, 2019, **23**, 860-868.
- [18] A. L. Rheingold, C. B. White, B. S. Haggerty, E. A. Maatta, *Acta Crystallogr. C*, 1993, **49**, 756-758.
- [19] A. C. Vaiana, H. Neuweiler, A. Schulz, J. Wolfrum, M. Sauer, J. C. Smith, *J. Am. Chem. Soc.*, 2003, **125**, 14564-14572.
- [20] L. K. Fraiji, D. M. Hayes, T. C. Werner, *J. Chem. Educ.*, 1992, **69**, 424-428.
- [21] H. Gampp, M. Maeder, C. J. Meyer, A. D. Zuberbühler, *Talanta*, 1985, **32**, 95-101.
- [22] D. W. Marquardt, *J. Soc. Ind. Appl. Math.*, 1963, **11**, 431-441.
- [23] M. Maeder, A. D. Zuberbuehler, *Anal. Chem.*, 1990, **62**, 2220-2224.



MAPYRO: the French Fellowship of the Pyrrolic Macrocyclic Ring / MAPYRO: la communauté française des macrocycles pyrroliques

Design and synthesis of triphenylphosphonium-porphyrin@xylan nanoparticles for anticancer photodynamic therapy

Conception et synthèse de nanoparticules constituées de xylane portant des porphyrines avec un groupement triphénylphosphonium pour la thérapie photodynamique anticancéreuse

Soukaina Bouramtane^{® a}, Ludovic Bretin^{® a}, Jérémy Godard^{® a}, Aline Pinon^{® a}, Yves Champavier^{® a, b}, Yann Launay^{® c}, David Léger^{® a}, Bertrand Liagre^{® a}, Vincent Sol^{® a}, Vincent Chaleix^{® a} and Frédérique Brégier^{® *, a}

^a Université de Limoges, Laboratoire PEIRENE, EA 7500, 87060 Limoges, France

^b BISCEM, NMR platform, Centre de Biologie et de Recherche en Santé (CBRS), Limoges, France

^c Université de Limoges, Centre Européen de la Céramique, Limoges, France

E-mails: soukaina.bouramtane@univ-lorraine.fr (S. Bouramtane), l.r.bretin@lic.leidenuniv.nl (L. Bretin), jeremy.godard@unilim.fr (J. Godard), aline.pinon@unilim.fr (A. Pinon), yves.champavier@unilim.fr (Y. Champavier), yann.launay@unilim.fr (Y. Launay), david.leger@unilim.fr (D. Léger), bertrand.liagre@unilim.fr (B. Liagre), vincent.sol@unilim.fr (V. Sol), vincent.chaleix@unilim.fr (V. Chaleix), frederique.bregier@unilim.fr (F. Brégier)

Abstract. Most photosensitizers (PS) suffer from a lack of water solubility and from a low selectivity toward tumor cells. Delivery systems using nanoparticles make it possible to improve PS water solubility, and also tumor targeting via the enhanced permeability and retention (EPR) effect. Among the organelles, mitochondria are attractive target sites for drug-delivery strategies since they perform a variety of key cellular processes. Our study was aimed at synthesizing nanoparticles consisting of xylan-carrying porphyrins attached to a triphenylphosphonium moiety, in order to enhance the PDT effect through mitochondrial targeting. Hybrid nanoparticles were designed that consisted of a silica core coated with xylan substituted with porphyrin derivatives carrying a triphenylphosphonium

* Corresponding author.

moiety. These hybrid nanoparticles have been constructed, along with their counterparts devoid of silica core, taking into consideration the controversy surrounding the use of silica nanoparticles. Phototoxicity experiments, conducted against the HCT-116 and HT-29 colorectal cancer cell lines, showed that nanoparticles with porphyrins bearing a triphenylphosphonium moiety exhibited an enhanced photocytotoxic effect in comparison with free porphyrin or nanoparticles with porphyrins without the triphenylphosphonium moiety.

Résumé. La plupart des photosensibilisateurs (PS) souffrent d'un manque de solubilité dans l'eau et d'une faible sélectivité envers les cellules tumorales. Les systèmes d'administration utilisant des nanoparticules permettent à la fois d'améliorer la solubilité dans l'eau du PS, ainsi que le ciblage des tumeurs via l'effet EPR. Parmi les organites, les mitochondries sont des cibles de choix pour les stratégies d'administration de médicaments puisqu'elles sont essentielles au fonctionnement cellulaire. Notre étude a pour objectif de synthétiser des nanoparticules constituées de xylane portant des porphyrines avec un groupement triphénylphosphonium, afin d'améliorer l'effet PDT grâce au ciblage mitochondrial. Des nanoparticules hybrides, constituées d'un cœur de silice recouvert de xylane substitué par des dérivés de porphyrine portant un groupement triphénylphosphonium ont été préparées ainsi que leurs homologues dépourvues du cœur inorganique. Des expériences de phototoxicité, menées sur les lignées cellulaires des cancers colorectaux HCT-116 et HT-29, ont montré que les nanoparticules avec des porphyrines portant un groupement triphénylphosphonium présentaient une photocytotoxicité plus importante que la porphyrine libre ou les nanoparticules avec des porphyrines sans groupement triphénylphosphonium.

Keywords. Xylan, Polysaccharides, Silica nanoparticles, Porphyrin, Photodynamic therapy.

Mots-clés. Xylane, Polysaccharides, Nanoparticules de silice, Porphyrine, Thérapie photodynamique.

Available online 23rd September 2021

1. Introduction

Current cancer treatments include surgery, radiotherapy and chemotherapy, the latter causing many side effects such as the killing of cancer cells along with healthy ones [1]. Photodynamic therapy (PDT) is an interesting alternative which allows cytotoxic species to be produced *in situ* after administration of a photosensitizer (PS) followed by light irradiation of the tumor area [2]. The most frequently studied PS are tetrapyrrolic compounds such as porphyrins, phthalocyanines, chlorins, and bacteriochlorins and some of them have been clinically approved [3,4]. However, the use of these molecules suffers from two major limitations. Most PS are highly hydrophobic and thus are sparingly soluble in water; they also exhibit a poor selectivity toward tumor cells. Several approaches have been developed to bypass these drawbacks. Among the most promising approaches is the use of water soluble nanoparticles associated with PS [5]. These particles increase the solubility of hydrophobic PS, while particles smaller than 100 nm with long circulation times will preferentially accumulate in the tumor tissue thanks to the enhanced permeability and retention (EPR) effect [6–8]. Many organic and inorganic carriers of photosensitizers have already been studied, including sil-

ica nanoparticles (SiNPS) [9–12]. Silica nanoparticles possess several advantages, notably biocompatibility, tunable size, large surface area and ease of functionalization [13]. In order to increase the circulation time of inorganic nanoparticles in the blood stream and to reduce their opsonization, it is possible to cover them with a hydrophilic polymer [14] such as polyethylene glycol [15] or polysaccharides such as chitosan [16] or dextran [17].

We have recently developed core-shell hybrid nanoparticles consisting of a silica core coated with xylan carrying a porphyrin shell. *In vitro* biological evaluations of this composite nanoparticle have shown a significant gain in efficiency against HCT-116 and HT-29 colorectal cancer cell lines as compared with the free porphyrin [18,19]. In order to further increase the efficiency of this system, we focused our work on mitochondrial targeting. Mitochondria are well known to play crucial roles in cell life and death [20]. Mitochondrial targeting of drugs can be achieved by the covalent binding of the triphenylphosphonium (TPP+) group which is a moiety of MitoTrackers such as MitoSOX™ Red reagent [21]. We report herein the synthesis and characterization of silica/xylan/porphyrin-TPP nanoparticles, along with xylan/porphyrin-TPP. The latter was included in our study in order to address the controversy

surrounding the use of silica nanoparticles. Preliminary phototoxicity studies of these platforms have been carried out against the HCT-116 and HT-29 colorectal cancer cell lines.

2. Experimental section

2.1. Materials

For a list of materials, see Supplementary Information (SI).

2.2. Analytical methods

FTIR analyses were performed on a PerkinElmer FTIR Spectrum 1000 spectrometer using KBr pellets (1–2 wt%). NMR analyses were carried out on a Bruker Avance III HD 500 MHz NMR spectrometer. UV–vis spectra were recorded on a AnalytikaJena SPECORD 210 double beam spectrophotometer, using 10 mm quartz cells. MALDI-TOF spectra were performed on a Shimadzu AXIMA confidence using dithranol as matrix. High resolution electrospray ionization mass spectrometry (HR ESI–MS) was performed at the ICOA/CBM platform (Orléans University) on a Bruker Q-TOF maXis mass spectrometer, coupled to an Ultimate 3000 RSLC chain (Dionex). Purifications were performed with Combiflash Rf 100[®] from Teledyne Isco. The stationary phase consisted of an 80 g silica column. The products to be purified were solubilized in a minimum amount of solvent and fixed on Florisil (60–100 mesh, VWR). For Scanning Electron Microscopy (SEM) studies, a droplet of nanoparticle suspension was lyophilized on a sample holder. The sample was metalized by sputtering of platinum using an Agar Sputter Coater. Images were taken with a LEO 1530 VP instrument. Particle size distribution was analyzed through Dynamic Light Scattering (DLS) using a Zetasizer Nano-ZS (Malvern, UK). NPS suspension was diluted in absolute ethanol and analyzed at 20 °C at a scattering angle of 173°. The mean diameter of NPS was expressed as the average value of two measurements, each one comprising 15 runs.

2.3. Syntheses

2.3.1. Synthesis of 5,15-bis(4-hydroxyphenyl)-10,20-bisphenylporphyrin (1)

4-Hydroxybenzaldehyde (7.02 g, 57.5 mmol) and benzaldehyde (6.10 g, 57.5 mmol) were dissolved

in 300 mL of propionic acid and heated till reflux. Once the aldehydes were dissolved, pyrrole (7.71 g, 115 mmol, 8 mL) was added dropwise and the solution was refluxed for 90 min. Propionic acid was removed in vacuo to leave a purple oily residue. The porphyrin was purified using column chromatography (silica gel, CH₂Cl₂, followed by 2% MeOH in CH₂Cl₂ and 6% MeOH in CH₂Cl₂), giving 5,15-bis(4-hydroxyphenyl)-10,20-bisphenylporphyrin (1) (260 mg, 0.4 mmol, 1,4%). ¹H NMR (CDCl₃, 500 MHz) δ_H, ppm: 8.87 (d, 4H, *J* = 4.6 Hz, H_{β-pyrrol}), 8.83 (d, 4H, *J* = 4.6 Hz, H_{β-pyrrol}), 8.21 (d, 4H, *J* = 7.4 Hz, H_{Ar}), 8.06 (d, 4H, *J* = 8.4 Hz, H_{Ar}), 7.75 (m, 6H, H_{Ar}), 7.19 (d, 4H, *J* = 8.4 Hz, H_{Ar}), –2.78 (s, 2H, NH); MS (ESI): *m/z* = C₄₄H₃₁N₄O₂, [M + H]⁺, 647.2435, calcd. 647.2442. UV–vis (CHCl₃) λ_{max} nm (ε, 10³ L·mol^{–1}·cm^{–1}): 420 (607), 519 (20), 553 (9), 591 (6), 649 (5).

2.3.2. Synthesis of tert-butyl 4-bromobutanoate (2)

Concentrated sulfuric acid (1.375 mL, 25 mmol) was added to a vigorously stirred suspension of anhydrous magnesium sulfate (12.02 g, 25 mmol) in dry CH₂Cl₂ (40 mL). The mixture was stirred for 15 min, after which 4-bromobutanoic acid (4.15 mL, 25 mmol) was added. *Tert*-butanol (11.95 mL, 100 mmol) was added last. The mixture was tightly stoppered and stirred for 48 h at room temperature. The reaction mixture was then quenched with cold saturated sodium bicarbonate solution (187 mL) and stirred until complete dissolution of magnesium sulfate. The organic phase was separated, washed with brine, dried (MgSO₄), and concentrated. The crude product was purified by flash chromatography (silica gel, CHCl₃) to yield *tert*-butyl 4-bromobutanoate as a pale yellow liquid (3.27 g, 14.65 mmol, 60%). ¹H NMR (CDCl₃, 500 MHz) δ_H, ppm: 3.45 (t, 2H, *J* = 6.8 Hz, Br–CH₂), 2.40 (t, 2H, *J* = 7.2 Hz, CH₂–C=O), 2.13 (qt, 2H, *J* = 6.8 Hz, CH₂–CH₂–CH₂), 1.45 (s, 9H, CH₃); MS (ESI): *m/z* = C₈H₁₅BrO₂, [M+H]⁺, 223.0331, calcd. 223.0328.

2.3.3. Synthesis of porphyrin (3)

5,15-Bis(4-hydroxyphenyl)-10,20-bisphenylporphyrin (1) (500 mg, 0.772 mmol) was dissolved in DMF (20 mL) and K₂CO₃ (2.69 g, 19.31 mmol) was added. *tert*-Butyl 4-bromobutanoate (2) (172 mg, 0.772 mmol) was then added to the solution

and the mixture was stirred for 2 h at 110 °C. After removal of DMF with a rotary evaporator, the resulting residue was dissolved in chloroform (15 mL) and the solution was washed three times with water. After purification by preparative thin-layer chromatography (EtOH/CHCl₃ = 5/95), the desired monosubstituted porphyrin **3** was obtained as a dark violet solid (279 mg, 0.347 mmol, 45% yield). ¹H NMR (CDCl₃, 500 MHz) δ_H, ppm: 8.87 (d, 4H, *J* = 4.7 Hz, H_{β-pyrro}l), 8.83 (d, 4H, *J* = 4.7 Hz, H_{β-pyrro}l), 8.21 (dd, 4H, *J* = 7.7 Hz, 1.4 Hz, H_{Ar}), 8.11 (dd, 4H, *J* = 8.4 Hz, 1.8 Hz, H_{Ar}), 7.79–7.72 (m, 6H, H_{Ar}), 7.27 (d, 2H, *J* = 8.6 Hz, H_{Ar}), 7.26 (d, 2H, *J* = 8.5 Hz, H_{Ar}), 4.29 (t, 2H, *J* = 5.9 Hz, O–CH₂), 2.60 (t, 2H, *J* = 7.4 Hz, CH₂–CO), 2.27 (tt, 2H, *J* = 6.9, 6.5 Hz, CH₂–CH₂–CO), 1.53 (s, 9H, *t*Bu), –2.76 (s, 2H, NH); MS (MALDI) : *m/z* = C₅₂H₄₅N₄O₄, [M+H]⁺, 789.50, calcd. 789.34. UV-vis (CHCl₃) λ_{max} nm (log ε L·mol⁻¹·cm⁻¹): 420 (5.78), 519 (4.30), 553 (3.85), 591 (3.78), 649 (3.70).

2.3.4. Synthesis of porphyrin (4)

Porphyrin (**3**) (285 mg, 0.361 mmol) was dissolved in DMF (12 mL) and K₂CO₃ (1.24 g, 9.03 mmol) was added. 1,4-Dibromobutane (1.95 g, 9.03 mmol) was then added to the solution and the mixture was stirred for 5 h at 110 °C. After removal of DMF with a rotary evaporator, the resulting residue was dissolved in chloroform (15 mL) and the solution was washed three times with water. After purification by preparative thin-layer chromatography (CHCl₃), the desired porphyrin **4** was obtained as a dark violet solid (237 mg, 0.271 mmol, 71% yield). ¹H NMR (CDCl₃, 500 MHz) δ_H, ppm: 8.88 (m, 8H, H_{β-pyrro}l), 8.21 (dd, 4H, *J* = 7.7, 1.4 Hz, H_{Ar}), 8.10 (d, 4H, *J* = 7.6 Hz, H_{Ar}), 7.79–7.70 (m, 6H, H_{Ar}), 7.27–7.23 (m, 4H, H_{Ar}), 4.37 (t, 2H, *J* = 5.8 Hz, O–CH₂–CH₂–CH₂–CO), 4.27 (t, 2H, *J* = 6.1 Hz, O–CH₂–CH₂–CH₂–CH₂–Br), 4.26 (t, 2H, *J* = 4.8 Hz, CH₂–Br), 2.59 (t, 2H, *J* = 7.3 Hz, CH₂–CO), 2.41 (tt, 2H, *J* = 6.8 Hz, *J* = 6.6 Hz, CH₂–CH₂–CO), 2.05 (m, 4H, O–CH₂–CH₂–CH₂–CH₂–Br), 1.52 (s, 9H, *t*Bu), –2.75 (s, 2H, NH). MS (MALDI): *m/z* = C₅₆H₅₁BrN₄O₄, [M+H]⁺, 923.10, calcd. 923.32. UV-vis (CHCl₃) λ_{max} nm (log ε L·mol⁻¹·cm⁻¹): 420 (5.76), 517 (4.38), 551 (4.19), 591 (3.98), 649 (3.95).

2.3.5. Synthesis of porphyrin (5)

Porphyrin (**4**) (224 mg, 0.242 mmol) was dissolved in DMF (25 mL). Triphenylphosphine (1.03 g, 3.93 mmol) was then added to the solution and the

mixture was stirred for 24 h at 110 °C. After removal of DMF with a rotary evaporator, the desired product was obtained after purification by preparative thin-layer chromatography (EtOH/CHCl₃ = 5/95) as a dark violet solid (210 mg, 73% yield). ¹H NMR (CDCl₃, 500 MHz) δ_H, ppm: 8.84 (m, 8H, H_{β-pyrro}l), 8.21 (dd, 4H, *J* = 7.1 Hz, *J* = 1.3 Hz, H_{Ar}), 8.10 (dd, 4H, *J* = 8.5 Hz, *J* = 8.5 Hz, H_{Ar}), 7.95 (dd, 3H, *J* = 7.5 Hz, *J* = 1.0 Hz, H_{Ar}), 7.93 (dd, 3H, *J* = 7.5 Hz, *J* = 1.0 Hz, H_{Ar}), 7.82 (dd, 3H, *J* = 8.2 Hz, *J* = 6.6 Hz, H_{Ar}), 7.79–7.72 (m, 12H, H_{Ar}), 7.26 (d, 2H, *J* = 8.5 Hz, H_{Ar}), 7.20 (d, 2H, *J* = 8.5 Hz, H_{Ar}), 4.39 (t, 2H, *J* = 5.3 Hz, O–CH₂–CH₂–CH₂–CO), 4.29 (t, 2H, *J* = 6.1 Hz, O–CH₂–CH₂–CH₂–CH₂–PPh₃), 4.08 (m, 2H, CH₂–PPh₃), 2.60 (t, 2H, *J* = 7.3 Hz, CH₂–CO), 2.42 (qt, 2H, *J* = 6.1 Hz, CH₂–CH₂–CO), 2.27 (qt, 2H, *J* = 6.7 Hz, O–CH₂–CH₂–CH₂–CH₂–PPh₃), 2.05 (m, 2H, O–CH₂–CH₂–CH₂–CH₂–PPh₃), 1.53 (s, 9H, *t*Bu), –2.76 (s, 2H, NH); MS (ESI): *m/z* = C₇₄H₆₆N₄O₄P, [M]⁺, 1105.4812, calcd. 1105.4816. UV-vis (CHCl₃) λ_{max} nm (log ε 10³ L·mol⁻¹·cm⁻¹): 421 (5.77), 518 (4.35), 554 (4.09), 592 (3.82), 648 (3.73).

2.3.6. Synthesis of porphyrin (6)

Porphyrin (**5**) (297 mg, 0.25 mmol) was dissolved in dichloromethane (16 mL) and mixed with TFA (4 mL). After 2 h stirring at room temperature, the reaction mixture was concentrated in vacuo, and the residue was dissolved in dichloromethane (30 mL). The solution was washed with a saturated sodium bicarbonate solution (100 mL), water (3 × 50 mL), dried over magnesium sulfate, filtered, and concentrated *in vacuo*. The product was purified by preparative thin-layer chromatography (EtOH/CHCl₃ = 15/85) to give porphyrin **6** as a dark violet solid in 94% yield (266 mg, 0.235 mmol). ¹H NMR (CDCl₃ + 10% TFA-D, 500 MHz) δ_H, ppm: 8.69 (d, 2H, *J* = 4.7 Hz, H_{β-pyrro}l), 8.67 (m, 4H, H_{β-pyrro}l), 8.62 (d, 2H, *J* = 4.7 Hz, H_{β-pyrro}l), 8.53 (dd, 4H, *J* = 7.5 Hz, *J* = 2.0 Hz, H_{Ar}), 8.48 (d, 4H, *J* = 7.5 Hz, H_{Ar}), 8.03 (m, 6H, H_{Ar}), 7.91 (dd, 3H, *J* = 8.0 Hz, *J* = 6.7 Hz, H_{Ar}), 7.77 (m, 6H, H_{Ar}), 7.68 (m, 6H, H_{Ar}), 7.55 (d, 2H, *J* = 8.5 Hz, H_{Ar}), 7.47 (d, 2H, *J* = 8.4 Hz, H_{Ar}), 4.44 (t, 2H, *J* = 5.8 Hz, O–CH₂–CH₂–CH₂–CO), 4.39 (t, 2H, *J* = 5.2 Hz, O–CH₂–CH₂–CH₂–CH₂–PPh₃), 3.28 (dt, 2H, *J* = 8.1 Hz, *J* = 12.9 Hz, CH₂–PPh₃), 2.88 (t, 2H, *J* = 7.1 Hz, CH₂–CO), 2.41 (qt, 2H, *J* = 6.4 Hz, CH₂–CH₂–CO), 2.25 (qt, 2H, *J* = 6.0 Hz,

O-CH₂-CH₂-CH₂-CH₂-PPh₃), 2.13 (m, 2H, O-CH₂-CH₂-CH₂-CH₂-PPh₃); MS (ESI): *m/z* = C₇₀H₅₈N₄O₄P, [M]⁺, 1049.4199, calcd. 1049.4190. UV-vis (DMSO) λ_{max} nm (log ε 10³ L·mol⁻¹·cm⁻¹): 422 (5.44), 518 (4.15), 554 (4.98), 593 (3.78), 649 (3.74).

2.4. Preparation of xylan/porphyrin 6 conjugate

After solubilizing porphyrin 6 (43 mg, 0.038 mmol) in 8 mL DMSO, *N,N*-carbonyldiimidazole (CDI) (37 mg, 0.23 mmol) was added and the mixture was stirred at 60 °C for 24 h. This solution was then added to 100 mg of xylan and allowed to react under stirring at 80 °C for 48 h. The product was precipitated with absolute ethanol and was washed three times with ethanol and three times with chloroform to remove unreacted starting material and then dried under vacuum. 106 mg of xylan/porphyrin 6 conjugate were obtained.

2.5. Preparation of the hybrid nanoparticles SiNPS@Xylan/Porphyrin-TPP

The hybrid nanoparticle SiNPS@Xylan/Porphyrin-TPP was prepared according to a previously published procedure [18]. Xylan/porphyrin 6 conjugate (10 mg) was dissolved in 20 mL of distilled water. Then, an ethanolic suspension of 100 mg of silica nanoparticles functionalized with APTES (3-aminopropyltriethoxysilane) was added dropwise and the mixture was ultrasonicated during addition and during the five following minutes. This mixture was then stirred for 15 min. The resulting SiNPS@Xylan/Porphyrin-TPP were centrifuged for 30 min at 8000 rpm and subjected to washing and centrifugation, three times in water and two times in absolute ethanol.

2.6. Acetylation of xylan

To a solution of xylan (200 mg, 1.51 mmol of xylose unit) in 20 mL of DMSO were added 10 mL of *N*-methylimidazole (125.43 mmol). The mixture was magnetically stirred at 80 °C for 1 h under nitrogen atmosphere. Then the mixture was cooled down to room temperature, and 0.25 to 4 equivalents of acetic anhydride were added. After 2 h stirring at room temperature, acetylated xylans were precipitated by addition of absolute ethanol, recovered by filtration, washed, and dried in vacuo. Seven

acetylated xylans (Ac-Xyl 1 to Ac-Xyl 7) were obtained with DS values ranging from 0.04 to 1.10. IR: 897 cm⁻¹ (β-glucosidic linkages), 1045 cm⁻¹ (C–O stretching in C–O–C linkages), 1220 cm⁻¹ (C–O stretching), 1370 cm⁻¹ (–C–CH₃), 1735 cm⁻¹ (C=O ester), 3400 cm⁻¹ (O–H stretching).

2.7. 5-(4-(3-carboxypropoxy)phenyl)-10,15,20-triphenylporphyrin grafting to acetylated xylan Ac-Xyl 3, Ac-Xyl 4 and Ac-Xyl 5

5-(4-(3-Carboxypropoxy)phenyl)-10,15,20-triphenylporphyrin (108 mg, 0.15 mmol), whose synthesis has been previously described [18], was solubilized in 20 mL DMSO, then six equivalents of CDI (147 mg, 0.903 mmol) were added. After stirring at 60 °C for 24 h, 100 mg of acetylated xylan (0.757 mmol of xylose residue) were added into the mixture and allowed to react under stirring at 50 °C for 24 h. The product was precipitated out in absolute ethanol and was washed three times with ethanol and three times with chloroform to remove unreacted starting material and then dried under vacuum.

2.8. Porphyrin 6 grafting to acetylated xylan Ac-Xyl 4

Porphyrin 6 (70 mg, 0.062 mmol) was solubilized in 12 mL DMSO, then six equivalent of CDI (61 mg, 0.37 mmol) were added. After stirring at 60 °C for 24 h, 40 mg of acetylated xylan Ac-Xyl 4 (0.31 mmol xylose unit) were added to the mixture and allowed to react under stirring at 50 °C for 24 h. The product was precipitated with absolute ethanol and was washed three times with ethanol and three times with chloroform to remove unreacted starting material and then dried under vacuum.

2.9. Preparation of self-assembled nanoparticles (NPS)

The self-assembled nanoparticles were prepared by a dialysis method. Acetylated xylan/porphyrin conjugates (20 mg or 15 mg) were dissolved in 5 mL of DMSO or DMAc (depending of their solubility). The solutions were placed in dialysis membranes (regenerated cellulose, Spectra/Por 3, molecular weight

Table 1. Mass concentrations and molar concentrations of porphyrins in the final solutions containing the self-assembled porphyrin nanoparticles of the three different samples, Ac-Xyl 4-Porphyrin, Ac-Xyl 5-Porphyrin and Ac-Xyl 4-Porphyrin-TPP

	Ac-Xyl 4-Porphyrin	Ac-Xyl 5-Porphyrin	Ac-Xyl 4-Porphyrin-TPP
Amount of xylan used (mg)	20	20	15
Mass concentration (g/L)	8.7	5.5	6.6
Porphyrin concentration (mol/L)	1.24×10^{-4}	1.59×10^{-5}	1.26×10^{-5}

cutoff of 3500 Da) of about 10 cm length and dialyzed against 500 mL of deionized water for 15 h. Water was renewed five times, every 3 h. After centrifugation at 10,000 rpm for 30 min the supernatant was removed. The obtained nanoparticles were redispersed in distilled water, then two washing/centrifugation cycles were carried out. Nanoparticles were redispersed in 5 mL of water and stored at +4 °C. 1 mL of this suspension of nanoparticles was freeze-dried to determine the mass concentration and then resolubilized in DMSO prior to UV-vis spectrophotometry analysis. Porphyrin concentrations in the final suspensions containing the self-assembled porphyrin nanoparticles were determined at 420 or 422 nm thanks to the molar extinction of the free porphyrin (444,347 L·mol⁻¹·cm⁻¹) or porphyrin-TPP (274,815 L·mol⁻¹·cm⁻¹). The mass concentrations and the porphyrin concentrations of the three different samples, Ac-Xyl 4-Porphyrin, Ac-Xyl 5-Porphyrin and Ac-Xyl 4-Porphyrin-TPP are listed in Table 1.

2.10. Determination of degree of substitution in acetyl groups and porphyrin

NMR is a common method to determine the degree of substitution of a polymer [22,23].

The formula to calculate the degree of substitution in acetyl groups per anhydroglucose unit is expressed as follows:

$$DS_{\text{Acetyl}} = \frac{I_{\text{Ac}}/3}{I_{\text{H}_1\text{-xylan}}}$$

where I_{Ac} represents the integral signals of the protons of the acetyl groups, and $I_{\text{H}_1\text{-xylan}}$ the integral signals of the anomeric protons of the xylose units (substituted and non-substituted ones), at δ 4.1–4.7 ppm.

The formula to calculate the degree of substitution in porphyrins per repeat unit composed of 10 xylose units and one 4-O-methyl glucuronic acid (MeGlcA) is expressed as follows:

$$DS_{\text{Porphyrin}} = \frac{I_{\text{H-aromatics}}/n_{\text{H-aromatics}}}{I_{\text{H}_1\text{-xylan}}/10}$$

where $I_{\text{H-aromatics}}$ represents the integral area of aromatic and β -protons of porphyrins at δ 7.26–9.12 ppm, and $I_{\text{H}_1\text{-xylan}}$ represents the integral area of the anomeric protons of the xylose units (substituted and non-substituted) at δ 4.1–4.7 ppm. $n_{\text{H-aromatics}}$ represents the total number of aromatic and β protons of porphyrins.

2.11. Determination of porphyrin-TPP concentration in SiNPS@Xylan/Porphyrin-TPP

The amount of porphyrin-TPP attached to the SiNPS was determined by UV-visible assay. SiNPS@Xylan/Porphyrin-TPP were dispersed in absolute ethanol at a concentration of 10 mg/mL and diluted with water to 0.5 mg/mL. Absorbance of this sample was measured at 420 nm, and absorbance of SiNPS was subtracted. The Xylan/Porphyrin-TPP content of nanoparticles was calculated from a calibration curve constructed with different concentrations of free Xylan/Porphyrin-TPP in distilled water (Figure S9). The concentration of porphyrin-TPP in mol per gram of silica was calculated according to the following equation:

$$C = \frac{DS_{\text{Porphyrin-TPP}} \times C_{(\text{Xylan/Porphyrin-TPP})}}{MW_{\text{repeat of xylan}} + DS_{\text{Porphyrin-TPP}} \times (MW_{\text{Porphyrin-TPP}} - 18)} \times 2$$

$DS_{\text{Porphyrin-TPP}} = 0.1$, calculated from the ¹H NMR spectrum;

$C_{(\text{Xylan/Porphyrin-TPP})}$ = concentration of Xylan/Porphyrin-TPP attached to SiNPS, calculated from the standard calibration curve = 0.09 g/L;

$MW_{\text{repeat of xylan}} (\text{xyl/MeGlcA} = 10:1) = 1511 \text{ g/mol}$;
 $MW_{\text{Porphyrin-TPP}} = 1163.25 \text{ g/mol}$.

2.12. *In vitro* phototoxicity of hybrid SiNPS@Xylan/Porphyrin-TPP and self-assembled nanoparticles

Human colorectal cancer cell lines, HCT-116 and HT-29, were purchased from American Culture Type Collection (LGC Standards) Middlesex, UK. HCT-116 and HT-29 cells were respectively grown in RPMI-1640 and DMEM, supplemented with 10% fetal bovine serum (FBS), 100 U/mL penicillin and 100 µg/mL streptomycin. For all experiments, cells were seeded at 4×10^3 cells/well and 7×10^3 cells/well for HCT-116 and HT-29 cells, respectively, and maintained in a humidified atmosphere with 5% CO₂ at 37 °C. Photocytotoxicity was determined using 3-(4,5-dimethylthiazol-2-yl)-2,5-diphenyltetrazolium bromide (MTT) assays. Cells were seeded in 96-well culture plates and grown for 24 h in culture medium prior to exposure to free porphyrin or nanoparticles. Stock solutions of porphyrins and nanoparticles were diluted in culture medium to obtain the appropriate final concentrations. The same amount of vehicle (percentage of ethanol did not exceed 0.6%) was added to control cells. After 24 h incubation, the culture medium was replaced by phenol red-free DMEM medium, then the cells were either irradiated or not irradiated with a 630–660 nm CURElight lamp (PhotoCure ASA, Oslo, Norway) at 42 mW/cm² for 30 min until a fluence of 75 J/cm². MTT assays were performed 48 h after irradiation and cell viability was expressed as relative absorbance (570 nm) as compared with cells maintained in the dark. Results are expressed as the mean ± standard error of the mean (SEM) of two separate experiments.

2.13. Intracellular localization

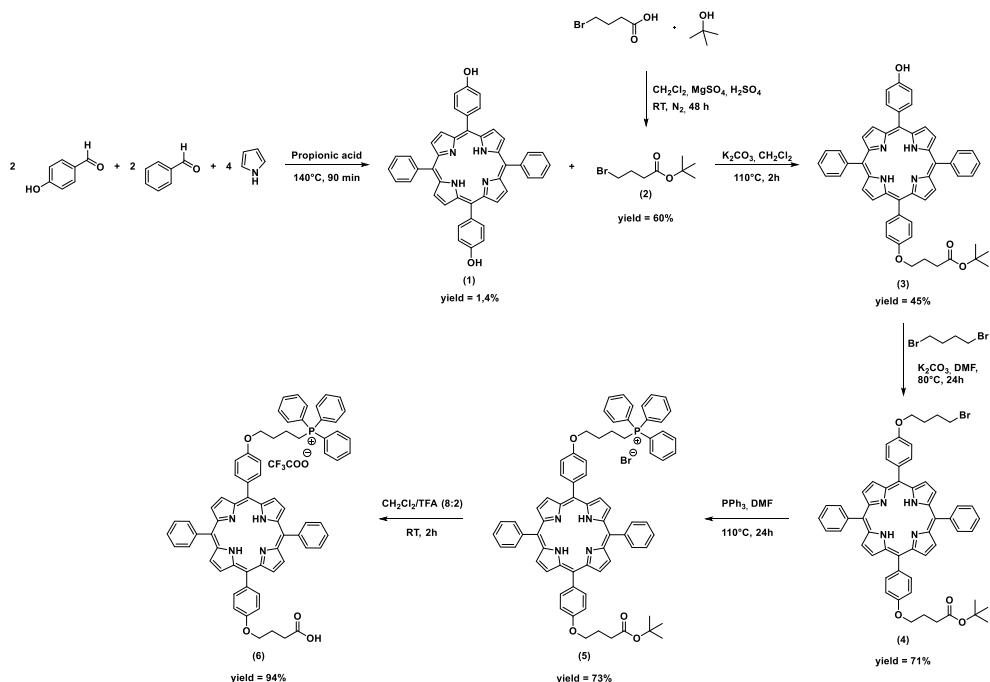
Cells were seeded in 6-well culture plates and were grown for 24 h prior to exposure to SiNPS@Xylan/Porphyrin or SiNPS@Xylan/Porphyrin-TPP at the same concentration (1 µM in porphyrin). After 24 h incubation, porphyrin fluorescence (excitation/emission: 405/650 nm) was determined by AMNIS[®] imaging flow cytometry analysis and studied with IDEAS software (Merck). To determine SiNPS@Xylan/Porphyrin and SiNPS@Xylan/Porphyrin-TPP local-

izations, cells were seeded and treated as described above and co-treated at 37 °C with 150 nM MitoTracker during 45 min. SiNPS@Xylan/Porphyrin and SiNPS@Xylan/Porphyrin-TPP localizations were determined by AMNIS[®] imaging flow cytometry and studied with IDEAS software using porphyrin fluorescence (excitation/emission: 405/650 nm) and MitoTracker fluorescence (excitation/emission: 490/516 nm). The same protocol was used for confocal microscopy analysis and photos were taken with a laser Zeiss LSM 510 Meta—×1000 confocal microscope.

3. Results and discussion

3.1. Synthesis of the triphenylphosphonium-monosubstituted porphyrin (6)

The different steps of triphenylphosphonium-monosubstituted porphyrin (6) synthesis are summarized in Scheme 1. First, 5,15-bis(4-hydroxyphenyl)-10,20-bisphenylporphyrin (1) was synthesized according to the Little's method [24]. After purification, the expected compound was obtained in 1.4% yield [25]. *Tert*-butyl 4-bromobutanoate (2) was synthesized according to the method described by Wright *et al.* [26]. This method, which involves the reaction between 4-bromobutanoic acid, in presence of magnesium sulfate and a catalytic amount of sulfuric acid, with isobutylene formed *in situ* by dehydration of *tert*-butanol, led to ester 2 in 60% yield. The subsequent Williamson ether reaction between porphyrin 1 and one equivalent of ester 2 in presence of potassium carbonate led to the formation of monosubstituted porphyrin 3 (45% yield). The triphenylphosphonium cation was then covalently bound to the second phenolic function in a very simple way, as described by Lei *et al.* [27]. Porphyrin 3 was reacted with 1,4-dibromobutane via a second Williamson reaction, affording 4 in 71% yield. This compound was then reacted with excess triphenylphosphine to generate porphyrin derivative 5 in 73% yield. The *tert*-butyl ester function was hydrolyzed by action of trifluoroacetic acid to produce porphyrin 6 with free carboxylic acid function in 94% yield. The chemical structures of each one of these compounds were confirmed by mass spectrometry and ¹H NMR spectroscopy.



Scheme 1. Synthesis of triphenylphosphonium-monosubstituted porphyrin **6**.

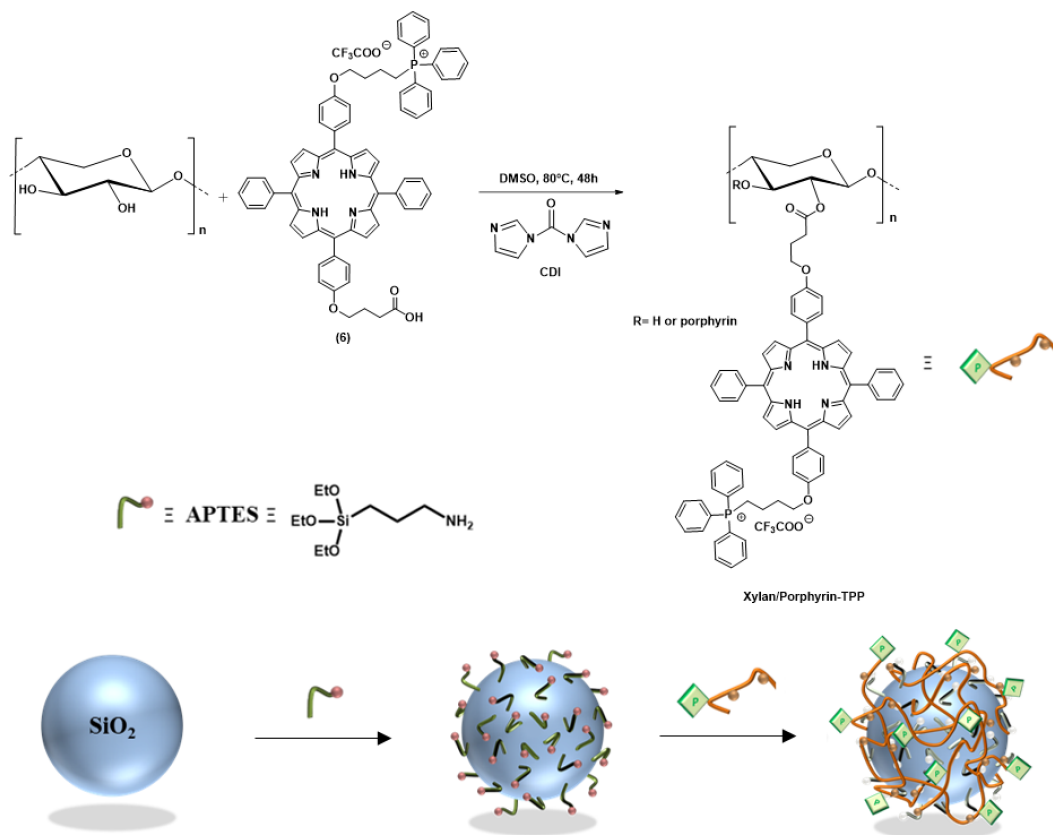
3.2. Synthesis of the hybrid nanoparticles *SiNPS@Xylan/Porphyrin-TPP*

The hybrid nanoparticles were prepared according to our previous work [18] (Scheme 2). Porphyrin **6** was then covalently bound to xylan by esterification. The synthesis of porphyrin-TPP-xylan was carried out by reaction of porphyrin **6** with CDI for 24 h at 60 °C to give the corresponding acyl-imidazole which was then coupled with xylan. ¹H NMR was used to calculate the degree of substitution (DS) of xylan, by measuring and comparing the integral area of the aromatic protons of porphyrin with those corresponding to the anomeric protons of xylan. On the average, one of every ten xylose residues was found to be substituted by porphyrin-TPP (DS = 0.1). A previously described method [18] was used to prepare core-shell hybrid nanoparticles. An ethanolic suspension of APTES-functionalized SiNPS (size = 80 nm) was added dropwise to a solution of Xylan/Porphyrin-TPP in water. The resulting nanoparticles were then recovered by centrifugation and washed several times with water to remove unbound polymers. Functionalization of SiNPS with Xylan/Porphyrin-TPP was confirmed by UV-

visible analysis (Figure S10, SI). A standard calibration curve obtained from different concentrations of Xylan/Porphyrin-TPP diluted in water was used to measure the concentration of Xylan/Porphyrin-TPP bound to SiNPS. A concentration of 1.1×10^{-5} mol Porphyrin-TPP per gram silica was determined.

3.3. Preparation and characterization of *Xylan/Porphyrin* and *Xylan/Porphyrin-TPP* nanoparticles (NPS)

SiNPS are subject to controversy due to their potential negative impact on human health [28]; this is why we decided to create nanoparticles without the silica core. It has recently been reported that conjugates consisting of hydrophilic xylan backbone and hydrophobic segments can form self-assembled nanoparticles in aqueous solution [29–33]. As a first step, we evaluated the self-assembly of different conjugates of xylan and 5-(4-hydroxyphenyl)-10,15,20-triphenylporphyrin with DS varying from 0.3 to 1.1. The preparation of these conjugates has been previously reported [18]. DLS and Scanning Electron Microscopy (SEM) showed that particles in the 1–2 μm size range were obtained. These particles were



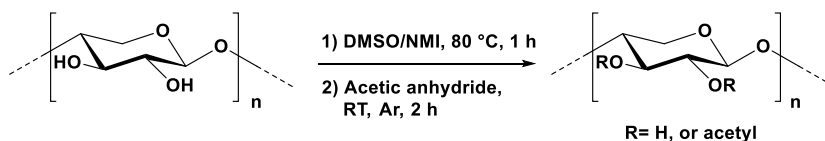
Scheme 2. Preparation of the SiNPS@Xylan/Porphyrin-TPP hybrid nanoparticles.

too large to penetrate tumor cells. The hydrophobic-hydrophilic balance backbone governs the formation of nanoparticles [34]. The DS in grafted porphyrin is probably too low to induce sufficient hydrophobicity to obtain nanoparticles; it is therefore necessary to introduce more hydrophobic groups. Xylan acetylation, practiced for many years to modify these properties, especially hydrophobicity, seemed appropriate [35]. Acetylation is most often carried out using acetic anhydride in presence of pyridine as a catalyst [36,37]. More recently, Zhang *et al.* published a milder method of xylan acetylation using DMSO/*N*-methylimidazole (NMI) mixture where NMI replaces pyridine as a catalyst, but also acts as a solvent [38]. Hence, following these conditions, seven acetylated xylans with different degrees of substitution ranging from 0.04 to 1.10 have been obtained (Scheme 3).

The ability of these seven acetylated xylans to form nanoparticles was then evaluated by the dialysis method, that is replacing the organic solvent, in which the acetylated xylans have been dissolved, by

water, by dialysis. The DLS method was used to characterize nanoparticle size; sizes were comprised between 80 to 120 nm for Ac-Xyl 5, 60 to 105 nm for Ac-Xyl 6 and 50 to 90 nm for Ac-Xyl 7 (Figure S12). As expected, increasing the amount of hydrophobic groups allowed to obtain smaller nanoparticles. However, SEM images showed that the nanoparticles with the highest DS (Ac-Xyl 7, DS = 1.10) no longer possess a spherical shape (Figure S13).

To obtain photosensitive nanoparticles of spherical shape and of nanometric size, acetylated xylans, Ac-Xyl 3, Ac-Xyl 4 and Ac-Xyl 5 with DS value of 0.21, 0.34, and 0.68, respectively, were chosen to be functionalized with porphyrins, which will consequently increase hydrophobicity of xylan. The two-step grafting procedure is illustrated in Scheme 4. 5-(4-(3-Carboxypropoxy)phenyl)-10,15,20-triphenylporphyrin [18] (TPPOH) was activated by reaction with CDI to furnish the corresponding acyl-imidazoles, which were then coupled with Ac-Xyl-3, Ac-Xyl 4 and Ac-Xyl 5 to



	Ac-Xyl 1	Ac-Xyl 2	Ac-Xyl 3	Ac-Xyl 4	Ac-Xyl 5	Ac-Xyl 6	Ac-Xyl 7
Molar ratio of acetic anhydride to anhydroxylose units	0.25	0.5	1	1.5	2.5	3	4
Degree of Substitution	0.04	0.11	0.21	0.34	0.68	0.80	1.10

Scheme 3. Acetylation of xylan with different molar ratios of acetic anhydride in DMSO/NMI at room temperature.

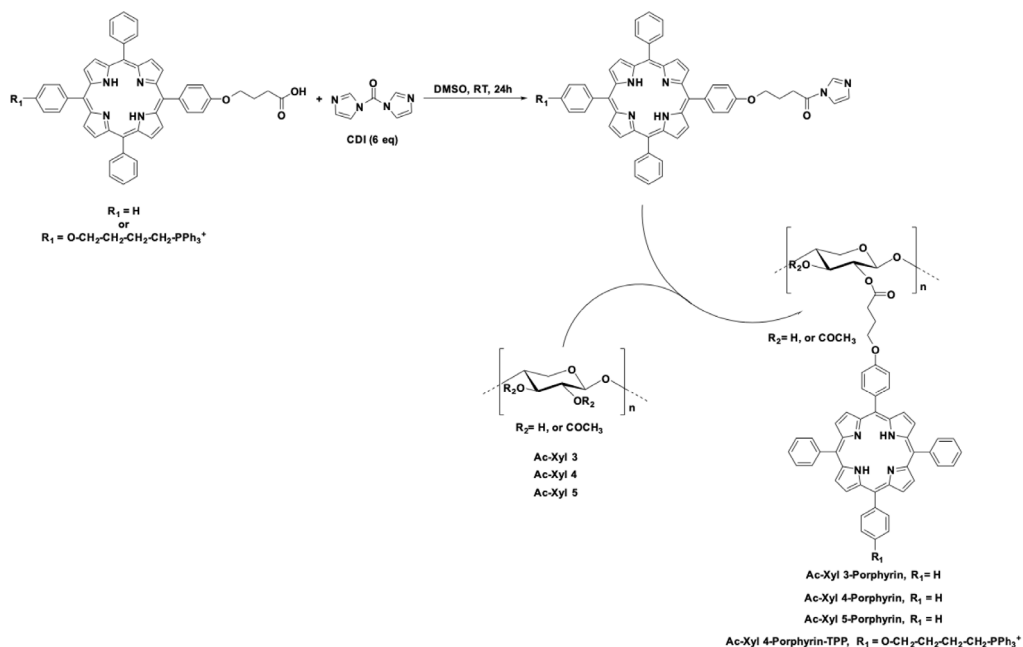
give Ac-Xyl 3-Porphyrin, Ac-Xyl 4-Porphyrin, Ac-Xyl 5-Porphyrin, respectively. DS in porphyrin, calculated from ^1H NMR spectra, were 0.71, 0.52 and 0.13 for Ac-Xyl 3-Porphyrin, Ac-Xyl 4-Porphyrin, Ac-Xyl 5-Porphyrin, respectively. Logically, the higher the acetyl DS of xylan, the harder it is to further graft porphyrin moieties.

The formation of nanoparticles from Ac-Xyl 3-Porphyrin, Ac-Xyl 4-Porphyrin and Ac-Xyl 5-Porphyrin was then investigated by the dialysis method. SEM images providing information on the morphology and size of the nanoparticles are shown in Figures 1B, D and F. Dialysis of Ac-Xyl 3-Porphyrin led to the formation of polymer aggregates instead of nanoparticles. On the other hand, Ac-Xyl 4-Porphyrin and Ac-Xyl 5-Porphyrin actually formed spherical nanoparticles. The mean hydrodynamic volumes of nanoparticles in water as measured by DLS (Figures 1A, C and E) were 128 ± 48 nm for Ac-Xyl 4-Porphyrin and $90 \text{ nm} \pm 35$ nm for Ac-Xyl 5-Porphyrin. Ac-Xyl 4-Porphyrin and Ac-Xyl 5-Porphyrin nanoparticles display polydispersity index (PDI) values of 0.221 and 0.235, which indicated a moderately polydisperse distribution [39]. It therefore appears that an acetylation ratio above 0.21 is essential for the formation of nanoparticles and that the higher the ratio, the smaller the

nanoparticles, provided that the ratio does not exceed 0.8.

In order to evaluate the effects of mitochondrial targeting, self-assembled xylan nanoparticles bearing porphyrin-TPP were prepared. Xylan polymer bearing acetyl groups was functionalized with porphyrin (**6**) bearing the triphenylphosphonium cation. Acetylated xylan Ac-Xyl 4 was chosen because it has made it possible to reach a porphyrin DS of 0.52, compared with the corresponding 0.13 value of Ac-Xyl 5. Triphenylphosphonium-monosubstituted porphyrin **6** was activated by reaction with CDI to furnish the corresponding acyl-imidazole, which was then coupled with Ac-Xyl 4 (Scheme 4). The degree of substitution of the product (Xyl-Ac 4-Porphyrin-TPP) was calculated from ^1H NMR data. Unexpectedly, a DS of 0.1 in porphyrin (**6**) was obtained. This degree of substitution is five times lower than that of xylan Ac-Xyl 4-Porphyrin (DS = 0.52), obtained in the same experimental conditions. The presence of the TPP positive charge on porphyrin **6** could limit its reactivity, by allowing ionic interaction with glucuronic acid substitutions or the hydroxyl groups of xylan.

Ac-Xyl 4-Porphyrin-TPP was then dissolved in DMSO and dialyzed against water for 15 h. After washing and centrifugation, nanoparticles were characterized using SEM and DLS (Figure 2).



Scheme 4. Grafting of TPPOH or porphyrin **6** onto acetylated xylans.

Spherical nanoparticles were observed in SEM image and the mean hydrodynamic size of particles in water as measured by DLS was 151 ± 25 nm with a PDI value of 0.332, which indicated a moderately polydisperse distribution type of these nanoparticles.

3.4. *In vitro* evaluation of nanoparticles against human colorectal cancer cells

The effect of hybrid SiNPS@Xylan/Porphyrin-TPP and Xylan/Porphyrin and Xylan/Porphyrin-TPP nanoparticles on cell viability was evaluated against HCT-116 and HT-29 colorectal cancer cells, via MTT assays (Table 2). This evaluation was carried out in the presence of photosensitizers free or with nanoparticles ranging from 0.01 to 5 μM during 48 h in the dark and under illumination. Within the concentration range tested, nanoparticles showed no or low cytotoxicity in the dark. Under illumination, all nanoparticles showed obvious cytotoxicity on HCT-116 and HT-29 at concentrations lower than 2 $\mu\text{g/mL}$. By comparison, organic nanoparticles showed significantly less photocytotoxicity than hybrid nanoparticles. One possible explanation is that the organic nanoparticles self-organize in such a way that the hydrophobic porphyrins tend to gather inside the

nanoparticle while the hydrophilic parts of xylan lie on the solvent-exposed periphery of the shell. Accordingly, the spatial promiscuity of porphyrins leads to self-quenching of the stacked PSs inside the nanoparticles. The lower fluorescence quantum yield of Xylan/porphyrin nanoparticles ($\Phi_F < 0.01$ in D_2O) compared to hybrid SiNPS@Xylan/Porphyrin nanoparticles ($\Phi_F = 0.04$ in EtOH) tends to confirm π -stacking interaction. Such an arrangement would justify the reduction in phototoxicity of the organic nanoparticles. However, their photocytotoxicities were still much stronger than those of free porphyrins. Interestingly, addition of the triphenylphosphonium cation resulted in reduction by factors of 2.8–3.5 the IC_{50} values of the hybrid nanoparticles.

Confocal microscopy was used to examine the subcellular localization of SiNPS@Xylan/Porphyrin and SiNPS@Xylan/Porphyrin-TPP in HT-29 cancer cells (Figure 3). Our previous investigations revealed that SiNPS@Xylan/Porphyrin localized predominantly in lysosomes [19]. Based on the yellowish color arising from the overlay of red fluorescence of SiNPS@Xylan/Porphyrin-TPP and the green fluorescence of the organelle marker, it can be concluded that SiNPS@Xylan/Porphyrin-TPP was localized in mitochondria. These first *in vitro* results are very

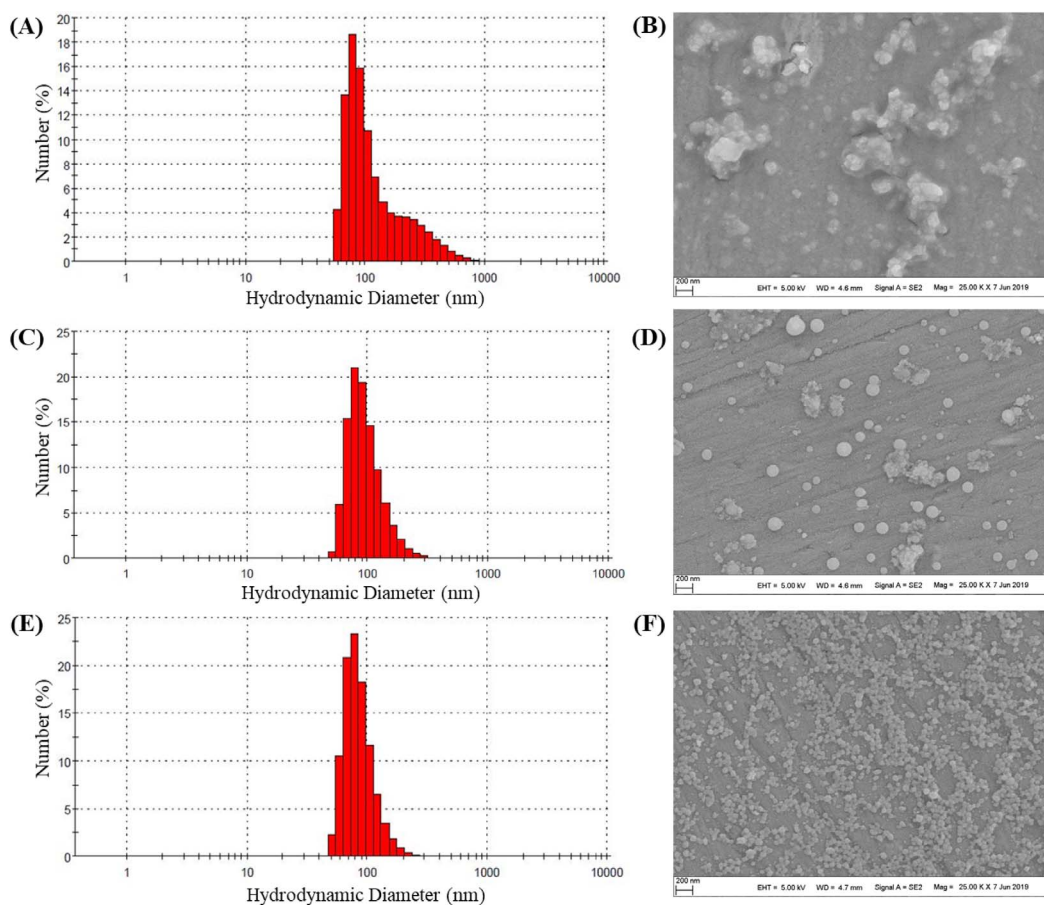


Figure 1. Particle size and morphology of nanoparticles: (A) DLS size measurement of Ac-Xyl 3-Porphyrin particles; (B) SEM image of Ac-Xyl 3-Porphyrin particles; (C) DLS size measurement of Ac-Xyl 4-Porphyrin particles; (D) SEM image of Ac-Xyl 4-Porphyrin particles; (E) DLS size measurement of Ac-Xyl 5-Porphyrin particles; (F) SEM image of Ac-Xyl 5-Porphyrin particles.

Table 2. *In vitro* photocytotoxicity of hybrid SiNPS@Xylan/Porphyrin-TPP and organic Xylan/Porphyrin and Xylan/Porphyrin-TPP nanoparticles in human colorectal cancer cells

	HCT-116		HT-29	
	Dark	Illumination	Dark	Illumination
TPPOH [18]	Not determined	2943 ± 102	Not determined	5959 ± 430
Porphyrin-TPP (6)	>5000	960 ± 430	>5000	1660 ± 40
SiNPS@Xylan/Porphyrin [18], ^a	>1000	72.6 ± 2.8	>1000	550.2 ± 7.5
SiNPS@Xylan/Porphyrin-TPP ^a	>1000	25 ± 15	> 1000	157.5 ± 17.5
Xylan/Porphyrin NPS ^a	> 5000	1045 ± 136	>5000	2280 ± 190
Xylan/Porphyrin-TPP NPS	>5000	<2000	>5000	1240 ± 180

^a IC₅₀ nM concentrations are directly corresponding to the amount of porphyrins.

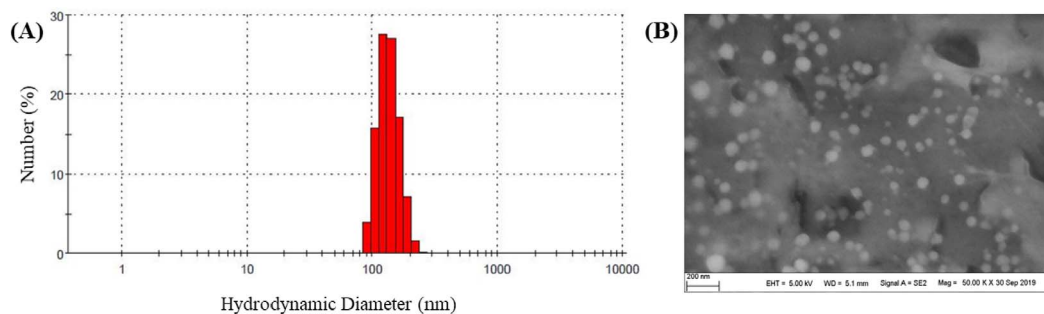


Figure 2. Particle size and morphology of nanoparticles: (A) DLS size measurement of Ac-Xyl 4-Porphyrin-TPP particles; (B) SEM image of Ac-Xyl 4-Porphyrin-TPP particles.

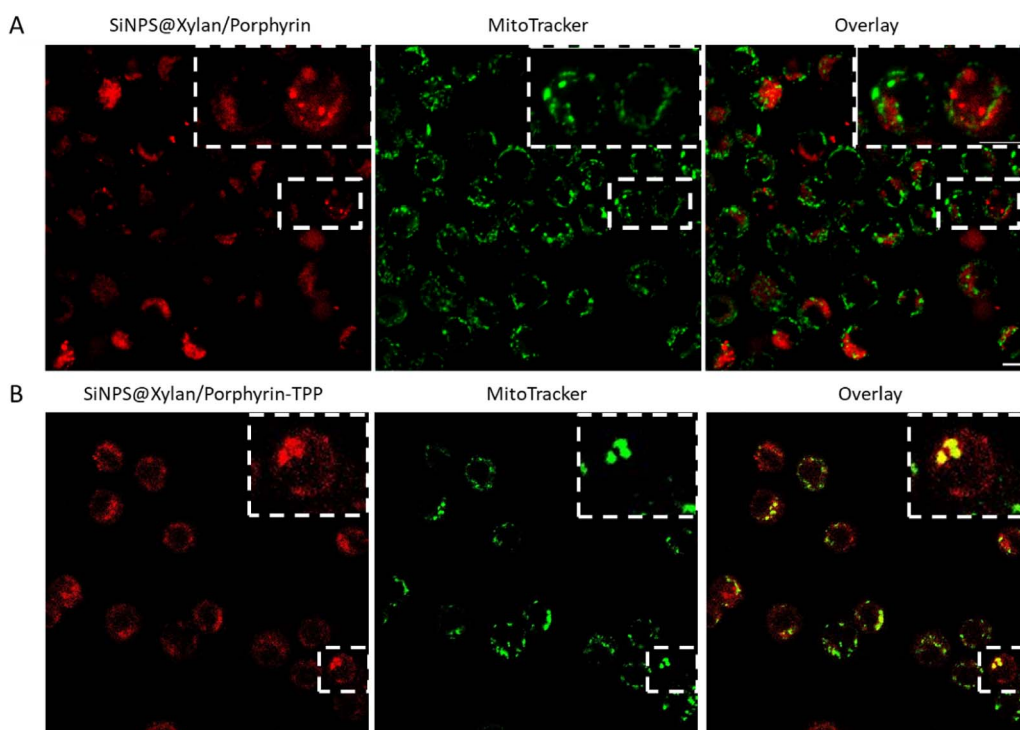


Figure 3. The intracellular localization of SiNPS@Xylan/Porphyrin and SiNPS@Xylan/Porphyrin-TPP in HT-29 cells with MitoTracker Green. Images were merged to indicate the overlap in fluorescence.

encouraging and suggest that mitochondrial targeting of nanoparticles would increase their photocytotoxicity.

4. Conclusion

Hybrid nanoparticles with a silica core coated with xylan substituted with porphyrins bearing a triphenylphosphonium cation have been constructed for

the first time. Addition of the triphenylphosphonium cation allowed to enhance threefold the photocytotoxicity of the nanoparticles against colorectal cancer cell lines HCT-116 and HT-29. The controversy surrounding the use of silica nanoparticles has led us to build xylan nanoparticles devoid of the silica core. The self-organization of xylan in water required an increase in its hydrophobicity which has been achieved by means of acetylation.

Post-functionalization of acetylated xylans with porphyrins, whether bearing the triphenylphosphonium cation or not, followed by nanoparticle shaping, has made it possible to obtain photosensitive organic nanoparticles. These organic nano-objects showed lower toxicity than hybrid nanoparticles, probably due to the self-quenching effect of the porphyrins inside the nanoparticles. However, organic nanoparticles retained a strong photocytotoxicity, much higher than that of the corresponding free porphyrin. This strategy therefore appears promising for the design and development of photosensitizer nanocarriers for oncological photodynamic therapy.

Acknowledgments

We thank Dr. Cyril Colas for ESI-HRMS analyses. We acknowledge financial support from GDR MAPYRO and the regional council of Nouvelle-Aquitaine, and Dr. Michel Guilloton for his help in manuscript editing.

Supplementary data

Supporting information for this article is available on the journal's website under <https://doi.org/10.5802/crchim.108> or from the author.

References

- [1] B. A. Chabner, T. G. Roberts, *Nat. Rev. Cancer*, 2005, **5**, 65-72.
- [2] T. J. Dougherty, C. J. Gomer, B. W. Henderson, G. Jori, D. Kessel, M. Korbekij, J. Moan, Q. Peng, *J. Natl Cancer Inst.*, 1998, **90**, 889-905.
- [3] H. Abrahamse, M. R. Hamblin, *Biochem. J.*, 2016, **473**, 347-364.
- [4] E. D. Sternberg, D. Dolphin, C. Brückner, *Tetrahedron*, 1998, **54**, 4151-4202.
- [5] J. Kydd, R. Jadia, P. Velpurisiva, A. Gad, S. Paliwal, P. Rai, *Pharmaceutics*, 2017, **9**, article no. 46.
- [6] Y. Matsumura, H. Maeda, *Cancer Res.*, 1986, **46**, 6387-6392.
- [7] H. Maeda, Y. Matsumura, *Crit. Rev. Ther. Drug Carrier Syst.*, 1989, **6**, 193-210.
- [8] H. Maeda, *Adv. Enzyme Regul.*, 2001, **41**, 189-207.
- [9] T. A. Debele, S. Peng, H.-C. Tsai, *Int. J. Mol. Sci.*, 2015, **16**, 22094-22136.
- [10] P. Couleaud, V. Morosini, C. Frochot, S. Richeter, L. Raehm, J.-O. Durand, *Nanoscale*, 2010, **2**, 1083-1095.
- [11] J. L. Vivero-Escoto, D. L. Vega, *RSC Adv.*, 2014, **4**, 14400-14407.
- [12] R. Chouikrat, A. Seve, R. Vanderesse, H. Benachour, B.-H. Barberi-Heyob, S. Richeter, L. Raehm, J.-O. Durand, M. Verelst, C. Frochot, *Curr. Med. Chem.*, 2012, **19**, 781-792.
- [13] I. Roy, T. Y. Ohulchanskyy, H. E. Pudavar, E. J. Bergey, A. R. Oseroff, J. Morgan, T. J. Dougherty, P. N. Prasad, *J. Am. Chem. Soc.*, 2003, **125**, 7860-7865.
- [14] C. Lemarchand, R. Gref, P. Couvreur, *Eur. J. Pharm. Biopharm.*, 2004, **58**, 327-341.
- [15] F. S. Mozar, E. H. Chowdhury, *J. Pharm. Sci.*, 2018, **107**, 2497-2508.
- [16] A. Zhu, L. Yuan, W. Jin, S. Dai, Q. Wang, Z. Xue, A. Qin, *Acta Biomater.*, 2008, **5**, 1489-1498.
- [17] J.-P. Mbakidi, F. Brégier, T.-S. Ouk, R. Granet, S. Alves, E. Rivière, S. Chevreux, G. Lemerrier, V. Sol, *ChemPlusChem.*, 2015, **80**, 1416-1425.
- [18] S. Bouramtane, L. Bretin, A. Pinon, D. Leger, B. Liagre, L. Richard, F. Brégier, V. Sol, V. Chaleix, *Carbohydr. Polym.*, 2019, **213**, 168-175.
- [19] L. Bretin, A. Pinon, S. Bouramtane, C. Ouk, L. Richard, M.-L. Perrin, A. Chaunavel, C. Carrion, F. Bregier, V. Sol, V. Chaleix, D. Y. Leger, B. Liagre, *Cancers (Basel)*, 2019, **11**, article no. 1474.
- [20] L. Dong, J. Neuzil, *Cancer Commun. (Lond)*, 2019, **39**, article no. 63.
- [21] J. Zielonka, A. Sikora, M. Hardy, O. Ouari, J. Vasquez-Vivar, G. Cheng, M. Lopez, B. Kalyanaraman, *Chem. Rev.*, 2017, **117**, 10043-10120.
- [22] S. Daus, T. Heinze, *Macromol. Biosci.*, 2010, **10**, 211-220.
- [23] S. E. Barrios, G. Giammanco, J. M. Contreras, E. Laredo, F. López-Carrasquero, *Int. J. Biol. Macromol.*, 2013, **59**, 384-390.
- [24] R. G. Little, J. A. Anton, P. A. Loach, J. A. Ibers, *J. Heterocycl. Chem.*, 1975, **12**, 343-349.
- [25] W. Sun, J. Li, X. Lü, F. Zhang, *Res. Chem. Intermed.*, 2013, **39**, 1447-1457.
- [26] S. W. Wright, D. L. Hageman, A. S. Wright, L. D. McClure, *Tetrahedron Lett.*, 1997, **38**, 7345-7348.
- [27] W. Lei, J. Xie, Y. Hou, G. Jiang, H. Zhang, P. Wang, X. Wang, B. Zhang, *J. Photochem. Photobiol. B: Biol.*, 2010, **98**, 167-171.
- [28] S. Murugadoss, D. Lison, L. Godderis, S. Van Den Brule, J. Mast, F. Brassinne, N. Sebaihi, P. H. Hoet, *Arch. Toxicol.*, 2017, **91**, 2967-3010.
- [29] S. Singh, V. Kumar, B. Kumar, R. Priyadarshi, F. Deeba, A. Kulshreshtha, A. Kumar, G. Agrawal, P. Gopinath, Y. S. Negi, *Mater. Sci. Eng. C*, 2020, **107**, article no. 110356.
- [30] Y. Qin, X. Peng, *ACS Biomater. Sci. Eng.*, 2020, **6**, 1582-1589.
- [31] S. Singh, U. Kumar, V. Kumar, R. Priyadarshi, P. Gopinath, Y. S. Negi, *Carbohydr. Polym.*, 2018, **188**, 252-259.
- [32] G.-Q. Fu, L.-Y. Su, P.-P. Yue, Y.-H. Huang, J. Bian, M.-F. Li, F. Peng, R.-C. Sun, *Cellulose*, 2019, **26**, 7195-7206.
- [33] X. Peng, Z. Xiang, F. Du, J. Tan, L. Zhong, R. Sun, *Cellulose*, 2018, **25**, 245-257.
- [34] M. Gericke, P. Schulze, T. Heinze, *Macromol. Biosci.*, 2020, **20**, article no. 1900415.
- [35] N. G. V. Fundador, Y. Enomoto-Rogers, A. Takemura, T. Iwata, *Carbohydr. Polym.*, 2012, **87**, 170-176.
- [36] M. Gröndahl, A. Teleman, P. Gatenholm, *Carbohydr. Polym.*, 2003, **52**, 359-366.
- [37] N. G. V. Fundador, Y. Enomoto-Rogers, A. Takemura, T. Iwata, *Polymer*, 2012, **53**, 3885-3893.
- [38] X. Zhang, A. Zhang, C. Liu, J. Ren, *Cellulose*, 2016, **23**, 2863-2876.
- [39] S. Bhattacharjee, *J. Control. Release*, 2016, **235**, 337-351.



MAPYRO: the French Fellowship of the Pyrrolic Macrocyclic Ring / *MAPYRO: la communauté française des macrocycles pyrroliques*

Photocatalytic recovery of metals by Lindqvist-type polyoxometalate–porphyrin copolymer

Récupération photocatalytique des métaux par un copolymère polyoxométallate-porphyrine de type Lindqvist

Zhaohui Huo^{a, b}, Vasilica Badets^{Ⓢ b}, Antoine Bonnefont^{Ⓢ b}, Corinne Boudon^b
and Laurent Ruhlmann^{Ⓢ *, b}

^a Department of Chemistry, Guangdong University of Education, Guangzhou 510303, PR China

^b Université de Strasbourg, Institut de Chimie, UMR CNRS 7177, Laboratoire d'Electrochimie et de Chimie Physique du Corps Solide, 4 rue Blaise Pascal, CS 90032, 67081 Strasbourg cedex, France

E-mails: zhaohuihuo@hotmail.com (Z. Huo), badets@unistra.fr (V. Badets), bonnefont@unistra.fr (A. Bonnefont), cboudon@unistra.fr (C. Boudon), lruhlmann@unistra.fr (L. Ruhlmann)

Abstract. Hybrid polyoxometalate–porphyrin copolymeric films can be obtained by the electro-oxidation of 5,15-ditolyl porphyrin (**H₂T₂P**) and zinc-β-octaethylporphyrin (**ZnOEP**) in the presence of the Lindqvist-type polyoxovanadates TBA₂[V₆O₁₃{(OCH₂)₃CNHCO(4-C₅H₄N)}₂] (**Py-V₆O₁₃-Py**). The photocatalytic properties of these films have been studied for the reduction of silver and platinum ions. In these hybrid materials, porphyrins can be excited by visible light and then play the role of photosensitizers able to give electrons to the polyoxovanadates catalysts.

Résumé. Des films copolymères hybrides polyoxométallate–porphyrine peuvent être obtenus par électrooxydation de la 5,15-ditolyl porphyrine (**H₂T₂P**) et du zinc-β-octaéthylporphyrine (**ZnOEP**) en présence des polyoxovanadates de type Lindqvist TBA₂[V₆O₁₃{(OCH₂)₃CNHCO(4-C₅H₄N)}₂] (**Py-V₆O₁₃-Py**). Les propriétés photocatalytiques de ces films ont été étudiées pour la réduction des ions argent et platine. Dans ces matériaux hybrides, les porphyrines peuvent être excitées par la lumière visible et jouer alors le rôle de photosensibilisateurs capables de donner des électrons aux catalyseurs polyoxovanadates.

Keywords. Porphyrin, Polyoxometalate, Photoreduction hybrid copolymer, Metal remediation, Silver and platinum nanoparticles.

Mots-clés. Porphyrine, Polyoxométallate, Photoréduction, Copolymère hybride, Dépollution métallique, Nanoparticules de platine et d'argent.

Available online 30th September 2021

* Corresponding author.

1. Introduction

Polyoxometalates (POMs), a large family of transition metal oxygen anion clusters with d^0 electronic configurations, exhibit interesting photocatalytic properties. Upon light irradiation, electrons are promoted from an oxygen-centered 2p orbital to an empty metallic d-orbital, generating a highly reactive charge-separated state [1]. The impregnation of polyvinylidene fluoride-based solid polymer electrolyte by POM was also shown to improve the performance of dye sensitized solar cell. The fabricated cell generated high open circuit voltage of 426 mV and short circuit current of 3.90 mA upon illumination with visible light [2]. The above-mentioned excellent properties and pioneering studies indicate that POMs are promising candidates to optimize the photocurrent generation efficiency.

Furthermore, POMs are also of interest for oxidative photodegradation of organic compounds in water purification technology [3].

Metal recovery is also a topic of great concern from economic and environmental aspect. Since many metals are either valuable or toxic, the development of methods that aim to recover them could contribute to save the limited resources and resolve the environmental problems.

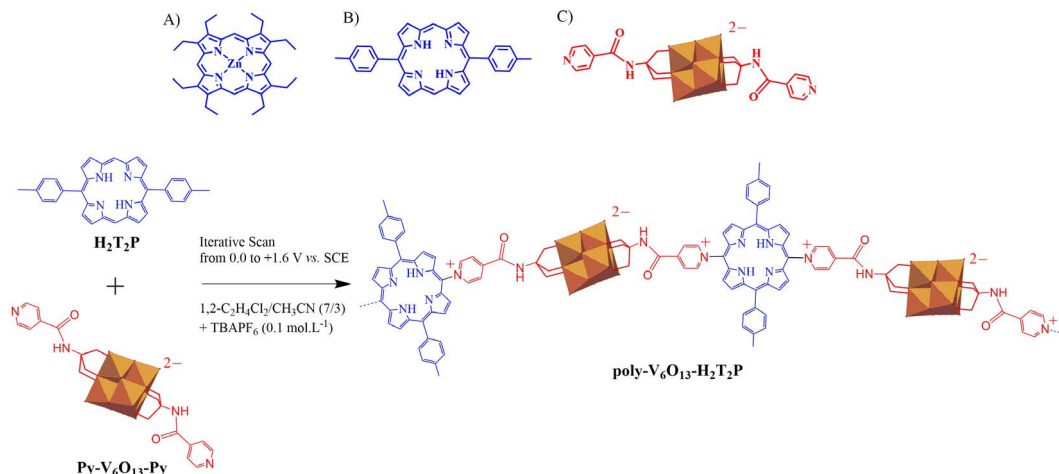
Metallic nanoparticles can be produced using various methods, such as thermal decomposition [4], electrochemical techniques [5,6], sonochemical synthesis [7,8] radiolysis [9], microwave irradiation [10] and photocatalysis [11].

In particular, polyoxometalates (POMs) can be used in photocatalytic processes for the recovery of metals or the synthesis of nanoparticles. Indeed, POMs are also excellent electron reservoirs as they exhibit variable oxidation states and the possibility of multiple reductions making the POMs an excellent candidate as photocatalysts for the reduction of metal ions. In the process, illumination at the $O \rightarrow M$ charge-transfer band (UV region), renders POM strong oxidants able to extract electrons from organic electron donors. POMs display remarkable activity and selectivity which can be adjusted by the choice of POM with suitable redox potential, while operational parameters such as the concentration of POM, organic substrate (sacrificial electron donor such as propan-2-ol), and metal ions should affect the photocatalytic efficiency.

Recovery of metallic ions from aqueous solutions can be obtained through a homogeneous photocatalytic process in the presence of a sacrificial electron donor such as propan-2-ol that undergoes photolysis under UV illumination. In these conditions, POMs are quantitatively reduced and this leads to the reduction of metallic ions. This procedure is a useful alternative for synthesis and recovery of metallic nanoparticles [12,13].

To expand the practical application range, their association to a light-harvesting antenna is so far necessary, since POMs themselves are mainly photoactive only in the UV part of the solar spectrum. Among photosensitizers, porphyrins offer the advantages of strong absorption coefficients in the visible domain. Synthesis of covalently bonded POM-porphyrin hybrid system [14,15] can be proposed in order to obtain efficient photoinduced intramolecular electron transfer from the porphyrin ring to the POM cluster. Formation of covalently bonded POM-porphyrin copolymers can be similarly proposed. Then the reduced POMs can be used for the reduction of metallic ions. The electrochemical synthesis of the POM-porphyrin copolymers uses the previously published nucleophilic substitution on porphyrins via an $E(EC_N EC_B)_n E$ process [16–21]. A polarization of a working electrode at the first ring-oxidation potential of porphyrins in the presence of pyridine induces a nucleophilic attack and leads to the attachment of the pyridyl nitrogen to the *meso* positions of the porphyrin. If the applied potential corresponds to the second ring-oxidation potential of porphyrins in the presence of bipyridine, copolymer with viologen spacers can be obtained. In the present work, the nucleophile pyridine groups came from the functionalized POM (Py-POM-Py) [22–24], resulting in the formation of $\{POM\text{-porphyrin}\}_n$ copolymers.

Preliminary study concerning the use of photosensitized systems coupled with POMs for the elaboration of metallic silver nanosheets and nanowires (heterogeneous photocatalysis) has been reported. In this case, the copolymers were composed of porphyrin and Anderson-type POM subunits [22]. Precisely, the hybrid copolymer was obtained by electropolymerization of zinc β -octaethylporphyrin (ZnOEP) or zinc 5,15-dipyridinium-octaethylporphyrin (5,15-ZnOEP(py) $_2^{2+}$) in the presence of a function-



Scheme 1. Top: representation of (A) zinc- β -octaethylporphyrin **ZnOEP**, (B) free base 5,15-ditolylporphyrin **H₂T₂P** and (C) Lindqvist-type polyoxometalate $[V_6O_{13}\{(OCH_2)_3CNHCO(4-C_5H_4N)\}_2]^{2-}$ (**Py-V₆O₁₃-Py**). Bottom: electropolymerization scheme of **H₂T₂P** in the presence of **Py-V₆O₁₃-Py** giving the copolymer **poly-V₆O₁₃-H₂T₂P**.

alized Anderson-type polyoxometalate bearing two pyridyl groups $[MnMo_6O_{18}\{(OCH_2)_3CNHCO(4-C_5H_4N)\}_2]^{3-}$ (**Py-MnMo₆O₁₈-Py**) [1,24]. The photocatalytic reduction of $Ag_2^I SO_4$ using this copolymer was conducted under visible light illumination and aerobic conditions in the presence of propan-2-ol. Quantitative formation of metallic Ag^0 nanowires as well as triangular nanosheets was observed.

The main goal of this work is to demonstrate that other hybrid porphyrin–POM copolymers are still working as photocatalysts for the reduction of metallic ions. By changing the nature of the porphyrin and of the polyoxometalate, a change in the photoreduction kinetics as well as in the shape of the nanoparticles is expected. In the present paper, we use copolymers obtained by electropolymerization of metalloporphyrin-type zinc- β -octaethylporphyrin (**ZnOEP**) or free-base-type 5,15-ditolyl porphyrin (**H₂T₂P**) with the functionalized Lindqvist polyoxovanadate bearing two pyridyl groups $[V_6O_{13}\{(OCH_2)_3CNHCO(4-C_5H_4N)\}_2]^{2-}$ (**Py-V₆O₁₃-Py**) (Scheme 1). The photocatalytic reduction of $Ag_2^I SO_4$ as well as the $H_2Pt^{IV}Cl_6$ is studied under visible irradiation in the presence of propan-2-ol, acting as sacrificial donor, at the 2D interface between water and the copolymeric films deposited on quartz substrate.

2. Results and discussion

2.1. Electrochemical synthesis of the copolymers

The syntheses of the copolymers were achieved using our electropolymerization method, as reported earlier [25,26]. It corresponds to the addition of the dipyriddy-substituted Lindqvist-type polyoxovanadate $[V_6O_{13}\{(OCH_2)_3CNHCO(4-C_5H_4N)\}_2]^{2-}$ (**Py-V₆O₁₃-Py**) to an electrogenerated dicationic 5,15-ditolylporphyrin (**H₂T₂P**) or zinc- β -octaethylporphyrin (**ZnOEP**) obtained by iterative scans between 0 V and +1.60 V versus SCE (Scheme 1) [27].

Using this method, the **poly-Py-V₆O₁₃-Py-H₂T₂P** and the **poly-Py-V₆O₁₃-Py-ZnOEP** hybrid copolymers were prepared as described previously [27].

Note that the free base *meso*-5,15-ditolylporphyrin (**H₂T₂P**) presents only two *meso* positions occupied by one substitutable proton at positions C10 and C20 while the zinc- β -octaethylporphyrin (**ZnOEP**) presents four substitutable *meso* positions at C5, C10, C15 and C20 (top of Scheme 1). The described electrochemical synthesis of the copolymers uses the previously reported $E(EC_N EC_B)_n E$ process of nucleophilic substitution on porphyrins [17–19,26–29]. As soon as the iterative scans were performed at an anodic potential suffi-

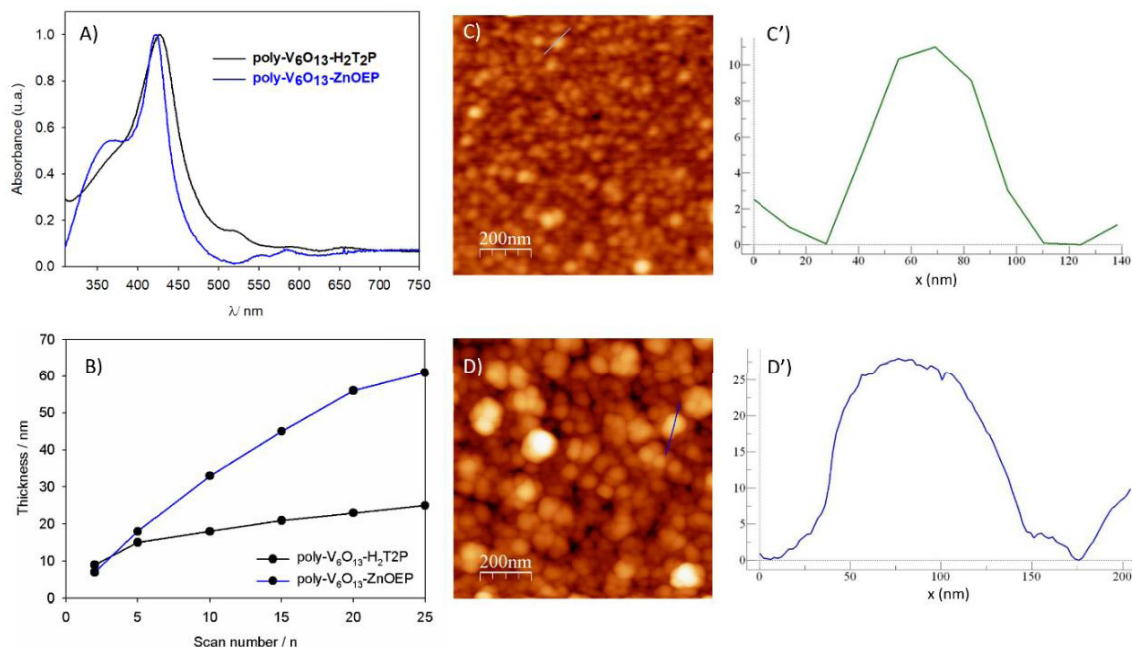


Figure 1. (A) UV-Vis absorption spectra of **poly-V₆O₁₃-ZnOEP** and **poly-V₆O₁₃-H₂T₂P** obtained after 20 iterative scans between 0.00 and +1.60 V versus SCE on ITO. (B) Thickness of **poly-V₆O₁₃-ZnOEP** and **poly-V₆O₁₃-H₂T₂P** measured by AFM versus different numbers of iterative scans. Tapping mode AFM topography and section analysis of the aggregate marked by a blue line of (C) and (C') **poly-V₆O₁₃-H₂T₂P**, and of (D) and (D') **poly-V₆O₁₃-ZnOEP** (film obtained after 20 scans, between 0.00 V and +1.60 V).

ciently high to allow the formation of the porphyrin dication, the formation of a copolymer coating the working electrode was observed.

The mechanism of the formation of the copolymer can be described such as: first, the porphyrin (abbreviated Porph) radical cation (Porph^{•+}, electrochemical step E) and dication (Porph²⁺, electrochemical step E) are electrogenerated. Then, the dication porphyrin Porph²⁺ can be attacked by a two pendant isonicotinate groups of the pyridyl-substituted Lindqvist-type polyoxovanadate [V₆O₁₃{(OCH₂)₃CNHCO(4-C₅H₄N)}₂]²⁻ (abbreviated **Py-V₆O₁₃-Py**) at *meso*-carbon position to yield an isoporphyrin (chemical step C_{Nmeso}). This later intermediate can be oxidized (electrochemical step E) and the hydrogen atom originally situated on the *meso*-carbon is released inducing the rearomatization of the porphyrin (chemical step C_B) which leads to the monosubstituted porphyrin Porph-*meso*-Py⁺-V₆O₁₃-Py. At this stage, monosubstituted porphyrin is obtained with one pyridinium covalently connected to the porphyrin and one pendant

pyridyl group which is still active for nucleophilic attack. This pendant pyridyl group can further attack oxidized porphyrin continuing the growth of the copolymer. Thus, the polarization of a working electrode at the porphyrin's second ring-oxidation potential in the presence of **Py-V₆O₁₃-Py**, leads to the formation of the two hybrid copolymer films with general formula [Py⁺-V₆O₁₃²⁻-Py⁺-porphyrin]_n (bottom of Scheme 1), namely **poly-V₆O₁₃-H₂T₂P** and **poly-V₆O₁₃-ZnOEP**.

UV-visible spectra of both copolymers on ITO electrodes presented similar characteristics [27]. They exhibit a large Soret absorption band (Figure 1A), which was red shifted by 15 and 20 nm compared to the **ZnOEP** and **H₂T₂P** monomer respectively [27]. It can be explained by intra- or intermolecular excitonic interactions between the porphyrin subunits [17,30]. The red shifts observed are in agreement with the presence of the disubstituted porphyrin ring by two pyridinium groups [31] in the copolymer.

The films were also examined by scanning atomic force microscopy (AFM) showing tightly packed coils with average diameters of 40–60 nm and a height of 5 nm in the case of **poly-V₆O₁₃-H₂T₂P** (Figures 1C and C'). The rms surface roughness of the film was 3.5 nm for 1 mm² area. For **poly-V₆O₁₃-ZnOEP** the diameter and the height of the coils were almost two times larger (Figures 1D and D') [27].

Thickness of the deposited copolymeric film was measured using AFM by scratching the film with a metallic tip. The thickness increased upon the number of iterative scans as shown in Figure 1B. The values obtained after 20 scans between 0.00 V and +1.60 V were about 23 nm for **poly-V₆O₁₃-ZnOEP** and 56 nm for **poly-V₆O₁₃-H₂T₂P**.

2.2. Photocatalytic recovery of silver

The electrochemically deposited **poly-V₆O₁₃-ZnOEP** or **poly-V₆O₁₃-H₂T₂P** copolymers were dissolved and removed from ITO with dimethyl formamide (DMF). Subsequently, the copolymer in DMF solution was deposited on a quartz slide, and the DMF solvent was evaporated in air. Then, the quartz slide was plunged in an optical cell containing a deaerated aqueous solution with 8×10^{-5} mol·L⁻¹ Ag₂SO₄ and 0.13 mol·L⁻¹ propan-2-ol. The whole sample was illuminated under visible light with a 385 nm cutoff filter to prevent POM photoexcitation allowing only the excitation of the porphyrin. Figure 2 presents the absorption spectra recorded during the experiment performed with the **poly-V₆O₁₃-ZnOEP** (Figure 2A) or **poly-V₆O₁₃-H₂T₂P** (Figure 2B) films. The absorbance increases in the whole visible domain during illumination and the solution becomes slightly yellow which reveals the formation of silver nanoparticles [22,32]. The initial rate of Ag⁺ reduction is 3.4×10^{-5} mol·L⁻¹·min⁻¹ for **poly-V₆O₁₃-ZnOEP** and 3.1×10^{-5} mol·L⁻¹·min⁻¹ for **poly-V₆O₁₃-H₂T₂P**. After almost 95 min (for **poly-V₆O₁₃-ZnOEP**) and 105 min (for **poly-V₆O₁₃-H₂T₂P**) of visible light irradiation, the absorption spectrum does not evolve anymore which indicates the end of the reaction.

After removal of the quartz slide covered with the film, the UV–visible spectrum of the solution exhibits a large plasmon band in the whole visible domain with a maximum around 410 nm (Figure 3). This can be attributed to the presence of silver nanoparticles in the solution. No change in the spectrum is

observed for one week indicating the good stability of the silver nanoparticles. Moreover, it has been found that the slides of quartz can be reused at least five times with almost no change in the efficiency of the photocatalysis. Silver ions Ag(I) are reduced quantitatively at the interface between water and the copolymeric films without poisoning the surface (as checked by AFM analysis, data not shown).

The TEM micrographs confirmed the formation of silver particles (Figures 4 and 5). The nanoparticles obtained with **poly-V₆O₁₃-ZnOEP** have an average diameter of 20 nm but are agglomerated (Figure 4).

The presence of Moiré pattern in TEM images of silver particles is due to the presence of metallic silver crystal planes with different spacing and/or orientations. Each silver nanoparticles seems to be crystalline as shown by electron diffraction analysis (Figure 4E).

The 6-fold rotational symmetry displayed by the diffraction spots implied that the faces represented the {111} planes. The first set of spots could be indexed to the formally forbidden 1/3 {422} reflections of face-centered cubic (fcc) silver with a corresponding lattice spacing of 2.48 Å. The second set corresponded to Bragg diffraction from the {220} planes of fcc silver with a lattice spacing of 1.44 Å (1.445 Å in JCPDS file 04-0783). These observations were in agreement with the usual published indexes for silver nanosheets [33,34]. We explain the observation of 1/3 {422} reflections that are formally forbidden for a perfect fcc structure by the presence of stacking faults [35]. These stacking faults could be caused by bending, which explains the presence of Moiré pattern in TEM images [36]. The EDS spectrum in Figure 4F reveals the presence of metallic Ag in the sample, the C and Cu detected belonging to the TEM grid.

Conversely, the nanostructures obtained with **poly-V₆O₁₃-H₂T₂P** exhibited larger dispersion in size and shape, because the samples presented not only spherical, elongated particles but also long linear silver nanowires (thickness ca. 20–40 nm and length ca. 200–500 nm) and large silver nanosheets (Figure 5). The EDS spectrum in Figure 5C reveals the presence of metallic Ag in the sample.

Two possible mechanisms can be involved to describe the formation of AgNPs. As shown in Figure 6A, the first mechanism consists in the reduction of the excited porphyrins by propan-2-ol, fol-

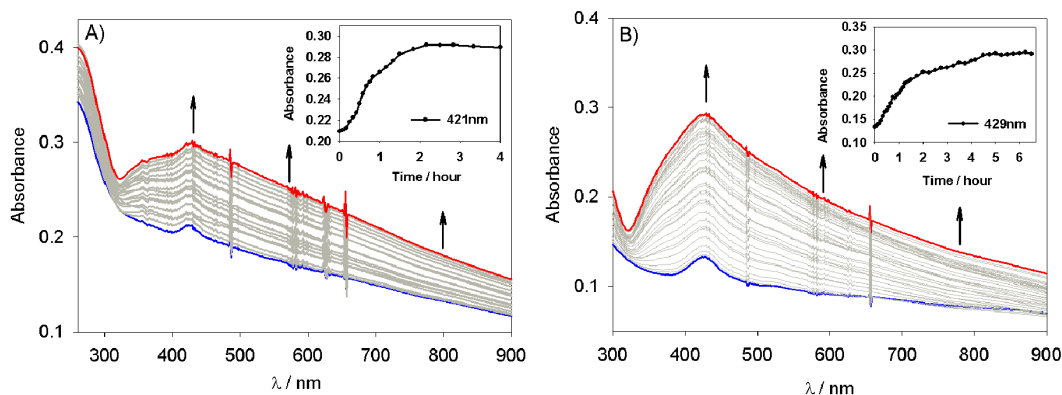


Figure 2. Change in the UV-Vis absorption spectra of a deaerated aqueous solution of $8.0 \times 10^{-5} \text{ mol}\cdot\text{L}^{-1}$ Ag_2SO_4 and $0.13 \text{ mol}\cdot\text{L}^{-1}$ propan-2-ol containing a slide of quartz modified with (A) **poly- V_6O_{13} -ZnOEP**, (B) **poly- V_6O_{13} - $\text{H}_2\text{T}_2\text{P}$** film under illumination. Inset: plot of the absorbance at (A) $\lambda = 421$ and (B) $\lambda = 429$ nm *versus* the time of irradiation.

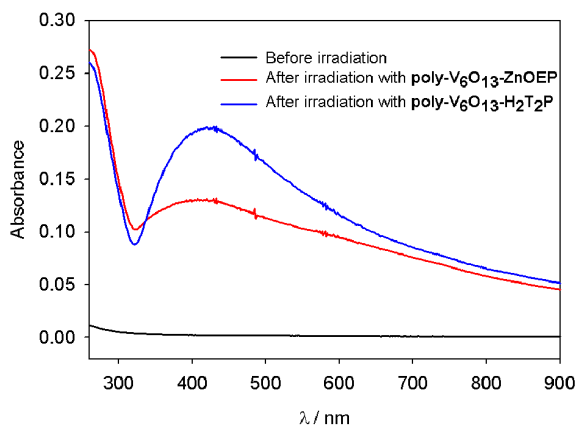
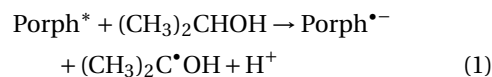


Figure 3. UV-Vis absorption spectra of the silver nanoparticles solution before and after the photocatalysis using the **poly- V_6O_{13} -ZnOEP** (red curve) or the **poly- V_6O_{13} - $\text{H}_2\text{T}_2\text{P}$** (blue curve) films.

lowed by the cascade electron transfer via the pyridinium to the POM subunit $\{\text{V}_6\text{O}_{13}\}^{2-}$ giving the reduced $\{\text{V}_6\text{O}_{13}\}^{3-}$. Then, $\{\text{V}_6\text{O}_{13}\}^{3-}$ can in turn reduce silver ions. A complexation step between alcohol radical and silver ions can initiate the formation of silver clusters (reactions (4)–(7)) before a thermodynamically possible direct reduction with the reduced POM ($\{\text{V}_6\text{O}_{13}\}^{3-}$) or with the alcohol radical $(\text{CH}_3)_2\text{C}\cdot\text{OH}$ (when the nuclearity of initial silver aggregates is sufficient).

The photoreduction processes should involve the reduction of the excited porphyrin (Porph^*) by propan-2-ol leading to the formation of the reduced porphyrin ($\text{Porph}^{\bullet-}$) and the alcohol radical according to the global reaction (1):



This reaction is thermodynamically favorable. Indeed, the reduction potentials of the excited porphyrins are evaluated according to the relation:

$$E(\text{Porph}^*/\text{Porph}^{\bullet-}) = E(\text{Porph}/\text{Porph}^{\bullet-}) + E_{\text{S}_0 \rightarrow \text{S}_1} \quad (2)$$

where $E(\text{Porph}/\text{Porph}^{\bullet-})$ is the first reduction potential of the porphyrin and $E_{\text{S}_0 \rightarrow \text{S}_1}$ corresponds to the energy of the lowest electronic transition determined from the absorbance spectrum.

The calculated $E(\text{Porph}^*/\text{Porph}^{\bullet-})$ values are higher than the reported values for $(\text{CH}_3)_2\text{C}\cdot\text{OH}/(\text{CH}_3)_2\text{CHOH}$ ($E = 0.80$ V versus NHE [37]).

The second mechanism (Figure 6B) corresponds to a direct intramolecular electron transfer from the excited porphyrins to polyoxovanadate via the reduction of the pyridinium subunit which acts as relay of electron followed by the reduction of silver ions by $\{\text{V}_6\text{O}_{13}\}^{3-}$. A fast intramolecular electron transfer agrees with fluorescence quenching of the films observed and is also thermodynamically favorable.

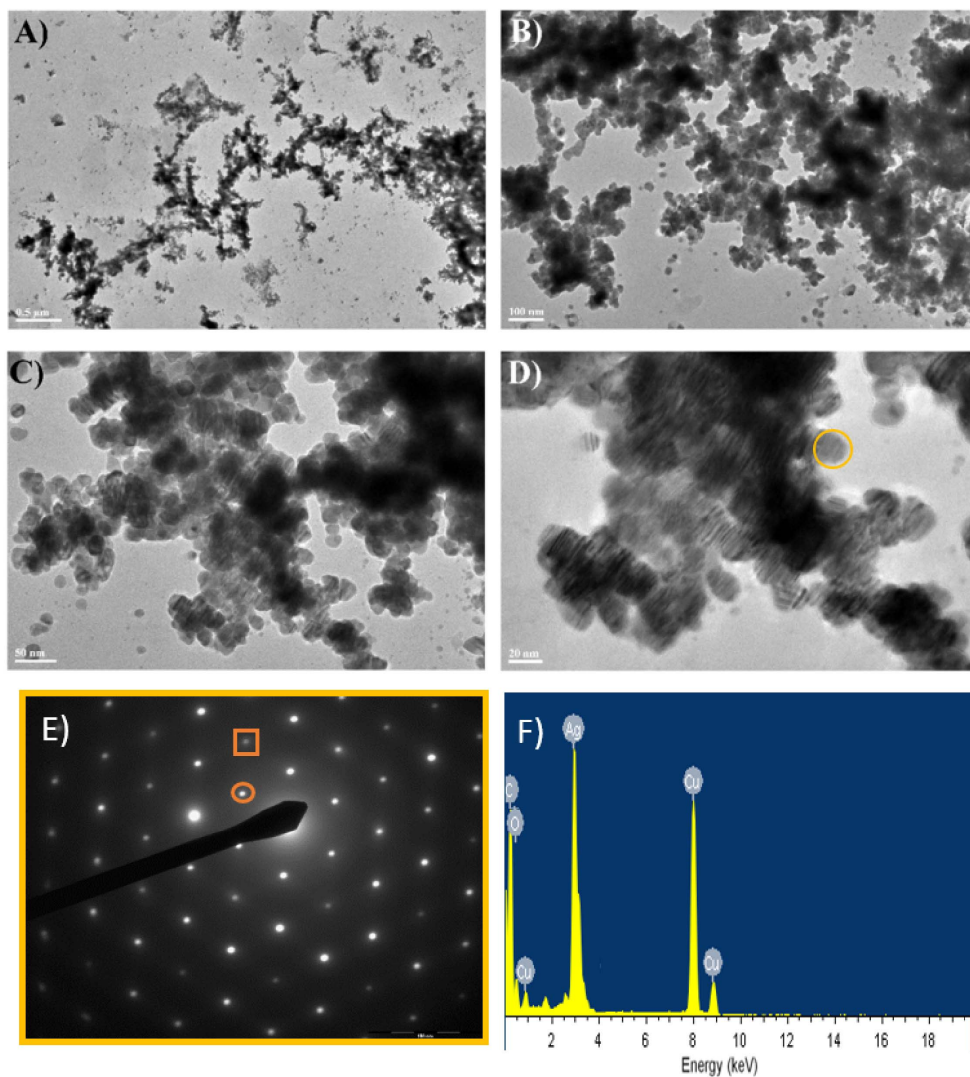


Figure 4. (A–D) TEM images of the silver nanoparticles obtained with the **poly-V₆O₁₃-ZnOEP** film in deaerated solution of $8.0 \times 10^{-5} \text{ mol} \cdot \text{L}^{-1} \text{ Ag}_2\text{SO}_4$. (E) Selected-area electron diffraction pattern of the silver nanoparticles. The inner spots (circled) corresponded to the formally forbidden $1/3 \{422\}$ reflections. The second spots (squared) could be indexed to the $\{220\}$ reflections. (F) EDS spectrum showing the presence of Ag in the sample.

Indeed, the reduction potentials of the excited porphyrins are evaluated according to the relation:

$$E(\text{Porph}^{+\bullet}/\text{Porph}^*) = E(\text{Porph}^{+\bullet}/\text{Porph}) - E_{S_0 \rightarrow S_1} \quad (3)$$

where $E(\text{Porph}^{+\bullet}/\text{Porph})$ is the first oxidation potential of the porphyrin and $E_{S_0 \rightarrow S_1}$ corresponds to the energy of the lowest electronic transition determined from the absorbance spectrum.

It should be mentioned that in the two proposed mechanisms, the simple consideration of the redox potential of the radical alcohol $(\text{CH}_3)_2\text{C}^{\bullet}\text{OH}$, the reduced porphyrin or the reduced $\{\text{V}_6\text{O}_{13}\}^{3-}$ does not allow to explain the subsequent photoreduction of Ag^+ ions. Indeed, the redox potential of the $(\text{Ag}^+/\text{Ag}_1)$ couple is too low ($E^\circ = -1.75 \text{ V}$ versus NHE [38]) to allow the direct reduction of Ag^+ to

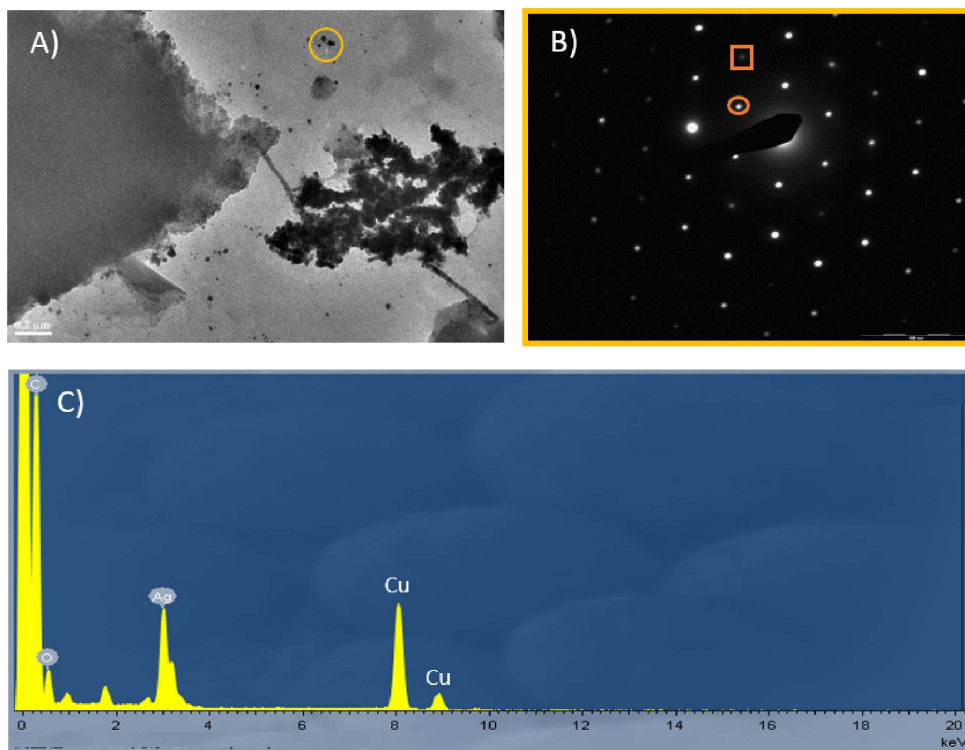
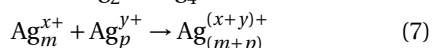
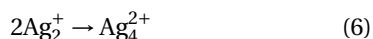
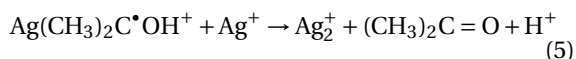
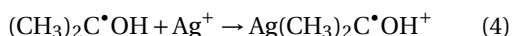


Figure 5. (A) TEM images of the silver nanomaterials obtained with the **poly-V₆O₁₃-H₂T₂P** film in deaerated solution of $8.0 \times 10^{-5} \text{ mol} \cdot \text{L}^{-1} \text{ Ag}_2\text{SO}_4$. (B) Selected-area electron diffraction pattern of the silver nanoparticles. The inner spots (circled) corresponded to the formally forbidden $1/3 \{422\}$ reflections. The second spots (squared) could be indexed to the $\{220\}$ reflections. (C) EDS spectrum showing the presence of Ag in the sample.

a single Ag_1 atom either by the reduced porphyrin ($E(\text{H}_2\text{T}_2\text{P}^*/\text{H}_2\text{T}_2\text{P}^{\bullet}) = 1.60 \text{ V}$ versus NHE) or the reduced $\{\text{V}_6\text{O}_{13}\}^{3-}$ ($E(\{\text{V}_6\text{O}_{13}\}^{2-}/\{\text{V}_6\text{O}_{13}\}^{3-}) = -0.58 \text{ V}$ versus NHE).

Referring to radiolytic studies, the reduction of the Ag^+ might be enabled by a complexation step between alcohol radical and silver ions that initiates the formation of silver clusters (4)–(7) [13,38,39]:



Another reasonable explanation is the formation of Ag_1^0 by reaction between Ag^+ and the alcohol radical $(\text{CH}_3)_2\text{C}^{\bullet}\text{OH}$ even if the potential ($E((\text{CH}_3)_2\text{CO}/(\text{CH}_3)_2\text{C}^{\bullet}\text{OH}) = -1.71 \text{ V}$ versus

NHE [40]) is slightly higher than the one the couple Ag^+/Ag_1 . This process cannot be excluded.

Finally, as the redox potential of the silver cluster, $E(\text{Ag}^{n+}/\text{Ag}_n)$, increases with the nuclearity n , the direct reduction of large clusters by the reduced porphyrin or the alcohol radical becomes thermodynamically feasible.

Note that the absence of reduced polyoxovanadate at the end of the reaction is in favor of the mechanism (B). It can be explained by an intramolecular back electron transfer between the reduced $\{\text{Py}^+ - \text{V}_6\text{O}_{13}^{3-} - \text{Py}\}$ and the porphyrins oxidized $\text{Porph}^{+\bullet}$ which is thermodynamically favorable.

To justify this electron transfer in the case of the mechanism B (Figure 6B), we can calculate the $\Delta_r G$ of this process using the Rehm–Weller equation: $\Delta G = E(\text{Porph}^{+\bullet}/\text{Porph}) - E(\text{POM}/\text{POMred}) - E_{\text{S0-S1}}$ where $E(\text{Porph}^{+\bullet}/\text{Porph})$ corresponds to

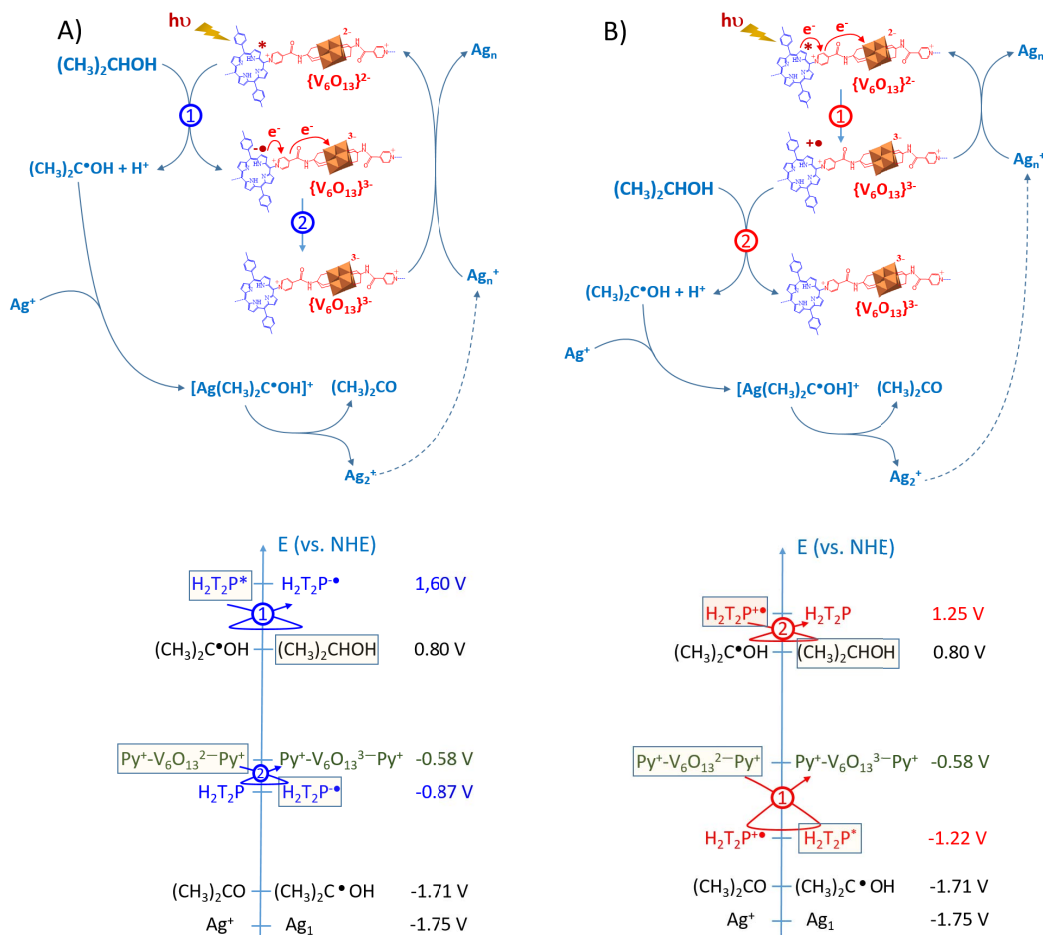


Figure 6. (A) and (B) Two possible mechanisms for the photoreduction of silver ions by the use of the **poly- V_6O_{13} - H_2T_2P** copolymer. Similar mechanism can be proposed for **poly- V_6O_{13} - $ZnOEP$** . Bottom: scale of apparent standard redox potentials of couples involved in this mechanism in the case of **H_2T_2P** . **ZnOEP** gives similar tendencies. Note that the reduction of the pyridinium group is achieved at a redox potential very close to that of the reduction of $\{V_6O_{13}\}$.

the first oxidation potential of the porphyrin ($E(\text{Porph}^{+\bullet}/\text{Porph}) = +1.25$ V versus NHE for H_2T_2P) and $E(\text{POM}/\text{POM}_{\text{red}})$ corresponds to the first reduction potential of the POM ($E(\{V_6O_{13}\}^{2-}/\{V_6O_{13}\}^{3-}) = -0.58$ V versus NHE) [27]. $E_{S_0-S_1}$ corresponds to the energy of the lowest electronic transition of the porphyrin estimated from its absorbance spectrum in solution. This value leads to negative ΔG (-61.5 $\text{kJ}\cdot\text{mol}^{-1}$), indicating that the electron transfers between the excited porphyrins and the POMs subunit $\{V_6O_{13}\}^{2-}$ are thermodynamically possible. These electronic transfers lead to oxidized porphyrins ($\text{porph}^{+\bullet}$) and reduced POMs (POM_{red} ,

namely $\{V_6O_{13}\}^{3-}$) via probably a relay including the reduction of the pyridium. Then, oxidized porphyrins $\text{porph}^{+\bullet}$ are regenerated by reaction with propan-2-ol which leads to the formation of alcohol radicals $(CH_3)_2C^{\bullet}OH$. This reaction is also really plausible, since the redox potential of the couple $(CH_3)_2C^{\bullet}OH/(CH_3)_2CHOH$ is estimated to 0.80 V versus NHE [37], that is lower than the oxidation potential of the porphyrin.

However, the potential of the couple $\{V_6O_{13}\}^{2-}/\{V_6O_{13}\}^{3-}$ is too high to permit the reduction of silver ions ($E(Ag^+/Ag_1) = -1.75$ V versus NHE), corresponding to the redox potential of a single $Ag(0)$

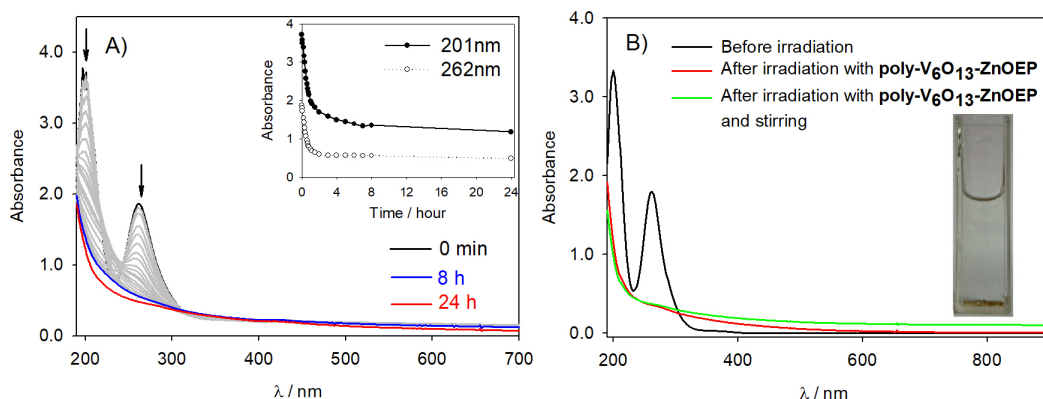


Figure 7. (A) Change in the UV-Vis absorption spectra of a deaerated aqueous solution of $1.6 \times 10^{-4} \text{ mol}\cdot\text{L}^{-1} \text{ H}_2\text{PtCl}_6$ and $0.13 \text{ mol}\cdot\text{L}^{-1}$ propan-2-ol containing a slide of quartz modified with **poly-V₆O₁₃-ZnOEP** film under illumination. Inset: plot of the intensity of the absorbance at $\lambda = 201$ and 262 nm versus the time of irradiation. (B) Spectrum of the platinum solution before and after photocatalysis. Inset: photo of the obtained solution in the cuvette after the irradiation.

atom, different from the one corresponding to metallic silver which is 0.799 V versus NHE. We can also exclude the possibility of a photoinduced electron transfer from the excited porphyrins to the silver ions, because the ΔG value of such transfer is positive and is estimated to $+77.2 \text{ kJ}\cdot\text{mol}^{-1}$.

2.3. Photocatalytic recovery of platinum

To extend the photocatalytic application, we have explored the photocatalysis of the reduction of $\text{Pt}^{\text{IV}}\text{Cl}_6^{2-}$ anions using the two covalent porphyrin-Lindqvist-type POM copolymers. The study is conducted under deaerated medium in the presence of $1.6 \times 10^{-4} \text{ mol}\cdot\text{L}^{-1} \text{ H}_2\text{Pt}^{\text{IV}}\text{Cl}_6$ (to keep the same concentration of metal ions) and $0.13 \text{ mol}\cdot\text{L}^{-1}$ propan-2-ol. Figure 7 illustrates the change in the UV-Vis absorption spectrum recorded during the visible light irradiation of a quartz slide covered with **poly-V₆O₁₃-ZnOEP**. The initial absorbance of $\text{Pt}^{\text{IV}}\text{Cl}_6^{2-}$ anions decreased during illumination and disappeared completely after 100 min, however, because the Pt nanoparticles do not possess plasmon band or other type of UV-visible absorbance, it is impossible to monitor the creation of the Pt nanoparticles from the UV-visible spectra.

After 24 h of illumination, a yellow sediment on the bottom of the cuvette is obtained, and after stirring, the absorbance in the whole domain increases.

The TEM micrographs confirm the formation of the Pt nanoparticles. The diameter of the basic nanoparticle subunit is $1.0\text{--}1.5 \text{ nm}$ which forms the closed-packed nanoparticles with a diameter of $10\text{--}20 \text{ nm}$ (Figure 8). The EDS spectrum in Figure 8E indicates the presence of merely pure Pt in the sample.

Figure 9 presents the absorption spectra of a deaerated aqueous solution containing $1.6 \times 10^{-4} \text{ mol}\cdot\text{L}^{-1} \text{ H}_2\text{PtCl}_6$ and $0.13 \text{ mol}\cdot\text{L}^{-1}$ propan-2-ol with **poly-V₆O₁₃-H₂T₂P** covered quartz slide during visible light irradiation. The initial absorbance of $\text{Pt}^{\text{IV}}\text{Cl}_6^{2-}$ anions disappeared completely after 110 min which is a little slower than for **poly-V₆O₁₃-ZnOEP**. After 24 h of illumination, we obtained a uniform and faint yellow solution which is different than the sediment obtained when using **poly-V₆O₁₃-H₂T₂P**. The TEM micrographs of the obtained Pt nanostructures are presented in Figure 10. The Pt nanoparticles showed again closed-packed spherical structure similar to the ones obtained using **poly-V₆O₁₃-ZnOEP** film. Nevertheless, such structures are also mixed with large nanosheets. The obtained Pt nanomaterial is in this case inhomogeneous in size and shape. The EDS spectrum in Figure 10E shows the presence of Pt nanoparticles in the sample.

After almost 3 h for **poly-V₆O₁₃-ZnOEP** and 4 h for **poly-V₆O₁₃-H₂T₂P** of visible light irradiation, the absorption spectrum does not evolve anymore which indicates the end of the reaction. The duration of the photocatalytic reduction is longer in comparison

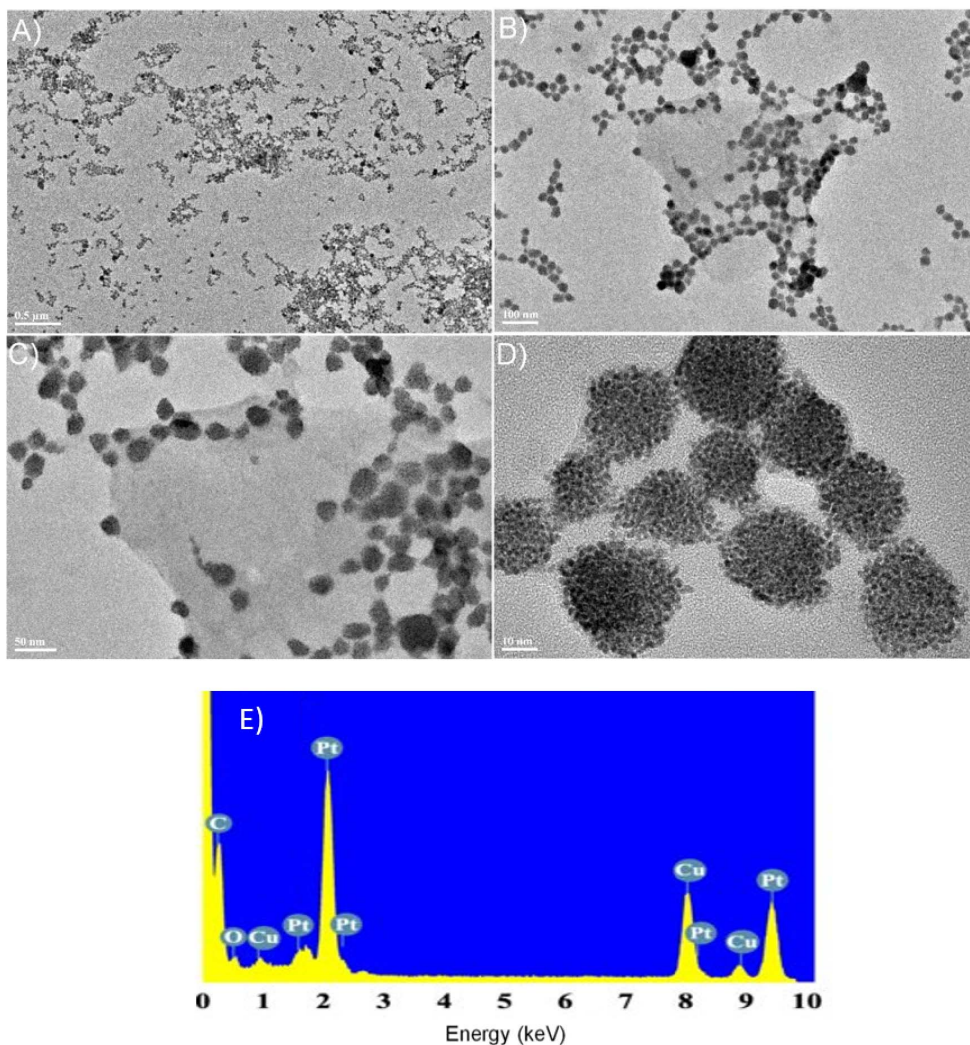


Figure 8. (A–D) TEM images of the platinum nanomaterial obtained with the **poly-V₆O₁₃-ZnOEP** in a deaerated solution of $1.6 \times 10^{-4} \text{ mol}\cdot\text{L}^{-1} \text{ H}_2\text{PtCl}_6$. (E) EDS spectrum showing the presence of Pt in the sample.

to the silver recovery which can be explained by the number of electron implied: 4 for the Pt(IV) *versus* 1 in the case of the Ag(I).

We assume that the mechanism for the photocatalysis Pt(IV) is much more complicated than the one proposed for the reduction of Ag(I) ions probably due to the fact that 4 electrons must be transferred between the catalysts and the metallic ion. We will therefore not provide a mechanism in this present case although there is a good chance that the first step is similar to that of the reduction of Ag(I) ions,

that is the electron transfer from the excited porphyrin via the pyridinium to the polyoxovanadates (mechanism B).

Last but not least, the heterogeneous photocatalysis can also be repeated at least five times while keeping the same efficiency. Platinum ions are reduced quantitatively and no deposition at the surface of the slide was observed (as checked by AFM analysis, data not shown).

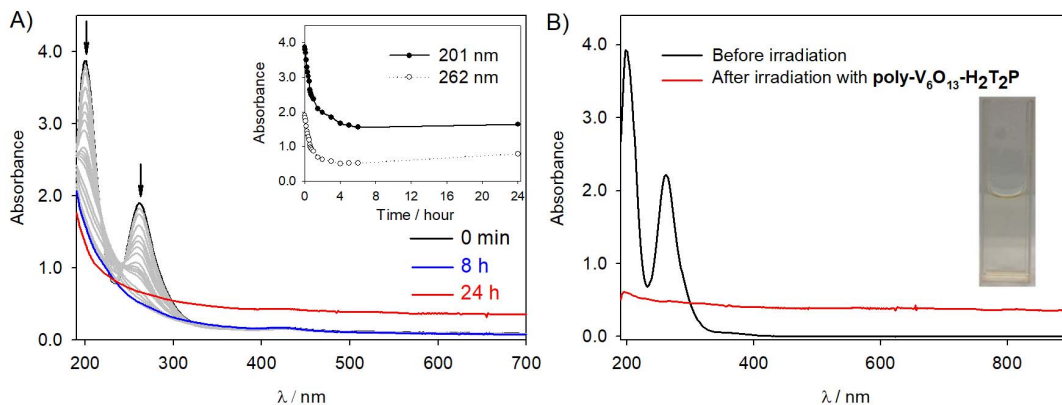


Figure 9. (A) Change in the UV-Vis absorption spectra of a deaerated aqueous solution of $1.6 \times 10^{-4} \text{ mol}\cdot\text{L}^{-1} \text{ H}_2\text{PtCl}_6$ and $0.13 \text{ mol}\cdot\text{L}^{-1}$ propan-2-ol containing a slide of quartz modified with **poly-V₆O₁₃-H₂T₂P** film under illumination. Inset: plot of the intensity of the absorbance at $\lambda = 201$ and 262 nm versus the time of irradiation. (B) Spectrum of the platinum solution before and after photocatalysis. Inset: photo of the obtained solution in the cuvette after the irradiation.

3. Conclusion

We demonstrated the efficiency of hybrid polyoxovanadate-porphyrin copolymers (**poly-V₆O₁₃-H₂T₂P** and **poly-V₆O₁₃-ZnOEP**) in the photocatalytic reduction of Ag(I) and Pt(IV) using visible light. Under ambient conditions, Ag_2SO_4 or $\text{H}_2\text{Pt}^{\text{IV}}\text{Cl}_6$ were reduced quantitatively at the interface between water and the copolymeric films without poisoning the surface. The heterogeneous catalysis can be repeated at least five times while keeping the same efficiency at room temperature and under mild reaction conditions.

This process verifies our starting hypothesis that the copolymerization of photosensitizers such as porphyrin and POMs yields photoactive materials that are useful for photocatalytic reduction in general. The obtained silver nanoparticles form aggregates while the Pt nanoparticles showed closed-packed spherical structures and some large sheets.

4. Experimental section

Most common laboratory chemicals were reagent grade, purchased from commercial sources and used without further purification.

The 5,15-ditolylporphyrin (**H₂T₂P**) was purchased from SAS PorphyChem[®] and zinc- β -octaethylporphyrin (**ZnOEP**) was purchased from

Sigma-Aldrich. Lindqvist-type polyoxovanadate $\text{TBA}_2[\text{V}_6\text{O}_{13}\{(\text{OCH}_2)_3\text{CNHCO}(4\text{-C}_5\text{H}_4\text{N})\}_2]$ (abbreviated **Py-V₆O₁₃-Py**) was synthesized according to the previous publications [24,41].

The corresponding copolymers **poly-Py-V₆O₁₃-Py-H₂T₂P** and **poly-Py-V₆O₁₃-Py-ZnOEP** were prepared as described previously [27].

Electropolymerization have been carried out under an argon atmosphere using a $0.1 \text{ mol}\cdot\text{L}^{-1}$ solution of $0.1 \text{ mol}\cdot\text{L}^{-1}$ TBAPF₆ in 1,2-C₂H₄Cl₂/CH₃CN (7/3) containing $0.25 \text{ mmol}\cdot\text{L}^{-1}$ of **ZnOEP** or **H₂T₂P** and $0.25 \text{ mmol}\cdot\text{L}^{-1}$ of **Py-V₆O₁₃-Py** (Scheme 1) between 0 and 1.6 V versus SCE. ITO electrodes, with a surface of 1 cm^2 , were used as working electrode. For each copolymer, the number of iterative scans (n) was 20. After electropolymerization, the modified working electrodes were washed with CH₃CN and then with CH₂Cl₂ in order to remove the monomers and the conducting salt present on the deposited films.

The electrochemically deposited **poly-V₆O₁₃-ZnOEP** or **poly-V₆O₁₃-H₂T₂P** films were dissolved and removed from ITO electrode with DMF. The operation is repeated six times. Subsequently, the DMF solution containing the copolymer was deposited on a quartz slide, and the DMF solvent was evaporated in air.

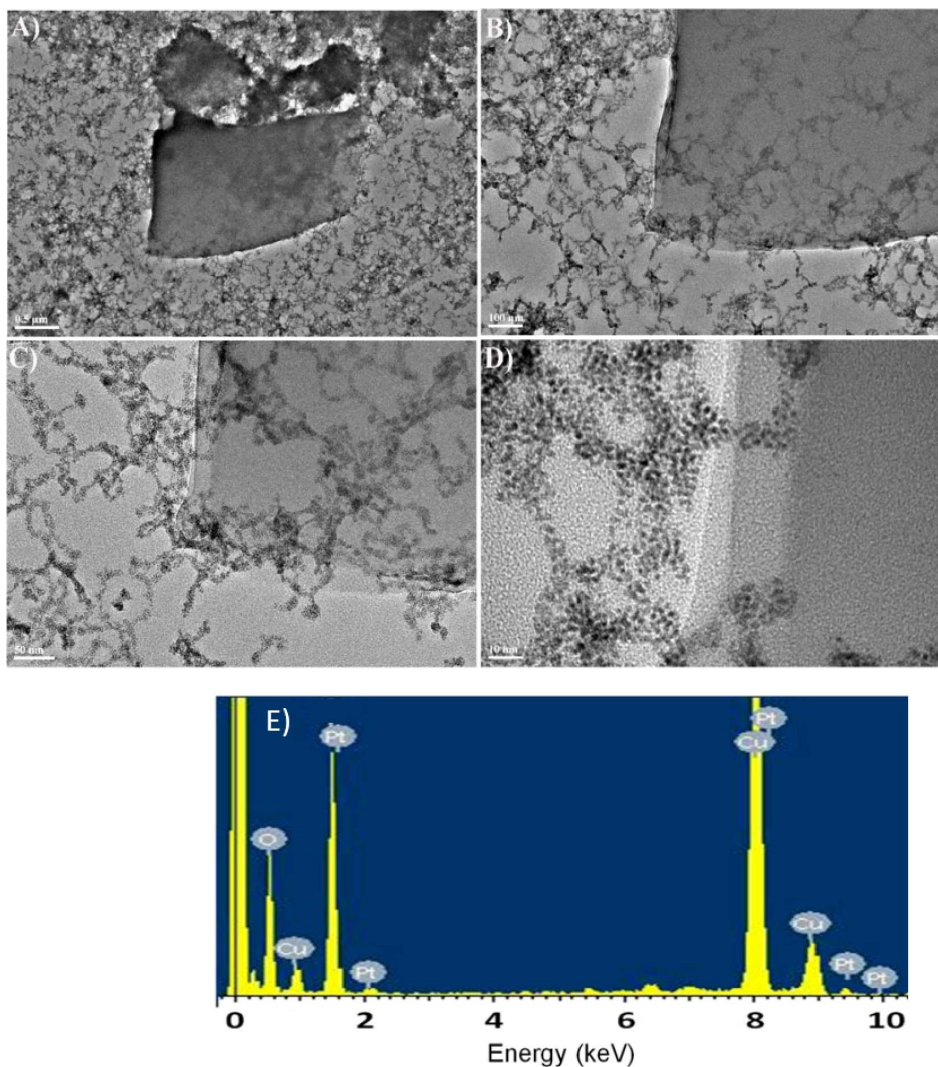


Figure 10. (A–D) TEM images of the platinum nanostructures obtained with the **poly-V₆O₁₃-H₂T₂P** film in a deaerated solution of $1.6 \times 10^{-4} \text{ mol}\cdot\text{L}^{-1} \text{ H}_2\text{PtCl}_6$. (E) EDS spectrum showing the presence of Pt in the sample.

Water was obtained by passing through a Milli-RO4 unit and subsequently through a Millipore Q water purification set.

Irradiation was performed using a 300 W Xe arc lamp (Lot, Quantum design) with intense focused output beams (50 mm beam diameter) equipped with a water cell filter to absorb the IR radiation. A spherical reflector collects the output from the rear of the lamp and focuses it on or near the arc for collection by the condenser. One condenser is positioned for compensating focal length change due to

dispersion and to produce a beam converging to the photochemical cell. According to the supplier, the irradiance of the lamp from 320 to 790 nm was around $50 \text{ mW}\cdot\text{m}^{-2}\cdot\text{nm}^{-1}$. The samples consisted of 4 mL of aqueous solutions with propan-2-ol, the quartz slide covered by the copolymer **Py-V₆O₁₃-Py-H₂T₂P** and **poly-Py-V₆O₁₃-Py-ZnOEP** and, Ag_2SO_4 or H_2PtCl_6 contained in a spectrophotometer quartz cell of 1 cm path length.

Deaerated solutions were obtained by bubbling with argon (Ar-U, from Air Liquide) before illumina-

tion. All experiments were carried out at room temperature.

We checked that the temperature of the solution did not increase by more than 1 degree during light illumination.

UV-Vis absorption spectra were recorded with a single beam Hewlett-Packard HP 8453 diode array spectrophotometer operated at a resolution of 2 nm.

Atomic force micrographs (AFM) measurements have been conducted directly on the ITO surfaces using a Veeco Dimension 3100 apparatus in the tapping mode under ambient conditions. Silicon cantilevers (Veeco probes) with a spring constant of 300 N/m and a resonance frequency in the range of 120–139 kHz have been used. The scanning rate was 1.0 Hz.

Transmission electronic microscopy (TEM) observations were performed with a JEOL 100 CXII TEM instrument operated at an accelerating voltage of 100 kV. Samples for TEM analysis were prepared by dropping the solution on carbon-coated copper TEM grids.

Conflicts of interest

The authors declare no conflicts of interest.

Acknowledgments

The authors are grateful to the University of Strasbourg and the CNRS for constant financial support. The authors also thank the Overseas Study Program of Guangzhou Elite Project (GEP) for the Ph.D. grant of Zhaohui Huo.

References

- [1] D.-L. Long, R. Tsunashima, L. Cronin, *Angew. Chem. Int. Ed. Engl.*, 2010, **49**, 1736-1758.
- [2] S. Anandan, S. Pitchumani, B. Muthuraaman, P. Maruthamuthu, *Sol. Energy Mater. Sol. Cells*, 2006, **90**, 1715-1720.
- [3] A. Mylonas, A. Hiskia, E. Papaconstantinou, *J. Mol. Catal. A Chem.*, 1996, **114**, 191-200.
- [4] Y. H. Kim, D. K. Lee, Y. S. Kang, *Colloids Surf. A: Physicochem. Eng. Asp.*, 2005, **273**, 257-258.
- [5] M. Reetz, W. Helbig, *J. Am. Chem. Soc.*, 1994, **116**, 7401-7402.
- [6] M. Starowicz, B. Stypuła, J. Banaś, *Electrochem. Commun.*, 2006, **8**, 227-230.
- [7] Y. Nagata, Y. Watanabe, S. Fujita, T. Dohmaru, S. Taniguchi, *J. Chem. Soc. Chem. Commun.*, 1992, **21**, 1620-1622.
- [8] T. Fujimoto, S. Y. Terauchi, H. Umehara, I. Kojima, W. Henderson, *Chem. Mater.*, 2001, **13**, 1057-1060.
- [9] J. Belloni, M. Mostafavi, H. Remita, J. L. Marignier, M. O. Delcourt, *New J. Chem.*, 1998, **11**, 1239-1255.
- [10] H. Yin, T. Yamamoto, Y. Wada, S. Yanagida, *Mater. Chem. Phys.*, 2004, **83**, 66-70.
- [11] B. Ohtani, M. Kakimoto, H. Miyadzu, S. Nishimoto, T. Kagiya, *J. Phys. Chem.*, 1988, **92**, 5773-5777.
- [12] A. Troupis, A. Hiskia, E. Papaconstantinou, *Appl. Catal. B: Environ.*, 2003, **42**, 305-315.
- [13] C. Costa-Coquelard, D. Schaming, I. Lampre, L. Ruhlmann, *Appl. Catal. B: Environ.*, 2008, **84**, 835-842.
- [14] C. Allain, D. Schaming, S. Sorgues, J.-P. Gisselbrecht, I. Lampre, L. Ruhlmann, B. Hasenknopf, *Dalton Trans.*, 2013, **42**, 2745-2754.
- [15] Y. Zhu, Y. Huang, Q. Li, D. Zang, J. Gu, Y. Tanf, Y. Wei, *Inorg. Chem.*, 2020, **59**, 2575-2583.
- [16] L. El Kahef, M. Gross, A. Giraudeau, *J. Chem. Soc. Chem. Commun.*, 1989, **49**, 963-963.
- [17] A. Giraudeau, L. Ruhlmann, L. El Kahef, M. Gross, *J. Am. Chem. Soc.*, 1996, **118**, 2969-2979.
- [18] L. Ruhlmann, S. Lobstein, M. Gross, A. Giraudeau, *J. Org. Chem.*, 1999, **64**, 1352-1355.
- [19] A. Giraudeau, S. Lobstein, L. Ruhlmann, D. Melamed, K. M. Barkigia, J. Fajer, *J. Porphyrins Phthalocyanines*, 2001, **05**, 793-797.
- [20] L. Ruhlmann, A. Giraudeau, *Chem. Commun.*, 1996, **17**, 2007-2008.
- [21] L. Ruhlmann, A. Giraudeau, *Eur. J. Inorg. Chem.*, 2001, 659-668.
- [22] D. Schaming, C. Allain, R. Farha, M. Goldmann, S. Lobstein, A. Giraudeau, B. Hasenknopf, L. Ruhlmann, *Langmuir*, 2010, **26**, 5101-5109.
- [23] S. Favette, B. Hasenknopf, J. Vaissermann, P. Gouzerh, C. Roux, *Chem. Commun.*, 2003, **21**, 2664-2665.
- [24] C. Allain, S. Favette, L. Chamoreau, J. Vaissermann, L. Ruhlmann, B. Hasenknopf, *Eur. J. Inorg. Chem.*, 2008, 3433-3441.
- [25] L. Ruhlmann, A. Schulz, A. Giraudeau, C. Messerschmidt, J.-H. Fuhrop, *J. Am. Chem. Soc.*, 1999, **121**, 6664-6667.
- [26] L. Ruhlmann, J. Hao, Z. Ping, A. Giraudeau, *J. Electroanal. Chem.*, 2008, **621**, 22-30.
- [27] Z. Huo, I. Azcarate, R. Farha, M. Goldmann, H. Xu, B. Hasenknopf, E. Lacôte, L. Ruhlmann, *J. Solid State Electrochem.*, 2015, **19**, 2611-2621.
- [28] A. Giraudeau, D. Schaming, J. Hao, R. Farha, M. Goldmann, L. Ruhlmann, *J. Electroanal. Chem.*, 2010, **638**, 70-75.
- [29] D. Schaming, I. Ahmed, J. Hao, V. Alain-Rizzo, R. Farha, M. Goldmann, H. Xu, A. Giraudeau, P. Audebert, L. Ruhlmann, *Electrochim. Acta*, 2011, **56**, 10454-10463.
- [30] J. L. Sessler, M. R. Johnson, S. E. Creager, J. C. Fettingner, J. Ibers, *J. Am. Chem. Soc.*, 1990, **112**, 9310-9329.
- [31] D. Schaming, Y. Xia, R. Thouvenot, L. Ruhlmann, *Chem. Eur. J.*, 2013, **19**, 1712-1719.
- [32] I. Ahmed, X. Wang, N. Boualili, H. Xu, R. Farha, M. Goldmann, L. Ruhlmann, *Appl. Catal. A: Gen.*, 2012, **447-448**, 89-99.

- [33] R. Jin, Y. Cao, C. A. Mirkin, K. L. Kelly, G. C. Schatz, J. G. Zheng, *Science*, 2001, **294**, 1901-1903.
- [34] Y. Sun, Y. Xia, *Adv. Mater.*, 2003, **15**, 695-699.
- [35] V. Germain, J. Li, D. Ingert, Z. L. Wang, M. P. Pileni, *J. Phys. Chem. B*, 2003, **107**, 8717-8720.
- [36] B. Rodríguez-Gonzalez, I. Pastoriza-Santos, L. M. Liz-Marzan, *J. Phys. Chem. B*, 2006, **110**, 11796-11799.
- [37] E. Gachard, H. Remita, J. Khatouri, B. Keita, L. Nadjo, J. Beloni, *New J. Chem.*, 1998, **22**, 1257-1265.
- [38] A. Henglein, *Ber. Bunsenges. Phys. Chem.*, 1977, **81**, 556-561.
- [39] R. Tausch-Treml, A. Henglein, J. Lilie, *Ber. Bunsenges. Phys. Chem.*, 1978, **82**, 1335-1343.
- [40] H. A. Schwarz, R. W. Dodson, *J. Phys. Chem.*, 1989, **93**, 409-414.
- [41] J. W. Han, K. I. Hardcastle, C. L. Hill, *Eur. J. Inorg. Chem.*, 2006, 2598-2603.



MAPYRO: the French Fellowship of the Pyrrolic Macrocyclic Ring / *MAPYRO: la communauté française des macrocycles pyrroliques*

Zinc phthalocyanine absorbance in the near-infrared with application for transparent and colorless dye-sensitized solar cells

Thibaut Baron^a, Ximena Zarate^{*,b}, Yoan Hidalgo-Rosa^{*,c}, Michael Zambrano-Angulo^d, Kevin Mall-Haidaraly^a, Ricardo Pino-Rios^d, Yann Pellegrin^{*,a}, Fabrice Odobel^{*,a} and Gloria Cárdenas-Jirón^{*,d}

^a Université de Nantes, CNRS, CEISAM UMR 6230, F-44000 Nantes, France

^b Instituto de Ciencias Químicas Aplicadas, Facultad de Ingeniería, Universidad Autónoma de Chile, Santiago, Chile

^c Doctorado en Fisicoquímica Molecular, Universidad Andres Bello, Santiago, Chile

^d Laboratory of Theoretical Chemistry, Faculty of Chemistry and Biology, University of Santiago de Chile (USACH), Santiago, Chile

E-mails: thibaut.baron@univ-nantes.fr (T. Baron), ximena.zarate@uautonoma.cl (X. Zarate), yoanhrj@gmail.com (Y. Hidalgo-Rosa), michael.zambrano@usach.cl (M. Zambrano-Angulo), kevin.mallhaidaraly@gmail.com (K. Mall-Haidaraly), ricardo.pino@usach.cl (R. Pino-Rios), Yann.Pellegrin@univ-nantes.fr (Y. Pellegrin), Fabrice.Odobel@univ-nantes.fr (F. Odobel), gloria.cardenas@usach.cl (G. Cárdenas-Jirón)

Abstract. Transparent and colorless solar cells are attractive new photovoltaic devices as they could bring new opportunities to harness sunlight energy and particularly for their integration in windows. In this work, a new zinc phthalocyanine was synthesized and investigated as sensitizer in dye-sensitized solar cell (DSSC) for this purpose. The zinc phthalocyanine features a benzoic acid anchoring group and six thio(4-tertbutylphenyl) substituents in α position of the phthalocyanine. The dye was characterized by absorption and emission spectroscopy and by electrochemistry. The physicochemical properties show that the dye fulfills the criteria for such an application. A detailed computational study indicates that the electronic communication with TiO₂ conduction is weak owing to the absence of overlapping of the wavefunctions of the dye with those of the TiO₂ semiconductor. The photovoltaic performances of the zinc phthalocyanine were measured in TiO₂-based DSSC that revealed inefficient electron injection, which certainly can be explained by the weak electronic coupling of the dye with TiO₂ that limits electron injection efficiency. A strategy is proposed to make better-performing sensitizers.

Keywords. Phthalocyanine, Solar cell, Solar energy, Dye sensitized solar cell, Near infrared.

Available online 15th October 2021

* Corresponding authors.

1. Introduction

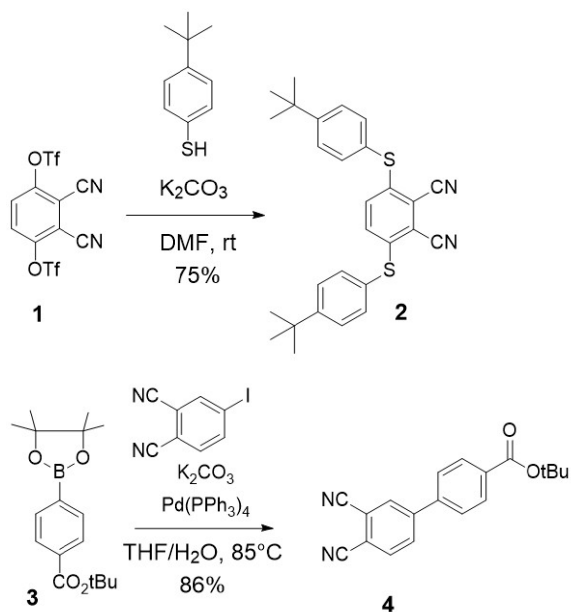
Finding sustainable and environmentally friendly strategies to generate energy represents a huge challenge for modern society because of the inevitable depletion of widely used fossil fuels and the pollution they generate. Solar energy, and more specifically photovoltaic (PV), appears like a perfect alternative to non-sustainable fossil fuels [1]. An original approach, consisting in developing transparent and colorless solar panels, represents a “disruptive technology” because it opens new applications. For examples, transparent solar cells would be suitable for integration in Building-Integrated Photovoltaics (BIPV) [2] such as in windows of buildings, but also for electric vehicles, and self-powered greenhouses [3–5]. However, the integration of PV into building windows require a visible light transmittance higher than 55% for good visual perception [6] and the absence of color is necessary in order to provide good aesthetics.

Over the years, the development of Transparent PhotoVoltaics (TPV) has grown considerably [7]. However, such devices are mainly absorbing visible light and the transparency is mostly modulated by the thickness of the active layer or by the introduction of microscopic holes in the film [8]. Another approach consists in the transmission of light in the visible region through selective absorption of UV (<380 nm) and NIR (>700 nm) light. Some inorganic [9] and organic [10] systems were investigated but although very high Average Visible Transmittance (AVT) [11] values were achieved, the technology requires further improvement to increase the final efficiency.

Mainly popularized by O'Regan and Grätzel in 1991 [12], Dye-Sensitized Solar Cells (DSSCs) represent a relevant candidate for highly transparent and neutral-colored photovoltaic devices. First, they are potentially cheap to produce. Second, their efficiencies are less dependent on the light incidence angle and intensity, and particularly they outperform classical inorganic-based cells under diffuse irradiance [13,14]. Third, the device is based on a thin layer of TiO₂ nanoparticles sensitized by light-harvesting dyes, meaning that DSSCs can virtually absorb within any desired spectral region, depending mainly only on the selected dye [15]. Historically, dyes employed on DSSCs are based on

Ru(II)-polypyridyl complexes [16], zinc porphyrins [17], or even metal-free organic dyes [18,19] reaching an efficiency higher than 14% [20], but all these dyes absorb in the visible range and the corresponding DSSCs exhibit an intense coloration. On the other hand, using dyes which absorb only NIR radiations is a tantalizing option to prepare efficient, transparent and colorless DSSCs, given the high photon flux of the solar spectra in the 700–1000 nm range. Finally, in DSSC, both the photoanode and the counter electrode can be transparent allowing illumination from both sides and are therefore compatible with see-through photovoltaics.

The first example of transparent DSSC for see-through photovoltaic windows was reported by Zhang *et al.* in 2014 and presents the combination of UV and NIR dyes that reach a final power conversion efficiency (PCE) of 3.66% with an AVT higher than 60% [21]. Very recently Sauvage and co-workers [22], reported a transparent DSSC with a cyanine dye (coded VG20) which exhibits a PCE of 3.1% with an impressive AVT of 76%. Among the NIR absorbing dyes in DSSC, such as cyanines [23–25] and squaraines [26–28], phthalocyanine derivatives represent suitable candidates due to an intense absorption close to NIR region of the solar spectrum, a high molar extinction coefficient and a high fluorescence quantum yield, a great stability and proved efficiency in DSSCs [29]. This is especially true since the seminal work of Ikeuchi *et al.* when highly bulky groups were tethered to the macrocycle in order to limit deleterious aggregation, leading to a very significant jump in the photoconversion efficiencies, reaching 6% [30]. Phthalocyanines are highly stable tetrapyrrolic macroheterocycles constituted by four isoindole units. Their properties can be easily tuned by the nature of the substituent linked to the macrocycle unit and by the atom or ion coordinated in the macrocycle. However, most phthalocyanine derivatives present an intense Q band centered around 650–700 nm [31]. In order to shift this transition further into the NIR, grafting electron-rich substituents in the α -positions of the Pc macrocycle has proven to be a successful strategy. Indeed, the addition of S-Aryl unit in α -positions induce a significant redshift of the absorption band (of about 80 nm) compared to previous Pcs substituted in β -position with O-Aryls substituent [32,33]. It thus appears relevant to graft



Scheme 1. Synthesis of phthalonitrile **2** and **4**.

very bulky groups *via* a thioether linkage on the Pc macrocycle in order to both redshift the absorption and prevent dye aggregation on TiO₂'s surface to some extent [34].

In this report, we have designed and synthesized a new phthalocyanine derivative **KMH63** containing six thiophenyl-tert-butyl units in α -positions of the macrocyclic and one carboxylic acid as anchoring group directly connected to the core by a phenyl spacer (Scheme 2). Our main finding is that **KMH63** displays adequate optical and electrochemical properties to design colorless transparent photoelectrodes. However, the performances of the DSSC remain weak because of a weak electron injection driving force that can be solved by changing the spacer linking the anchoring group and the phthalocyanine unit.

2. Synthesis

The synthesis of **KMH63** requires the two key phthalonitriles **2** [35] and **4** [36] as reagents (Scheme 1). 3,6-bis(thiophenyl-tert-butyl)phthalonitrile **2** was prepared in 75% yield by nucleophilic aromatic substitution of phthalonitrile-3,6-ditriflate **1** by 4-tertbutylthiophenol [37].

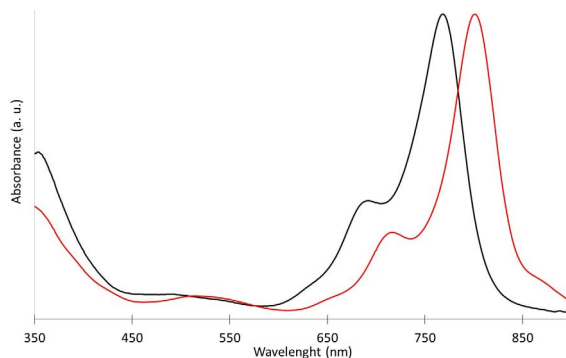


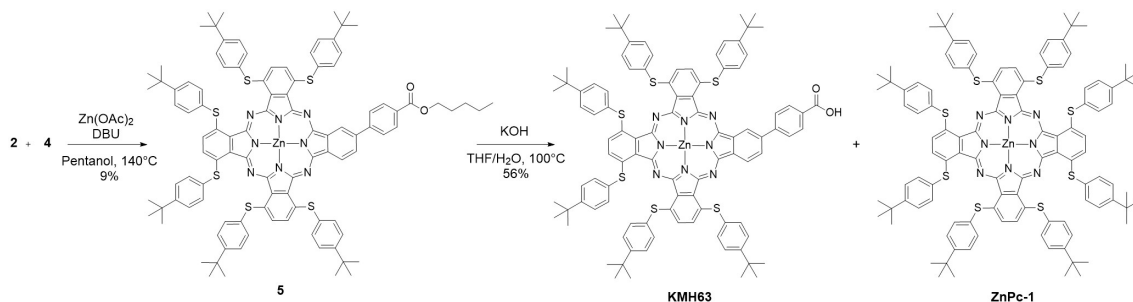
Figure 1. Normalized absorption of **KMH63** (black) and **Zn-Pc-1** (red) recorded in dichloromethane solution.

The second phthalonitrile **4** was synthesized according to a Suzuki–Miyaura cross-coupling reaction between the boronic ester **3** [38] with iodophthalonitrile with a good yield of 86%. Following the conditions described by Giribabu *et al.* [39], using zinc(II) as template and 1,8-diazabicyclo[5.4.0]undec-7-ene (DBU) as a base, the cross-condensation of both phthalonitrile derivatives **2** and **4** in pentanol afforded the ester-protected phthalocyanine **5** in 9% yield after purification by preparative thin layer chromatography (Scheme 2). ¹H NMR spectrum and mass spectrometry analysis revealed that the tert-butyl ester was transesterified by pentanol during this reaction. However, this side reaction does not have any consequence since the pentyl ester was saponified by potassium hydroxide to lead to the desired product **KMH63** in 56% yield (Scheme 2).

3. Electronic absorption and emission properties

The absorption and emission spectra of **KMH63** were recorded in dichloromethane solution at room temperature (Figures 1 and S5). The optical data including wavelengths of maximal absorption (λ_{abs}), extinction coefficients (ϵ), wavelength of maximal emission (λ_{em}) and zero-zero energy level of the lowest singlet excited state (E_{00}), are collected in Table 1.

The absorption spectrum of **KMH63** displays the usual spectral signatures of zinc phthalocyanine derivatives [31]. It is dominated by an intense and thin Q band, corresponding to π - π transitions, at 768 nm and a lower intensity Soret band at 358 nm.



Scheme 2. Synthesis of zinc phthalocyanine **KMH63**.

Table 1. Wavelength of maximal absorption (λ_{abs}) with extinction coefficient (ϵ), wavelength of maximal emission (λ_{em}) recorded at room temperature in dichloromethane and zero-zero energy level of the lowest excited state (E_{00})

Dye	$\lambda_{\text{abs}}/\text{nm}$ ($\epsilon \times 10^{-3}/\text{M}^{-1}\cdot\text{cm}^{-1}$)	$\lambda_{\text{em}}/\text{nm}$	E_{00}/eV
KMH63	358 (40800); 696 (28700); 768 (75500)	787	1.59

Weaker Q band at 696 nm is also observed and can be attributed to vibronic overtone [40]. As expected, the presence of six S-Aryl units in α -position of the macrocyclic system allows a significant redshift of the absorption band compared to classical unsubstituted or O-Aryls substituted zinc phthalocyanines. Importantly, there is a large wavelength region where the phthalocyanine derivative does not absorb (between 450 and 600 nm), which is favorable to provide transparency in the visible region. Interestingly, the spectrum of the parent octa α -substituted S-Aryles zinc phthalocyanine is even more shifted to the red region [33], with maximum absorption wavelength around 800 nm, underscoring that the removal of only two aryl thioether units on the phthalocyanine has a significant effect on the electronic properties (Figure 1).

KMH63 is a fluorescent dye with an emission maximum wavelength located at 787 nm enabling us to calculate the E_{00} , which was estimated to 1.59 eV (Figure S5 and Table 1).

Then, the absorption spectrum of the phthalocyanine **KMH63** was recorded on thin TiO_2 film with several concentrations of chenodeoxycholic acid (CDCA) in the dyeing bath (Figures 2 and S1). On TiO_2 surface, the dye clearly exhibits a significant broadening and a hypsochromic shift of the Q band, which is assigned to the formation of H-type

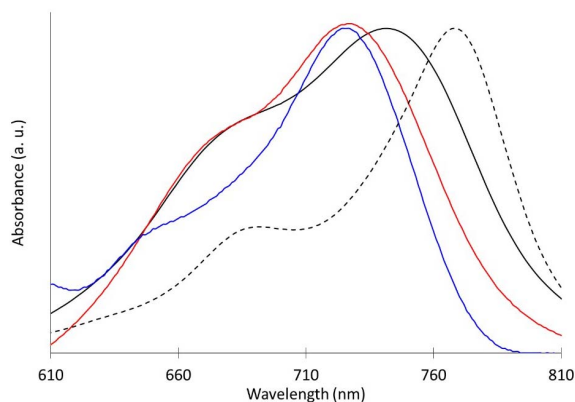


Figure 2. Normalized absorption spectra of **KMH63** on 2 μm thick TiO_2 nanocrystalline film 0 mM (black), 5 mM (red) and 20 mM (blue) of CDCA along that in solution (black dotted line).

aggregates. In order to support this hypothesis, controlled amounts of anti-aggregate CDCA were added during the chemisorption step. Indeed, the presence of CDCA (20 mM) reduces the intensity of the shoulder at 675 nm band and of the bathochromic shift indicating a diminution of the aggregation process. Lower quantities of CDCA (5 mM) proved to be less efficient to overcome this problem.

Table 2. Redox potentials recorded by cyclic voltammetry at room temperature in dimethylformamide solution with Bu₄NPF₆ (0.1 M) as supported electrolyte and referenced versus saturated calomel electrode (SCE)

Dye	$E(S^+/S)$ V <i>vs.</i> SCE	$E(S/S^-)$ V <i>vs.</i> SCE	$E(S^+/S^*)$ V <i>vs.</i> SCE	ΔG_{inj}° (eV)	ΔG_{reg}° (eV)
KMH63	0.63	-0.77	-0.96	-0.26	-0.43

Calculated Gibbs free energies for electron injection (ΔG_{inj}°) and dye regeneration (ΔG_{reg}°).

4. Electrochemical properties

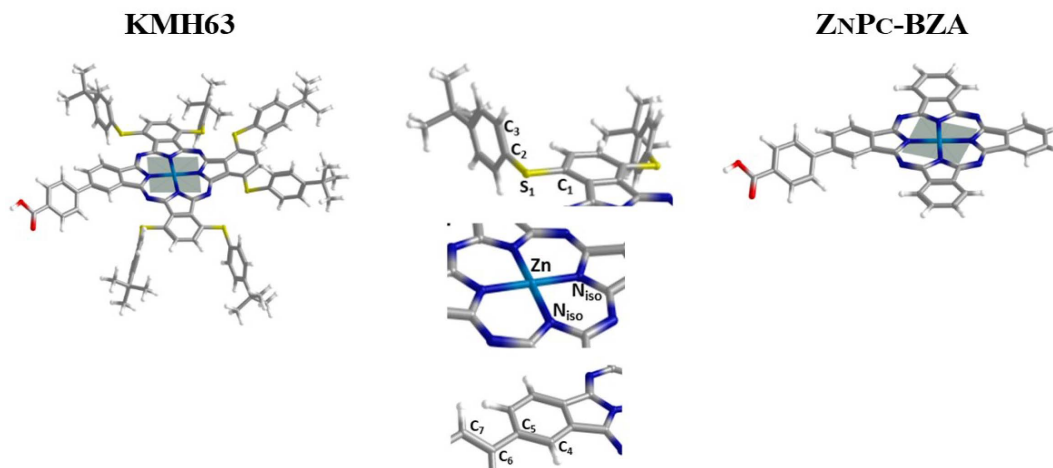
The new phthalocyanine **KMH63** was studied by cyclic voltammetry to determine its redox potentials and to calculate the hole injection (ΔG_{inj}°) and dye regeneration (ΔG_{reg}°) driving forces (Table 2). The cyclic voltammogram of **KMH63** is shown in Figure S4. **KMH63** exhibits a reversible one-electron oxidation wave at 0.63 V *vs.* SCE, corresponding to the formation of the radical cation on the phthalocyanine macrocycle. A reversible reduction wave is observed at -0.77 V, followed by an irreversible one at -1.17 V *vs.* SCE. The calculated oxidative potential of the singlet excited state of **KMH63** is not as negative (-0.96 V *vs.* SCE) as previously reported β -S-Ar or β -O-Ar-substituted zinc phthalocyanines [41], resulting in a moderate, though suitable ΔG_{inj}° . On the one hand, the oxidation potential of **KMH63** is much higher than that of the redox potential of I^-/I_3^- (0.2 V *vs.* SCE) thus affording a calculated ΔG_{reg}° value around -0.4 eV, suggesting a significant dye regeneration driving force with iodide. On the other hand, the injection driving force is significant to expect a good injection quantum yield, particularly if the electrolyte contains lithium cation to bend downward the conduction band.

5. Computational study

The UV-Vis absorption spectrum for **KMH63** was calculated in the solution phase using the optimized molecular geometry employing the time-dependent density functional theory (TDDFT) approach [42–46] at the M06/6-31G(d,p) level of theory. More details about the optimization method used are included in the supporting information. This functional (M06) [47] has been used by us in previous works with excellent results [48–50]. The electronic excitations were modeled as singlet–singlet vertical

transitions of the Franck–Condon type. We computed 30 excited states to cover the region of both the Q and B bands. We choose dichloromethane (CH₂Cl₂) as the solvent because the UV-Vis spectrum of **KMH63** was measured in that solvent. The solvent was simulated with the Conductor-like Polarizable Continuum Model (CPCM) [51,52] and a dielectric constant of 8.93. To understand the absorption bands, isosurfaces for the molecular orbitals (MOs) involved in the electronic transitions were built up, i.e. the highest occupied (HOMOs) and lowest unoccupied (LUMOs) MOs. In cases where the excited state is formed from several electronic transitions, we have preferred to calculate the natural transition orbitals (NTO) [53]. These ones have the advantage that all the transitions are considered and an account of the whole excited state is given. In order to get a better comprehension about the electronic absorption properties of **KMH63**, we compared our theoretical results with the absorption spectrum of Zn(II) phthalocyanine, where we have maintained the benzoic acid (BZA) in the β -position as in **KMH63**, because it is the moiety that interacts with the semiconductor (TiO₂). This system was coded **ZnPc-BZA** (Scheme 3). All the calculations related to the molecular geometry optimization, electronic absorption spectra and molecular orbitals were performed with the package Gaussian 09, rev.D.01 [54].

To determine the interaction between the dye and the semiconductor (TiO₂), systems were computed after grafting the dye on a TiO₂ anatase cluster model. This model was prepared from the anatase-phase (101) crystallographic structure and corresponds to a surface consisting of 40 titanium atoms, 82 oxygen atoms and four hydrogen atoms [Ti₄₀, O₈₂, H₄] saturating the oxygen dangling bonds. The geometry of the complex is partially optimized, where TiO₂ is frozen to retain the anatase-phase structure, and the dye with the anchoring group (-COOH)



Scheme 3. Optimized molecular structures of **KMH63** and **ZnPc-BZA** where the plane formed by Zn(II) and the four N atoms of the macrocycle is shown.

approaching to a titanium atom are fully optimized. The interaction between the fragments is monodentate meaning that one -O(OH) interacts with one titanium atom. The complex was optimized at the DFT level of theory with the D3 Grimme's dispersion correction using the Quantum ATK package [55]. All of the atoms were represented by a double- ζ -polarized (DZP) basis set, along with the PseudoDojo norm-conserving pseudopotential, employing the Perdew–Burke–Ernzerhof (GGA-PBE) [56,57] exchange-correlation functional. The interaction energy was calculated by using the following formula $\Delta E_{\text{int}} = E_{\text{dye-TiO}_2} - (E_{\text{TiO}_2} + E_{\text{dye}})$ and the fragments dye and TiO_2 were used with the optimized geometry obtained in the complex. The correction of the ΔE_{int} for the basis set superposition error was not calculated because of the size of the system dye- TiO_2 .

On the other hand, aromaticity has been assessed using three different criteria: the magnetic one [58] via the gauge independent atomic orbital (GIAO) method [59]. The module of magnetically induced current density [60] (MICD) have been plotted 1.0 a.u. above the molecular plane obtained by means of Quantum Theory of Atoms in Molecules (QTAIM) [61]. In addition, the popular nucleus independent chemical shift (NICS) and its z -component [62] (NICS_{zz}) have been measured in strategic positions, these indexes are especially reliable for π -aromaticity analysis [62–65] and allows quantifying the magnetic response due to ring

currents. These calculations were performed using Gaussian 09 in conjunction with AIMAll software [66] and MICD module planes were plotted using VisIt software [67].

Additionally, the delocalization criteria [68] have been applied using the recently proposed AV1245 index [69], specially designed for macrocycles such as porphyrinoids, whereas the multi-center index [70] (MCI) and para-delocalization index [71] (PDI) have been used to analyze the six-membered rings (6MR). Finally, the geometric criteria has been evaluated using the Harmonic Oscillator Model of Aromaticity [72] (HOMA), these indexes were calculated using the Multiwfn program [73].

The optimization of the ground-state geometries of **KMH63** and **ZnPc-BZA**, in general, successfully reproduced the geometrical parameters of these compounds. In both dyes, the average bond lengths between Zn (II) ions and the four isoindole nitrogen atoms are 1.991 Å. A good correlation was obtained for the Zn–N calculated bond lengths with other phthalocyanines reported, such as Zn(II) phthalocyanine and Zn(II)octa- β -methoxyphthalocyanine, whose average Zn–N bond lengths are 2.010 Å and 2.011 Å, respectively, computed at the BP86/def2-SVP+D3BJ level of theory [74]. Others studies also include reported theoretical values of the mean bond distances Zn–N of 2.012 Å for a family of dimers di-Zn(II)-pyrazinoporphyrazine-phthalocyanine complexes with different peripheral substituents (R), cal-

Table 3. Singlet→Singlet absorption vertical transitions computed at the M06/6-31G(d,p) theoretical level considering the solvent effect via conductor polarizable continuum model (CPCM)/dichloromethane

System	E_{HL}	E	λ	f	Band	Assignment	Main MOs
KMH63	2.11	1.64	756	0.80	Q	$\pi(\text{pht}) \rightarrow \pi^*(\text{pht})$	H → L
		1.66	748	0.88	Q	$\pi(\text{pht}) \rightarrow \pi^*(\text{pht})$	H → L + 1
		3.30	375	0.17	B	$\pi(\text{pht}) \rightarrow \pi^*(\text{pht})$	NTO 14 occ → virt
ZnPc-BZA	2.35	1.89	655	0.77	Q	$\pi(\text{pht}) \rightarrow \pi^*(\text{pht})$	H → L
		1.93	641	0.62	Q	$\pi(\text{pht}) \rightarrow \pi^*(\text{pht})$	H → L + 1
		3.80	327	0.58	B	$\pi(\text{pht}) \rightarrow \pi^*(\text{pht})$	NTO 19 occ → virt

Excitation wavelength (λ/nm), energy (E/eV), oscillator strength (f) and the corresponding molecular orbitals (MOs) involved in the electronic transitions, as also the band assignment. The HOMO–LUMO energy difference (E_{HL}/eV) is also included.

culated at the BP86/Slater-type orbital (STO) basis sets with triple- ζ accuracy plus polarization function (TZP) theoretical level [75].

The presence of tert-Butylbenzenethiol groups in **KMH63** clearly produces an out-of-the-plane deviation of the isoindole moieties by 2°–3°, compared to **ZnPc-BZA** where the macrocycle structure is completely planar. In compound **KMH63**, the optimized conformation displays the phenyl ring of the tert-Butylbenzenethiol substituents perpendicularly to the macrocycle, with average dihedral angles $\langle C_1 - S_1 - C_2 - C_3$ between the phenyl rings of substituent in the α -position from 88.7° to 91.5°. In **KMH63** and **ZnPc-BZA**, the average bond angle formed between isoindole N atoms and Zn (II) ion ($\langle \text{Niso} - \text{Zn} - \text{Niso}$) is 90°. The dihedral angle $\langle C_4 - C_5 - C_6 - C_7$ formed by isoindole units and benzyl ring of the benzoic acid (anchor group) in the β -position does not show significant differences, which is 143.89° and 143.27° for **KMH63** and **ZnPc-BZA**, respectively. The optimized structures for these compounds do not indicate a displacement of Zn(II) ion from the molecular plane defined by the four isoindole N atoms (Scheme 3).

The electronic absorption spectrum of **KMH63** has been simulated using the time-dependent DFT (TDDFT) approach in the solution phase and the analysis of the resulting parameters; excitation wavelength (energy), the oscillator strength and the electronic transitions between MOs, were performed (Table 3). To investigate the effect of the tert-Butylbenzenethiol substituents in the α -positions in the phthalocyanine, we have compared the spec-

trosopic results of **KMH63** with the substituent-free macrocycle (**ZnPc-BZA**) (Scheme 3).

Table 3 shows that both compounds (**KMH63**, **ZnPc-BZA**) present two strong Q bands and one B band of lower intensity, as expected for phthalocyanines, but the presence of the substituents in **KMH63** increases much more the difference in the intensity of the Q and B bands, 0.80(0.88) against 0.17, respectively. Another notorious effect is the redshifting of the two Q bands from **ZnPc-BZA** to **KMH63** by 101 and 107 nm, respectively, and for the B bands in 48 nm. It means that one form to achieve an important absorption near to infrared is to use these kinds of substituents, where the tert-butyl and the benzenethiol are electron donor moieties that inject electron density to the macrocycle. This behavior of the substituents can be seen in the electrostatic potential calculated for the ground state, as shown in Figure 3. The system **ZnPc-BZA** presents four blue regions localized on the aza nitrogen atoms that represent negative regions and charge concentration, as the color scale indicates. The blue region is widely increased along the macrocycle core in **KMH63** indicating a larger charge concentration available to be excited to higher energy levels (LUMOs).

The theoretical value for the Q band of longest wavelength in **KMH63** is well compared with the experimental value measured in this work of 768 nm (1.61 eV), with a very small deviation of 0.03 eV. This confirms that the theoretical method used (M06/6-31G(d,p)) for the simulation of the spectrum has been adequate.

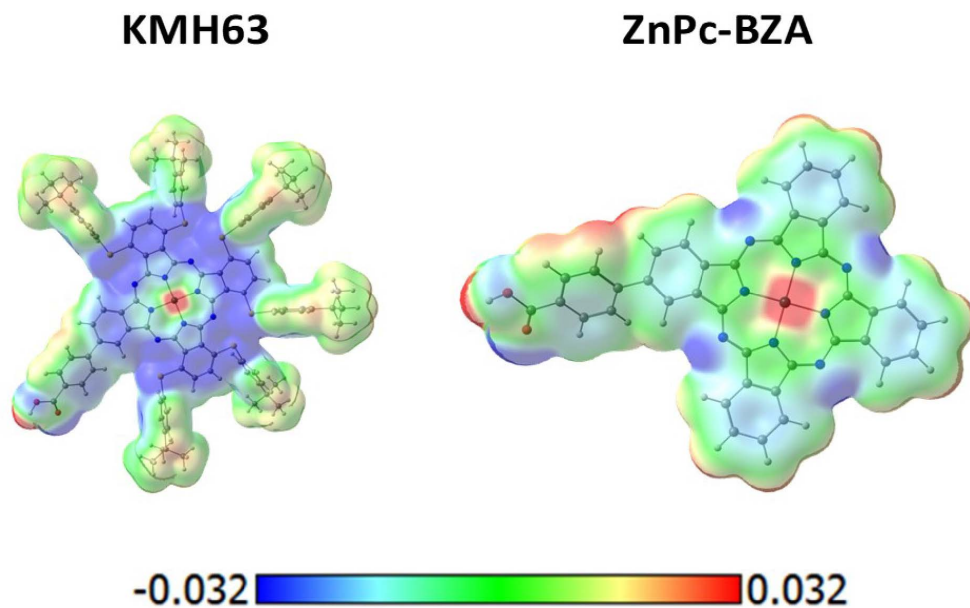


Figure 3. Molecular electrostatic potential calculated at the M06/6-31G(d,p) level of theory in dichloromethane. The color scale is added at the bottom.

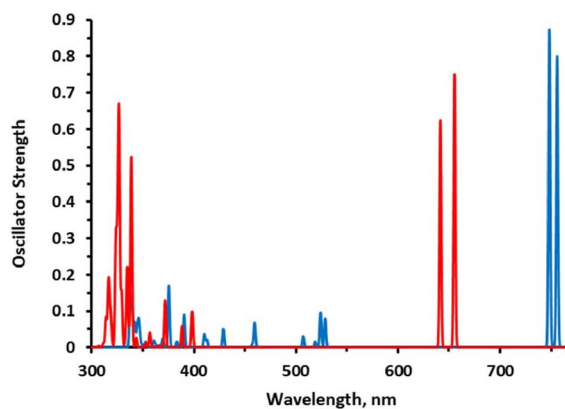
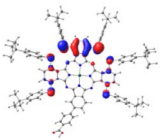
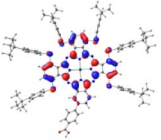
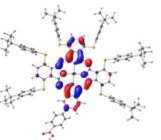
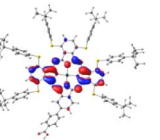
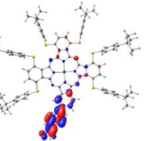
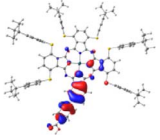
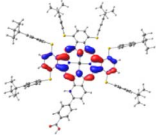



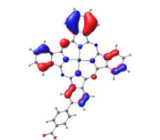
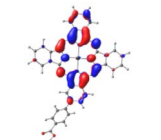


Figure 4. Electronic absorption spectra calculated at the M06/6-31G(d,p) level of theory in dichloromethane; **KMH63** blue and **ZnPc-BZA** red.

Figure 4 shows a comparison of the spectra of **KMH63** and **ZnPc-BZA**, and clearly Q higher and pronounced bands can be seen as also an important bathochromic shifting for the former. For **KMH63** a wider absorption is observed in the B region in about 350–550 nm, but in contrast to the case of **ZnPc-BZA** the absorption is concentrated in a shorter region (300–400 nm), but the bands with a higher intensity near to 300 nm.

Table 4 shows the frontier MOs from HOMO–1 to LUMO+2 to understand the absorption bands calculated as mentioned above. In both systems, the excited states belonging to the two Q bands correspond to the electronic transitions $H \rightarrow L$ and $H \rightarrow L+1$. In both cases, the orbitals are centered mainly on the phthalocyanine macrocycle and there is neither the participation of the substituents nor of the anchor group. These results suggest that the electron

Table 4. Surfaces of the frontier MOs with their energies (eV), and the natural transition orbitals (NTO) calculated at the M06/6-31G(d,p) level of theory in dichloromethane

System	HOMO-1	HOMO	LUMO	LUMO+1	LUMO+2
KMH63					
	-5.886	-4.992	-2.882	-2.859	-1.589
	NTO14 occ	NTO 14 virt			
ZnPc-BZA					
	-6.794	-5.228	-2.880	-2.843	-1.585
	NTO19 occ	NTO 19 virt			
					

injection process from the virtual orbitals (L, L+1) of **KMH63** or **ZnPc-BZA** to the conduction band of the semiconductor (TiO₂) would not be favorable. Zhang and co-workers [76,77] reported that heteroatom-metal interaction in metal phthalocyanines, such as S-Zn, is possible. For this reason, the optimization of J and H dimers (Figure S6) was performed at the B3LYP/6-31G(d,p) level of theory. However, distances of 4.98 Å and 6.67 Å, respectively were found. These distances are much larger than those reported for the Zn-S interaction (2.3 Å–2.6 Å), which evidences the absence of metal-sulfur interactions. This interaction is avoided due to the presence of bulky substituents, which prevents the formation of such aggregates.

However, the theoretical results indicate that the electron injection could occur from L+2 to the semiconductor because it is completely centered on the benzoic acid, but it would require an energy of

3.4 eV (365 nm), very high (UV region) to be an attractive compound to be used in DSSCs. On the other hand, the B bands of **KMH63** and **ZnPc-BZA** that correspond to the excited state 14 and 19, respectively, were analyzed with the natural transition orbitals (NTO). These correspond to transitions between NTOs centered on the macrocycle, as expected for these kinds of bands. All the bands correspond to $\pi \rightarrow \pi^*$ electronic transitions.

In summary, the compound **KMH63** has the advantage over **ZnPc-BZA** in that it presents redshifted absorption and more intense Q bands, although this characteristic is not enough to be a good photosensitizer for DSSCs. The electron injection would not be favorable in the visible light region, as shown by the molecular orbitals.

Finally, the interaction of **KMH63** and **ZnPc-BZA** with a TiO₂ anatase model was simulated. The optimized molecular structures shown in Figure 5

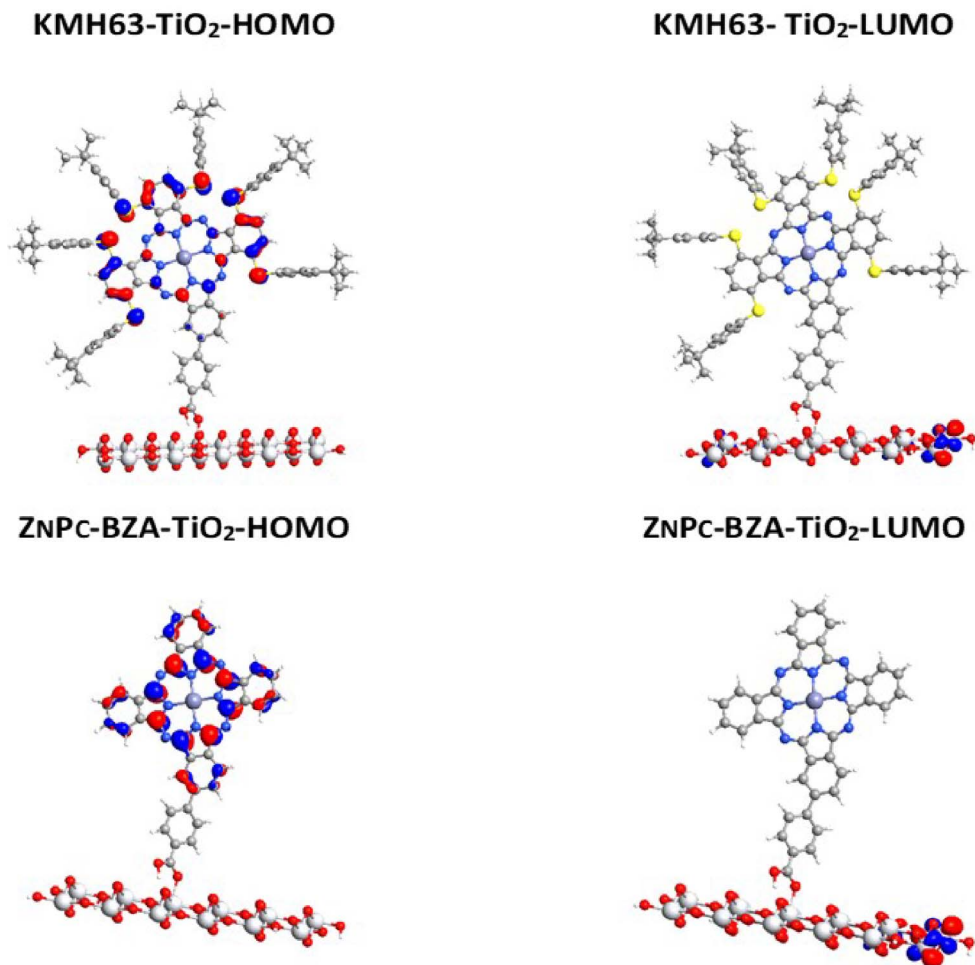


Figure 5. Frontier molecular orbitals for the complexes **KMH63-TiO₂** and **ZnPc-BZA-TiO₂**. Color coding: silver = titanium, red = oxygen, blue = nitrogen, light blue = zinc, gray = carbon, white = hydrogen.

indicate an approaching of the oxygen atom of the carbonyl group ($-\text{O}(\text{C}=\text{O})$) toward one titanium atom with a distance of 2.10 Å in both **KMH63** and **ZnPc-BZA**. The finding is in agreement (2.26 Å) with the adsorption of acetic acid on a surface model of TiO₂ anatase (101) calculated by Manzhos *et al.* [78] using the self-consistent charge density functional tight binding scheme (SCC-DFTB) for a monodentate interaction mode. Furthermore, the hydrogen atom of the hydroxyl group ($-\text{O}(\text{OH})$) shows the formation of a hydrogen bonding with an oxygen atom of TiO₂ cluster with a distance of 1.30 Å for both **KMH63** and **ZnPc-BZA**, which is comparable to the distance calculated by Manzhos *et al.* [78] of 1.62 Å. Our results indicate that the interaction distance

would not be affected by the substituent groups but also confirm that a favorable interaction is given between the $-\text{COOH}$ moiety and both the titanium and oxygen atoms of TiO₂.

We also calculated the interaction energy (E_{int}) and found that both phthalocyanines present a negative value that indicates a favorable interaction between the fragments (**KMH63/ZnPc-BZA** and TiO₂). The complex **KMH63-TiO₂** (−2.6 eV) shows a larger interaction of 0.2 eV (4.6 kcal/mol) than the complex **ZnPc-BZA-TiO₂** (−2.4 eV), although the difference of E_{int} could be considered small. Moreover, the calculations indicate that the three tert-Butylbenzenethiol substituents do not hinder the binding of the phthalocyanine on TiO₂ surface.

Table 5. Photovoltaic parameters for DSSCs sensitized with **KMH63** dye measured under simulated AM 1.5G, 1 Sun illumination

Cell	Additives	TBP	J_{sc} (mA/cm ²)	V_{oc} (mV)	FF (%)	PCE (%)
1	no CDCA	0 M	0.84 ± 0.14	442 ± 2	68 ± 1	0.26 ± 0.04
2	20 mM CDCA	0 M	1.23 ± 0.32	461 ± 7	72 ± 2	0.41 ± 0.12
3	20 mM CDCA	0.2 M	0.47 ± 0.01	559 ± 1	71 ± 2	0.19 ± 0.01

Additionally, we calculated the frontier molecular orbitals of both complexes to confirm their donor–acceptor nature. Figure 5 shows that in both, the donor species is the phthalocyanine because the HOMO is located there, and the acceptor species is the TiO₂ because the LUMO is located on this fragment. However, the HOMO surface of **KMH63** displays that the higher energy electrons are centered in the benzene rings and on the sulfur atoms. In contrast, HOMO surface of **ZnPc-BZA** is concentrated on the pyrrole and the benzene rings. Furthermore, the gap HOMO–LUMO of **KMH63**-TiO₂ (0.39 eV) is lower than that of **ZnPc-BZA**-TiO₂ (0.69 eV), which suggests a more reactive complex in the former and could be of benefit for the charge transfer to the semiconductor TiO₂.

The analysis of the aromaticity reveals a strong diatropic ring current in the main rings of **KMH63** and **ZnPc-BZA**. In addition, the benzenoid rings (6MR) of **KMH63** present a significant reduction in aromaticity due to the substituent effect when compared to **ZnPc-BZA**. Computed indexes show that there is a notable difference in the magnetic response, degree of delocalization, bonding distance and conjugation of the macrocycle. The internal cross of the macrocycle in **KMH63** is less aromatic than **ZnPc-BZA**, as well as the 6MRs, except for those attached to the carboxyl group (See Figure S7 in the SI), which is the most aromatic because it is not affected by the thiophenyl-tert-butyl units and shows similar values for both compounds. Further details can be found in the supporting information.

6. Photovoltaic characterizations

Dye-sensitized solar cells were assembled using **KMH63** as sensitizer on mesoporous TiO₂ as working electrode, platinized conducting glass as the counter electrode and iodide/triiodide in acetonitrile as electrolyte (see experimental part for details). The

photovoltaic performances of solar cells recorded under AM 1.5 are summarized in Table 5 and the current–voltage characteristics are given in supporting information material (Figure S3). The first measurements were performed with two different ratios of CDCA (0 mM and 20 mM) and using an electrolyte without tert-butyl-pyridine (TBP) (composition: 50 mM I₂, 0.1 M LiI, 0.6 M LI in acetonitrile). In the absence of CDCA, the overall performances are lower than those with 20 mM of CDCA, passing from 0.26% to 0.41% power conversion efficiencies (PCEs) owing to weaker J_{sc} , V_{oc} and even FF. This result can be reasonably explained by a diminution of the H-aggregates in the presence of CDCA that certainly quenches the excited state and diminishes electron injection efficiency. Overall, the PCE of this new dye **KMH63** is quite low compared to previous phthalocyanines reported in the literature, which presents very good efficiency around 6% and even higher [16]. In a second step, the addition of TBP in the electrolyte was investigated. TBP is known to adsorb on TiO₂ surface to prevent interfacial charge recombination with the electrolyte and to induce an upward conduction band bending, which enables enhancing of the V_{oc} [79,80]. With TBP, the DSSC exhibits a significant drop of the photocurrent density (from 1.23 to 0.47 mA/cm²), reflecting a lower electron injection quantum yield that might be due to a sluggish injection reaction owing to a decrease of the driving force resulting in a more negative TiO₂ conduction band. This result confirms that the electron injection from the dye to TiO₂ is one the main limiting factors of **KMH63**. Even if the low ΔG_{inj}° is thermodynamically favorable and theoretically permits an efficient electron injection, the driving force and the electronic coupling are certainly too low to guarantee efficient injection. This is consistent with computational studies that show that the spin density of the LUMO orbital in **KMH63**, is poorly distributed on the anchoring group, thus limiting the

electronic communication with the TiO₂ conduction band. In a recent publication, Torres and co-workers reported a very bulky zinc phthalocyanine sensitizer exhibiting similar low PCE as **KMH63** [81]. It was proposed that the low dye loading of this bulky phthalocyanine was at the origin of weak light capture, restricting its light-harvesting efficiency. Although this possibility cannot be fully excluded here, this study shows that upon addition of CDCA in the dye bath, the photoconversion of the solar cell is raised (Table 2), while the dye loading is necessarily decreased as confirmed by the lower coloration of the TiO₂ film (Figure S1). Accordingly, we can conclude that the dye loading of **KMH63** is certainly not the main reason for the low efficiency of this dye.

7. Conclusion

In this study, a new zinc phthalocyanine sensitizer was prepared to explore the possibility of making transparent and colorless DSSCs. The absorption and photoelectrochemical properties indicate that this compound fulfills the criteria for such application. Detailed computational calculations enable a deeper understanding of the electronic properties of this sensitizer and particularly that the presence of bulky thio-aryl substituents does not hinder the approach of the dye on the surface and do not perturb its chemisorption on TiO₂ surface. On the other hand, it was shown that the electronic communication of **KMH63** with TiO₂ conduction is weak owing to the absence of overlapping of LUMO and LUMO+1 with the semiconductor wavefunction, precluding a sluggish electron injection. The modest photovoltaic performances measured in TiO₂-based DSSC are certainly due to inefficient electron injection and could be certainly enhanced with a different spacer connecting the phthalocyanine to the anchoring group. For example, the utilization of a more π -conjugated system such as acrylic acid or cyano-acrylic acid would be more favorable to assist electron injection. We are working towards this goal and the results will be communicated in due course.

Acknowledgments

We acknowledge financial support by Agence Nationale de la Recherche (ANR) through the program Vision-NIR (ANR-17-CE05-0037-02) Région des Pays

de la Loire for the project LUMOMAT and ECOS Sud-CONICYT (Chili). We thank the financial support of ANID/CHILE under the following projects: FONDECYT 1171719 (GC-J) and 1180565 (XZ), FONDECYT Postdoctoral 3180119 (RP-R) and ECOS C19E03 (GC-J, XZ). MZ-A is grateful for the graduate fellowship awarded by the Vicerrectoría de Postgrado (VIPO) of USACH/CHILE, and YH-R is grateful for the PhD Program in Molecular Physical Chemistry from University Andres Bello/CHILE. Powered@NLHPC: This research was partially supported by the supercomputing infrastructure of the NLHPC (ECM-02) of the Universidad de Chile.

Supplementary data

Supporting information for this article is available on the journal's website under <https://doi.org/10.5802/crchim.113> or from the author.

References

- [1] V. V. Tyagi, N. A. A. Rahim, N. A. Rahim, J. A. L. Selvaraj, *Renew. Sustain. Energy Rev.*, 2013, **20**, 443-461.
- [2] B. Joseph, T. Pogrebnaya, B. Kichonge, *Int. J. Photoenergy*, 2019, article no. 5214150.
- [3] E. Ravishankar, M. Charles, Y. Xiong, R. Henry, J. Swift, J. Rech, J. Calero, S. Cho, R. E. Booth, T. Kim, A. H. Balzer, Y. Qin, C. Hoi Yi Ho, F. So, N. Stingelin, A. Amassian, C. Saravitz, W. You, H. Ade, H. Sederoff, B. T. O'Connor, *Cell Rep. Phys. Sci.*, 2021, **2**, article no. 100381.
- [4] A. Dessi, D. A. Chalkias, S. Bilancia, A. Sinicropi, M. Calamante, A. Mordini, A. Karavioti, E. Stathatos, L. Zani, G. Reginato, *Sustain. Energy Fuels*, 2021, **5**, 1171-1183.
- [5] G. P. Kini, S. J. Jeon, D. K. Moon, *Adv. Funct. Mater.*, 2021, **31**, article no. 2007931.
- [6] C. Tuchinda, S. Srivannaboon, H. W. Lim, *J. Am. Acad. Dermatol.*, 2006, **54**, 845-854.
- [7] K. Lee, H.-D. Um, D. Choi, J. Park, N. Kim, H. Kim, K. Seo, *Cell Rep. Phys. Sci.*, 2020, **1**, article no. 100143.
- [8] A. Takeoka, S. Kouzuma, H. Tanaka, H. Inoue, K. Murata, M. Morizane, N. Nakamura, H. Nishiwaki, M. Ohnishi, S. Nakano, Y. Kuwano, *Sol. Energy Mater. Sol. Cells*, 1993, **29**, 243-252.
- [9] Y. Zhao, R. R. Lunt, *Adv. Energy Mater.*, 2013, **3**, 1143-1148.
- [10] R. R. Lunt, V. Bulovic, *Appl. Phys. Lett.*, 2011, **98**, article no. 113305.
- [11] C. Yang, D. Liu, M. Bates, M. C. Barr, R. R. Lunt, *Joule*, 2019, **3**, 1803-1809.
- [12] B. O'Regan, M. Grätzel, *Nature*, 1991, **353**, 737-740.
- [13] M. Freitag, J. Teuscher, Y. Saygili, X. Zhang, F. Giordano, P. Liska, J. Hua, S. M. Zakeeruddin, J.-E. Moser, M. Grätzel, A. Hagfeldt, *Nat. Photonics*, 2017, **11**, 372-378.
- [14] D. Zhang, M. Stojanovic, Y. Ren, Y. Cao, F. T. Eickemeyer, E. Socie, N. Vlachopoulos, J.-E. Moser, S. M. Zakeeruddin,

- A. Hagfeldt, M. Grätzel, *Nat. Commun.*, 2021, **12**, article no. 1777.
- [15] M. Godfroy, J. Liotier, V. M. Mwalukuku, D. Joly, Q. Huaulmé, L. Cabau, C. Aumaitre, Y. Kervella, S. Narbey, F. Oswald, E. Palomares, C. A. G. Flores, G. Oskam, R. Demadrille, *Sustain. Energy Fuels*, 2021, **5**, 144-153.
- [16] S. Aghazada, M. K. Nazeeruddin, *Inorganics*, 2018, **6**, article no. 52.
- [17] T. Higashino, H. Imahori, *Dalton Trans.*, 2014, **44**, 448-463.
- [18] K. Kakiage, Y. Aoyama, T. Yano, K. Oya, J. Fujisawa, M. Hanaya, *Chem. Commun.*, 2015, **51**, 15894-15897.
- [19] P. S. Chandrasekhar, P. K. Parashar, S. K. Swami, V. Dutta, V. K. Komarala, *Phys. Chem. Chem. Phys.*, 2018, **20**, 9651-9658.
- [20] J.-M. Ji, H. Zhou, Y. K. Eom, C. H. Kim, H. K. Kim, *Adv. Energy Mater.*, 2020, **10**, article no. 2000124.
- [21] K. Zhang, C. Qin, X. Yang, A. Islam, S. Zhang, H. Chen, L. Han, *Adv. Energy Mater.*, 2014, **4**, article no. 1301966.
- [22] W. Naim, V. Novelli, I. Nikolinakos, N. Barbero, I. Dzeba, F. Grifoni, Y. Ren, T. Alnasser, A. Velardo, R. Borrelli, S. Haacke, S. M. Zakeeruddin, M. Graetzel, C. Barolo, F. Sauvage, *JACS Au*, 2021, **1**, 409-426.
- [23] T. Ono, T. Yamaguchi, H. Arakawa, *Sol. Energy Mater. Sol. Cells*, 2009, **93**, 831-835.
- [24] W. Ghann, H. Kang, E. Emerson, J. Oh, T. Chavez-Gil, F. Nesbitt, R. Williams, J. Uddin, *Inorganica Chim. Acta*, 2017, **467**, 123-131.
- [25] K. Funabiki, H. Mase, A. Hibino, N. Tanaka, N. Mizuhata, Y. Sakuragi, A. Nakashima, T. Yoshida, Y. Kubota, M. Matsui, *Energy Environ. Sci.*, 2011, **4**, 2186-2192.
- [26] C. Qin, Y. Numata, S. Zhang, X. Yang, A. Islam, K. Zhang, H. Chen, L. Han, *Adv. Funct. Mater.*, 2014, **24**, 3059-3066.
- [27] F. M. Jradi, X. Kang, D. O'Neill, G. Pajares, Y. A. Getmanenko, P. Szymanski, T. C. Parker, M. A. El-Sayed, S. R. Marder, *Chem. Mater.*, 2015, **27**, 2480-2487.
- [28] A. K. Vats, A. Pradhan, S. Hayase, S. S. Pandey, *J. Photochem. Photobiol. A*, 2020, **394**, article no. 112467.
- [29] M. Urbani, M.-E. Ragoussi, M. K. Nazeeruddin, T. Torres, *Coord. Chem. Rev.*, 2019, **381**, 1-64.
- [30] T. Ikeuchi, H. Nomoto, N. Masaki, M. J. Griffith, S. Mori, M. Kimura, *Chem. Commun.*, 2014, **50**, 1941-1943.
- [31] A. Ogunsipe, D. Maree, T. Nyokong, *J. Mol. Struct.*, 2003, **650**, 131-140.
- [32] L. Yu, W. Shi, L. Lin, Y. Guo, R. Li, T. Peng, *Dyes Pigm.*, 2015, **114**, 231-238.
- [33] D. K. Muli, B. L. Carpenter, M. Mayukh, R. A. Ghiladi, D. V. McGrath, *Tetrahedron Lett.*, 2015, **56**, 3541-3545.
- [34] M. Ince, R. Kuboi, T. Ince, K. Yoshimura, D. Motoyoshi, M. Sonobe, R. Kudo, S. Mori, M. Kimura, T. Torres, *Sustain. Energy Fuels*, 2021, **5**, 584-589.
- [35] K. Sakamoto, S. Yoshino, M. Takemoto, K. Sugaya, H. Kubo, T. Komoriya, S. Kamei, S. Furukawa, *J. Porphy. Phthalocyanines*, 2015, **19**, 688-694.
- [36] G. d. I. Torre, C. G. Claessens, T. Torres, *Chem. Commun.*, 2007, 2000-2015.
- [37] K. Sakamoto, S. Yoshino, M. Takemoto, N. Furuya, *J. Porphy. Phthalocyanines*, 2013, **17**, 605-627.
- [38] K. U. Rao, K. Venkateswarlu, *Synlett*, 2018, **29**, 1055-1060.
- [39] V. K. Singh, P. Salvatori, A. Amat, S. Agrawal, F. De Angelis, M. K. Nazeeruddin, N. V. Krishna, L. Giribabu, *Inorganica Chim. Acta*, 2013, **407**, 289-296.
- [40] T. Keleş, Z. Biyiklioglu, E. Güzel, M. Nebioğlu, İ. Şişman, *Appl. Organomet. Chem.*, 2021, **35**, article no. e6076.
- [41] W. Shi, B. Peng, Y. Guo, L. Lin, T. Peng, R. Li, *J. Photochem. Photobiol. A*, 2016, **321**, 248-256.
- [42] M. E. Casida, C. Jamorski, K. C. Casida, D. R. Salahub, *J. Chem. Phys.*, 1998, **108**, 4439-4449.
- [43] F. Furche, R. Ahlrichs, *J. Chem. Phys.*, 2002, **117**, 7433-7447.
- [44] R. E. Stratmann, G. E. Scuseria, M. J. Frisch, *J. Chem. Phys.*, 1998, **109**, 8218-8224.
- [45] C. Van Caillie, R. D. Amos, *Chem. Phys. Lett.*, 1999, **308**, 249-255.
- [46] C. Van Caillie, R. D. Amos, *Chem. Phys. Lett.*, 2000, **317**, 159-164.
- [47] Y. Zhao, D. G. Truhlar, *Theor. Chem. Acc.*, 2008, **120**, 215-241.
- [48] G. Tunç, E. Güzel, İ. Şişman, V. Ahsen, G. Cárdenas-Jirón, A. G. Gürek, *New J. Chem.*, 2019, **43**, 14390-14401.
- [49] G. Cardenas-Jiron, M. Borges-Martínez, E. Sikorski, T. Baruah, *J. Phys. Chem. C*, 2017, **121**, 4859-4872.
- [50] R. Urzúa-Leiva, R. Pino-Rios, G. Cárdenas-Jirón, *Phys. Chem. Chem. Phys.*, 2019, **21**, 4339-4348.
- [51] V. Barone, M. Cossi, *J. Phys. Chem. A*, 1998, **102**, 1995-2001.
- [52] M. Cossi, N. Rega, G. Scalmani, V. Barone, *J. Comput. Chem.*, 2003, **24**, 669-681.
- [53] R. L. Martin, *J. Chem. Phys.*, 2003, **118**, 4775-4777.
- [54] M. J. Frisch, G. W. Trucks, H. B. Schlegel, G. E. Scuseria, M. A. Robb, J. R. Cheeseman, G. Scalmani, V. Barone, B. Mennucci, G. A. Petersson, H. Nakatsuji, X. Li, M. Caricato, A. Marenich, J. Bloino, B. G. Janesko, R. Gomperts, B. Mennucci, H. P. Hratchian, J. V. Ortiz, A. F. Izmaylov, J. L. Sonnenberg, D. Williams-Young, F. Ding, F. Lipparini, F. Egidi, J. Goings, B. Peng, A. Petrone, T. Henderson, D. Ranasinghe, V. G. Zakrzewski, J. Gao, N. Rega, G. Zheng, W. Liang, M. Hada, M. Ehara, K. Toyota, R. Fukuda, J. Hasegawa, M. Ishida, T. Nakajima, Y. Honda, O. Kitao, H. Nakai, T. Vreven, K. Throssell, J. A. Montgomery Jr., J. E. Peralta, F. Ogliaro, M. Bearpark, J. J. Heyd, E. Brothers, K. N. Kudin, V. N. Staroverov, T. Keith, R. Kobayashi, J. Normand, K. Raghavachari, A. Rendell, J. C. Burant, S. S. Iyengar, J. Tomasi, M. Cossi, J. M. Millam, M. Klene, C. Adamo, R. Cammi, J. W. Ochterski, R. L. Martin, K. Morokuma, O. Farkas, J. B. Foresman, D. J. Fox, *Gaussian 09, Revision A.02*, Gaussian, Inc., Wallingford, CT, 2016.
- [55] QuantumATK, Version Q- 2020 .09, Synopsys QuantumATK.
- [56] J. P. Perdew, K. Burke, M. Ernzerhof, *Phys. Rev. Lett.*, 1996, **77**, 3865-3868.
- [57] J. P. Perdew, K. Burke, M. Ernzerhof, *Phys. Rev. Lett.*, 1997, **78**, 1396.
- [58] R. Gershoni-Poranne, A. Stanger, *Chem. Soc. Rev.*, 2015, **44**, 6597-6615.
- [59] K. Wolinski, J. F. Hinton, P. Pulay, *J. Am. Chem. Soc.*, 1990, **112**, 8251-8260.
- [60] D. Sundholm, H. Fliegl, R. J. Berger, *Wiley Interdiscip. Rev. Comput. Mol. Sci.*, 2016, **6**, 639-678.
- [61] C. F. Matta, R. J. Boyd, *The Quantum Theory of Atoms in Molecules: From Solid State to DNA and Drug Design*, John Wiley & Sons, 2007.

- [62] Z. Chen, C. S. Wannere, C. Corminboeuf, R. Puchta, P. V. R. Schleyer, *Chem. Rev.*, 2005, **105**, 3842-3888.
- [63] R. Báez-Grez, L. Ruiz, R. Pino-Rios, W. Tiznado, *RSC Adv.*, 2018, **8**, 13446-13453.
- [64] R. Pino-Rios, G. Cárdenas-Jirón, W. Tiznado, *Phys. Chem. Chem. Phys.*, 2020, **22**, 21267-21274.
- [65] R. Islas, T. Heine, G. Merino, *Acc. Chem. Res.*, 2012, **45**, 215-228.
- [66] T. A. Keith, *TK Gristmill Software, Version 19.02.13*, AIMAll, Overland Park, KS, USA, 2019, <http://aim.tkgristmill.com>.
- [67] E. W. Bethel, H. Childs, C. Hansen, *High Performance Visualization: Enabling Extreme-Scale Scientific Insight*, CRC Press, 2012.
- [68] F. Feixas, E. Matito, J. Poater, M. Solà, *Chem. Soc. Rev.*, 2015, **44**, 6434-6451.
- [69] E. Matito, *Phys. Chem. Chem. Phys.*, 2016, **18**, 11839-11846.
- [70] M. Giambiagi, M. S. de Giambiagi, K. C. Mundim, *Struct. Chem.*, 1990, **1**, 423-427.
- [71] J. Poater, X. Fradera, M. Duran, M. Solà, *Chem. Eur. J.*, 2003, **9**, 400-406.
- [72] J. Kruszewski, T. Krygowski, *Tetrahedron Lett.*, 1972, **13**, 3839-3842.
- [73] T. Lu, F. Chen, *J. Comput. Chem.*, 2012, **33**, 580-592.
- [74] A. G. Martynov, J. Mack, A. K. May, T. Nyokong, Y. G. Gorbunova, A. Y. Tsivadze, *ACS Omega*, 2019, **4**, 7265-7284.
- [75] X. Zarate, E. Schott, T. Gomez, R. Arratia-Pérez, *J. Phys. Chem. A*, 2013, **117**, 430-438.
- [76] X.-F. Zhang, Q. Xi, J. Zhao, *J. Mater. Chem.*, 2010, **20**, 6726-6733.
- [77] W. G. Touw, B. van Beusekom, J. M. G. Evers, G. Vriend, R. P. Joosten, *Acta Crystallogr. D*, 2016, **72**, 1110-1118.
- [78] S. Manzhos, G. Giorgi, K. Yamashita, *Molecules*, 2015, **20**, 3371-3388.
- [79] S. A. Haque, E. Palomares, B. M. Cho, A. N. M. Green, N. Hirata, D. R. Klug, J. R. Durrant, *J. Am. Chem. Soc.*, 2005, **127**, 3456-3462.
- [80] R. Katoh, A. Furube, M. Kasuya, N. Fuke, N. Koide, L. Han, *J. Mater. Chem.*, 2007, **17**, 3190-3196.
- [81] B. Ghazal, K. Azizi, E. F. Ewies, A. S. A. Youssef, V. M. Mwalukuku, R. Demadrille, T. Torres, S. Makhseed, *Molecules*, 2020, **25**, article no. E1692.

Comptes Rendus

Chimie

Objet de la revue

Les *Comptes Rendus Chimie* sont une revue électronique évaluée par les pairs de niveau international, qui couvre l'ensemble des domaines de la discipline. Ils publient principalement des numéros thématiques, mais également des articles originaux de recherche, des annonces préliminaires, des articles de revue, des mises en perspective historiques, des textes à visée pédagogique ou encore des actes de colloque, sans limite de longueur, en anglais ou en français. Les *Comptes Rendus Chimie* sont diffusés selon une politique vertueuse de libre accès diamant, gratuit pour les auteurs (pas de frais de publications) comme pour les lecteurs (libre accès immédiat et pérenne).

Directeur de la publication : Pascale Cossart

Rédacteurs en chef : Pierre Braunstein

Comité scientifique : Rick D. Adams, Didier Astruc, Guy Bertrand, Azzedine Bousseksou, Bruno Chaudret, Avelino Corma, Janine Cossy, Patrick Couvreur, Stefanie Dehnen, Paul J. Dyson, Odile Eisenstein, Marc Fontecave, Pierre Grandclaoudon, Robert Guillaumont, Paul Knochel, Daniel Mansuy, Bernard Meunier, Armando J. L. Pombeiro, Michel Pouchard, Didier Roux, João Rocha, Clément Sanchez, Philippe Sautet, Jean-Pierre Sauvage Patrice Simon, Pierre Sinaÿ

Secrétaire scientifique : Julien Desmarests

À propos de la revue

Toutes les informations concernant la revue, y compris le texte des articles publiés qui est en accès libre intégral, figurent sur le site <https://comptes-rendus.academie-sciences.fr/chimie/>.

Informations à l'attention des auteurs

Pour toute question relative à la soumission des articles, les auteurs peuvent consulter le site <https://comptes-rendus.academie-sciences.fr/chimie/>.

Contact

Académie des sciences
23, quai de Conti, 75006 Paris, France
Tél. : (+33) (0)1 44 41 43 72
CR-Chimie@academie-sciences.fr



Les articles de cette revue sont mis à disposition sous la licence
Creative Commons Attribution 4.0 International (CC-BY 4.0)
<https://creativecommons.org/licenses/by/4.0/deed.fr>

COMPTES RENDUS DE L'ACADÉMIE DES SCIENCES

Chimie

Volume 24, n° S3, 2021

Special issue / Numéro thématique

MAPYRO: the French Fellowship of the Pyrrolic Macrocyclic Ring / *MAPYRO : la communauté française des macrocycles pyrroliques*

Guest editors / Rédacteurs en chef invités

Bernard Boitrel (Institut des Sciences Chimiques de Rennes, CNRS-Université de Rennes 1, France)

Jean Weiss (Institut de Chimie de Strasbourg, CNRS-Université de Strasbourg, France)

Cover illustration / Illustration de couverture

Emily Weiss

Bernard Boitrel, Jean Weiss

MAPYRO: the French Fellowship of the Pyrrolic Macrocyclic Ring 1-2

Guest editors 3-4

Manel Hanana, Christophe Kahlfuss, Jean Weiss, Renaud Cornut, Bruno Jousset, Jennifer A. Wytko, Stéphane Campidelli

ORR activity of metalated phenanthroline-strapped porphyrin adsorbed on carbon nanotubes 5-12

Wael Barakat, Ismail Hijazi, Thierry Roisnel, Vincent Dorcet, Stéphane Le Gac, Bernard Boitrel

Stereoselective formation of bismuth complexes by transmetalation of lead with adaptable overhanging carboxylic acid 5,10-strapped porphyrins 13-26

Paul-Gabriel Julliard, Simon Pascal, Olivier Siri, Diego Cortés-Arriagada, Luis Sanhueza, Gabriel Carnard

Functionalized porphyrins from *meso*-poly-halogeno-alkyl-dipyrromethanes: synthesis and characterization 27-45

Amy Edo-Osagie, Daniel Sánchez-Resca, Dylan Serillon, Elisa Bandini, Christophe Gourlaouen, Henri-Pierre Jacquot de Rouville, Barbara Ventura, Valérie Heitz

Synthesis, electronic and photophysical properties of a bisacridinium-Zn(II) porphyrin conjugate 47-55

Dandan Yao, Limiao Shi, Zhipeng Sun, Mireille Blanchard-Desce, Olivier Mongin, Frédéric Paul, Christine O. Paul-Roth

New fluorescent tetraphenylporphyrin-based dendrimers with alkene-linked fluorenyl antennae designed for oxygen sensitization 57-70

W. Ryan Osterloh, Yuanyuan Fang, Nicolas Desbois, Mario L. Naitana, Stéphane Brandès, Sandrine Pacquelet, Claude P. Gros, Karl M. Kadish

Here's looking at the reduction of noninnocent copper corroles *via* anion induced electron transfer 71-82

Clémence Rose, Laure Lichon, Morgane Daurat, Sébastien Clément, Magali Gary-Bobo, Sébastien Richeter

In vitro toxicity and photodynamic properties of porphyrinoids bearing imidazolium salts and N-heterocyclic carbene gold(I) complexes 83-99

Adelais Trapali, Philipp Gotico, Christian Herrero, Minh-Huong Ha-Thi, Thomas Pino, Winfried Leibl, Georgios Charalambidis, Athanassios Coutsolelos, Zakaria Halime, Ally Aukauloo

Imbroglia at a photoredox-iron-porphyrin catalyst dyad for the photocatalytic CO₂ reduction 101-114

Raphaël Lamare, Romain Ruppert, Mourad Elhabiri, Gilles Ulrich, Laurent Ruhlmann, Jean Weiss

Design and synthesis of charged porphyrin dimers for polyoxometalate recognition 115-126

Soukaina Bouramtane, Ludovic Bretin, Jérémy Godard, Aline Pinon, Yves Champavier, Yann Launay, David Léger, Bertrand Liagre, Vincent Sol, Vincent Chaleix, Frédérique Brégier

Design and synthesis of triphenylphosphonium-porphyrin@xylan nanoparticles for anticancer photodynamic therapy 127-140

Zhaohui Huo, Vasilica Badets, Antoine Bonnefont, Corinne Boudon, Laurent Ruhlmann

Photocatalytic recovery of metals by Lindqvist-type polyoxometalate-porphyrin copolymer 141-155

Thibaut Baron, Ximena Zarate, Yoan Hidalgo-Rosa, Michael Zambrano-Angulo, Kevin Mall-Haidaraly, Ricardo Pino-Ríos, Yann Pellegrin, Fabrice Odobel, Gloria Cárdenas-Jirón

Zinc phthalocyanine absorbance in the near-infrared with application for transparent and colorless dye-sensitized solar cells

157-170

COMPTONS PENNDS GYNIA DE LA CADENHE DES SOCIENORS VOLUNTE 2021